UNIVERSITÉ LAVAL

DEVELOPMENT OF Pb AND Cd CHALCOGENIDE NANOMATERIALS, NANOCOMPOSITES AND THIN FILMS:

SYNTHESIS, CHARACTERIZATION AND APPLICATIONS IN SOLAR CELLS AND PHOTOCATALYSIS

Thèse

JAYESHKUMAR DINESHBHAI PATEL

Doctorat en génie chimique
Philosophiae Doctor (Ph.D.)

Québec, Canada

Résumé

Les Chalcogénures métalliques ont émergé comme une classe importante de matériaux en raison de leur grand potentiel dans de nombreuses applications technologiques. Dans cette thèse, des approches faciles et peu onéreuses ont été adoptées pour développer des nanomatériaux de chalcogénures métalliques et des films minces à partir de leurs précurseurs, les complexes organo-métalliques. L'utilisation des nanomatériaux synthétisés et des couches minces dans les cellules solaires et dans la purification photocatalytique de l'eau a été discutée.

La première approche adoptée implique la synthèse de nanomatériaux de sulfure métallique à partir du complexe metal-thiourée (M-TU) comme précurseur. Des nanocristaux (NCs) de sulfure de plomb (PbS) ainsi que des nanostructures ont été synthétisés à partir des complexes méthanoliques plomb-thiourée (Pb-TU) via diverses techniques de précipitation basées sur la décomposition du complexe méthanolique Pb-TU. Nous avons aussi synthétisé des nanostructures de sulfure de cadmium (CdS) par décomposition hydrothermale et solvothermale du précurseur du complexe cadmium-thiourée mélangé à l'ACA. Les nanostructures de CdS telles que synthétisées ont montré des activités photocatalytiques très efficaces pour la dégradation du méthylorange et de la rhodamine B (RhB) en milieu aqueux.

On a aussi développé des voies simples de synthèse pour préparer des nanomatériaux d'halogénure métallique à partir des complexes (M-O). La sulfurisation des précurseurs du complexe M-O à une température relativement basse produit des nanocristaux de sulfure métallique très stable vu que l'acide oléique (OA) est chimisorbé en tant que carboxylate à la surface des NCs. Le précurseur du complexe oléate de cadmium Cd-O a aussi été utilisé pour préparer des NCs de CdSe. Le traitement de surface des NCs de CdSe ainsi synthétisés avec de la pyridine et du tert-butylamine a été très efficace pour remplacer les ligands AO à longues chaines. Les cellules solaires à hétérojonction volumique fabriquées à partir des NCs de CdSe à surface traitée montrent une meilleure amélioration dans les performances photovoltaiques par rapport aux NCs de CdSe non traités. La décomposition solvothérmale du précurseur du complexe Cd-O mélangé à la thio-urée produit aussi des nanocristaux

composés de microsphères de CdS en forme de chou-fleur ayant de bonnes propriétés physicochimiques et une capacité photocatalytique à dégrader le RhB en milieu aqueux.

La technique de déposition de revêtement par centrifugation 'spin coating' a été utilisée pour fabriquer les films minces de CdS et de PbS à partir de leurs précurseurs, les complexes méthanoliques M-TU. Les films obtenus avaient une surface lisse et affichaient des bandes interdites à taille quantifiée. Les raisons possibles de la faible efficacité des dispositifs de cellules solaires à films minces de CdS/PbS ont été discutées.

Abstract

Metal chalcogenides have emerged as an important class of materials due to their potential significance in many technological applications. In this work, easy and low cost approaches have been developed to prepare metal chalcogenide nanomaterials and thin films from their metal-organic complex precursors. The use of synthesized nanomaterials and thin films in solar cells and photocatalytic water purification has been discussed.

The first approach adopted involves the synthesis of metal sulphide nanomaterials using metal-thiourea (M-TU) complex precursors. Lead sulphide (PbS) nanocrystals (NCs) and nanostructures were synthesized from methanolic lead-thiourea (Pb-TU) complex via various precipitation techniques based on the decomposition of methanolic Pb-TU complex. We have also synthesized cadmium sulphide (CdS) nanostructures through hydrothermal and solvothermal treatment of aminocaproic acid (ACA)-mixed cadmium-thiourea complex precursor. The as-synthesized CdS nanostructures were found to exhibit highly efficient photocatalytic activities for the degradation of methyl orange and rhodamine B (RhB) in aqueous medium.

We have also developed simple synthetic routes to prepare metal chalcogenide nanomaterials from metal-oleate (M-O) complexes. Sulphurizations of M-O complex precursors at relatively low temperatures produced highly stable metal sulphide NCs because oleic acid (OA) is chemisorbed as a carboxylate onto the surface of NCs. The cadmium-oleate (Cd-O) complex precursor was also used to prepare CdSe NCs. Surface treatments of the as-synthesized CdSe NCs with pyridine and tert-butylamine were very effective to replace long chain OA ligands. Bulk-heterojunction solar cells made from surface treated cadmium selenide (CdSe) NCs showed greater improvement in photovoltaic performances compared to those made from untreated CdSe NCs. Solvothermal decomposition of thiourea-mixed Cd-O complex precursor also produced nanocrystals composed of cauliflower-like CdS microspheres with good physicochemical properties and photocatalytic ability to degrade RhB in aqueous medium.

The spin-coating deposition technique was used to develop PbS and CdS thin films from their methanolic M-TU complex precursors. The obtained films had smooth surface and showed size quantized band gaps. The possible reasons behind the low efficiency of CdS/PbS thin film solar cell device were also discussed.

Table of Contents

Foreword

This Ph.D thesis is built in the form of a collection of scientific papers already published, under press, or submitted at the time of the initial thesis deposit.

The thesis is divided into eleven chapters and the objectives of the thesis are elaborated at the end of the introduction chapter (**Chapter 1**). Literature review is presented in **Chapter 2**. In the first part of this chapter, the history and the characterization of solar cells are presented. A background and solution processing strategies of bulk heterojunctions (BHJ) solar cells based on lead (Pb) and cadmium (Cd) chalcogenides are also reviewed. The second and third parts respectively present a review on the preparation of cadmium sulfide (CdS)/lead sulfide (PbS) thin film heterojunction solar cells and CdS nanomaterials for photocatalytic degradation of organic dyes in aqueous medium. **Chapter 3** summaries the characterization techniques used throughout this Ph.D work.

Chapter 4 studies the morphology and size control of PbS nanoparticles produced using methanolic Pb-TU complex via different precipitation techniques. This chapter is published in ***Materials Chemistry and Physics*** 132 (2012) 747-755. I'm the first author of this manuscript.

Chapter 5 presents a simple high yield solvothermal method to prepare star-shape PbS crystals using an environmentally friendly ACA-mixed methanolic Pb-TU complex precursor. The corresponding results are published in ***Materials Letters*** 74 (2012) 183-186. I'm the first author of this manuscript.

Chapter 6 reports a generalized chemical route to prepare OA-capped highly dispersed metal sulphide NCs using M-O complexes. The corresponding results are already published in ***Materials Research Bulletin*** 47 (2012) 2016-2021. I'm the first author of this manuscript.

Chapter 7 presents a new simple route to prepare OA-capped cadmium selenide NCs and their further application in BHJ solar cells after surface modifications. The corresponding results are presently discussed in the form of a manuscript, which is submitted for publication

in ***Journal of Materials Science: Materials in Electronics***. I'm the first author of the manuscript.

Chapter 8 presents i) the spin-coating deposition method used to prepare PbS and CdS thin films and CdS/PbS thin film solar cells from methanolic M-TU complexes, and ii) their specific characterizations. A part of the characterizations used in this chapter are conducted in collaboration with Mr. Devendra Tiwari and Prof. Tapas Kumar Chaudhuri (CHARUSAT, India) who are also the co-authors of this manuscript, presently under preparation. I'm the first author of the manuscript.

Chapter 9 reports a simple solvothermal route to prepare high yield cauliflower-like CdS mesostructures using methanolic cadmium-oleate complex precursor. It also presents the application of these mesostructures in photocatalytic degradation of RhB in aqueous medium. The corresponding results are published in ***Materials Letters*** 110 (2013) 94-97. I'm the first author of this manuscript.

Chapter 10 presents the synthesis of two different CdS nanostructures via hydrothermal and solvothermal routes using ACA-mixed Pb-TU complex precursors along with their application in photocatalytic degradation of RhB and methyl orange. The results are presently under press in ***Journal of Nanoscience and Nanotechnology*** (2014). I'm the first author of this manuscript.

Finally, **Chapter 11** completes the thesis by presenting general conclusions and prospects for future work.

Acknowledgements

I am extremely grateful to Professor Frej Mighri, for his guidance and support during my graduate studies at Université Laval. I am thankful to my associate advisor, Professor Abdellah Ajji (Chemical Engineering Department, École Polytechnique de Montréal) for his advice and guidance during my Ph.D. I am grateful to Dr. Hamed Najari (Chemistry Department, Université Laval), for his help in the fabrication and measurements of solar cell devices. I would also like to thank Yann Giroux for his support and valuable help in the laboratory.

I wish to extend my heartfelt thanks to the present and former team members of Professor Mighri's lab for their friendship and generous help during my Ph.D work: Thi Thuy Duong Vu, Fatma Ben Dhieb, Mohamed Ali Souissi, Hugues Gilbert-Tremblay, Athmouni Nafaa, and Amine Methenni. Especially, Fatma Ben Dhieb helped me to translate the thesis abstracts into French. I would like to extend my sincere gratitude to all the professors, staff and graduate students of Chemical Engineering Department, Université Laval for their assistance and co-operation.

I am also thankful to the Natural Science and Engineering Research Council of Canada (NSERC) and Chemical Engineering Department, Université Laval for their financial support.

My heartfelt gratitude to Professor Tapas Kumar Chaudhuri (Dr. K. C. Patel Research and Development Centre, CHARUSAT, Changa, India) who has been the source of constant motivation, support and guidance throughout my doctoral studies. My special thanks to Chaturkaka, Anjanadidi, Amit, Mitesh, Devendra and Professor Arabinda Ray at Dr. K.C. Patel Research and Development Centre, for their help in some characterizations and useful discussions.

Thank you would not be enough to express my gratitude to my mother, Vitthalmama, Sarlamami, Swatiaunty (Ahmedabad) my sisters (Ushma, Nilpa and Kamini) and my beloved wife Dharti, for their strong support and emotional backing.

My heartfelt thanks to all my close Indian friends Ranjan, Prakash, Priyanka, Sai, Pallavi, Minty, Arojit, Pranavbhai, Kallolda, Wajidbhai, Niraj and Senthil for their friendship, encouragement, and support.

I thank Lord Krishna for his grace and blessings.

Abbreviations

Al	Aluminium
Ag	Silver
Au	Gold
A	Acceptor
AM1.5G	Air Mass 1.5 Global
APFO-3	Poly(2,7-(9,9-dioctyl-fluorene)-alt-5,5-(4',7'-di-2-thienyl-2',1',3'-benzothiadiazole))
AFM	Atomic force microscopy
ACA	Aminocaproic acid
BHJ	Bulk heterojunction
BDT	Benzene-1,3-dithiol
BA	Butylamine
BET	Braunauer-Emmer-Teller
CB	Conduction band
CV	Crystal violate
Cd	Cadmium
CdS	Cadmium sulphide
CdSe	Cadmium selenide
CdTe	Cadmium telluride
$CuInGaSe_2$	Copper indium gallium selenide
$CuInSe_2$	Copper indium selenide
$CuInS_2$	Copper indium sulphide
CZTS	Copper zinc tin sulphide
Ca	Calcium
CBD	Chemical bath deposition
CACBD	Capping assisted chemical bath deposition
CdS	Cadmium sulphide
Cd-O	Cadmium-oleate
Cd-Tu	Cadmium-thiourea

D	Donor
DLS	Dynamic light scattering
EQE	External quantum efficiency
EDAX or EDS	Energy dispersive X-ray spectroscopy
eV	Electron volt
Fe_2O_3	Iron (III) oxide
FF	Fill factor
FTIR	Fourier transform infrared
FWHM	Full width at half maximum
HOMO	Highest occupied molecular orbital
HAD	Hexadecylamine
HA	Hexanoic acid
ITO	Indium tin oxide
In_2S_3	Indium sulphide
LUMO	Lowest unoccupied molecular orbital
MB	Methylene blue
M-TU	Metal-thiourea
MgO	Magnesium oxide
MEG	Multiple exciton generation
MEH-PPV	Poly[2-methoxy-5-(2-ethylhexyloxy)-1,4-phenylenevinylene]
MDMO-PPV	Poly[2-methoxy-5-(3′,7′-dimethyloctyloxy)-1,4-phenylenevinylene]
MA	2-aminoethanethiol hydrochloride,
MACBD	Microwave-assisted chemical bath deposition
M-O	Metal-oleate
MSs	Microspheres
MeO	Methyl orange
n-BT	n-Butanethiol
NPs	Nanoparticles
NCs	Nanocrystals
nm	Nanometer
OC1C10-PPV	Tetrapods and poly(2-methoxy-5-(3′,7′-dimethyloctyloxy)-*p*-

	phenylenevinylene)
OA	Oleic acid
PV	Photovoltaic
Pb	Lead
PbS	Lead sulphide
PbSe	Lead selenide
PbTe	Lead telluride
PCE	Power conversion efficiency
PEDOT:PSS	Poly(3,4-ethylenedioxythiophene)-poly(styrenesulfonate)
P3HT	Poly(3-hexylthiophene-2,5-diyl)
PPVP	Poly(*p*-phenylene vinylene)
PNV	Poly(1,4-naphthalenevinylene).
PDTPBT	Poly(2,6-(*N* -(1-octylnonyl)dithieno[3,2-*b* :20,30- *d*]pyrrole)- *alt*-4,7-(2,1,3-benzothiadiazole))
PDPPTPT	Poly[{2,5-bis(2-hexyldecyl)-2,3,5,6-tetrahydro-3,6-dioxopyrrolo[3,4-c]pyrrole-1,4-diyl}-alt-{[2,20-(1,4-phenylene)bisthiophene]-5,50-diyl}]
PCPDTBT	Poly[2,6-(4,4-bis-(2-ethylhexyl)-4H-cyclopenta[2,1-b;3,4-b′]dithiophene)-alt-4,7-(2,1,3-benzothiadiazole)],
PDTTTPD	2,5-di(thiophen-2-yl)thieno[3,2-b]thiophene and thieno[3,4-c]pyrrole-4,6-dione,
PSBTBT-NH2	Mono-aniline-capped-poly[(4,4'-bis(2-ethylhexyl)dithieno[3,2-b:2',3'-d]silole)-2,6-diyl-alt-(2,1,3-benzothiadiazole)-4,7-diyl],
POP3HT-50	Phosphonate functionalized poly-3-hexylthiophene
P3EBT	Poly(3-(ethyl-4-butanoate) thiophene)
PCBM	Phenyl-C61-butyric acid methyl ester
PL	Photoluminescence
Pb-TU	Lead-thiourea
PVP	Poly(vinyl-pyrrolidone)
QDs	Quantum dots
RhB	Rhodamine B

S	Sulpher
SnS_2	Tin sulphide
$SrTiO_3$	Strontium titanate
Se	Selenium
Si	Silicon
SeU	Selenourea
SEM	Scanning electron microscopy
Se	Selenium
SCBD	Sonochemical bath deposition
Te	Tellurium
TiO_2	Titanium dioxide
TCB	1,2,4-trichlorobenzene
TEM	Transmission electron microscopy
TGA	Thermogravimetric analysis
TOP	Trioctylphosphine
TOPO	Trioctyl phosphine oxide
TEP	Thermoelectric power
TU	Thiourea
t-BA	Tert-butylamine
UV-vis	Ultraviolet-visible spectroscopy
VB	Valence band
XRD	X-ray diffraction
XPS	X-ray photoelectron microscopy
ZnO	Zinc oxide
ZnS	Zinc sulphide

Symbols

Eg	Band gap
λ	Wavelength
E	Photon energy
h	Planck's constant
Hz	Hertz
ν	Frequency of electromagnetic radiation
J	Current density
V	Voltage
P_{max}	Maximum power
I_L	Incident light
J_{sc}	Short-circuit current density
V_{oc}	Open-circuit voltage
η	Conversion efficiency or Dynamic viscosity
Rq	Square roughness
J	Joule
Å	Angstrom
d	Lattice plane distance
θ	Angle of incidence
D	Particle size
E_k	Kinetic energy of photoelectron
ϕ	Spectrophotometer work function
α	Absorption coefficient
D_h	Hydrodynamic diameter
D_t	Translational diffusion coefficient
k_B **or k**	Boltzmann's constant
T	Temperature
n	Amount adsorbed at the relative pressure P/P_o
n_m	Monolayer capacity
c	Constant related exponentially to the heat of adsorption in the first

	adsorbed layer
q_1	Heat of adsorption of the first layer of gas molecules
q_L	Heat of the gas liquefaction
R	Gas constant
α_m	Molecular cross-sectional area
n_m	Monolayer capacity
L	Avogadro constant
t	Time
k_{app}	Apparent degradation rate constant,
C_0	Initial dye concentration
C_t	Concentration measured at any time
p	Hole concentration
p_{n0}	Hole concentration in equilibrium
N_D	Donor concentration
n_i	Intrinsic carrier concentration
N_A	Acceptor concentration
n	Electron concentration
n_{n0}	Electron concentration in equilibrium
S	Siemens
μV	Microvolt
K	Kelvin
N_v	Effactive density of state at valence band
A	Constant depending on scattering
e	Electronic charge
σ	Room temparature dark conductivity
V	Volt
s	Second
cm	Centimeter

Index of Figures

Chapter-2

Chapter-3

Chapter-4

Chapter-5

Chapter-6

Chapter-7

Chapter-8

Chapter-9

Chapter-10

Index of Tables

Chapter 1: Introduction

1.1 General Introduction

Over the last few years, the synthesis of nanomaterials has been intensively pursued, not only for their fundamental scientific interest, but also for their various technological applications.[1] Nanomaterials exhibit very interesting size-dependent electrical, optical, magnetic, and chemical properties that cannot be achieved by their bulk counterparts. Size and shape controlled synthesis of nanomaterials is very important for many future applications because their physical and chemical properties are strongly dependent on their dimensions, which are generally referred to as the quantum size effect.[1,2] The latter is very important in nanomaterials because their properties can be tuned by varying the size and shape. The precise controlled synthesis of the size, shape, chemical composition, crystal structure, and surface chemistry of nanomaterials allows access to their unique properties, which became one of the most challenging issues faced by nanomaterial researchers.

Metal chalcogenide is a chemical compound made from comnbination of metal element and chalcogen anion such as sulphur, selenium or tellurium. There are two different approaches to synthesize metal chalcogenides: the top-down approach (physical processes) and the bottom-up approach (chemical methods). The physical processes can produce nanomaterials on large scale, whereas the synthesis of size-controlled nanomaterials is very difficult to achieve. On the other hand, chemical methods can be used to synthesize uniform nanomaterials with a controlled particle size.[1]

Especially, nanoscale metal chalcogenides have attracted significant attention due to their unique properties, which make them suitable for many technological applications. In the past few years, great emphasis is placed towards the synthesis of various metal chalcogenides in form of NCs, nanostructures and thin films for potential applications in solar cells,[3-8] tunable near-infrared detectors,[9] biological labelling and bio-diagnostics,[10,11] light-emitting diodes,[12,13] lasers,[14,15] thin film transistors,[16] photocatalysis,[17,18] and other nanoscale devices.[19] Metal chalcogenide NCs and nanostructures have been synthesized via various synthesis routes, such as liquid crystals and micelles,[20-22] solventless,[23] microvave-assisted,[24,25] sonochemical,[24] thermolysis of metal-alkanethiolate precursors,[26,27] high

temperature routes based on metal-organic complexes,[28,29] solvothermal and hydrothermal,[30,31] hot injection,[32,33] thermolysis of single-source precursors[34] and green chemical approaches.[35] On the other hand, the deposition of nanostructured metal chalcogenide thin films by vacuum evaporation, sputtering, chemical vapor deposition, spray pyrolysis, electrodeposition, and chemical bath deposition are also well known.[36] Most of growth methods usually require high temperature, a series of complicated procedures, expensive equipment, surfactants, catalysts or templates, which cause a cost increase, contamination and energy-consumption. Therefore, searching for simple, efficient, low cost, and environmentally friendly approaches for the high-yield production of metal chalcogenide NCs, nanostructures and thin films is necessary.

Environmentally friendly reducing agents and nontoxic solvents are some of the key issues that merit significant consideration in a green synthetic strategy. Amino acids have special structures and fascinating self-assembling functions, which make them an appropriate medium for the design and synthesis of metal chalcogenide nanostructures. Recently, biomolecule-assisted synthesis routes became promising for the production of various kinds of metal sulfide nanomaterials.[37,38] Beside the reductive properties of biomolecules, they also have strong shape or size directing functionality in the reaction process.[39]

Up to date, there is a great challenge for the production of nanomaterials and thin films of metal chalcogenides through simple, low cost, and environmentally friendly routes.

1.2 Objectives of the thesis

General objective:

The present Ph.D work has been undertaken with the aim of simple, low cost and environment friendly fabrication of metal chalcogenide nanomaterials and thin films for solar cells and photocatalysis applications.

Specific objectives:

The first objective is to develop simple, low cost, and environmentally friendly synthetic routes to prepare metal chalcogenide nanostructures using M-TU complex precursors.

1. The second objective is to develop simple generalized synthetic route to prepare highly dispersed metal chalcogenide NCs using M-O complex precursors.
2. The third objective is to develop simple ammonia free deposition route to fabricate metal chalcogenide thin films using M-TU complex precursors.
3. The fourth objective is the fabrication of BHJ and thin film solar cells.
4. Implementation of CdS nanostructures into photocatalytic degradation of organic dyes under visible light irradiation is the last objective of this thesis.

1.3 References

1. J. Park, J. Joo, S.G. Kwon, Y. Jang, T. Hyeon, *Angewandte Chemie International Edition* 46 **(2007)** 4630-4660.
2. M.A. El-Sayed, *Accounts of Chemical Research* 37 **(2004)** 326-333.
3. A.A.R. Watt, D. Blake, J.H. Warner, E.A. Thomsen, E.L. Tavenner, H. Rubinsztein-Dunlop, P. Meredith, *Journal of Physics D: Applied Physics* 38 **(2005)** 2006-2012.
4. S. Ren, L.-Y. Chang, S.-K. Lim, J. Zhao, M. Smith, N. Zhao, V. Bulovic, M. Bawendi, S. Gradečak, *Nano Letters* 11 **(2011)** 3998-4002.
5. W.U. Huynh, J.J. Dittmer, A.P. Alivisatos, *Science* 295 **(2002)** 2425-2427.
6. H. Moreno-García, M.T.S. Nair, P.K. Nair, *Thin Solid Films* 519 **(2011)** 2287-2295.
7. K. Ramanathan, M.A. Contreras, C.L. Perkins, S. Asher, F.S. Hasoon, J. Keane, D. Young, M. Romero, W. Metzger, R. Noufi, J. Ward, A. Duda, *Progress in Photovoltaics: Research and Applications* 11 **(2003)** 225-230.
8. J. Hernández-Borja, Y.V. Vorobiev, R. Ramírez-Bon, *Solar Enrgy Materials and Solar Cells* 95 **(2011)** 1882-1888.
9. S.A. McDonald, G. Konstantatos, S. Zhang, P.W. Cyr, E.J.D. Klem, L. Levina, E.H. Sargent, *Natural Materials* 4 **(2005)** 138-142.
10. M. Bruchez Jr, M. Moronne, P. Gin, S. Weiss, A.P. Alivisatos, *Science* 281 **(1998)** 2013-2016.
11. W.C.W. Chan, S.M. Nie, *Science* 281 **(1998)** 2016-2018.
12. P.O. Anikeeva, J.E. Halpert, M.G. Bawendi, V. Bulović, *Nano Letters* 9 **(2009)** 2532 2536.
13. V.L. Colvin, M.C. Schlamp, A.P. Alivisatos, *Nature* 360 **(1994)** 354-357.

14. P.T. Guerreiro, S. Ten, N.F. Borrelli, J. Butty, G.E. Jabbour, *Applied Physics Letters* 71 **(1997)** 1595-1597.
15. V.I. Klimov, A.A. Mikhailovsky, S. Xu, A. Malko, J.A. Hollingsworth, C.A Leatherdale, H.J. Eisler, M.G. Bawendi, *Science* 290 **(2000)** 314-317.
16. X.F. Duan, C.M. Niu, V. Sahi, J. Chen, J.W. Parce, S. Empedocles, J.L Goldman, *Nature* 425 **(2003)** 274-278.
17. A.L. Linsebigler, G. Lu , J. T. Yates, *Chemical Reviews* 95 **(1995)** 735-758.
18. X. Chen, W. Shangguan, *Frontiers in Energy* 7 **(2013)** 111-118.
19. I. Gur, N.A. Fromer, M.L. Geier, A.P.livisatos, *Science* 310 **(2005)** 462-465
20. C. Tura, N. Coombs, O. Dag, *Chemistry of Materials* 17 **(2005)** 573-579.
21. Y. Zhang, Y. Chen, H. Niu, M. Gao, *Small* 2 **(2006)** 1314-1319.
22. W. Xu, D.L. Akins, *Materials Letters* 58 **(2004)** 2623-2626.
23. L. Chen, Y.B. Chen, L.M. Wu, *Journal of American Chemical Society* 126 **(2004)** 16334-16335.
24. Y. Zhao, X-H. Liao, J-M. Hong, J-J. Zhu, *Materials Chemistry Physics* 87 **(2004)** 149-153.
25. T. Ding, J-J. Zhu, *Materials Science and Engineering B* 100 **(2003)** 307-313.
26. M.A. Hines, G.D. Scholes, *Advanced Materials* 15 **(2003)** 1844-1849.
27. T. Kuzuya, S. Yamamuro, T. Hihara, K. Sumiyama, *Chemistry Letters* 33 **(2004)** 352-353.
28. J.H. Yu, J. Joo, H.M. Park, S.-I. Baik, Y.W. Kim, S.C. Kim, T. Hyeon, *Journal of American Chemical Society* 127 **(2005)** 5662-5670.
29. S.-H. Choi, K. An, E.-G. Kim, J.H. Yu, J.H. Kim, T. Hyeon, *Advanced Functional Materials* 19 **(2009)** 1645-1649.
30. G. Li, C. Li, H. Tang, K. Cao, J. Chen, *Materials Research Bulletin* 46 **(2011)** 1072-1079.
31. G.Q. Xu, B. Liu, S.J. Xu, C.H. Chew, S.J. Chua, L.M. Gana, *Journal of Physics and Chemistry of Solids* 61 **(2000)** 829-836.
32. C.B. Murray, D.J Norris, M.G. Bawendi, *Journal of American Chemical Society* 115 **(1993)** 8706-8715.

33. S. Flamee, R. Dierick, M. Cirillo, D.V. Genechten, T. Auberta, Z. Hens, *Dalton Transactions* 42 **(2013)** 12654-12661.
34. J. Aldana, N. Lavelle, Y. Wang, X. Peng, *Journal of American Chemical Society* 127 **(2005)** 2496-2504.
35. Z.A. Peng, X.G. Peng, *Journal of American Chemical Society* 123 **(2001)** 183-184.
36. R.S. Mane, C.D. Lokhande, *Materials Chemistry and Physics* 65 **(2000)** 1-31
37. Y. Guo, L. Jiang, L. Wang, X. Shi, Q. Fang, L. Yang, F. Dong, and C. Shan, *Materials Lett*ers 74 **(2012**) 26-29.
38. C. Mao, D.J. Solis, B.D. Reiss, S.T. Kottmann, R.Y. Sweeney, A. Hayhurst, G. Georgiou, B. Iverson, A.M. Belcher, *Science* 303 **(2004)** 213-217.
39. Q.Y. Lu, F. Gao, S. Komarneni, *Journal of American Chemical Society* 126 **(2004)** 54-55.

Chapter 2: Literature Review

2.1 History of Solar cells

The history of solar electricity has shown since 1970s that human uses a limited portion of its electrical power without burning fossil fuels (coal, oil or natural gas) or creating nuclear fission reactions.[1] The Sun provides a tremendous amount of free, environmentally friendly, quiet and reliable energy. In comparison, Earth's ultimate recoverable resource of oil, estimated at 3 trillion barrels, contains 1.7×10^{22} joules of energy, that the Sun delivers to Earth in 1.5 days.[2] Since 120,000 TW of solar radiation strikes on the surface of Earth, solar conversion systems (10% efficient) covering 0.16% of the land would produce 20 TW of power, nearly twice the annual global energy consumption.[3] Photovoltaic (PV) energy conversion is the most direct way to convert solar radiation into electricity and is based on the PV effect. Edmond Becquerel discovered the PV effect in 1838, when he observed a small voltage and current when two silver halide coated platinum plates immersed in an acidic solution were exposed to light.[4] In 1877, Charles Fritts constructed the first true solar cells (at least, the first resembling modern cell made from only solid materials) by using junctions obtained by coating the semiconductor selenium with an ultrathin, nearly transparent layer of gold. Fritts's device was very inefficient, transforming less than 1% of the absorbed light into electrical energy.[5] Later (in 1946), Russell Ohl patented the modern junction semiconductor solar cell.[6] The modern era of PV started in 1954 when Chapin, Fuller and Pearson obtained a solar efficiency of 6% for a Si junction cell.[7]

PV device can generate electricity for a wide range of applications, scales, and climates; it is a cost-effective way to provide power for remote areas and space applications. The enormous gap between the potential of solar energy and the current underuse of this energy is due to low power conversion efficiencies (PCEs) of PV devices and the cost of materials currently required. The cost effective improvement of PCE is a primarily scientific challenge: breakthroughs in fundamental understanding enable the development of materials and methods potentially leading to PV market progress. Consequently, it is not surprising that a lot of effort is still ongoing on the search for new materials. Requirements for the ideal solar

cell material are: Band gap (Eg) between 1.1 and 1.7 eV to absorb along the maximum visible spectrum;

- Direct band structure;
- Consisting of readily available, non-toxic materials;
- Reproducible deposition technique, suitable for large area;
- Good photovoltaic PCE;
- Long-term stability

Modern research in the area of PV technologies has led to the creation of a vast spectrum of solar cells, which are commonly classified in four generations, differing from each other based on the materials and the processing technologies used to fabricate them. The material used to make the solar cell determines its basic properties, including the typical range of efficiencies. The first generation of solar cells, also known as Si wafer-based PV device, is the dominant technology for terrestrial applications today, accounting for more than 85% of the solar cell market. Single-crystalline and multi-crystalline wafers, used in commercial production, allow PCEs up to 25%,[8] Most of the disadvantages with this first generation comes from the manufacturing process because it requires expensive manufacturing technologies and highly expensive crystalline Si wafers. The second generation of PV materials is based on the use of thin-film deposits of semiconductors, such as amorphous Si, CdTe, $CuInGaSe_2$ or $CuInS_2$.[9] Thin-film technologies reduce the amount of material, consequently lowering the prices. However, it may also reduce the PCE. Indeed, the efficiencies of thin film solar cells tend to be lower compared to conventional solar cells (around 6 to 10%), but manufacturing costs are also lower**.** Third generation solar cells are potentially able to overcome the theoretical efficiency limit of 31-41% for single Eg solar cells.[10] This generation greatly differs from the previous semiconductor devices and does not rely on a traditional p-n junction to separate photogenerated charge carriers.[11,12] Third generation solar cells include low cost technology as found in tandem solar cell,[13] dye-sensitized solar cells,[14] and polymer solar cell (combination of small organic molecules and conjugated polymer).[15,16] The fourth generation of solar cells known as BHJ solar cells provides the combined advantages of both organic and inorganic semiconductors. Hybrid PV devices contain conjugated polymers that absorb light as the donor and transport holes.[17]

Inorganic materials in bulk-heterojunction (BHJ) solar cells are used as the acceptor and electron transporter in the structure. These BHJ solar cells have several advantageous features over their pure inorganic counterparts: lower production costs through solution processing, greater flexibility, lighter weight, and additional versatility provided by the ability to control the shapes and sizes of the inorganic nanocrystals (NCs).[18-20] So far, various BHJ solar cells have been reported using ZnO,[21] TiO_2,[22] PbSe,[23] PbS,[24] CdSe ,[18] CdS,[25] $CuInSe_2$[26] and $CuInS_2$[27] NCs. Over the last few years, Pb and Cd chalcogenide (PbX and CdX, X=S, Se or Te) NCs attracted more attention in BHJ solar cells due to their tunability of Eg via size control[28] and possible multiple exciton generation (MEG).[29-31] Furthermore, the performance of Pb and Cd chalcogenide NCs based BHJ solar cells strongly depends on their size and interface structure in the polymer matrix. The major problem with BHJ solar cells is the lack of the absence of a desirable cooperation between the generation of charge photocarriers and charge carrier transport during the high solubility of NCs in solution processing of films.[32]

2.2 Characterization of solar cells

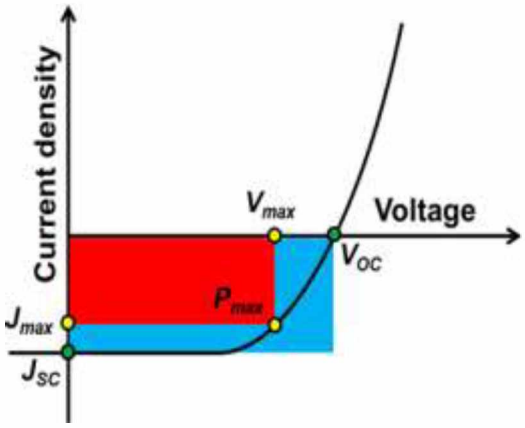

Figure 2.1 *J-V* characteristic of a typical solar cell device under illumination and typical solar cell parameters J_{SC}, V_{OC}, and P_{max} are illustrated on the graph.

Several efficiency definitions are used to describe the electrical characteristics of solar cells under illumination. The most relevant one is the PCE, which is the ratio between the obtainable electrical power (P_{max}), and the incident light power (I_L).

$$\mathrm{PCE} = \frac{P_{\max}}{I_L} \times 100\% \qquad \textbf{(2-1)}$$

The point of P_{max} is located in the fourth quadrant on the current density-voltage (J-V) curve where the product of current density J and voltage V reaches its maximum value **(Figue 2.1).**

In order to relate this maximum power point to the short-circuit current density (J_{SC}), the open-circuit voltage (V_{OC}), and the diode behavior of the solar cell, a fill factor (FF) is introduced. FF describes the ratio of (or the rectangle of) P_{max} with the product of (or the rectangle defined by) J_{SC} and V_{OC}.

$$\mathrm{FF} = \frac{P_{\max}}{J_{SC}V_{OC}} \qquad \textbf{(2-2)}$$

For a simple single-semiconductor photovoltaic model FF lies between 0.25 and 1.0. Equation **(2-1)** can be rewritten in its most practical form as:

$$\mathrm{PCE} = \frac{J_{SC}V_{OC}FF}{\lambda I_L(\lambda)} \times 100\% \qquad \textbf{(2-3)}$$

Therefore, the optimization of the performance of solar cell involves the maximization of the three parameters J_{SC}, V_{OC} and FF. The PCE should be measured under standard test conditions. These conditions consist of a radiant density of 100 mW/cm^2 with a spectral distribution defined as "Air Mass 1.5 Global" (AM1.5G, IEC 904-3) at a cell temperature of 25°C. AM1.5 approximates the intensity of sunlight that would be received on a tilted plane surface during a clear day, and for a model atmosphere containing specified concentrations of water vapor and aerosol. Apart from PCE, the external quantum efficiency (EQE) is often used. The EQE compares the number of charge carriers collected at zero bias (J_{SC}) to the number of incident monochromatic photons:

$$\mathrm{EQE}\,(\lambda) = \frac{1240J_{SC}(\lambda)}{\lambda I_L(\lambda)} \times 100\% \qquad \textbf{(2-4)}$$

where J_{SC} is in mA/cm^2, λ in nm, and I_L in mW/cm^2. The measure of EQE at different wavelengths results in a spectral response of the solar cell. Because the J_{SC} does not necessarily increase linearly with I_L, the EQE values generally depend on the I_L of the monochromatic light. Of course, the same hold for PCE. This explains the necessity for both PCE and EQE measurements to be done under appropriate standard test conditions. Hence, apart from the monochromatic light, continuous irradiation under standard test conditions is required for meaningful comparison of the EQE spectra.

2.3 BHJ solar cells based on Pb and Cd chalcogenides

2.3.1 Materials

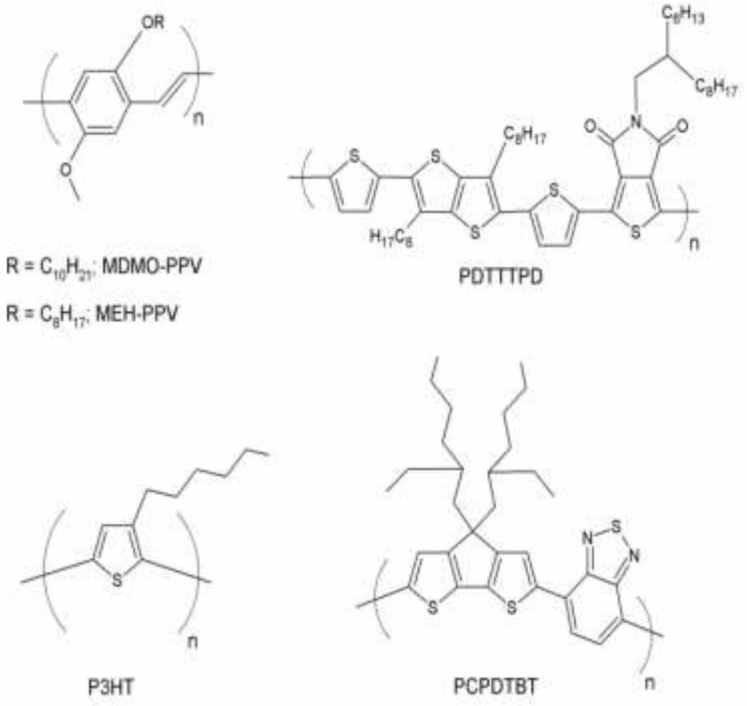

Figure 2.2 Chemical structures of conjugated polymers used as a donor in BHJ solar cells.

So-called BHJ solar cells are the outcome of the replacement of small organic molecules by inorganic semiconductor NCs as electron acceptors. NCs of different size and shape such as PbS, PbSe, PbTe, CdS, CdSe, CdTe, ZnO, TiO_2, SnO_2 and Si are used as acceptors and electron transporters in this type of cells. NCs synthesized in organic media are usually soluble in common organic solvents and can incorporate conjugated polymers soluble in the

same solvent. It is well known that by tuning the size of the NCs, their band gap as well as their energy level can be varied based on the quantum size effect.[33] Furthermore, quantum confinement effect leads to an enhancement of the absorption coefficient compared to that of the bulk materials.[34] Therefore, in the BHJ solar cell, both NCs and polymer have the ability to absorb incident photons. BHJ cells include conjugated polymers that absorb light as the donor and transport holes.[17] **Figure 2.2** shows some chemical structures of p-type semiconducting organic materials commonly used in BHJ solar cells. The device structure and principle of BHJ solar cells are similar to those of polymer solar cells and are described later in detail.

2.3.2 Multiple exciton generation in Pb and Cd chalcogenide nanocrystals

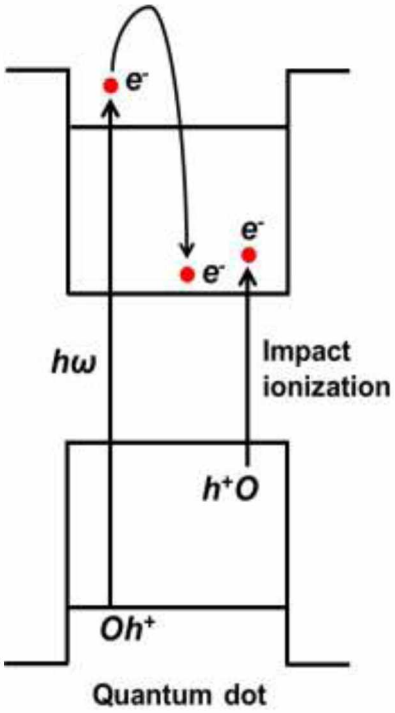

Figure 2.3 In impact ionization, a high-energy exciton created by absorbing a photon of energy ≥2Eg, relaxes to the band edge via transfer of energy to a valence band electron that is concomitantly.

The use of Pb and Cd chalcogenides has the additional advantage of the possibility of MEG.[29-31] Pb and Cd chalcogenide NCs based BHJ solar cells have the potential to reach

efficiencies exceeding the thermodynamic conversion efficiency by utilizing the photon energy above the Eg. Nanosized Pb and Cd chalcogenide crystals can provide a regime where energetic hot carriers produce a second electron-hole pair through impact ionization. Impact ionization is a process where a high-energy exciton, created in a semiconductor by absorbing a photon of energy ≥2Eg, relaxes to the band edge via transfer of energy to a valence band electron that is concomitantly excited above the Eg **(Figure 2.3)**. The result of this energy transfer is that two electron-hole pairs are formed for each absorbed photon. For impact ionization to occur, the rate must be greater than the rate for carrier cooling and any other relaxation process. Because of the slower carrier cooling, NCs can provide a regime where energetic hot carriers produce a second electron-hole pair through impact ionization. Rather than increasing the photovoltage, impact ionization has the potential to increase the photocurrent because more than one electron hole pairs are formed per (high energy) photon. Broad band impact ionization efficiency has been analyzed theoretically by several authors,[35,36] and may give PCEs close to 40% for Eg = 1 eV.[37]

2.3.3 Structure

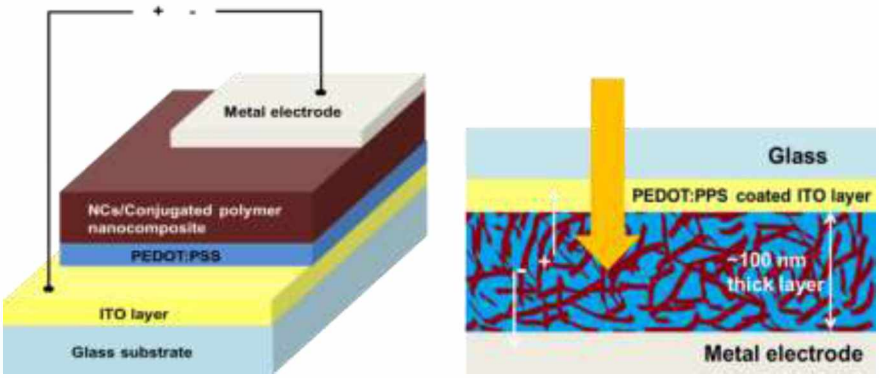

Figure 2.4 Schematic structure of typical BHJ solar cell device.

The structure of BJH solar cell devices consist of a photoactive layer sandwiched between two electrodes of different work functions (**Figure 2.4**). Transparent indium tin oxide (ITO) substrate covered with the conducting polymer mixture PEDOT:PSS is used as the anode. The PEDOT:PSS not only acts as a hole transporter and exaction blocker but it is also used as an anode buffer material for smoothening the ITO surface. The smoothed ITO surface

enhance the adhesion of the upper light absorbing layer, sealing the active layer from oxygen, and keeping the anode material from diffusing into the active layer, which can lead to unwanted trap sites.[38-40] On the top of the PEDOT:PSS, the photoactive layer is usually deposited by spin-coating NCs/conjugated polymer nanocomposite solution to form a thin-film of around 100-200 nm. The cathode, typically made of Al, Ca, Ag and Au is vacuum deposited on top of the photoactive layer.

2.3.4 Working principle

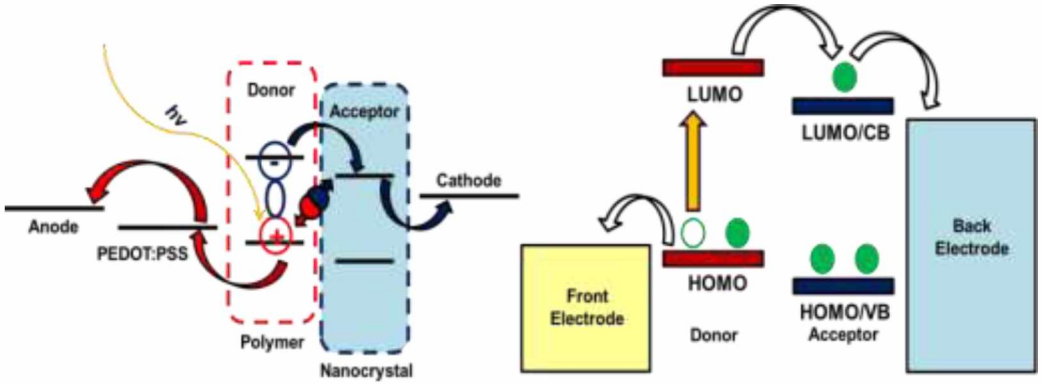

Figure 2.5 Schematics of the different energy levels and the individual processes: (1) excitons generation, (2) excitons diffusion, (3) charge transfer, (4) charge carrier transport and collection.

In contrast to inorganic semiconductors, photoexcitation of organic semiconductors generally results in a strongly bound electron-hole pair, called an exciton.[41,42] In organic semiconductors, these excitons are only effectively separated at an interface between a p-type (electron donating) and n-type (electron accepting) materials. Hence, in BHJ solar cell devices, the second step after absorption of a photon is a photoinduced electron transfer between donor and acceptor type semiconducting materials, yielding a charge-separated state. This photoinduced electron transfer between donor and acceptor boosts the photogeneration of free charge carriers compared to the individual, pure materials. In general, the exciton lifetime and diffusion length in organic semiconductors are limited by radiative and non-radiative decay. In conjugated polymers the exciton diffusion length is about 10-20 nm.[43-45] This implies that for effective charge separation, the photogeneration of excitons

should occur within a few nanometers from a p–n junction. These short exciton diffusion lengths impose an important condition for efficient charge generation. Anywhere in the active layer, the distance to the interface should be on the order of the exciton diffusion length. As shown in **Figure 2.5**, in BHJ solar cells, photocurrent generation is a multistep process and occurs according to the following four main steps;

A. Absorption of photon

In the first step, incident photons (*hv*) are absorbed by the donor/acceptor (D/A) nanocomposite and excite the electrons from the highest occupied molecular orbital (HOMO) to the lowest unoccupied molecular orbital (LUMO) level, creating excitons with a certain binding energy.

B. Diffusion of excitons at D/A interface

In order to generate separated positive and negative charges, the excitons need to diffuse to the D/A interface. As discussed earlier, the exciton diffusion length of conjugated polymers (around 10-20 nm) helps in the charge transfer and excitons dissociate into free charge carriers before recombination takes place.

C. Charge transfer

Excitons dissociate at the D/A interface (**Figure 2.5**): the HOMO level of the polymer is higher than that of the NCs and the LUMO level of the NCs is lower than that of the polymer. The difference in both HOMO and LUMO levels must be larger than the difference between exciton binding energy and columbic binding energy of the charge separated states.[46]

D. Transport of charges towards electrodes for collection

After charge transfer at the D/A interface, separated electrons and holes are distributed within the acceptor and donor phases, respectively. Further, an internal electric field (deriving from the Fermi level difference of the electrodes) contributes in transportation of holes and electrons towards the respective electrodes.

2.4 Solution processed approaches for BHJ solar cells

For the Pb and Cd chalcogenide NCs based BHJ solar cell devices, the following solution processed approaches were investigated to fabricate NCs/conjugated polymer active nanocomposite materials;

1. Direct blending of NCs with conjugated polymers,
2. Blending of NCs with conjugated polymers after surface modification,
3. Direct (in situ) synthesis of NCs in conjugated polymer matrix,

2.4.1 Direct blending of NCs with conjugated polymers

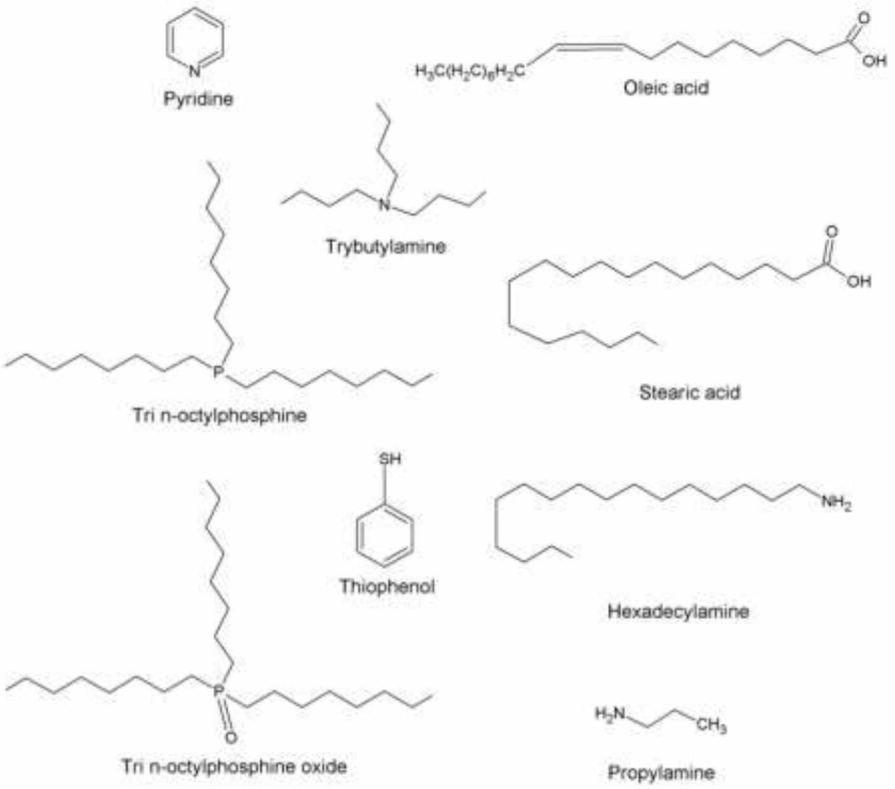

Figure 2.6 Chemical structures of ligands used to cap NCs.

In this approach, NCs are prepared separately and blended directly with conjugated polymers.[24] It's well known that the size and morphology of semiconducting phase plays an important role for efficiency improvement in BHJ solar cells.[18,47] Therefore, NCs of different size and morphology were obtained using various types of surfactants (**Figure 2.6**).

However, in the direct blending approach, the surfactant coating on NCs is incorporated between the polymer matrix and NCs surface, which results in poor charge transfer between NCs and the polymer matrix. Another drawback of direct blending approach is linked to co-solvent requirement because utilization of a co-solvent affects NCs solubility as well as the orientation of polymer chain.[48]

Sargent et al.[49,24] studied nanocomposites consisting of MEH-PPV and PbS NCs via direct blending approach, whose optical absorption was tuned by the quantum size effect. The PV devices consisted of a sandwich structure of glass, an ITO front electrode, a PbS NCs:MEH-PPV active layer, and a Mg back contact. The short-circuit current EQE at 975 nm, however, was extremely small (~0.0008%), which leaves serious doubt as to whether or not the electron transfer between the PbS and MEH-PPV is efficient. In fact, the same authors showed previously that MEH-PPV with embedded PbS NCs transfers the excitation energy rather than a charge after photoexcitation with up to 60% efficiency for ligands with relatively short octylamine side chains.[50] To improve the performance of PV devices, the effect of thermal annealing was investigated. Annealing of PbS NCs:MEH-PPV above 160°C, leads to noticeable changes in J_{SC} and a ~25-fold rise of the EQE (~0.002%).[51] Another attempt was made by Wang et al.,[52,53] where they have synthesized PbS nanoparticles (NPs) and PbS nanorods using MDMO-PPV as a capping material and again dispersed those NPs and nanorods in to MDPO-PPV. In both cases, the efficiencies were extremely low. Jiang et al.[57] were the first to report a PV effect in nanocomposite of P3HT and PbSe NCs via direct blending approach. The thin film devices showed a good diode behavior with PCE of 0.04%, providing evidence of electron transfer between the polymer and PbSe NCs. Also the quenching of PbSe NCs has been studied to gain more understanding of energy and charge transfer in this system. Recently, Yang et al.[61] demonstrated an alternative aqueous processing technique to prepare nanocomposite of water soluble polymer matrix and CdTe NCs. The PV device based on the nanocomposite of water soluble polymer and CdTe NCs had shown PCE of 0.86%. BHJ solar cells based on Pb or Cd chalcogenide NCs/conjugated polymers nanocomposites fabricated via direct blending approach are summarized in **Table 2.1**.

Table 2.1 Summary of BHJ solar cell devices based on direct blending of Pb or Cd chalcogenide NCs.

Author's name	D	A	Ligand	Shape	V_{oc} (V)	J_{sc} (mA/cm^2)	FF	PCE (%)	Illumination (mW/cm^2)	Ref. No.
Wang et al. (2008)	MDMO-PPV	PbS	MDMO-PPV	Quantum dot	0.78	0.025	0.56	0.013	100	52
Wang et al. (2009)	MDMO-PPV	PbS	MDMO-PPV	Nanorod	0.952	0.019	0.53	0.0094	100	53
Guchhait et al. (2011)	P3HT	PbS	OA	Nanoparticle	0.42	1	0.39	0.16	-	54
Seo et al. (2011)	PDTPBT	PbS	OA	Nanocrystal	0.57	13.06	0.51	3.78	100	55
Piliego et al. (2012)	PDPPTPT	PbS	OA	Nanocrystal	0.47	12.5	0.49	2.9	100	56
Jiang et al. (2005)	P3HT	PbSe	OA	Quantum dot	0.4	0.2	0.43	0.04	100	57
Cui et al. (2006)	P3HT	PbSe	OA	Quantum dot	0.35	1.08	0.37	0.14	100	58
Tan et al. (2009)	P3HT	PbSe	OA	Nanocrystal	0.28	0.9	0.39	0.1	100	59
Zhang et al. (2013)	P3HT	PbSe	OA	Quantum dot	0.76	4.16	0.35	1	100	60
Yang et al. (2011)	PNV	CdTe	MA	Nanocrystal	0.44	6.14	0.32	0.86	100	61
Yang et al. (2013)	PNV	CdTe	MA	Nanocrystal	0.36	11.4	0.42	1.74	100	62

2.4.2 Blending of NCs with conjugated polymers after surface modification

In the direct blending approach, low electron mobility transport could be due to the electronic insulating organic ligands on the NC surface.[63] Final charge transfer between NCs and the polymer matrix depends on NCs. In NCs synthesis, long alkyl chain ligands are often use to prevent aggregation during synthesis. Long alkyl chains forms electrically insulating layers on NCs surface, which prevent an efficient charge transfer between NCs and the polymer matrix, as well as electron transfer between NCs.[64,65] To overcome this problem, a surface treatment is carried out to decrease interparticle distance and helping in electron transport through the NC domain phases.

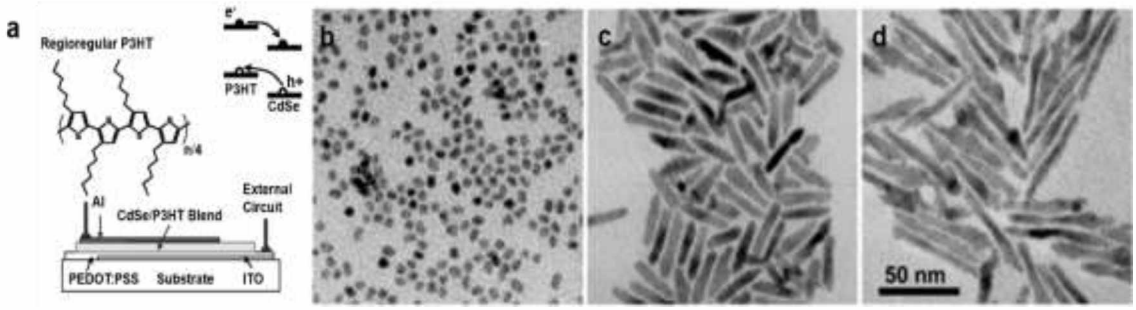

Figure 2.7 The device structure of BHJ solar cell based on CdSe/P3HT nanocomposite (a), TEM pictures of dots (b) and rods (c & d).[18]

Seo et al.[66] developed PbS:P3HT nanocomposite using oleic acid capped PbS NPs. In order to improve the PCE, the BHJ solar cell film was treated with acetic acid. After treatment with acetic acid the PCE increases up to 0.01%. CdSe NCs were the first candidate used in BHJ solar cells and still have the highest PCE compared with BHJ solar cells made of other NCs. A post-synthetic ligand exchange with pyridine is the most effective procedure to improve the efficiencies of CdSe NCs based BHJ solar cells.[64] In this procedure, long alkyl chain capped CdSe NCs are washed by methanol several times and then overnight in pyridine at the boiling point of pyridine under inert atmosphere. After treatment, pyridine replaces the insulating ligand with shorter and more conducting pyridine molecules. After treatment, the CdSe NCs are precipitated with hexenes, recollected by centrifuging and

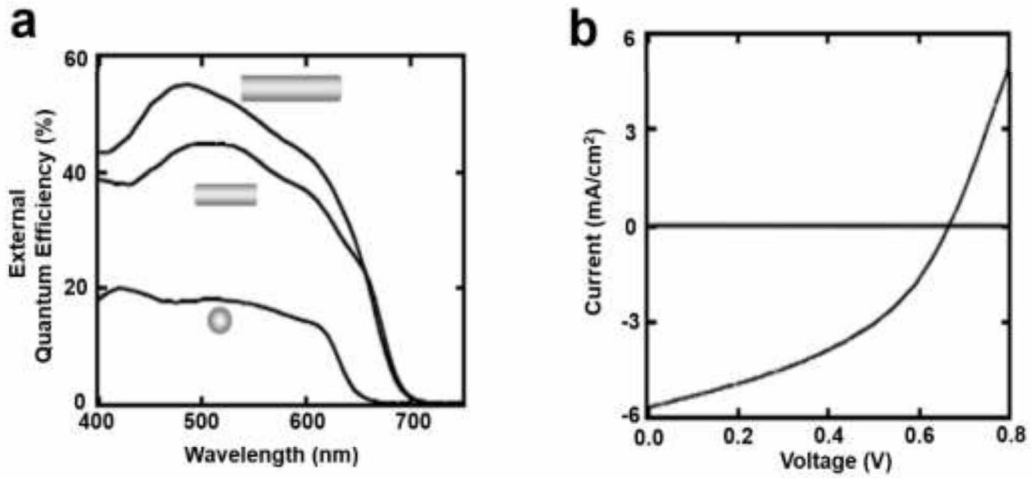

Figure 2.8 Dependence of EQE on the Nanorods length (a). J-V characteristic of a CdSe nanorod (7 nm in diameter, 60 nm in length)/conjugated polymer nanocomposite under AM1.5G illumination (b).[18]

then dispersed into a mixture of chloroform/pyridine (90:10, v/v) solvent. Similar types of treatment with other materials (such as amine, chloride and thiols) were also reported.[69-72] The first examples on surface modified CdSe NCs in poly MEH-PPV showed EQEs up to 12%.[73] In these cells, the surface modified CdSe NCs:MEH-PPV nanocomposite was sandwiched between a transparent ITO front electrode and an Al metal back electrode, to harvest the photogenerated holes and electrons, respectively. It appeared to be of extreme importance to control the surface chemistry of the NCs. The photoinduced electron transfer from conjugated polymers to CdSe has been studied in detail by Greenham et al.[74,75] using photoluminescence and photoinduced absorption spectroscopy for three different PPV derivatives and monodisperse NPs with diameters from 2.5 to 4.0 nm. A major improvement of the PV effect came with the introduction of CdSe rods combined with P3HT.[18,65,76] Surface modified CdSe rods allow a more efficient electron transport through the film, and P3HT. **Figure 2.7** shows the device layout and TEM pictures of CdSe rods and dots. For the film preparation, the challenge is to keep these rods soluble in organic solvents. This has been achieved after surface treatment with pyridine, making the rods soluble in pyridine-chloroform mixtures. PV device prepared in this way shows a PCE of 1.7% **(Figure 2.8)**.[18] One evident drawback of nanorods is that they only improve transport in the direction of their

alignment. CdSe tetrapods, i.e., NCs with four crystalline arms in a tetrahedral configuration, can be used to overcome this drawback, because these tetrahedral branched structures cannot lie in a plane. Sun et al.[47,77] showed that surface treated branched CdSe tetrapods in MDMO-PPV gives an improved electron transport compared to linear CdSe nanorods, leading to solar cells with PCEs of 2.4 to 2.8%. They have also used treated branched CdSe NPs in combination with a reduced Eg copolymer, APFO-3, to improve the absorption of light in visible region.[78] This has resulted in a PV device with a PCE of 2.4%. Li et al.[80] has synthesized a series of ternary tetrapodal NCs of $CdSe_xTe_{1-x}$ with x = 0 (CdTe), 0.23, 0.53, 0.78, and 1 (CdSe), and prepared BHJ solar cells with MEH-PPV as an electron donor via blending approach after surface treatment of NCs with pyridine.[81] They found that the V_{OC}, J_{SC}, and PCE of the devices all increased with decreasing Te content in the $CdSe_xTe_{1-x}$ NCs. Tetrapodal CdSe NCs and MEH-PPV (9:1 w/w) shows the highest PCE (1.13%) under AM1.5 with an EQE of 47% at 510 nm. Recently, Chen et al.[97] reported on an air stable device with a PCE of 3.2% fabricated from the surface treated CdTe tetrapod blended with PSBTBT-NH_2.

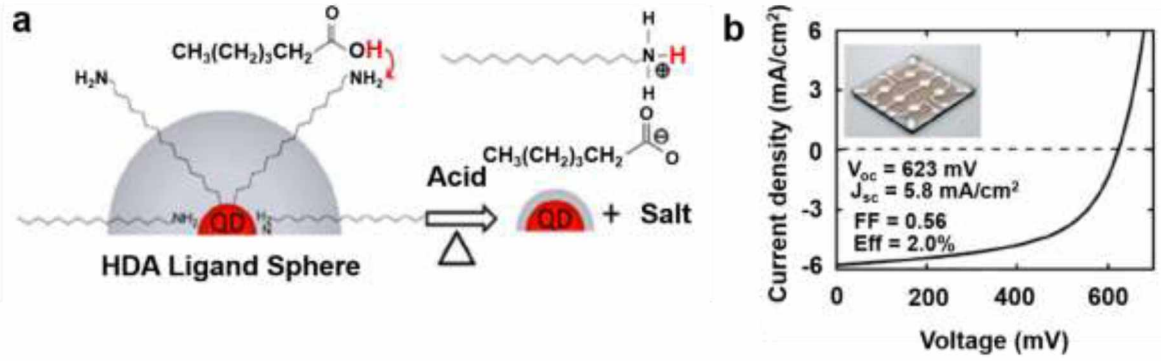

Figure 2.9 Schematic illustration of hexanoic acid treatment (a). *J-V* characteristic of a device containing nanocomposite of CdSe QDs and P3HT as photoactive layer. Inset: photograph of the BHJ solar cell device prototype.[102]

As an alternative to this approach, improvement in the PCE of CdSe NCs/P3HT nanocomposite based device was also achieved by shortening of the insulating ligands by thermal decomposition.[32] Fu et al.[98] investigated BHJ solar cell devices based on surface treated CdSe NCs by short-chain ligands and achieved their highest PCE of 3.09% using

monothiol of *n*-butanethiol (*n*-BT). In a similar way, Greaney el al.[99] also achieved a PCE of 1.9% with a device made from tert-butythiol (*t*BT) treated CdSe NCs blended with P3HT. However, after surface treatment with small molecules, CdSe NCs tend to aggregate and precipitate out from the organic solvent once the long alkyl chain ligands are replaced, which creates stability problems for CdSe NCs:polymer nanocomposites.[18,100] Kwon et al.[101] introduced a new method to improve the performance of P3HT:CdSe nanocomposite based device by using selenourea (SeU) for ligand exchange. SeU induces interconnection of CdSe nanorods, which helps in efficient charge transport and results in improved PCEs from 1.71% to 2.63%. In a different way, Zhou et al.[102] demonstrated a novel non-ligand exchange post-synthetic treatment on CdSe quantum dots (QDs). According to this approach, QDs were treated by a simple and fast hexanoic acid (HA)-assisted washing procedure. Devices based on these QDs and P3HT nanocomposites exhibited reproducible PCEs up to 2% with optimized ratios of QDs to P3HT **(Figure 2.9)**. Recently, Fu et al.[103] reported post- deposition ligand exchange by acetic acid and achieved PCE of about 2% in CdSe QDs/P3HT device. BHJ solar cells based on Pb or Cd chalcogenide NCs/conjugated polymers nanocomposite fabricated through the surface modification approach are summarized in **Table 2.2**.

Table 2.2 Summary of BHJ solar cell devices based on blending of Pb or Cd chalcogenide NCs with conjugated polymers after surface modification.

Author's name	D	A	Treatment	Shape	V_{oc} (V)	J_{sc} (mA/cm^2)	FF	PCE (%)	Illumination (mW/cm^2)	Ref. No.
Seo et al. (2009)	P3HT	PbS	Acetic acid	Nanocrystal	0.35	0.04	0.36	0.01	90	66
Wang et al. (2007)	MEH-PPV	CdS	Pyridine	Multiarmed nanorod	0.85	2.96	0.46	1.17	100	67
Ren et al. (2011)	P3HT	CdS	BA	Quantum dot	1.1	10.9	0.35	4.1	100	68
Huynh et al. (2002)	P3HT	CdSe	Pyridine	Nanorod	0.7	5.7	0.4	1.7	100	18
Wang et al. (2006)	APFO-3	CdSe	Pyridine	Branched nanoparticle	0.95	7.23	0.38	2.4	100	78
Sun et al. (2006)	P3HT	CdSe	Pyridine	Nanorod	0.62	8.79	0.5	2.9	92	79
Zhou et al. (2006)	MEH-PPV	CdSe	Pyridine	Tetrapod	0.69	2.86	0.46	1.13	80	81
Gur et al. (2007)	P3HT	CdSe	Pyridine	Hyperbranched nanorod	0.6	-	-	2.18	100	82
Olson et al. (2009)	P3HT	CdSe	BA	Nanocrystal	0.55	6.9	0.47	1.8	100	69
Heinemann et al. (2009)	P3HT	CdSe	Pyridine	Nanocrystal	0.67	2.6	0.36	0.65	100	83
Dayal et al. (2010)	PCPDTBT	CdSe	Pyridine	Tetrapod	0.678	10.1	0.51	3.19	100	84
Wu et al. (2010)	P3HT	CdSe	Pyridine	Nanorod	0.553	9.7	0.49	2.65	100	85
Lokteva et al. (2010)	P3HT	CdSe	Pyridine	Quantum dot	0.5	1.15	0.49	0.3	100	86
Zhou et al. (2011)	P3HT	CdSe	HA	Quantum dot	0.6	6	0.56	2.1	100	87
Zhou et al. (2011)	PCPDTBT	CdSe	HA	Quantum dot	0.58	8.1	0.55	2.7	100	87
Park et al. (2011)	P3HT	CdSe	Pyridine	Nanoparticle	0.45	1.4	0.36	0.23	-	88
Zhou et al. (2011)	PCPDTBT	CdSe	HA	Nanorod: quantum dot	0.63	8.6	0.56	3.1	100	89

Table 2.3 Summary of BHJ solar cell devices based on blending of Pb or Cd chalcogenide NCs with conjugated polymers after surface modification (continue).

Kuo et al. (2011)	PDTTTPD	CdSe	Pyridine	Tetrapod	0.88	7.26	0.46	2.9	100	90
Radychev et al. (2011)	P3HT	CdSe	Pyridine	Quantum dot	0.78	5.5	0.47	2	100	91
Jeltsch et al. (2012)	PCPDTBT	CdSe	Pyridine	Nanorod: quantum dot	0.48	13.86	0.51	3.64	100	92
Lek et al. (2012)	PCDTBT	CdSe	Pyridine	Nanorod	0.67	6.17	0.46	1.91	100	93
Lek et al. (2012)	P3HT	CdSe	Pyridine	Nanorod	0.52	4.68	0.55	1.35	100	93
Celik et al. (2012)	PCPDTBT	CdSe	Pyridine	Nanorod	0.63	12.1	0.45	3.42	100	94
Park et al. (2012)	P3HT	CdSe	BA	Nanoparticle	0.7	2.69	0.61	1.17	100	95
Fu et al. (2012)	P3HT	CdSe	*n*-BT	Quantum dot	0.68	7.91	0.50	3	100	98
Greaney et al. (2012)	P3HT	CdSe	tBT	Nanocrystal	0.8	5.62	0.43	1.9	100	99
Qiao et al. (2013)	P3HT	CdSe	Pyridine	Quantum dot	0.49	0.37	0.48	1.22	100	96
Kwon et al. (2013)	P3HT	CdSe	Pyridine	Nanorod	0.613	8.4	0.51	2.63	100	101
Zhou et al. (2006)	MEH-PPV	CdTe	Pyridine	Tetrapod	0.33	0.024	0.33	0.003	80	81
Chen et al. (2011)	PSBTBT-NH_2	CdTe	Pyridine	Tetrapod	0.79	7.23	0.56	3.2	100	97
Zhou et al. (2010)	P3HT	CdSe	HA	Quantum dot	0.623	5.8	0.56	2	100	102
Fu et al. (2013)	P3HT	CdSe	Pyridine & Acetic acid	Quantum dot	0.65	5.40	0.56	1.95	100	103

2.4.3 Direct (in situ) synthesis of NCs in conjugated polymer matrix

Another solution processed approach was adopted to prepare in situ Pb or Cd chalcogenide NCs network in conjugated polymer matrix, where the polymer matrix works as a size and growth directing template. In this approach, NCs being synthesized directly in the polymer matrix without surfactant and resulted nanocomposite was used to deposit an active layer. Conversely, film layer from the precursor contained conjugated polymer and soluble inorganic components treated thermally after deposition to convert inorganic components into NCs.[104] On the contrary, in situ synthetic approaches provide better control of stoichiometry and prevent separation of NCs from the polymer matrix as the NCs growth is directly promoted in the polymer matrix.[105,106] However, this approach is not suitable for the preparation of nanocomposites with flexible and large-range tunable properties because it is not possible to control the stoichiometry of the inorganic NCs as well as to tailor their size and size dispersion.[107] These drawbacks are completely overcome if a unimolecular precursor, containing both the metal and the nonmetal part of the NC, is directly introduced into the polymer matrix, and the precursor solution or films are subsequently thermally treated in order to induce the decomposition for the NC nucleation and growth [104-106]. In situ decomposition of a metal sulphide precursor in the polymer matrix may also results in strong interaction between NCs and host polymer matrix which can improve optoelectronic properties of NCs/polymer nanocomposites.[108-110] The major problem with in situ approach is regarding the solubility of inorganic and organic materials. However, an appropriate selection of miscible solvents in both cases may help to overcome this problem.

Watt et al.[111-115] reported the in situ synthesis of PbS NCs in conjugated polymers and achieved a PCE of 0.7 %. Another BHJ solar cell device based on PbS NCs/POP3HT-50 nanocomposite synthesized through Watts's method was also reported with a PCE of 0.011%[116]. Alternatively, metal sulphide NCs/P3EBT nanocomposite layers also prepared via solid state in situ reaction using thiourea and metal acetates. However, performance of the resulted BHJ solar cell devices remains modest due to formation of non-volatile by-products after thermal treatment.[117] Recently, numerous in situ synthetic pathways have been reported for the synthesis of CdS NCs in conjugated polymers.[104,107,11-122] Liao et al.[118] explored the in situ synthetic route to prepare single-crystal nanorods using P3HT matrix as

a soft template. The nanorods with higher aspect ratios forming a connected network in P3HT provide pathways for electron transport, improving the PCE to 2.9%. The controlled in situ low temperature thermal decomposition of cadmium xanthate precursor is the ideal way to form CdS network in P3HT matrix. Such a CdS/P3HT nanocomposite film has been shown to exhibit high yield and long-lived charge photogeneration for an efficient photovoltaic device with a PCE of 0.7% upon illumination at 100mW/cm^2.[104] Further, a study of Dowland et al.[120] showed that nanomorphology, photogeneration and PV performance of the CdS/P3HT nanocomposite films synthesized via a cadmium xanthate precursor route are strongly dependent on annealing temperature. They found the best PCE of 2.17% for a nanocomposite film baked at 160 °C. The same kind of unimolecular precursor based on cadmium-bis(benzylthiolates) was also invented for the fabrication of polymer/CdS nanocomposite materials through a simple and inexpensive synthetic route.[107] However this in situ approach is not limited to PbS or CdS only but is also known for CdSe and CdTe.[123-126] Recently, the in situ synthesis of P3HT capped superstructures and their further application in BHJ solar cell was reported by Peng et al.[125] Importantly, the amount of P3HT has no effect on CdSe superstructure and phases but the presence of P3HT on CdSe superstructure surface enhances their absorption and emission properties. The PV device based on P3HT-capped superstructures demonstrated an overall PCE of 1.32%. Similarly, in situ synthesis of CdTe NCs in P3HT was also reported recently and further use of these P3HT capped CdTe NCs in blending with PCBM resulted in a PV active blend with a PCE of 0.79%.[126,127] BHJ solar cells based on Pb or Cd chalcogenide NCs/conjugated polymers nanocomposite fabricated via in situ approach are summarized in **Table 2.3**.

Table 2.4 Summary of BHJ solar cell devices based on in situ synthesis of Pb or Cd chalcogenide NCs in conjugated polymer matrix.

Author's name	D	A	Shape	V_{oc} (V)	J_{sc} (mA/cm^2)	FF	PCE (%)	Illumination (mW/cm^2)	Ref. No.
Watt et al. (2007)	MEH-PPV	PbS	Nanocrystal	1	0.13	0.28	0.7	5	115
Zhou et al. (2011)	POP3HT-50	PbS	Nanocrystal	0.72	0.082	0.19	0.011	100	116
Maier et al. (2011)	P3EBT	CdS	Nanoparticle	0.51	0.46	0.28	0.06	100	117
Leventis et al. (2010)	P3HT	CdS	Nanostructure	0.61	3.54	0.33	0.72	100	104
Liao et al. (2010)	P3HT	CdS	Nanorod	-	-	-	2.9	-	118
Dowland et al. (2011)	P3HT	CdS	Nanocrystal	0.84	4.8	0.53	2.17	100	120
Peng et al. (2013)	P3HT	CdSe	Superstructure	0.54	4.25	0.57	1.32	100	125
Khan et al. (2011)	P3HT	CdTe	Nanocrystal	0.8	3.88	0.32	0.79	80	127

2.5 Limiting factors and additional strategies for the PCE improvement

The performance of the BHJ solar cell devices depends on exciton generation, charge separation and charge transport towards electrodes. Any factors supporting this procedure are advantageous to the improvement in PCE of BHJ solar cell. NCs network within the polymer matrix is necessary for the PCE improvement. The D/A interface structure and interparticle distance decides the final charge transport and electron transfer. Therefore, the morphology control of the composite film at the nanoscale level is the next important factor for the PCE improvement in BHJ solar cells.[128-129]

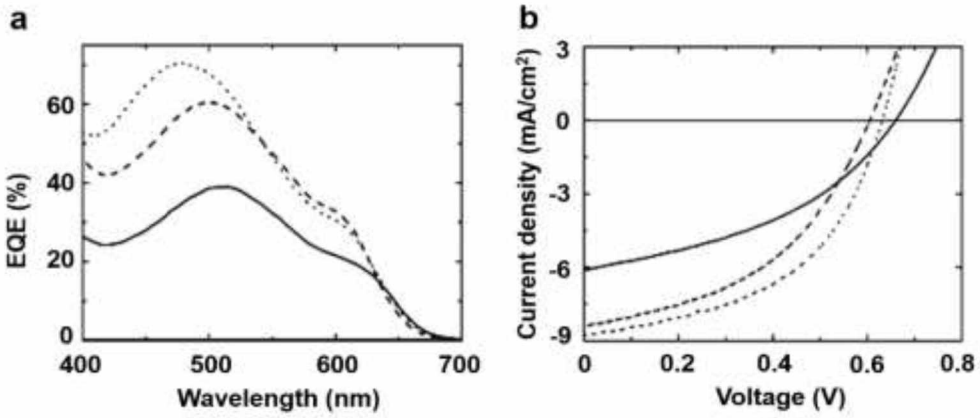

Figure 2.10. EQE spectra of BHJ solar cells with 90 wt% CdSe nanorods and P3HT fabricated by using chloroform (solid line), thiophene (dashed line) and TCB (dotted line) (a). *J-V* characteristics for the same devices under AM1.5G illumination (b).[79]

Huynh et al.[65] have investigated the morphology control in CdSe NC/P3HT BHJ solar cells . Solvent mixtures of chloroform and pyridine were used to control the nanomorphology of composite films. The nanoscale phase separation between NCs and polymer could be adjusted by varying the concentration of the solvent mixture. An optimum concentration of pyridine in chloroform of about 8% by volume was observed. In addition, using suitable solvents for processing NCs/polymer nanocomposites has been demonstrated as another crucial approach for nanomorphology control. Sun et al.[77] reported on improved PCE up to 2.8% for branched CdSe NCs/OC_1C_{10}-PPV BHJ solar cell device treated with TCB solvent. The CdSe tetrapods seem to favorably segregate towards the

vertical direction to the electrodes, which is beneficial for efficient electron transport through the NC phases.[77] In a similar way, **Figure 2.10** shows the comparison of EQE and *J-V* characteristics for CdSe nanorods/P3HT BHJ solar cell devices fabricated by using TCB, thiophene and chloroform as solvents for the materials during the spin coating of the respective photoactive layers. By using TCB as solvent, a significant improvement in the EQE and the J_{SC} of the device projected that the slow evaporation rate during the spin-coating process results in a favorable ordering of P3HT, which improves the hole mobility.[79]

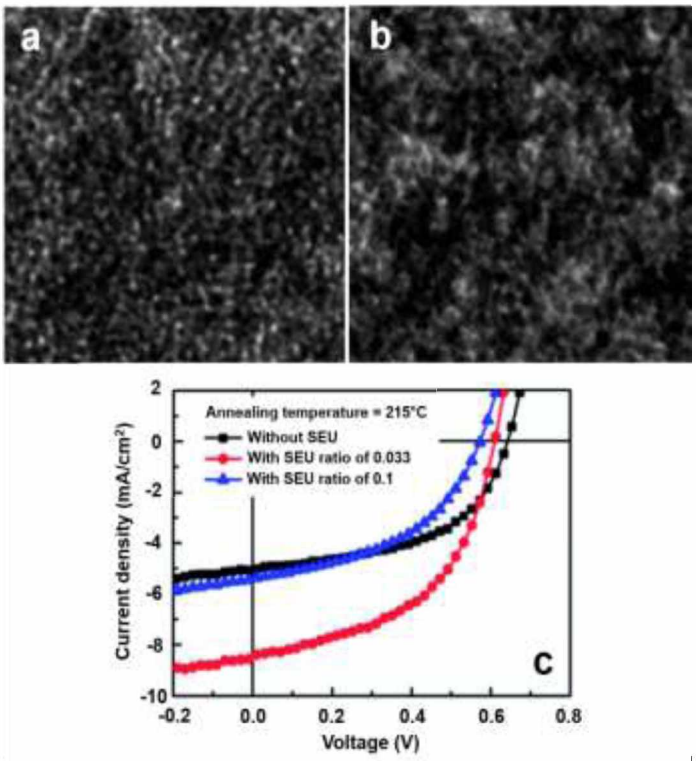

Figure 2. 11 TEM images of CdSe/P3HT nanocomposite without (a) and with (b) SEU. *J-V* characteristic curves of CdSe/P3HT device with and without SEU after annealing at 215 °C (c).[101]

Thermal and solvent annealing has also been found to be an effective ways to control the nanomorphology of composite films thus enhancing PCEs of the BHJ solar cells.[65, 69, 97] It is well known that thermal annealing induces the crystallization of P3HT and improves the absorption and hole mobility of P3HT in nanocomposite films.[130] Furthermore, the PCE of CdSe nanorods/P3HT was improved from 1.71 to 2.63% after addition of SEU for ligand

exchange (**Figure 2.11**). After thermal annealing at 215 °C, SeU was completely decomposed into selenide and induced the interconnection of CdSe nanorods in the nanoscale range without severe aggregation, thus electron transport toward the cathode was greatly enhanced.[101] Wu el al.[85] has demonstrated an approach to enhance the charge separation and charge transport by using chemical vapor annealing treatment. A film of CdSe nanorods/P3HT nanocomposite was put in a closed glass vessel while the film was still wet. Benzene-1,3-dithiol was then added at the bottom edge of the vessel and the whole vessel was heated to 120 °C and kept for 20 min. Compared to the non-treated devices, the PCEs improved significantly from 1.56% to 2.65%, along with an enhancement of J_{SC} from 5.8 mA/cm^{-2} to 9.7 mA/cm^{2}. Chen el al.[97] also reported on the functionalization of the PSBTBT-NH_2 with a mono-aniline-capped anchoring group and improved nanomorphology through the BDT solvent vapor annealing of the CdTe/PSBTBT-NH_2 device with an excellent PCE of 3.2%.

Polymer side chain modification is one of the ways to improve the dispersion and electronic interaction between the polymer and NCs.[131] The amine group in the polymer provides for interactions with NCs through covalent bonding.[108] The pyridine -treated CdSe nanorods can form well dispersed nanocomposite with amine-terminated regioregular P3HT, exhibiting a maximum PCE of 1.4%. The functionalized P3HT is expected to provide intimate contact between NCs and polymer through covalent interactions, thereby enhancing the dispersion of CdSe nanorods in P3HT matrix, and resulting in a favorable morphology improving the charge transfer.[132] Further, the functionalization of P3HT end-groups using H/(-SH), H/Br, and Br/allyl as terminating chemical groups have also been reported recently. BHJ solar cell devices with CdSe QDs and Br/allyl -terminated and H/(-SH)-terminated P3HT led to efficiencies of 0.9% and 0.6%, respectively.[133] Dayal et al.[123] successfully synthesized homogeneously dispersed CdSe NCs in P3HT solution directly. Photoinduced charge separation was observed, indicating that this nanocomposite could be promising material for BHJ solar cells.

2.6 Thin film heterojunction solar cells

As an alternative to widely used Si based homojunction solar cells, research interest is presently focused on the development of thin film based p-n heterojunction solar cells. The easy preparation of these semiconductors by physical and chemical methods, together with their stability and high absorption co-efficient encourages their use for solar energy conversion. The unique interfacial structure between window (n-type) and absorber (p-type) layer attributes the efficient conversion of light energy.

The II-VI and IV-VI semiconductors offer a spectrum of materials having superior optical conversion efficiencies due to their band gap energy that covers the entire wavelength range of solar light. These semiconductors have a direct band gap with sharp optical edge and large absorption coefficient at above band gap wavelengths. They also have higher band gap energy due to their larger ionicity and high carrier effective mass, while the radiative carrier life time and carrier diffusion lengths are small.[134] Silicon, an indirect band gap material (E_g=1.1 eV), is a material of choice for more than 90 % of phtovoltaïc production. However, the major drawbacks of a silicon solar cell originate from its high fabrication cost, shortage of silicon feedback and its low absorption coefficient (100 cm^{-1}), which require several hundred microns of thickness to absorb most of the incident light.[135,136] Although amorphous silicon solar cells are also used, they are sensitive for degradation upon exposure to sunlight with an efficiency loss of 10-20 %.[137] Therefore, research interest is focused on the development of other types of solar cells.

2.6.1 Device structure and working principle

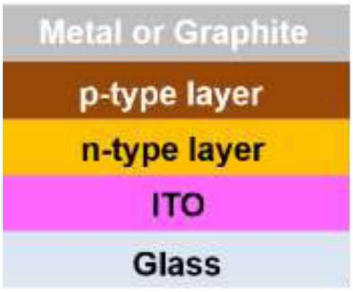

Figure 2.12 Schemetic of thin film heterojunction solar cell.

The working principle of all solar cells is essentially the same. In general, it consists of the generation of a potential difference at the junction of two different materials in response to visible or other radiation. Thin film heterojunction solar cell structure consists of an absorber (p-type) layer **(Figure 2.12)**, in which the photons of incident radiation are efficiently absorbed, resulting in the creation of electron-hole pairs. The window (n-type) layer, which has a large conductivity for electrons and a small conductivity of holes helps in separation of charges. Electrons can easily flow through the n-type semiconductor, while the transport of holes, which are the minority carriers in such material, is due to the limited recombination processes.

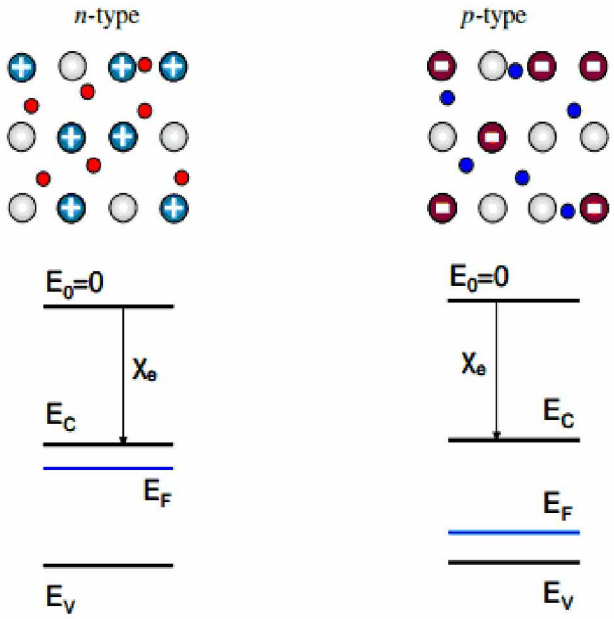

Figure 2.13 Schematic representation of an isolated p-type and n-type semiconductor and corresponding band diagrams.

Figure 2.13 shows schematically isolated fragments of a p-type and an n-type semiconductor and their corresponding band diagrams. In both fragments, the charge neutrality is maintained. In the n-type semiconductor, the large concentration of negatively- charged free electrons is compensated by the positively-charged ionized donor atoms. In the p-type semiconductor, holes are the majority carriers and the positive charge of holes is compensated by the negatively-charged ionized acceptor atoms. For the n-type semiconductor:

$$n = n_{n0} \approx N_D \tag{2-5}$$

$$p = p_{n0} \approx \frac{n_i^2}{N_D} \tag{2-6}$$

For the p-type semiconductor:

$$p = p_{n0} \approx N_A \tag{2-7}$$

$$n = n_{n0} \approx \frac{n_i^2}{N_A} \tag{2-8}$$

where n is the electron concentration

P is the hole concentration

P_{n0} is the hole concentration in equilibrium

n_{n0} is the electron concentration in equilibrium

ni is the intrinsic carrier concentration

N_D is the donor concentration

N_A is the acceptor concentration

When p-type and n-type semiconductors are brought together, a very large difference in electron concentration between the two causes a diffusion current of electrons from the n-type material across the metallurgical junction into the p-type material. Similarly, the difference in hole concentration causes a diffusion current of holes from the p- to the n-type material. Due to this diffusion process, the region close to the metallurgical junction becomes almost completely depleted of mobile charge carriers. The gradual depletion of the charge carriers gives rise to a space charge created by the charge of the ionized donor and acceptor atoms that is not compensated by the mobile charges any more. This region of the space charge is called the space-charge region or depleted region and is schematically illustrated in **Figure 2.14**. Regions outside the depletion region, in which the charge neutrality is conserved, are denoted as the quasi-neutral regions.

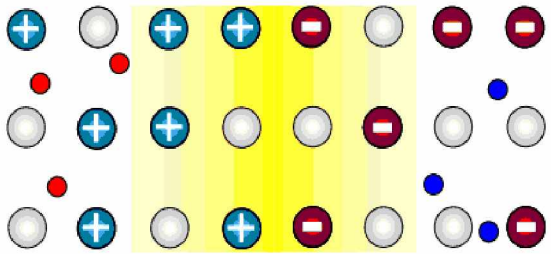

Figure 2.14 Formation of a space-charge region, when n-type and p-type semiconductors are brought together to form a junction. The colored part represents the space-charge region.

The space charge around the metallurgical junction results in the formation of an internal electric field which forces the charge carriers to move in the opposite direction than the concentration gradient. The diffusion currents continue to flow until the forces acting on the charge carriers, namely the concentration gradient and the internal electrical field, compensate each other. The driving force for the charge transport does not exist anymore and no net current flows through the p-n junction.

2.6.2 CdS/PbS thin film solar cells

Bulk PbS has a narrow direct energy band gap of 0.41 eV at 300 K. Thus the absorption edge of PbS can be tuned to anywhere between near-infrared to violet, covering the entire visible spectrum. Therefore, PbS thin films made of nanocrystallites having a bandgap of around 1 eV can be used as an absorber for thin film solar cells. In recent years, vigorous investigations are being conducted to fabricate efficient solar cells based on PbS quantum dot thin films.[138-144] In an alternative way, chemically deposited PbS thin film layers were also used in thin film solar cells as p-type absorber layers.[145,146]

The CdS is the most widely used window material for thin film solar cells. CdS acts as a window layer relating to spectral response at shorter wavelength region. The CdS is used either for establishing electric field at the heterojunction interface that collects the photogenerated charge carriers or as "buffer layer" that avoids the interface mismatch between ITO and and absorber layer. If CdS is used as "buffer layer", its resistivity should be high enough in order to reduce the trap state density at the interface to improve junction properties. Earlier, Romeo et al.[147] achieved a highly efficient 14.6% CdS/CdTe thin film

solar cell. Afterwards, Ramanathan et al.[148] also achieved a 19.2% efficiency in a ZnO/CdS/$CuInGaSe_2$ thin film solar cell.

Recently, Vorobive et al.[149] fabricated a CdS/PbS thin film solar cell of 1.6% efficiency through ammonia free CBD technique. Similarly, Obaid et al.[150] reported on a CdS/PbS thin film solar cell of 1.3% efficiency via microwave-assisted CBD route. The PbS and CdS thin films deposited via CBD method have interesting properties for solar cells. However, the majority of CBD techniques are ammonia based, which is highly volatile, toxic and harmful to the environment at large scale deposition. Furthermore, the volatility of ammonia results in irreproducible film properties.[150] Naoadays, the new ammonia-free simple precursors based on large scale deposition techniques of less environmental issues are of great interest to prepare metal chalcogenide thin films for solar cell applications.

2.7 CdS nanostructures and QDs for photocatalytic degradation of organic dyes

A wide range of organic wastes contaminate the water systems in various fields, such as industrial, agricultural and chemical fiels. Organic dyes become a main part of the industrial waste because of their wide use in many industrial activities. Every year, around 450000 tons of organic dyes are produced and more than 11% are lost in wastes during manufacturing and application stages.[151] These dyes are potentially carcinogenic and their removal from the industrial waste is a major environmental problem.[152] Various approaches have been applied to remove the dye from waste water; these include the biodegradation, coagulation, adsorption, advanced oxidation process, and membrane process.[153-158] Compared to each other, all these approaches have advantages or disadvantages. The development of appropriate techniques for the degradation of organic dyes from waste waters is necessary. Researchers started intensive studies on semiconductor photocatalysis after the discovery of the photo-induced splitting of water on TiO_2 electrodes.[159] Semiconductor photocatalysis is a potentially promising approach to solve such environmental issues.[160] In this approach, photocatalysts used solar energy to decompose pollutants from the air and aqueous medium.[161-163] The photocatalyst generates reactive hydroxyl radicals, which oxidize the toxic organic pollutants and break them into smaller fragments.[164,165] However, the high oxidative capacity and stability of semiconductor materials are the main criteria in order to be selected as a photocatalyst.[165,166] Anatase TiO_2 is the most studied photocatalyst due to its

low cost, high stability and biocompatibility.[167] However, TiO_2 responds to UV light only and its wide band gap limits its practical application as photocatalyst. Therefore, an interesting task is to find an efficient photocatalyst that can effectively degrade organic pollutants under visible light irradiation. Metal oxides, like CdS sensitized TiO_2, doped ZnO, MgO, Fe_2O_3, or $SrTiO_3$ and metal sulphides, like ZnS, In_2S_3 or SnS_2 are also used as a photocatalysts to degrade organic pollutants from the waste water.[168-175] For efficient degradation of dyes, a photocatalyst that has a suitable band gap, flat band energy levels and good absorption properties in the visible region is needed. In both respects, CdS with a direct band gap of around 2.4 eV is a promising material to be used as a photocatalyst to decompose organic pollutants from the aqueous medium.

2.7.1 Mechanism of photodegradation

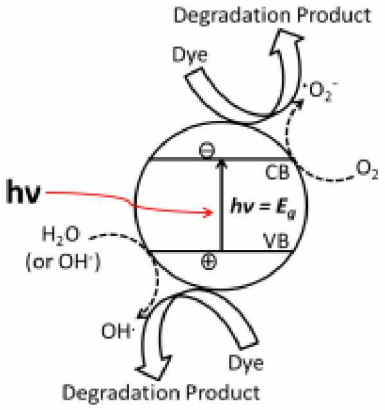

Figure 2.15 Possible mechanism of photocatalytic degradation of dye pollutants by CdS photocatalyst.

For semiconductor photocatalysts, physical and chemical mechanisms have been reported in the literature.[176,177] In fact, the reactivity of photocatalysts depends on the number electron/hole pairs. As the catalyst surface is photoexcited, the produced electrons in the conduction band (CB) and holes in the valence band (VB) are transferred on the photocatalysts sites. Concomitantly, a series of reactions take place at solid-fluid interface. In fact, the exited electrons in CB and holes in VB are respectively captured by oxygen molecules and OH^- or H_2O species dissolved in the suspension. The transfer of electrons to oxygen molecules generates superoxide anions and the presence of holes on semiconductor

surface leads to the production of hydroxyl radicals ($OH^{\cdot}$). The attack of these produced radicals to the organic dye molecules adsorbed on the semiconductor oxide surface leads to the oxidization of pollutant molecules and their transformation to a degradated product. As a result of this process, the dye molecules are decomposed and water treatment is completed. **Figure 2.15** presents the probable mechanism of this process by CdS photocatalyst.

2.7.2 Synthesis of CdS nanomaterials for photocatalysis

It is well known that photocatalytic properties of semiconductor photocatalyst materials is depend not only on their particle size but also their morphology and surface area. Therefore, different studies have been devoted to synthesize CdS nanomaterials with controlled size and various architectures for photocatalytic applications. Di et al.[178] have prepared flower-like CdS nanostructures through a simple solvothermal route and used them to decompose MeO (**Figure 2.16a**). Recently, solvothermally synthesized lotus flower and flower-like 3D assemblies of CdS nanostructures were also developed and used to decompose MB, MeO and RhB (**Figure 2.16b and c**).[179,130]

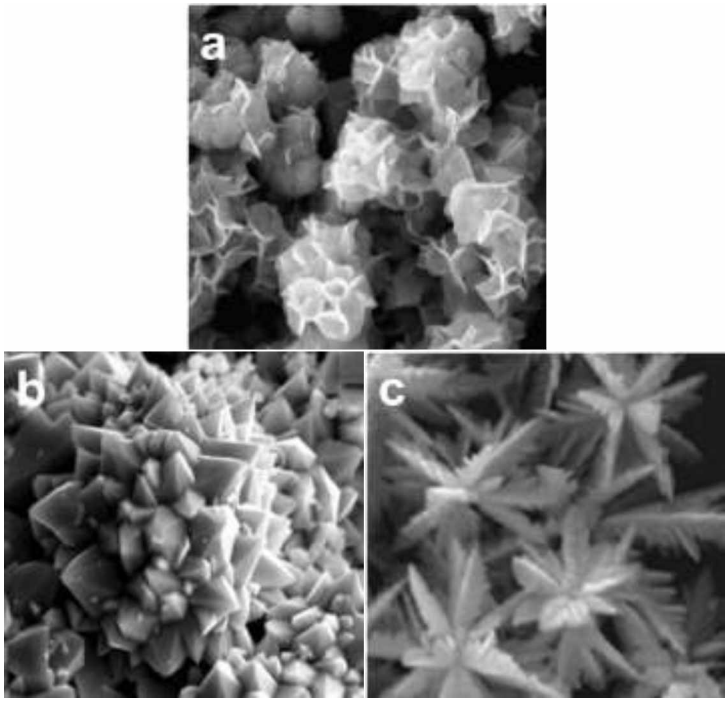

Figure 2.16 CdS nanostructures of different flower-like shapes.[178-180]

Other shapes like microspheres,[181] nanowhiskers,[182] and nanospheres[183] of CdS were also reported and used to decompose MB and RhB. Recently, the synthesis of different amino acids capped CdS QDs were developed and used to degrade MB, RhB and CV.[184-188] **Table 2.4** summarizes the details on recently reported CdS nanostructures and QDs for photocatalytic degradation of organic dyes.

Table 2.5 Summary on photocatalytic degradation of organic dyes by CdS nanostructures and QDs.

Author	Shape	Catalyst amount (mg/mL)	Dye	Dye concentration (ppm)	Irradiation time (min)	Degradation (%)	Ref. No.
Di et al. (2009)	Flower	0.25	MeO	40	240	68	178
Guo et al. (2011)	Flower-like 3D assemblies	1.5	MeO	10	90	88	180
		1.5	RhB	10	90	79	
Guo et al. (2011)	QD	1	MB	50	90	91.6	184
		1	RhB	50	90	45	
Guo et al. (2012)	Nanosphere	0.6	RhB	20	120	97.44	183
		0.6	MB	20	120	98.15	
Guo et al. (2012)	Methionine-capped QD	1	RhB	50	110	84.9	185
	Valine-capped QD	1	RhB	50	110	89.7	
Guo et al. (2012)	Aspartate-capped QD	1	RhB	50	110	98.98	186
	Glutamate-capped QD	1	RhB	50	110	99.04	
Upadhyay et al. (2012)	Nanoparticle	0.5	CV	-	105	96	187
		0.5	MB	-	105	87	
Sahoo et al. (2013)	Lotus-flower	0.4	MB	-	90	90	179
	Hierarchical star	0.4	MB	-	90	78	
	Nanoparticle	0.4	MB	-	90	94	
Ardona et al. (2013)	Nanowhisker	1	RhB	10	300	60	182
Chen et al. (2013)	Nanoparticle	0.5	RhB	10	80	95	188

Table 2.6 Summary on photocatalytic degradation of organic dyes by CdS nanostructures and QDs (continue).

Eskandri et al. (2013)	Nanostructure	1	MB	15	90	99	189
Deng et al. (2013)	Nanosphere	1	MB	10	120	75	190
		1	RhB	10	180	65	
	Hierarchical rod-like	1	MB	10	120	83	
		1	RhB	10	180	50	
	Microsphere	1	MB	10	120	95	
		1	RhB	10	180	90	
Chauhan et al. (2013)	Nanoparticle	1	MB	10	300	100	191

2.8 Summary of Literaure Review

The use of Pb and Cd chalcogenide NCs as inorganic acceptor materials can theoretically improve the performance of BHJ solar cells due to their enhanced absorption and MEG. However, the efficiency of BHJ solar cells based on Pb and Cd chalcogenide NCs have been very low compared to the best known BHJ solar cells based on PCBM/polymer materials. The surface chemistry of NCs is the most important factor for stability, size distribution and dispersion in organic media. The long chain alkyl ligands are beneficial for controlled size distribution, stability and dispersion but also responsible for poor charge separation at interfaces and poor charge transport due to their insulating nature. Synthetic efforts have also been made for the preparation of rods or branched structured NCs with a higher aspect ratio for improved pathways and electron transport in the nanocomposite layer. A number of techniques were reported for removing or replacing ligands before or after deposition of the NCs/polymer nanocomposite layer. In general, BHJ solar cell devices that were fabricated with smaller or without ligands showed higher PCE but the fundamental effect of ligands is still not well understood. A new solution processed approach to grow in situ Pb or Cd chalcogenide NCs network in conjugated polymer matrix is also reported. This new approach shows promise to increase the quantum efficiency of BHJ solar cell devices by increasing transport efficiency via formation of extended NCs networks in the polymer matrix without ligands. Further, additional strategies such as the use of suitable solvents, functionalization of polymers through chemical modification, thermal and solvent annealing were employed to improve the nanomorphology and the PCE of the active layer of BHJ solar cell device.

The PbS and CdS thin films deposited via CBD method have interesting properties for solar cell appications. However, the majority of CBD routes are ammonia based, and it is known that ammonia is highly volatile, toxic and harmful to the environment at large scale deposition. Furthermore, the volatility of ammonia generally leads to irreproducible film properties. To prepare metal chalcogenide thin films, the new ammonia-free simple deposition routes with less environmental issues are of great interest nowadays.

Recently, various metal oxides and sulphides have been used as photocatalysts to degrade organic pollutants from the waste water. CdS became a promising material to be used as a photocatalyst to decompose organic pollutants from the aqueous medium due to its suitable

band gap and good aborption properties in the visible region. Therefore, it is very interesting to synthesize different CdS nanostructures for their further application in photocatlytic water purification.

2.9 References

1. Luque, S. Hegedus, *Handbook of photovoltaic science and engineering*, John Wiley & Sons, New York **(2011)**.
2. G.W. Crabtree, N.S. Lewis, *Physics Today* 60 **(2007)** 37-42.
3. R.M. Nault, *Report on the basic energy sciences workshop on solar energy utilization*, Argonne National Laboratory, USA **(2005)**.
4. A.E. Becquerel, *Comptes Rendus des Séances Hebdomadaires* 9 **(1839)** 561-567.
5. S. Sun, Z. Fan, Y. Wang, Y, Haliburton, *Journal of Material science* 40 **(2005)** 1429-1443.
6. S.O. Russell, **U.S. Patent**, 2,402,662 **(1946)**.
7. S.M. Chapin, C.S. Fuller, G.L. Pearson, *Journal of Applied Physics* 25 **(1954)** 676-677.
8. M.A. Green, J. Zhao, A. Wang, S.R. Wenham, *IEEE Transactions on Electron Devices* 46 **(1999)** 1940-1947.
9. M.A. Green, K. Emery, Y. Hishikawa, W. Warta, *Progress in Photovoltaics: Research and Applications* 17 **(2009)** 320-326.
10. W. Shockley, H.J. Queisser, *Journal of Applied Physics* 32 **(1961)** 510-519.
11. M.A. Green, *Third Generation Photovoltaics: Ultra-High Efficiency at Low Cost*, Springer-Verlag, Berlin **(2003)**.
12. W. Wang, A.S. Lin, J.D. Phillips, *Applied Physics Letters* 95 **(2009)** 011103.
13. R.R. King, D.C. Law, K.M. Edmondson, C.M. Fetzer, G.S. Kinsey, H. Yoon, R.A. Sherif, N.H. Karam, *Applied Physics Letters* 90 **(2007)** 183516.
14. M. Pagliaro, G. Palmisano, R. Ciriminna, V. Loddo, *Energy & Environmental Science* 2 **(2009)** 838–844.
15. M. Riede, T. Mueller, W. Tress, R. Schueppel, K. Leo, *Nanotechnology* 19 **(2008)** 424001.
16. P. Peumans, A. Yakimov and S. R. Forrest, *Journal of Applied Physics* 93 **(2003)** 3693-3723.

17. Merhari L, *Hybrid Nanocomposites for Nanotechnology-Electronic, Optical, Magnetic and Biomedical Applications*, US, Springer **(2009)**.
18. W. U. Huynh, J. J. Dittmer, A. P. Alivisatos, *Science* 295 **(2002)** 2425-2427.
19. K.M. Coakley, Y. Liu, M.D. McGehee, K.L. Frindell, G. D. Stucky, *Advanced Functional Materials* 13 **(2003)** 301-306.
20. I. Gur, N.A. Fromer, A.P. Alivisatos, *Journal of Physical Chemistry B* 110 **(2006)** 25543-25546.
21. W.J.E. Beek, M.M. Wienk, R.A.J. Janssen, *Advanced Materials* 16 **(2004)** 1009-1013.
22. C.Y. Kwong, A.B. Djurisic, P.C. Chui, K.W. Cheng, W.K. Chan, *Chemical Physics Letters* 384 **(2004)** 372–375.
23. D. Qi, M. Fischben, M. Drndic, S. Selmic, *Applied Physics Letters* 86 **(2005)** 093103.
24. S.A. McDonald, G. Konstantatos, S. Zhang, P.W. Cyr, E.J.D. Klem, L. Levina, *Nature Materials* 4 **(2005)** 138-142.
25. H. Cortina, C. Martinez-Alonso, M. Castillo-Ortega, H. Hu, *Materials Science and Engineering B* 177 **(2012)** 1491-1496.
26. E. Arici, H. Hoppe, F. Schaffler, D. Meissner, M.A. Malik, N.S. Sariciftci, *Applied Physics A Material Science & Processing* 79 **(2004)** 59-64.
27. E. Arici, N.S. Sariciftci, D. Meissner, *Advanced Functional Materials* 13 **(2003)** 165-171.
28. Y. Wang, A. Suna, W. Mahler, R. Kasowski, *Journal of Chemical Physics* 87 **(1987)** 7315-7322.
29. R.J. Ellingson, M.C. Beard, J.C. Johnson, P. Yu, O.I. Micic, A.J. Nozik, A. Shabaev, A.L. Efros *Nano Letters* 5 **(2005)** 865-871.
30. J.J.H. Pijpers, R. Ulbricht, K.J. Tielrooij, A. Osherov, Y. Golan, C. Delerue, G. Allan, M. Bonn, *Nature Physics* 5 **(2009)** 811-814.
31. R.D. Schaller, M.A. Petruska, V.I. Klimov, *Applied Physics Letters* 87 **(2005)** 253102.
32. J. Seo, W.J. Kim, S.J. Kim, K.S. Lee, A.N. Cartwright, P.N. Prasad, *Applied Physics Letters* 94 **(2009)** 133302.
33. L.E. Brus, *Journal of Chemical Physics* 80 **(1984)** 4403-4409.
34. A.P. Alivisatos, *Science* 271 **(1996)** 933-937.

35. P.T. Landsberg, H. Nussbaumer, G.J. Willeke, *Journal of Applied Physics* 74 **(1993)**1451-1452.
36. P. Würfel, *Solar Energy Materials and Solar Cells* 46 **(1997)** 43-52.
37. A. de Vos, B. Desoete, *Solar Energy Materials and Solar Cells* 51 **(1998)** 413-424.
38. S.A. Carter, M. Angelopoulos, S. Karg, P.J. Brock, J.C. Scott, *Applied Physics Letters* 70 **(1997)** 2067-2069.
39. C. Jonda, A.B.R. Mayer, U. Stolz, A. Elschner, A. Karbach, *Journal of Material Science* 35 **(2000)** 5645-5651.
40. A. Elschner, F. Bruder, H.W. Heuer, F. Jonas, A. Karbach, S. Kirchmeyer, S. Thurm, R. Wehrmann, *Synthetic Metals* 111 **(2000)** 139-143.
41. B. Schweitzer, H. Bässler H, *Synthetic Metals* 109 **(2000)** 1-6.
42. J.J.M. Halls, C.A. Walsh, N.C. Greenham, E.A. Marseglia, R.H. Friend, S.C. Moratti, A.B. Holmes, *Nature* 395 **(1995)** 498-500.
43. J.J.M. Halls, K. Pichler, R.H. Friend, S.C. Moratti, A. B. Holmes, *Applied Physics Letters* 68 **(1996)** 3120-3122.
44. D.E. Markov, C. Tanase, P.W.M. Blom, J. Wildeman, *Physical Review B: Condensed Matter and Materials Physics* 72 **(2005)** 045217.
45. D.E. Markov, E. Amsterdam, P.W.M. Blom, A.B. Sieval, J.C. Hummelen, *Journal of Physical Chemistry A* 109 **(2005)** 5266-5274.
46. J.J.M. Halls, J. Cornil, D.A. dos Santos, R. Silbey, D.H. Hwang, A.B. Holmes, J.L. Bredas, R.H. Friend, *Physical Review B: Condensed Matter and Materials Physics* 60 **(1999)** 5721-5727.
47. B. Sun, E. Marx, N.C. Greenham, *Nano Letters* 3 **(2003)** 961-963.
48. A.A.R. Watt, D. Blake, J.H. Warner, E.A. Thomsen, E.L. Tavenner, H. Rubinsztein Dunlop, P. Meredith, *Journal of Physics D: Applied Physics* 38 **(2005)** 2006-2012.
49. S. A. McDonald, P.W. Cyr, L. Levina, E.H. Sargent, *Applied Physics Letters* 85 **(2004)** 2089-2091.
50. T.W.F. Chang, S. Musikhin, L. Bakueva, L. Levina, M.A. Hines, P.W. Cyr, E.H. Sargent, *Applied Physics Lett*ers 84 **(2004)** 4295-4297.
51. Zhang S, Cyr PW, McDonald SA, Konstantatos G, Sargent EH, *Applied Physics Letters* 87 **(2005)** 233101.

52. Z. Wang, S. Qu, X, Zeng, C. Zhang, M. Shi, F. Tan, Z. Wang, J. Liu, J. Hou, F. Teng, Z. Feng, *Polymer* 49 **(2008)** 4647-4651.
53. Z. Wang, S. Qu, X. Zeng, J. Liu, C. Zhang, M. Shi, F. Tan, Z. Wang, *Current Applied Physics* 9 **(2009)** 1175-1179.
54. A. Guchhait, A.K. Rath, A.J. Pal, *Solar Energy Materials and Solar Cells* 95 **(2011)** 651-656.
55. J. Seo, M.J. Cho, D. Lee, A.N. Cartwright, P. N. Prasad, *Advanced Materials* 23 **(2011)** 3984-3988.
56. C. Piliego, M. Manca, R. Kroon, M. Yarema, K. Szendrei, M.R. Andersson, W. Heiss, M.A. Loi, *Journal of Materials Chemistry* 22 **(2012)** 24411-24416.
57. X. Jiang, S.B. Lee, I.B Altfeder, A.A. Zakhidov, R.D. Schaller, J.M. Pietryga, V.I. Klimov, *Proceedings of SPIE* 5938 **(2005)** 59381F1- 59381F9.
58. D. Cui, J. Xu, T. Zhu, G. Paradee, S. Ashok, M. Gerhold, *Applied Physics Letters* 88 **(2006)** 183111.
59. Z.N. Tan, T. Zhu, M. Thein, S.A. Gao, A. Cheng, F. Zhang, C.F. Zhang, H.P. Su, J. K. Wang, R. Henderson, J.I. Hahm, Y.P. Yang, J. Xu, *Applied Physics letters* 95 **(2009)** 063510.
60. H. Zhang, X. Dua,, Y. Wang, Q. Guana, Y. Sunb, Y. Cui, J. Zhanga, *Physica E: Low-dimensional Systems and Nanostructures* 49 **(2013)** 1-4.
61. Z. Fan, H. Zhang, W. Yu, Z. Xing, H. Wei, Q. Dong, W. Tian, B. Yang, *ACS Applied Materials and Interfaces* 3 **(2011)** 2919-2923.
62. Z. Chen, H. Zhang, Z. Xing, J. Hou, J. Li, H. Wei, W. Tian, B. Yang, *Solar Energy Materials and Solar Cells* 109 **(2013)** 254-261.
63. Y.F. Zhou, F.S. Riehle, Y. Yuan, H.F. Schleiermacher, M. Niggemann, G.A. Urban, M. Krueger, *Applied Physics Letters* 96 **(2010)** 013304.
64. N.C. Greenham, X.G. Peng, A.P. Alivisatos, *Physical Review B: Condensed Matter and Materials Physics* 54 **(1996)** 17628-17637.
65. W.U. Huynh, J.J. Dittmer, W.C. Libby, G.L. Whiting, A.P. Alivisatos, *Advanced Functional Materials* 13 **(2003)** 73-79.
66. J. Seo, S.J. Kim, W.J. Kim, R. Singh, M. Samoc, A.N. Cartwright, P.N. Prasad, *Nanotechnology* 20 **(2009)** 095202.

67. L. Wang, Y.S. Liu, X. Jiang, D.H. Qin, Y. Cao, *Journal of Physical Chemistry C* 111 **(2007)** 9538-9542.
68. S. Ren, L.-Y. Chang, S.-K. Lim, J. Zhao, M. Smith, N. Zhao, V. Bulovic, M. Bawendi, S. Gradečak, *Nano Letters* 11 **(2011)** 3998-4002.
69. J.D. Olson, G.P. Gray, S.A. Carter, *Solar Energy Materials and solar cells* 93 **(2009)** 519-523.
70. J.S. Owen, J. Park, P.E. Trudeau, A. P. Alivisatos, *Journal of American Chemical Society* 130 **(2008)** 12279-12281.
71. B.C. Sih, M. Wolf, *Journal of Physical Chemistry C* 111 **(2007)** 17184-17192.
72. D. Aldakov, F. Chandezon, R. De Bettignies, M. Firon, P. Reiss, A. Pron, *European Physical Journal Applied Physics* 36 **(2006)** 261-265.
73. N.C. Greenham, X. Peng, A.P. Alivisatos, *Synthetic Metals* 84 **(1997)** 545-546.
74. D.S. Ginger, N.C. Greenham, *Physical Review B* 59 **(1999)** 10622-10629.
75. D.S. Ginger, N.C. Greenham, *Synthetic Metals* 101 **(1999)** 425-428.
76. W.H. Huynh, X. Peng, A.P. Alivisatos, *Advanced Materials* 11 **(1999)** 923-927.
77. B. Sun, H.J. Snaith, A.S. Dhoot, S. Westenhoff, N.C. Greenham, *Journal of Applied Physics* 97 **(2005)** 014914.
78. P. Wang, A. Abrusci, H.M.P. Wong, M. Svensson, M.R. Andersson, N.C. Greenham, *Nano Letters* 6 **(2006)** 1789-1793.
79. B. Sun, N.C. Greenham, *Physical Chemistry Chemical Physics* 8 *(2006)* 3557-3560.
80. Y. Li, H. Zhong, R. Li, Y. Zhou, C. Yang, Y. Li Y, *Advanced Functional Matererials* 16 **(2006)** 1705-1716.
81. Y. Zhou, Y.C. Li, H.Z. Zhong, J.H. Hou, Y.Q. Ding, C.H. Yang, Y.F. Li, *Nanotechnology* 17 **(2006)** 4041-4047.
82. I. Gur, N.A Former, C.-P. Chen, A. G. Kanaras, A. P. Alivisatos *Nano Letters* 7 **(2007)** 409-414.
83. M.D. Heinemann, K. von Maydell, F. Zutz, J. Kolny-Olesiak, H. Borchert, I. Riedel J. Parisi, *Advanced Functional Materials* 19 **(2009)** 3788-3795.
84. S. Dayal, N. Kopidakis, D.C. Olson, D.S. Ginley, G. Rumbles, *Nano Letters* 10 **(2010)** 239-242.
85. Y. Wu, G. Zhang, *Nano Letters* 10 **(2010)** 1628-1631.

86. I. Lokteva, N. Radychev, F. Witt, H. Borchert, J. Parisi, J. Kolny-Olesiak, *Journal of Physical Chemistry C* 114 **(2010)** 12784-12791.
87. Y. Zhou, M. Eck, C. Veit, B. Zimmermann, F. Rauscher, P. Niyamakom, S. Yilmaz, I. Dumsch, S. Allard, U. Scherf, M. Krüger, *Solar Energy materials and Solar Cells* 95 **(2011)** 1232-1237.
88. N.T.N. Truong, W.K. Kim, U. Farva, X.D. Luo, C. Park, *Solar Energy materials and Solar Cells* 95 **(2011)** 3009-3014.
89. Y. Zhou, M. Eck, C. Men, F. Rauscher, P. Niyamakom, S. Yilmaz, I. Dumsch, S. Allard, U. Scherf, M. Krüger, *Solar Energy materials and Solar Cells* 95 **(2011)** 3227-3232.
90. C.-Y. Kuo, M.-S. Su, G.-Y. Chen, C.-S. Ku, H.-Y. Lee, K.-H. Wei, *Energy and Environmental Science* 4 **(2011)** 2316-2322.
91. N. Radychev, I. Lokteva, F. Witt, J. Kolny-Olesiak, H. Borchert, J. Parisi, *Journal of Physical Chemistry C* 115 **(2011)** 14111-14122.
92. K.F. Jeltsch, M. Schädel, J.-B. Bonekamp, P. Niyamakom, F. Rauscher, H. W. A. Lademann, I. Dumsch, S. Allard, U. Scherf, K. Meerholz, *Advanced Functional Materials* 22 **(2012)** 397-404.
93. J.Y. Lek, Y.M. Lam, J. Niziol, M. Marzec, *Nanotechnology* 23 **(2012)** 315401.
94. D. Celik, M. Krueger, C. Veit, H.F. Schleiermacher, B. Zimmermann, S. Allard, I. Dumsch, U. Scherf, F. Rauscher, P. Niyamakom, *Solar Energy materials and Solar Cells* 98 **(2012)** 433-440.
95. N.T.N. Truong, C. Park, *Japanese Journal of Applied Physics* 51 **(2012)** 10NE27. 93
96. Fen Qiao, *Solid-State Electronics* 82 **(2013)** 25-28.
97. H.-C. Chen, C.-W. Lai, I.-C. Wu, H.-R. Pan, I.-W. P. Chen, Y.-K. Peng, C.-L. Liu, C.-h. Chen, P.-T. Chou, *Advanced Materials* 23 **(2011)** 5451-5455.
98. W. Fu, Y. Shi, W. Qiu, L. Wang, Y. Nan, M. Shi, H. Li, H. Chen, *Physical Chemistry Chemical Physics* 14 **(2012)** 12094-12098.
99. M.J. Greaney, S. Das, D.H. Webber, S.T. Bardforth, R.L. Brutchey, *ACS Nano* 6 **(2012)** 4222-4230.
100. W.U. Huynh, J.J. Dittmer, N. Teclemariam, D.J. Milliron, A.P. Alivisatos, K.W.J. Barnham, *Physical Review B: Condensed Matter and Materials Physics* 67 **(2003)** 115326.

101. S. Kwon, H.C. Moon, K.-G. Lim, D. Bae, S. Jang, J. Shin, J. Park, T.-W. Lee, J.K. Kim, *Journal of Materials Chemistry A* 1 **(2013)** 2401-2405.

102. Y.F. Zhou, F.S. Riehle, Y. Yuan, H.F. Schleiermacher, M. Niggemann, G.A. Urban, M. Krueger, *Applied Physics Letters* 96 **(2010)** 013304.

103. W.-F. Fu, Y. Shi, L. Wang, M.-M. Shi, H.-Y. Li, H.-Z. Chen, *Solar Energy Materials and Solar Cells* 117 **(2013)** 329-335.

104. Henry C. Leventis, Simon P. King, Anna Sudlow, Michael S. Hill, Kieran C. Molloy, Saif A. Haque, *Nano Letters* 10 **(2010)** 1253-1258.

105. T.D. Luccio, A.M. Laera, L. Tapfer, *Journal of Physical Chemistry B* 110 **(2006)** 12603-12609

106. D. Fragouli, V. Resta, P.P. Pompa, A.M. Laera, G. Caputo, L. Tapfer, R. Cingolani, A. Athanassiou, *Nanotechnology* 20 **(2009)** 155302.

107. V. Resta, A.M. Laera, E. Piscopiello, M. Schioppa, L. Tapfer, *Journal of Physical Chemistry C* 114 **(2010)** 17311-17317.

108. J.D. Patel, T.K. Chaudhuri, *Materials Research Bulletin* 44 **(2009)** 1647- 1651.

109. T.K. Chaudhuri, M.G. Patel, *AIP Conference Proceedings* 1313 **(2010)** 275-277.

110. T.K. Chaudhuri, A.J. Kothari, D. Tiwari, A. Ray, *Physica status solidi A* 210 **(2013)** 356-360.

111. A. Watt, E. Thomsen, P. Meredith, H. Rubinsztein-Dunlop, *Chemical Communications* **(2004)** 2334-2335.

112. A. Watt, P. Meredith, J.D. Riches, S. Atkinson, H. Rubinsztein-Dunlop, *Current Applied Physics* 4 **(2004)** 320-322.

113. A. Stavrinadis, R. Beal, J.M. Smith, H.E. Assender, A.A. R. Watt, *Advanced Materials* 20 **(2008)** 3105-3109.

114. P.E. Schwenn, A.A.R. Watt, H. Rubinsztein-Dunlop, P. Meredith, *Proc. SPIE* 6038 **(2006)** 603818.

115. A.A.R. Watt, D. Blake, J.H. Warner, E.A. Thomsen, E.L. Tavenner, H. Rubinsztein-Dunlop, P. Meredith, *Journal of Physics D: Applied Physics* 38 **(2005)** 2006-2012.

116. M. Zhou, B. Wang, X. Jiang, A.A. Zakhidov, J.P. Ferraris, *International Journal of Nanoscience* 10 **(2011)** 521-531.

117. E. Maier, A. Fischereder, W. Haas, G. Mauthner, J. Albering, T. Rath, F. Hofer, E.J.W. List, G. Trimmel, *Thin Solid Films* 519 **(2011)** 4201-4206.

118. H.-C. Liao, S.-Y. Chen, D.-M. Liu, *Macromolecules* 42 **(2009)** 6558-6563.

119. A.M. Laera, V. Resta, M.C. Ferrara, M. Schioppa, E. Piscopiello, L. Tapfer, *Journal of Nanoparticle Research* 13 **(2011)** 5705-5717.

120. S. Dowland, T. Lutz, A. Ward, S.P. King, A. Sudlow, M.S. Hill, K.C. Molloy, S.S. Haque, *Advanced Materials* 23 **(2011)** 2739-2744.

121. S. Masala, S.D. Gobbo, C. Borriello, V. Bizzarro, V.L. Ferrara, M. Re, E. Pesce, C. Minarini, M.D. Crescenzi, T.D. Luccio, *Journal of Nanoparticle Research* 13 **(2011)** 6537-6544.

122. R.K. Bhardwaj, H.S Kushwaha, J. Gaur, T. Upreti, V. Bharti, V. Gupta, N. Chaudhary, G.D. Sharma, K. Banerjee, S. Chand, *Materials Letters* 89 **(2012)** 195-197.

123. S. Dayal, N. Kopidakis, D.C. Olson, D.S. Ginley, G. Rumbles, *Journal of American Chemical Society* 131 **(2009)** 17726-17727.

124. W.E. Mahmoud, H.M. El-Mallah, *Journal of Physics D: Applied Physics* 42 **(2009)** 035502.

125. Y. Peng, G. Song, X. Hu, G. He, Z. Chen, X. Xu, J. Hu, *Nanoscale Research Letters* 8 **(2013)** 106.

126. M.T. Khan, A. Kaur, S.K. Dhawan, S. Chand, *Journal of Applied Physics* 109 **(2011)** 114509.

127. M.T. Khan, A. Kaur, S.K. Dhawan, S. Chand, *Journal of Applied Physics* 110 **(2011)** 044509.

128. J. Jo, S.S. Kim, S.I. Na, B.K. Yu, D.Y. Kim, *Advanced Functional Materials* 19 **(2009)** 866-874.

129. H. Hoppe, M. Niggemann, C. Winder, J. Kraut, R. Hiesgen, A. Hinsch, D. Meissner, N.S. Sariciftci, *Advanced Functional Materials* 14 **(2004)** 1005-1011.

130. W. Ma, C. Yang, X. Gong, K. Lee, A. J. Heeger, *Advanced Functional Materials* 15 **(2005)** 1617-1622.

131. G. Zotti, B. Vercelli, A. Berlin, M, Pasini, T.L. Nelson, R.D. McCullough, A. Virgili, *Chemistry of Materials* 22 **(2010)** 1521-1532.

132. J. Liu, T. Tanaka, K. Sivula, A.P. Alivisatos, J.M.J. Fréchet, *Journal of American Chemical Society* 126 **(2004)** 6550-6551.

133. K. Palaniappan, J.W. Murphy, N. Khanam, J. Horvath, H. Alshareef, M. Quevedo-Lopez, M.C. Biewer, S.Y. Park, M.J. Kim, B.E. Gnade, M.C. Stefan, *Macromolecules* 42 **(2009)** 3845-3848.

134. T. L. Chu, S.S. Chu, *Solid State Electronics* 38 **(1995)** 533-549.

135. A.D. Compaan, *Solar Energy Materials and Solar Cells* 90 **(2006)** 2170-2180.

136. V. Avrutin, N. Izyumskaya, H. Morkoc, *Superlattices and Microstructures* 49 **(2011)** 337-364.

137. M. Afzaal, P.O. Brien, *Journal of Materiials Chemistry* 16 **(2006)** 1597-1602.

138. J. Tang, X. Wang, L. Brzozowski, D.A.R. Barkhouse, R. Debnath, L. Levina, E.H. Sargent, *Advanced Materials* 22 **(2010)** 1398-1402.

139. J.M. Luther, J. Gao, M.T. Lloyd, O.E. Semonin, M.C. Beard, A.J. Nozik, *Advanced Materials* 22 **(2010)** 3704-3707.

140. K.P. Bhandari, P.J. Roland, H. Mahabaduge, N.O. Haugen, C.R. Grice, S.Jeong, T. Dykstra, J. Gao, R.J. Ellingson, *Solar Energy Materials and Solar Cells* 117 **(2013)** 476-482.

141. P.R. Brown, R.R. Lunt, N. Zhao, T.P. Osedach, D.D. Wanger, L.-Y. Chang, M.G. Bawendi, V. Bulović, *Nano Letters* 11 **(2011)** 2955-2961.

142. K. Szendrei, W. Gomulya, M. Yarema, W. Heiss, M.A. Loi, *Applied Physics Letters* 97 **(2010)** 203501.

143. J. Gao, C.L. Perkins, J.M. Luther, M.C. Hanna, H.-Y. Chen, O.E. Semonin, A.J. Nozik, R.J. Ellingson, M.C. Beard, *Nano Letters* 11 **(2010)** 3263-3266.

144. A.G. Pattantyus-Abraham, I.J. Kramer, A.R. Barkhouse, X. Wang, G. Konstantatos, R. Debnath, L. Larissa, I. Raabe , M.K. Nazeeruddin, M. Grätzel, E. H. Sargent *ACS Nano* 4 **(2010)** 3374-3380.

145. H. Moreno-García, M.T.S. Nair, P.K. Nair, *Thin Solid Films* 519 **(2011)** 2287-2295.

146. H. Moreno-García, M.T.S. Nair, P.K, Nair, *Thin Solid Films* 519 **(2011)** 7364-7368.

147. N. Romeo, A. Bosio, R. Tedeschi, A. Romeo, V. Canevari, 58 **(1999)** 209-218.

148. K. Ramanathan, M.A. Contreras, C.L. Perkins, S. Asher, F.S. Hasoon, J. Keane, D. Young, M. Romero, W. Metzger, R. Noufi, J. Ward, A. Duda, *Progress in Photovoltaics: Research and Applications* 11 **(2003)** 225-230.

149. J. Hernández-Borja, Y.V. Vorobiev, R. Ramírez-Bon, *Solar Enrgy Materials and Solar Cells* 95 **(2011)** 1882-1888.

150. A.S. Obid, M.A. Mahdi, Z. Hassan, M. Bououdina, *International journal of Hydorgen Energy* 38 **(2013)** 807-815.

151. E. Forgas, T. Cserhati, G. Oros, *Environmental International* 30 **(2004)** 953-971.

152. S. Parsons, *Advanced oxidation processes for water and waste water*, IWA Publishing, **(2004)**.

153. M. Derudi, G. Venturini, G. Lombardi, G. Nano, R. Rota, *European Journal of Soil Biology* 43 **(2007)** 297-303.

154. M.J. Martin, A. Artola, M.D. Balaguer, M. Rigola, *Chemical Engineering Journal* 94 **(2003)** 231-239.

155. A.L. Ahmad, S.W. Puasa, *Chemical Engineering Journal* 132 **(2007)** 257-265.

156. I. Arslan, I.A. Balcioglu, D.W. Bahnemann, *Dyes and Pigments* 47 **(2000)** 207-218.

157. J.H. Mo, Y.H. Lee, J. Kim, J.Y. Jeong, J. Jegal, *Dyes and Pigments* 76 **(2008)** 429-434.

158. M.A. Rauf, S.S. Ashraf, S.N. Alhadrami, *Dyes and Pigments* 66 **(2005)** 197-200.

159. A. Fujishima, K. Honda, *Nature* 238 **(1972)** 37-38.

160. X.B. Chen, L. Liu, P.Y. Yu, S.S. Mao, *Science* 331 **(2011)** 746-750.

161. Z.G. Yi, J.H. Ye, N. Kikugawa, T. Kako, S.X. Ouyang, H. Stuart-Williams, H. Yang, J.Y. Cao, W.J. Luo, Z.S. Li, Y. Liu, R.L. Withers, *Nature Materials* 9 **(2010)** 559-564.

162. H. Tong, S.X. Ouyang, Y.P. Bi, N. Umezawa, M. Oshikiri, J.H. Ye, *Advanced Materials* 24 **(2012)** 229-251.

163. P. Wang, B.B. Huang, X.Y. Qin, X.Y. Zhang, Y. Dai, J.Y. Wei, M.H. Whangbo, *Angewandte Chemie International Edition* 47 **(2008)** 7931-7933.

164. R. Comparelli, E. Fanizza, M.L. Curri, P.D. Cozzoli, G. Mascolo, A. Agostiano, *Applied Catalysis B: Environmental* 60 **(2005)** 1-11.

165. S. Baruah, M.A. Mahmood, M.T.Z. Myint, T. Bora, J. Dutta, *Beilstein Journal of Nanotechnology.* 1 **(2005)** 14-20.

166. R. Wahab, I.H. Hwang, Y.S. Kim, H.-S. Shin, *Chemical Engineering Journal* 168 **(2011)** 359-366.

167. M. Mrowetz, E. Selli, *Journal of Photochemistry and Photobiology A: Chemistry* 180 **(2006)** 15-22.

168. H. Xie, T. Zeng, S. Jin, Y. Li, X. Wang, X. Sui, X. Zhao, *Journal of Nanoscience and Nanotechnol*ogy 13 **(2013)** 1461-1466.

169. R. Ullah, J. Dutta, *Journal of Hazardous Materials* 156 **(2008)** 194-200.

170. T. Sriskandakumar, N. Opembe, C-H. Chen, A. Morey, C. King'ondu, S.L. Suib, *Journal of Physical Chemistry A* 113 **(2009)** 1523-1530.

171. X. Zhou, J. Lan, G. Liu, K. Deng, Y. Yang, G. Nie, J. Yu, L. Zhi, *Angewandte Chemie International Edition* 51 **(2012)** 178-182.

172. Q.I. Rahman, M. Ahmad, S.K. Misra, M. Lohani, *Journal of Nanoscience and Nanotechnology* 12 **(2012)** 7181-7186.

173. X. Wu, K. W. Li, H. Wang, *Journal of Alloys and Compounds* 487 **(2009)** 537-544.

174. Y. He, D. Li, G. Xiao, W. Chen, Y. Chen, M. Sun, H. Huang, X. Fu, *Journal of Physical Chemistry C* 113 **(2009)** 5254-5262.

175. R. Lucena, F. Fresno, J.C. Conesa, *Applied Catalysis A: General* 415-416 **(2012)** 111-117.

176. K. Natarajan, T.S. Natarajan, H.C. Bajaj, R.J. Tayade, *Chemical Engineering Journal* 178 **(2011)** 40-49.

177. T.K. Ghorai, M. Chakraborty, P. Pramanik, *Journal of Alloys Compound* 509 **(2011)** 8158-8164.

178. X. Di, S.K. Kansal, W. Deng, *Separation and Purification Technol*ogy 68 **(2009)** 61-64.

179. A. K. Sahoo, S. K. Srivastava, *Journal of Nanoparticle Res*earch 15 **(2013)** 1591 -1598.

180. Y. Guo, J. Wang, L. Yang, J. Zhang, K. Jiang, W. Li, L. Wang, L. Jiang, *CrystEngComm* 13 **(2011)** 5045-5048.

181. S. Rengaraj, S.H. Jee, S. Venkataraj, Y. Kim, S. Vijayalakshmi, E. Repo, A. Koistinen, M. Sillanpaa, *Journal of Nanoscience and Nanotechnology* 11 **(2011)** 2090-2099.

182. H.A.M. Ardona, F. U.Paredes, I.H.J. Arellano, S. D. Arco, *Materials Letters* 91 **(2013)** 96-99.

183. Y. Guo, J. Wang, Z. Tao, F. Dong, K. Wang, X. Ma, P. Yang, P. Hu, Y Xu, L. Yang, *CrystEngComm* 14 **(2012)** 1185-1188.

184. Y. Guo, L. Wang, L. Yang, J. Zhang, L. Jiang, X. Ma, *Materials Lett*ers 65 **(2011)** 486-489.

185. Y. Guo, L. Jiang, L. Wang, X. Shi, Q. Fang, L. Yang, F. Dong, and C. Shan, *Materials Lett*ers 74 **(2012)** 26-29.

186. Y. Guo, X. Shi, J. Zhang, Q. Fang, L. Yang, F. Dong, K. Wang, *Materials Lett*ers 86, **(2012)** 146-149.

187. R. K. Upadhyay, M. Sharma, D. K. Shinh, S.S. Amritphale, N. Chandra, *Separation Purification Technol*ogy 88 **(2012)** 39-45.

188. F. Chen, Y. Cao, D. Jian, X. Niu, *Ceramic International* 39 **(2013)** 1511-1517.

189. P. Eskandari, F. Kazemi, Y. Azizian-Kalandaragh, *Separation and Purification Technology* 120 **(2013)** 180-185.

190. C. Deng, X. Tian, *Materials Research Bulletin* 48 **(2013)** 4344-4350.

191. Ruby Chauhan, Ashavani Kumar, Ram Pal Chaudhary, *Applied Surface Science* 270 **(2013)** 655-660.

Chapter 3: Characterizations

3.1 Introduction

The as-synthesized metal chalcogenide nanomaterials and thin films were extensively characterized for their structural, morphological, optical, thermal and surface properties. To accomplish the characterization work, X-ray diffraction (XRD), X-ray photoelectron microscopy (XPS), electron microscopy such as transmission electron microscopy (TEM) and scanning electron microscopy (SEM) with complimentary energy dispersive X-ray spectroscopy (EDS), ultraviolet-visible spectroscopy (Uv-vis), photoluminescence spectroscopy (PL), thermogravimetric analysis (TGA), fourier transform infrared spectroscopy (FTIR), gas sorption and atomic force microscopy (AFM) characterization techniques have been used. In this chapter, the fundamental principles of the above characterization techniques are outlined.

3.2 X-ray diffraction (XRD)

XRD is a powerful tool for material science, which provides valuable information on the crystallographic structure and different phases of nanocrystalline products. X-rays are generated by beam of fast electrons bombarding a metal target in an evacuated tube and directed toward the sample. The interaction of the incident rays with the sample produces constructive interference and a diffracted ray when conditions satisfy Bragg's Law (**Figure 3.1**).[1]

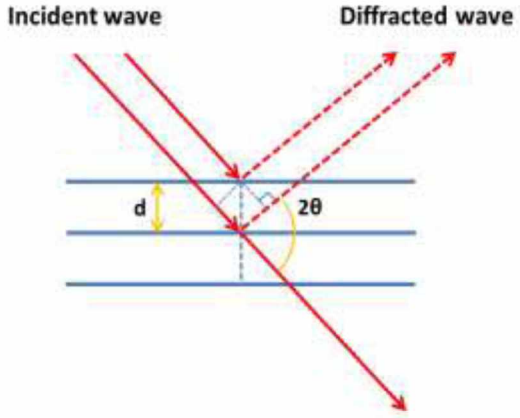

Figure 3.1 Schematic illustration of the Bragg's law.

$$n\lambda=2d\sin\theta \quad \textbf{(3-1)}$$

Where n is the order of interface

λ is the wavelength of X-ray (nm)

d is the lattice plane distance (nm)

θ is the angle of incidence (Degrees)

These diffracted X-rays are then detected, processed and counted. All possible diffraction directions of the lattice should be achieved due to the random orientation of the powdered material. The conversion of the diffraction peaks to d-spacings allows identification of the mineral because each mineral has a set of unique d-spacings. Typically, this is achieved by comparing the d-spacings with standard reference patterns.

The Debye-Scherrer equation is very useful to calculate the mean size of particles from XRD peaks:

$$D = K\lambda / \beta\cos\theta \quad \textbf{(3-2)}$$

Where D is the particle size (Å).

k is the shape factor (taken as 0.9).

λ is the wavelength of X-ray used (1.54051 Å for CuK_α).

B is the broadening of line at half the intensity (Radians).

θ is the diffraction angle of line under consideration (Degrees).

3.3 X-ray photoelectron microscopy (XPS)

XPS is based on photoelectric effect and widely used for the surface analysis[2]. Every atom in the surface has core electron with the characteristic binding energy, which is conceptually equal to the ionization energy of that electron. The energy of the X-ray photon is absorbed completely by the core electron of an atom. If the photon energy ($h\nu$) is large enough, then the core electron will escape from the atom and emits out from the surface. The emitted electron with kinetic energy (Ek) is referred to as the photoelectron. The binding energy of the core electron is given by the Einstein relationship:

$$h\nu = E_b + E_k + \phi \quad \textbf{(3-3)}$$

$$E_b = h\nu - E_k + \phi \quad \textbf{(3-4)}$$

Where h: Planck constant (J.s)

ν: frequency of the radiation (Hz)

E_k is the kinetic energy of photoelectron (J)

ϕ is the spectrophotometer work function (J)

3.4 Electron microscopy

3.4.1 Transmission electron microscopy (TEM)

This technique is most common for determining the size and shape of the nanomaterials. In this technique, high energy electron beams are transmitted through a very thin sample to image and analyze the structure of materials with atomic scale resolution. The electron beam is focused with electromagnetic lenses and the image is observed on fluorescent screen or photographed with a camera. The electrons are accelerated at several hundred kV, giving wavelength much smaller than that of light.

3.4.2 Scanning electron microscopy (SEM)

This technique is used to obtain information about the size and morphology of the powder or thin film samples. The primary electron beam strikes the sample and gives rise a variety of signals, including low energy secondary electrons from the upper layers of the sample. Some of the secondary electrons are collected, processed, and eventually translated as a series of pixels on a cathode ray tube or monitor. The brightness of the pixel is directly proportional to the number of secondary electrons generated from the sample surface. The samples that are not conductive must need an additional sputter coating of gold/palladium to obtain a reasonable image.

Due to the high energy electron irradiation, the electrons in inner shells of the atoms in the sample are emitted and leave vacant orbits. The vacant orbits occupied by the outer shell electrons result in the emission of X-ray photons. The X-ray emitted through this process

provides a signature emission for elemental identification because all elements have a unique electronic structure.

3.5 Ultraviolet-visible spectroscopy (Uv-vis)

Optical properties of the molecules provide perception into their band gap, size and shape. The energy of photons from the visible to the near ultraviolet region can excite electrons from the valence band to the conduction band of a semiconductor material (**Figure 3.2**). The absorption of photon energy equal or more than the band gap of the semiconductor induces a photoexcitation.

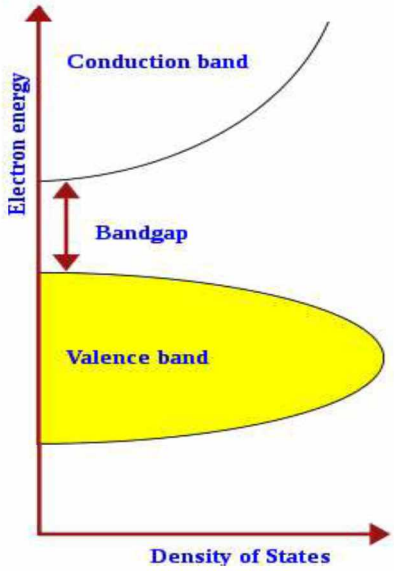

Figure 3.2 Semiconductor band structure.

The energy band gaps (Eg) of the NCs are determined from the Tauc relation:

$$(\alpha h\nu)^2 \sim h\nu - Eg \qquad \textbf{(3-5)}$$

where α is the absorption coefficient (cm^{-1})

h is the Plank constant (J.s)

ν is the frequency of radiation (Hz)

Eg is the energy band gap of the semiconductor (eV)

3.6 Photoluminescence spectroscopy (PL)

PL is a process in which the material absorbs photons and then re-radiates them. Quantum mechanically, this can be described as an excitation to a higher energy state and then a return to a lower energy state accompanied by the emission of a photon. The period between the absorption and the emission is extremely short, in the order of 10 nanoseconds. For a direct band gap, transition photons with enough energy excite an electron from the ground state valence band into an excited state in the conduction band. In terms of semiconductor physics, the incoming energy creates an electron-hole pair of positive and negative charges, and these pairs or exciton retain that excited energy which is then released when the electron and hole recombine.

3.7 Dynamic light scattering (DLS)

Particle size can be determined by measuring the random changes in the intensity of light scattered from a suspension or a solution. This technique is commonly known as DLS. DLS is most commonly used to analyze nanoparticles. Examples include the determination of nanogold size, protein size, latex size, and colloid size. In general, the technique is best used for submicron particles and can be used to measure particles with sizes less than a nanometer. Small particles in suspension undergo random thermal motion known as Brownian motion. This random motion is modeled by the Stokes-Einstein equation. The following equation is the Stokes-Einstein relation that connects diffusion coefficient measured by dynamic light scattering to particle size.

$$D_h = \frac{k_B T}{3\pi\eta D_t} \qquad \textbf{(3-6)}$$

Where D_h is the hydrodynamic diameter

D_t is the translational diffusion coefficient

k_B is Boltzmann's constant

T is thermodynamic temperature

η is dynamic viscosity

The calculations are handled by instrument software. However, the equation does serve as important reminder about a few points. The first is that sample temperature is important, as it appears directly in the equation. Temperature is even more important due to the viscosity term, since viscosity is a stiff function of temperature. Finally, and most importantly, it should be mentioned that the particle size, determined by dynamic light scattering, is the hydrodynamic size.

3.8 Thermogravimetric analysis (TGA)

TGA measures weight changes in a material as a function of increasing temperature (or time) under a controlled atmosphere.[3] Its principle uses include the measurement of a material's thermal stability, moisture and solvent content, and the percent composition of components in a compound. It gives valuable information about the removal of molecules, thermal stability of the material at certain temperature and the amount of the components present in the sample. The weight of the sample is plotted against the temperature or time to illustrate thermal transitions in the material such as loss of solvent, water of hydration in inorganic materials, and, finally, the decomposition of the material.

3.9 Fourier transform infrared spectroscopy (FTIR)

FTIR spectroscopy is a technique for collecting spectra by the infrared radiation (IR) in the range of 400 to 4000cm^{-1}.[4] IR radiation causes the excitation of the vibrations of covalent bonds within the molecule. These vibrations include the stretching and bending modes.[5] The stretching vibrations cause stronger absorptions of IR radiation compared to bending vibrations. The spectra can be interpreted by checking the peaks with the IR database to determine the chemical structure of the sample. In the case of nanoparticles, this technique is very useful to know how the surfactant bonds to the surface of the nanoparticles by comparing FTIR spectra of the pure surfactant with the FTIR spectra of nanoparticles.

3.10 Gas sorption

3.10.1 Physisorption isotherm

The isotherm is the plot of absorbed volume at the standard pressure against the corresponding equilibrium pressure at a constant temperature. The physisorption isotherms

are grouped in to the six types (**Figure 3.3(a)**). The reversible Type I isotherm is obtained for mesoporous materials having relatively small external surfaces. The reversible Type II and III isotherms forms are very common for non-porous or macroporous materials. Type IV and V isotherms are characteristics of mesoporous materials. Type V is uncommon isotherm related to the type III isotherm in that the adsorbent adsorbate interaction is week. Type VI isotherm is a typical characteristic of stepwise multilayer adsorption on a uniform non-porous surface.[6]

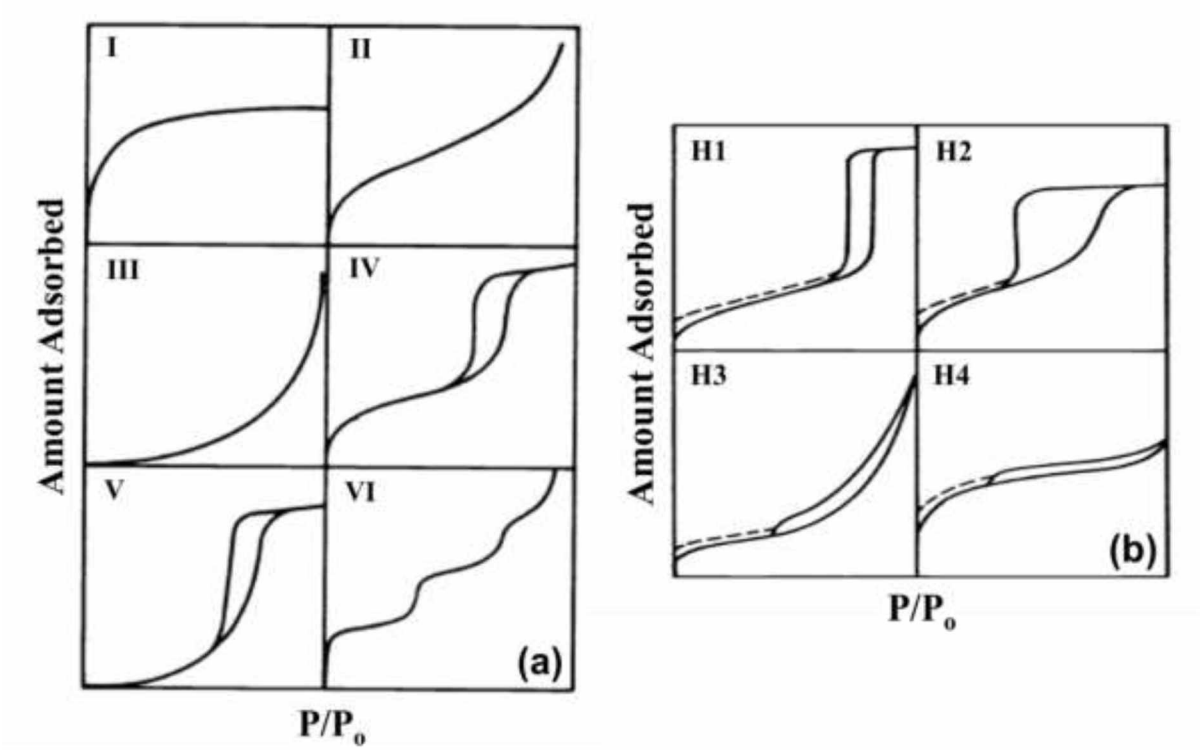

Figure 3.3. Types of physisorption isotherms (a) and hysteresis loops (b).[6]

The hysteresis appearing in the multilayer range of physisorption isotherms is usually associated with capillary condensation in mesopore structure. The hysteresis loops exhibit a variety of shapes (**Figure 3.3(b)**). In type H1, the two branches (adsorption/desorption branches) are almost vertical and nearly parallel, which are attributed to uniform cylindrical pores with narrow pore size distribution. Type H2 is an asymmetrical loop consisting of a desorption branch much steeper than the adsorption branch, which is assigned to 'ink bottle' type pores. Type H3 is associated with slit-shaped pores formed by the aggregate of plate-

like particles. Type H4 is associated with narrow slit-like pores with nearly horizontal and parallel branches over a wide range of P/P_o.[6]

3.10.2 Surface area

The most common technique to measure the surface area of mesoporous materials is the Braunauer-Emmer-Teller (BET) technique. The surface area is determined by using the following equation[7]:

$$\frac{P/P_o}{n(1-P/P_o)} = \frac{1}{n_m c} + \frac{c-1}{n_m c} \times \frac{P}{P_o} \qquad \textbf{(3-7)}$$

Where n is the amount adsorbed at the relative pressure P/P_o

n_m is the monolayer capacity

c is a constant related exponentially to the heat of adsorption in the first adsorbed layer.

The c value is taken as:

$$c = e^{(q_1 - q_L)/RT} \qquad \textbf{(3-8)}$$

Where q_1 is the heat of adsorption of the first layer of gas molecules

q_L is the heat of the gas liquefaction

R is the gas constant

T is the absolute temperature

The BET equation gives a linear relationship between $\frac{P/P_o}{n(1-P/P_o)}$ and P/P_o. The values of n_m and c are calculated form the intercept $1/n_m c$ and the slope $(c-1)/ n_m c$. The surface area can thus be calculated from the monolayer capacity on the assumption of close packing as:

$$A = n_m \alpha_m L \qquad \textbf{(3-9)}$$

Where α_m is the molecular cross-sectional area

n_m is the monolayer capacity

L is the Avogadro constant

Generally, nitrogen is considered to be the suitable gas for surface area determination and it is usually assumed that the BET monolayer is close-packed, giving $\alpha_m = 0.162$ nm^2 at 77 K.

3.11 Atomic force microscopy (AFM)

AFM is very useful in thin film surface analysis. In this technique, the interactions of a tip and a sample surface are used for imaging. The interaction between the tip and the sample surface is of the order of nano Newton, which is not directly measured in AFM. The displacement of the cantilever is monitored by the reflection of a laser from the back of the cantilever, detected on a segmented photodetector. A four segment photodiode is used for this purpose.

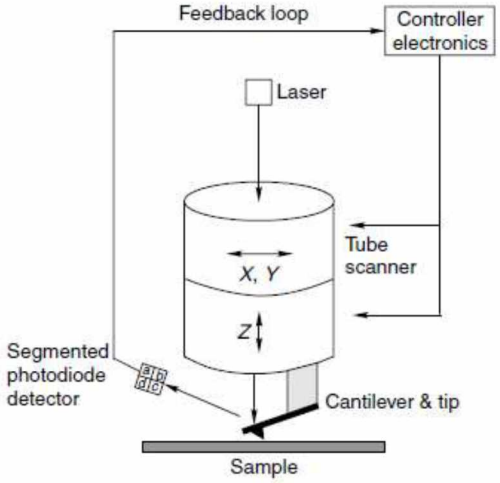

Figure 3.4 Schematic representation of an AFM. The sample surface is scanned by the cantilever, connected to a tubular scanner. The principle functional units in it are three piezoelectric scanners. The deflections of the cantilever monitored are by the segmented photodiode detectore.[8]

AFM is operated in two modes, the contact (tapping) mode and the non-contact mode (intermittent). In the contact mode, the tip comes into contact with the surface. The force between the sample surface and the tip is the product of the displacement of the tip and the force constant of the cantilever. The contact with the surface allows an evaluation of the

surface friction. The strong interaction may damage the surface, which makes the contact mode difficult to be used for soft materials.

In the non-contact mode, the tip is oscillated at its resonant frequency by an actuator. The decrease in the amplitude of the motion when the cantilever comes close to the sample surface is used to measure the tip-sample interaction. The drop in the amplitude is set to a pre-determined value. The intermittent contact that the tip makes is gentle and does not damage the sample surface, though the probes are generally harder. Since it is a gentle mode of scanning, the non-contact mode is the most often used, especially in the case of samples with surfaces delicate such as a polished silicon wafer.[8]

3.12 References

1. M.F. Toney, *In Encyclopedia of materials characterization*, C.R. Brundle, C.A. Evans, S. Wilson, EdS., Manning Publications, Greenwich (**1992**).
2. P.V.D. Heide, *X-ray Photoelectron Spectroscopy: An introduction to principles and practices*, John Wiley and Sons, Inc., Hoboken, New Jersey, (**2011**).
3. A.W. Coast, J.P. Redfern, *Analyst* 88 (**1963**) 906-924.
4. P.R. Grifftiths, J.A.D Haseth, *Fourier Transform Infrared Spectrometry*, John Wiley & Sons Inc., Hoboken New Jersey (**2011**).
5. H. Kuzmany, *Solid–State Spectroscopy: An introduction*, Second Ed. Springer, New York (**2009**).
6. K.S.W. Sing, D.H. Everett, R.A.W. Haul, L. Moscou, R.A Pierotti, J. Rouquerol, T. Siemieniewska, *Pure & Applied Chemistry* 57 (**1985**) 603-619.
7. S. Brunauer, P.H. Emmett, E. Teller, E. *Journal of American Chemical Society* 60 (**1938**) 309-319.
8. T. Pradeep, *NANO: The Essentials: Understanding Nanoscience and Nanotechnology*, Tata McGraw-Hill Education, New Delhi (**2007**).

Chapter 4: Morphology and size control of lead sulphide nanoparticles produced using methanolic lead-thiourea complex via different precipitation techniques

Jayesh D. Patel[a,b], Frej Mighri[a,b,*], Abdellah Ajji[a,c] and Tapas K. Chaudhuri[d]

[a]Center for Applied Research on Polymers and Composites, CREPEC

[b]Chemical Engineering Department, Laval University, Quebec, QC, G1K 7P4 Canada

[c]Chemical Engineering Department, Ecole Polytechnique, C.P. 6079, Succ. Centre- Ville Montreal, QC, H3C 3A7 Canada

[d]Dr. K.C. Patel Research and Development Centre, Charotar University of Science and Technology (CHARUSAT), Changa, Tal.-Petlad, Anand District, Gujarat 388421, India

Published in ***Materials Chemistry and Physics*** 132 (2012) 747-755

Résumé

Dans cette étude, des particules de sulfure de plomb (PbS) ont été synthétisées à partir du complexe plomb méthanolique-thiourée (Pb-TU) via des techniques de précipitation variées basées sur la décomposition du complexe thiourée-plomb méthanolique. L'influence de ces techniques sur la morphologie, la taille et les propriétés physiques des particules de PbS a été étudiée en détail. En général, la microscopie électronique à balayage des particules de PbS produit par dépôt conventionnel en bain chimique, déposition en bain sonochimique et la déposition en bain chimique assistée par micro-ondes ont révélé que les particules de PbS sont nanostructurées avec différentes tailles et formes. La diffraction des rayons X a confirmé leur grande pureté, tandis que la spectroscopie photoéléctronique des rayons X (XPS) a montré que ces particules de PbS étaient partiellement oxydées à cause de leur importante énergie de surface. L'absorption optique, la microscopie électronique à transmission, la diffraction des électrons à zones désignées et la XPS des nanoparticules de PbS recouvert, produit via la déposition en bain chimique à recouvrement assisté en utilisant le poly (vinyl-pyrrolidone) (PVP) et l'acide oléique (AO) ,ont indiqué que les NPs de PbS distribuées de petites tailles absorbent fortement dans la région visible avec une phase cristalline cubique sans aucune preuve d'oxydation de surface. La spectroscopie infrarouge à transformée de Fourier (FTIR) des nanoparticules NPs de sulfure de plomb (PbS) recouvert de PVP montre une forte interaction entre les NPs de PbS et la matrice de polymère, tandi que pour les NPs de PbS recouvert d'acide oléique AO, l'AO a été chimiquement absorbé sur la surface des NPs de PbS.

Abstract

In this study, lead sulphide (PbS) particles were synthesized from methanolic lead-thiourea (Pb-TU) complex via various precipitation techniques based on the decomposition of methanolic Pb-TU complex. The influence of these techniques on the morphology, size and physical properties of PbS particles was studied in details. In general, scanning electron microscopy of PbS particles produced by conventional chemical bath deposition, sonochemical bath deposition and microwave-assisted chemical bath deposition revealed that PbS particles are nanostructured with different size and shape. X-ray diffraction confirmed their high purity, while X-ray photoelectron spectroscopy (XPS) showed that these PbS particles were partially oxidized due to their high surface energy. Optical absorption, transmission electron microscopy, selective area electron diffraction and XPS of capped PbS nanoparticles (NPs) produced via capping assisted chemical bath deposition using poly (vinyl-pyrrolidone) (PVP) and oleic acid (OA) indicated that narrow size distributed PbS NPs absorbed strongly in visible region with cubic crystalline phase without any evidence of surface oxidation. Fourier transform infrared spectroscopy of PVP-capped PbS NPs showed strong interaction between PbS NPs and polymer matrix, while for OA-capped PbS NPs, OA was chemically absorbed on the surface of PbS NPs.

4.1 Introduction

It is well known that optical, electronic, and magnetic properties of semiconductor NPs are strongly dependent on their size, shape and surface quality. Therefore, the optimization of synthesis parameters of these NPs is important in order to improve their properties. A variety of new synthesis methods of semiconducting nanomaterials have been reported in recent years amongst them chemical bath deposition (CBD) and its variants, like sonochemical bath deposition (SCBD) and microwave-assisted chemical bath deposition (MACBD) and capping assisted chemical bath deposition (CACBD). Much attention was given to these synthesis methods in material's chemistry due to their industrial application for a variety of semiconducting materials because of their low cost and simplicity.[1,2] These techniques do not rely on expensive equipment and can be employed for large area deposition.

Ultrasonic irradiation has been widely used to produce a variety of novel materials with remarkable photocatalytic properties, including metal doped oxide nanomaterials.[3] Nanomaterials obtained via this synthesis technique have much smaller particle size and higher surface area than those obtained by some other reported methods.[4] For example, SCBD technique was used to synthesize useful nanoscale metal chalcogenides;[5] the shape and size of particles obtained by ultrasonic irradiation strongly depend on the frequency of ultrasonic irradiation. The exposure of the precursor under high intensity of ultrasonic irradiation may also destroy the original morphology of the material.[6]

The chemical bath deposition based on rapid thermal processing via microwave irradiation, designated as a MACBD, is a rapid synthesis technique, which is presently used to prepare nanostructured films and particles.[6-9] It is essentially based on microwave dielectric heating of the precursor solution, which leads to volumetric heating of the solvents and reagents. Hence, it is faster, simpler, and more energy efficient than conventional heating sources, such as, water or oil baths.

The fabrication technique of nanoscale materials with controlled shape and high dispersion using polymeric or other conventional capping materials is known as CACBD technique. Various optically transparent polymers were already used to produce different NPs having

exceptional optical properties.[10,11] Conventional capping materials, such as oleic acid and oleylamine, were frequently used to produce magnetic and semiconducting NPs.[12,13]

It is known that PbS is an important direct band gap semiconductor.[14] Bulk PbS has a narrow direct energy band gap of 0.41 eV at 300 K with a large exciton Bohr radius of 18 nm. Thus the absorption edge of PbS NPs can be tuned to anywhere between near-infrared to violet (0.4 μm), covering the entire visible spectrum. Large exciton Bohr radius and relatively small band gap make PbS one of the important candidates for size quantization studies. Recently, about 300% of quantum efficiency due to multiple exciton generation was also observed in PbS NPs.[15] Also, PbS NPs have exceptional optical properties[16] and they are considered as emerging novel materials for inorganic-organic bulk hybrid solar cells[17] and tunable near infrared detectors.[18]

During the recent years, PbS nanostructures and NPs have been prepared via different chemical techniques, such as, CBD,[2] SCBD,[6] MACBD,[6,8,9] surfactant assisted chemical bath deposition,[19,20] CACBD,[13,21,22] solvotherma,[20] hydrothermal,[23-25] electrochemical[26] and mechanochemical[27] techniques. These PbS nanostructures and NPs are reported in literature with diverse morphologies such as, nanoflake spheres,[2] nanobelts,[19] velvet-flower-like NPs,[19] dendritic NPs,[19] nanorods,[19,23] wires,[23] cubes,[23] spheres,[25] star-shaped NPs,[25] tubes,[28] and flower-shaped NPs.[29] Also, literature shows that thiourea is a favorable sulphur source for the controlled fabrication of semiconducting sulphide NPs, such as, CdS, CuS, ZnS, NiS.[30-33] In the case of PbS, the decomposition of Pb-TU complex under basic condition (pH 9 to 10) was already studied for controlled PbS thin-films or particles precipitation through CBD in aqueous media.[34,35] However, few of the reported synthesis techniques were based on the decomposition of Pb-TU complex in non-aqueous media.[2,6] It is well known that the combination of PbAc and TU produces a metastable complex in alcoholic media;[2] the Pb-TU complex is decomposed slowly into PbS NPs even at room temperature. Also, it can be thermally decomposed at higher temperatures (50 to 60°C) and can allow two different decomposition routes to produce PbS NPs with and without surface capping.

To the best of our knowledge, there is no systematic investigation on the synthesis of PbS particles by CBD, SCBD, MACBD and CACBD precipitation techniques from non-aqueous (methanolic) solution containing Pb-TU complex. In the present work, we try to show how

the morphology, size and physical properties of PbS particles are affected by the way they are synthesized using the above techniques.

4.2 Experimental

4.2.1 Materials

Lead acetate trihydrate (PbAc), thiourea (TU), methanol, poly (vinyl-pyrrolidone) (MW 40,000), oleic acid, oleylamine and n-hexane (purchased from Sigma Aldrich, Canada) were used without any further purification.

Earlier, Chaudhuri et al.[2] showed that, by using CBD synthesis technique, methanolic solutions of 0.1 mol/L of PbAc and 0.1 mol/L of TU (mixed at room temperature in 1:1 molar ratio) yielded nanostructured PbS NPs. Hence, in the present investigation, a similar CBD method was used to produce PbS particles at room temperature. In order to study the influence of different CBD variants on the morphology, size and physical properties of PbS particles, a similar method was used to produce methanolic Pb-TU complex solution. In a first step, separate solutions (0.05 mol/L) of PbAc and TU in methanol were prepared. These solutions were then mixed in equal proportions inside a beaker and stirred for few minutes to produce a 0.025 mol/L Pb-TU complex.

4.2.2 Synthesis of PbS nanostructured particles via CBD, SCBD and MACBD techniques

For the CBD synthesis technique, 20 ml of the above methanolic solution (0.025 mol/L) of Pb-TU complex were taken in a beaker. The opening of the beaker was then covered with a paraffin film and kept at room temperature (~25°C). The complex solution, which was initially clear, slowly turned to brown during the first 15 minutes. Then after 20 minutes, suspended brown particles became black and after 6 hours, these black particles precipitated at the bottom of the beaker. Precipitated particles were then filtered, washed in methanol and distilled water, then dried in warm air.

For the SCBD synthesis technique, 20 ml of the same methanolic solution (0.025 mol/L) of Pb-TU complex were taken in a beaker then kept in an ultrasonic bath (Toshcon, SH-4) for 45 minutes. After sonication, the temperature of the mixture increased from room

temperature by about 15 °C and black particles were formed. These particles were then filtered, washed in methanol and distilled water repeatedly, then dried in warm air.

For MACBD synthesis technique, also 20 ml of the same methanolic solution of Pb-TU was taken in a beaker, which was heated during 20s in a domestic microwave oven (Whirlpool, 800 W) at 50 % power level. After 20s of heating, the temperature of the methanolic solution increased from room temperature to the boiling point of the solvent (~65°C) and black precipitated particles were formed. These particles were then filtered and washed in methanol and distilled water repeatedly then dried in warm air.

4.2.3 Synthesis of PbS NPs via CACBD

For CACBD synthesis technique, two different types of capping materials were used:

i) A methanol soluble polymer (poly (vinyl-pyrrolidone) (PVP)) was used to develop capped PbS NPs at room temperature. For this, 500 mg of PVP were mixed with 20 ml of methanolic solution (0.025 mol/L) of Pb-TU complex. The resulting solution, initially transparent, was left undisturbed at room temperature (~25 °C). After 10 minutes, the color of the solution became reddish brown due to the formation of PbS NPs inside the PVP matrix.

ii) Oleic acid was used to develop PbS capped NPs via thermal decomposition. For this, 20 ml of methanolic solution (0.025 mol/L) of Pb-TU complex were mixed with 2 ml of OA and 10 ml of n-hexane inside a round bottom flask (capacity of 100 ml). This mixture was then heated at 120°C under continuous stirring in an oil bath using water condenser. After 30 minutes of heating, 2 ml of oleylamine (OM) were added to the mixture leading to a slightly yellowish solution, which, after 10 minutes of additional heating at the same temperature became brownish due to the formation of PbS NPs. Before the measurement of the absorption spectrum, PbS NPs were dispersed in toluene then precipitated by adding excess of ethanol. The precipitated PbS NPs were centrifuged then washed many times with ethanol and hot water to remove the excess of surfactant. The final PbS NPs were dried in a vacuum oven at 50°C for 2h then redispersed in toluene. Before optical measurement, the solvent absorption was masked by baseline correction with toluene.

4.2.4 Characterization

The composition of produced PbS particles and PbS NPs (with CBD, SCBD, MACBD and CACBD) was determined by X-ray diffraction (XRD) using Philips (X'Pert) X-ray Diffractometer (with Ni-filtered Cu K_α radiation). Particle size was estimated from the following Scherrer equation:

$$D = K\lambda / \beta\cos\theta \quad \textbf{(4-1)}$$

where, D is the particle size, k is the shape factor (taken as 0.9), λ is the wavelength of X-ray used, B is the broadening of line at half the intensity, and θ is the diffraction angle of line under consideration. The morphology and microstructure were studied by a Jeol (JSM-5610LV) Scanning Electron Microscope (SEM). PbS NPs synthesized by CACBD technique were characterized by TEM and selected area electron diffraction (SAED) using a JEOL JEM 1230 electron microscope operated at 200 kV. For TEM characterization, carbon coated copper grids were used. Samples were prepared by dropping dilute solutions of capped PbS NPs onto the carbon-coated copper grid. The absorption spectra of capped PbS NPs were recorded on Varian Cary Bio 300 UV-Vis spectrophotometer. The energy band gap (Eg) of the PbS capped NPs was determined from the following Tauc relation.

$$(\alpha h\nu)^2 \sim Eg - h\nu \quad \textbf{(4-2)}$$

where α (cm^{-1}) is the absorption coefficient, h (J.s) is the Plank constant, ν (Hz) is the frequency of radiation, and Eg (eV) is the energy band gap for direct band gap semiconductor. XPS of PbS non-capped and capped particles was realized using Axis Ultra Kratos, X-ray photoelectron spectrometer under a vacuum of 2-5 $x10^{-8}$ Torr. The binding energy values were charge-corrected to the C 1s signal (285.0 eV). Infrared (IR) spectra of PbS capped NPs were measured using a Bio-Red FTS-165 IR spectrometer.

4.3 Results and discussion

4.3.1 Effect of CBD, SCBD and MACBD on the size, shape and surface of PbS nanostructured particles

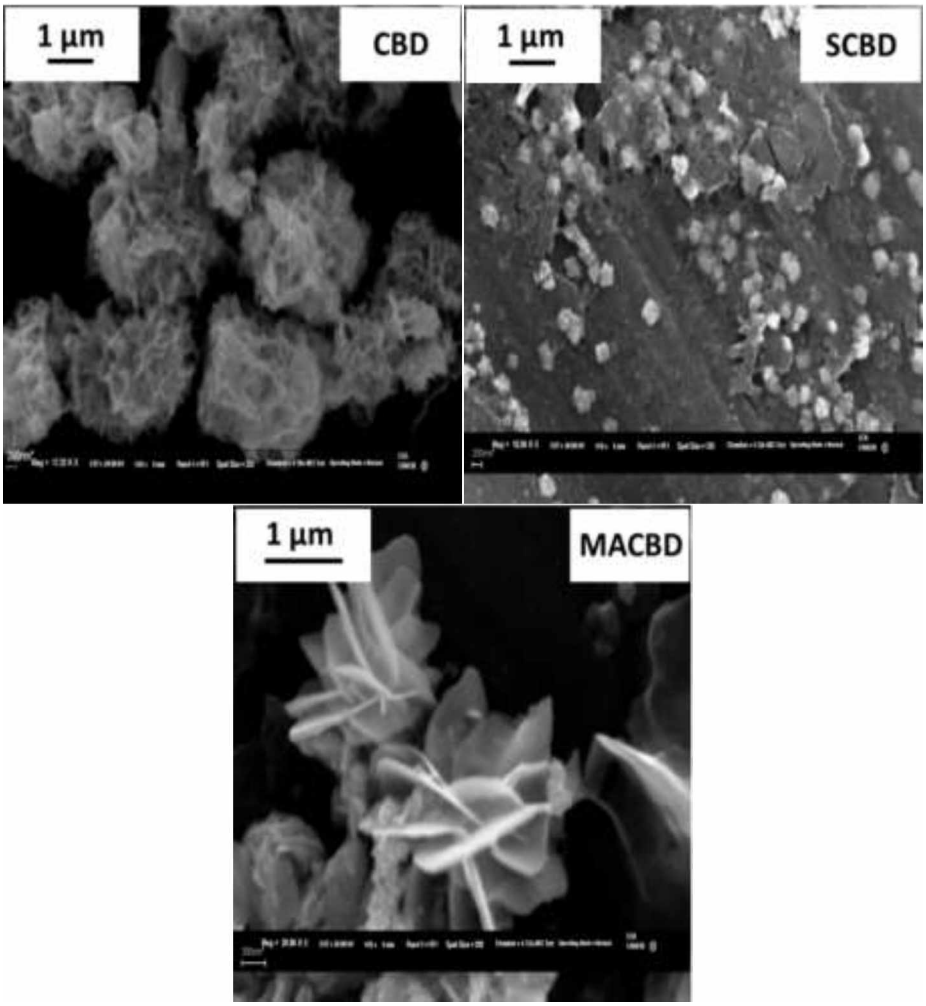

Figure 4.1 Scanning electron micrographs of PbS particles produced via CCBD, SCBD and MACBD.

Figure 4.1 shows SEM micrographs of PbS particles synthesized via CBD, SCBD and MACBD techniques. In general, these PbS particles show a significant variation in size and shape**. Figure 4.1** shows that PbS particles produced by CBD technique are spherical with an intricate network of flakes and their particle size is around 1.6 µm. However, PbS particles synthesized by SCBD technique are either cubic or spherical with particle size of around 0.20 µm, and those synthesized by MACBD technique consist of layers of thin flakes with particle size varying from 0.5 to 1.5 µm.

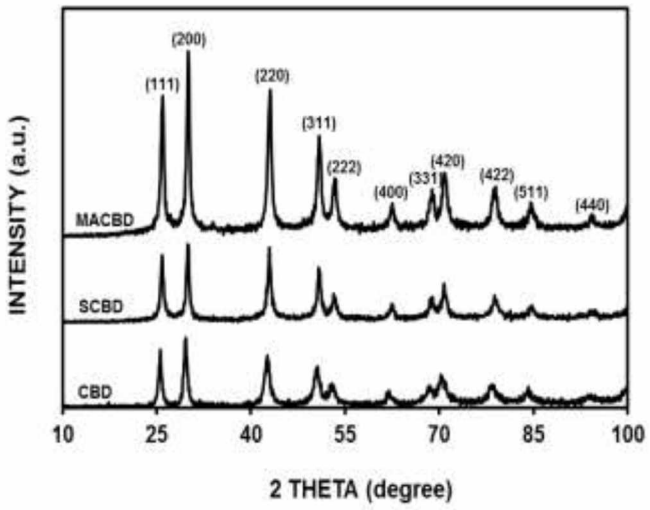

Figure 4.2 X-ray deffractographs of PbS particles produced via CCBD, SCBD and MACBD.X-ray deffractographs of PbS particles produced via CCBD, SCBD and MACBD.

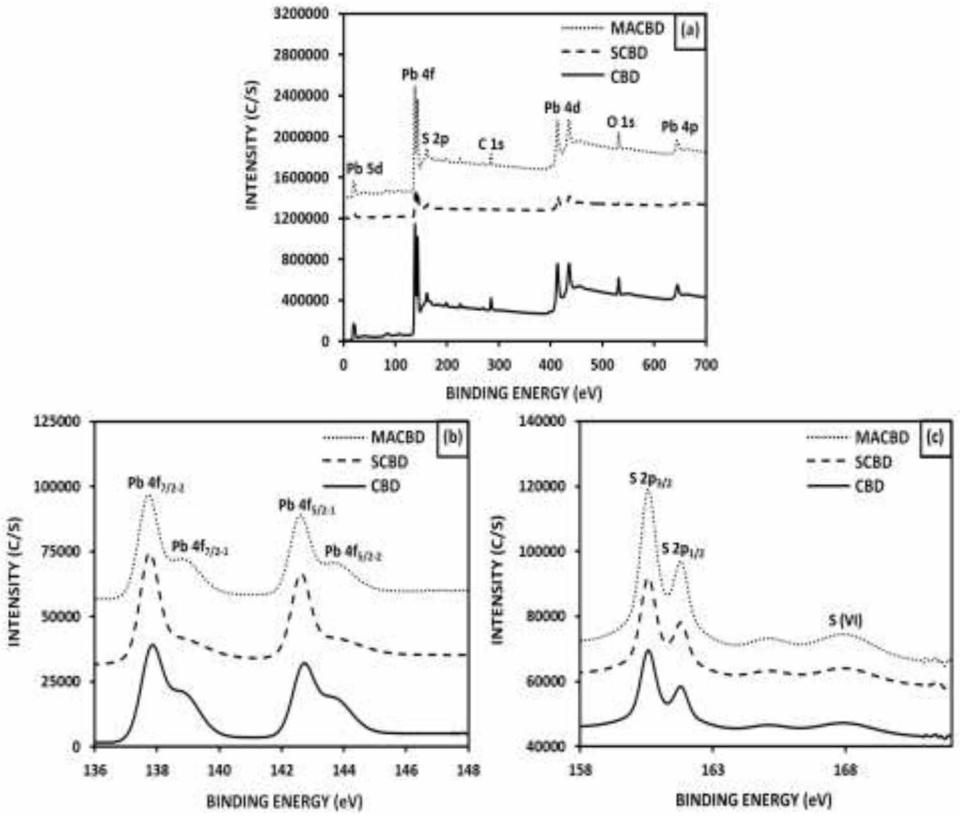

Figure 4.3 XPS spectra of PbS particles produced via CCBD, SCBD and MACBD: (a) a typical XPS survey scan; (b) HR XPS scans for Pb 4f core; (c) HR XPS scans for S 2p core.

XRD plots of PbS particles obtained by CBD, SCBD and MACBD techniques are presented in **Figure 4.2**. All these plots are similar and correspond to cubic PbS (JCPDS File No. 05-592). The corresponding diffraction peaks are indexed as (111), (200), (220), (311), (222), (400), (331), (420), (422), (440) and (511) planes of the cubic crystal lead sulfide. The broadening of XRD lines indicates that the average size of PbS crystallites is in the nanometer range. As estimated by the Scherrer equation **(Eq. 4.1)**, PbS nanostructured particles synthesized by CBD, SCBD and MACBD techniques have an average crystallites size of 26, 16 and 28 nm, respectively.

The XPS analysis of PbS NPs produced via these three precipitation techniques are shown in **Figure 4.3**. The binding energies obtained in this analysis are corrected according to the standard binding energy value of C 1s (285.0 eV). In wide-scan XPS spectra, **Figure 4.3** (graph (a)) shows no peaks other than those corresponding to C, O, Pb and S. High-resolution (HR) XPS spectra for the Pb 4f and S 2p regions are also recorded and respectively shown in the same figure (graphs (b) and (c)). Graph (b) shows that, for the three techniques used, the Pb core in spin orbit shows $4f_{7/2\text{-}1}$ peaks at around 137.5 eV, $4f_{7/2\text{-}2}$ shoulder peaks at around 138.8 eV, $4f_{5/2\text{-}1}$ peaks at around 142.6 eV and $4f_{5/2\text{-}2}$ shoulder peaks at around 143.7 eV. Graph (c) also shows that, for the three techniques used, the S core in spin orbit shows S $2p_{3/2}$ peaks at around 160.7 eV, S $2p_{1/2}$ peaks at around 161.9 eV, and S (VI) peaks at around 168.1 eV. Compared to XPS spectrum of pure PbS , the additional splitting of 4f orbital in the form of $4f_{7/2\text{-}2}$ and $4f_{5/2\text{-}2}$ (graph (b)) and splitting of S in the form of S $2p_{3/2}$, S $2p_{1/2}$ and S (VI) (graph (c)) are due to the presence of PbO.[22,36]

The formation of solid particles inside a solution occurs only if the ionic product of the reactants in the solution exceeds the solubility product of the solid (final solid product). First, nucleation centers are formed homogeneously in the solution and grow into primary particles. Then, these primary particles aggregate to form larger particles. The size and shape of these particles depend on the rate of formation of nuclei or primary particles, the time of precipitation, the solution temperature and the growth properties of the material. If the rate of formation of molecules/nucleation is slow, then the time taken to complete the precipitation is consequently long. In such case, primary particles have sufficient time to aggregate and grow into large particles until a terminal size is reached. On the other hand,

the precipitation time for solid particles is short when the rate of formation of nuclei or primary particles is fast. Since the time for aggregation is very short, the solid particles formed are small. Thus, faster formation rate leads to smaller terminal particle size.

During CBD of PbS NPs, a clear mixture was obtained when TU solution was added to PbAc solution. The mixture remained clear till about 15 minutes after which it slowly turned to brown. Suspended black particles appeared after 20 minutes and settled at the bottom of the beaker after 6 hours. The phenomena can be explained as follows: When TU solution was added to PbAc solution, a metastable complex of PbAc and TU was formed according to the following reaction:

$$Pb(CH_3COO)_2 + (NH_2)_2CS \rightarrow (Pb\text{-}TU)\text{-complex} \quad \textbf{(4-3)}$$

The Pb-TU complex obtained was metastable (the solution remains clear for first 15 minutes then turns to brown). It decomposed very slowly (~ 6 hours) at room temperature to form PbS nanoparticles:

$$(Pb\text{-}TU)\text{-complex} \rightarrow PbS \quad \textbf{(4-4)}$$

Since the decomposition of Pb-TU into PbS is very slow at room temperature, PbS nucleation centers formed initially by decomposition of (Pb-TU) complex attract other PbS molecules to form clusters. Then, aggregates of about 1-1.5 μm size are developed due to the long growth time.

When SCBD technique is used, the chemical effects of ultrasound arise from acoustic cavitations, that is, formation, growth and impulsive collapse of bubbles in liquid. The impulsive collapse of bubbles generates localized hot spots through adiabatic compression or shock wave formation within the gas phase.[37] These hot spots have transient temperature of ~5000 K, pressure of ~1800 atm. and cooling rate in excess of around 10^8 K/s. Ultrasound affects the formation of PbS particles in two ways: i) it provides the energy to decompose the complex to PbS and ii) it prevents the formation of aggregates. The former leads to faster formation of PbS particles. High kinetic energy of PbS primary particles, due to ultrasound agitation, thwarts the initial formation of large clusters and hence may lead to nanoscale particles. PbS particles obtained from methanolic solution of Pb-TU complex presented

shorter precipitation time (~ 0.75 hours), compared to the precipitation time measured for the CBD technique. Particle size also decreased from 1-1.5 μm to about 0.2 μm, due to the effect of ultrasonic waves on precursor solution. First, the ultrasonic radiation provided the thermal energy needed to break the complex to form PbS primary particles at a faster rate than that in CBD technique; and second, these PbS primary particles were imparted with high kinetic energy so that aggregation was prevented, which ultimately led to smaller PbS particles than obtained with CBD.

MACBD is essentially CBD at higher temperature due to rapid microwave heating of the solvent. The exact nature of microwave interaction with reactants during the synthesis step is somewhat unclear and speculative. Energy transfer from microwave to the material is believed to occur either through resonance or relaxation,[38] which results in rapid heating. Electric dipoles present in such materials respond to the applied electric field. This constant reorientation creates friction and collisions between molecules, which subsequently generates heat. This heating mechanism is developed directly from the molecules of the materials. Hence, compared to conventional heating in a bath, which is realized mainly by heat conduction, microwave heating is more efficient and rapid.[38] In MACBD technique, PbS particles with methanolic solution of Pb-TU complex is an accelerated CBD technique and hence led to an aggregate size varying from 0.5 to 1.5 μm.

4.3.2 Effect of CACBD on the size, shape and surface of PbS NPs

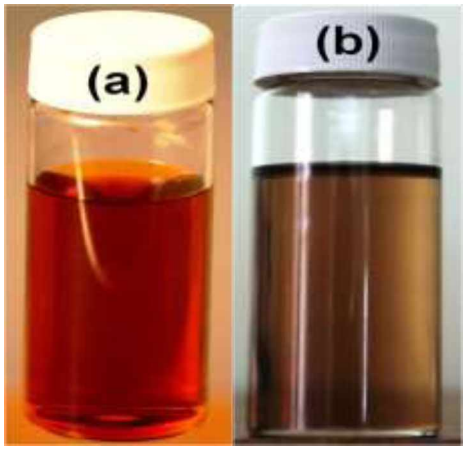

Figure 4.4 Images of vials: (a) PVP-capped PbS NPs; (b) OA-capped PbS NPs.

As mentioned above in experimental section, the two capping materials were PVP and OA, respectively used to synthesize PbS capped NPs at room temperature and via thermal decomposition. **Figure 4.4(a)** and **(b)** show images of vials of PVP and OA-capped PbS NPs, respectively. The methanolic solution of the complex remains transparent even after addition of PVP. However, after 10 minutes, the colorless transparent precursor solution turns into transparent reddish brown due to the formation of PbS NPs and remains stable up to three days at room temperature with no visible agglomeration (**Figure 4.4(a)**). For PVP, Pb-TU complex decomposed itself at room temperature to produce PbS NPs in the PVP matrix, while for OA, Pb-TU complex was decomposed thermally to produce PbS NPs. In both cases, decomposition routes are different from each other leading to an exceptional variation in the size and shape of PbS NPs.

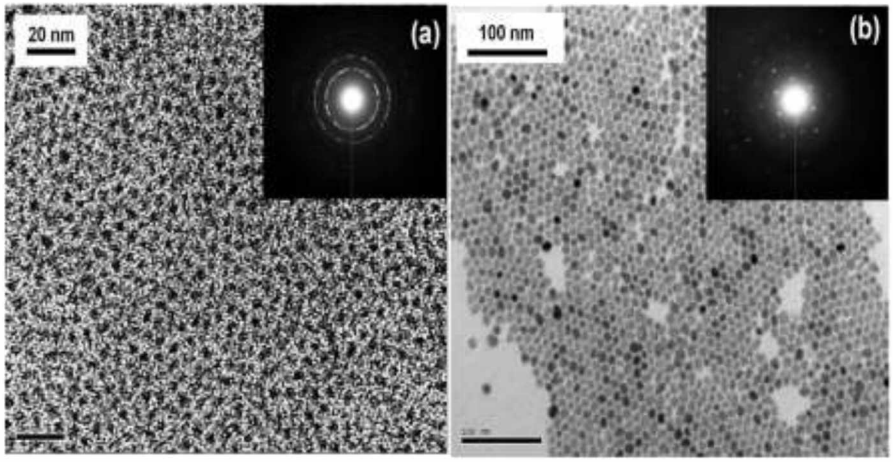

Figure 4.5 TEM images of (a) PVP and (b) OA-capped PbS NPs along with SAED.

Figure 4.5(a) and **(b)** show TEM images of PVP and OA-capped PbS NPs, respectively, along with SAED. As shown in **Figure 4.5(a)**, PVP-capped PbS NPs are spherical, homogeneously dispersed and have an average size of around 3 nm. The SAED of PVP-capped NPs consists of concentric rings with brighter spots. These rings are identified to be those of PbS rock salt structure (JCPDS card no. 5-0592) with reflections only from (111), (200), (220), (311), (222), (400) and (420) planes. **Figure 4.5(b)** shows that OA-capped PbS NPs are spherical/cubic in shape with an average size of 8 nm. The SAED pattern of OA-capped PbS NPs indicates that these NPs are highly crystalline with single crystal like pattern

and rock salt structure. Their TEM image shows that PbS NPs are uniformly dispersed and have uniform shape, as previously observed.[13,39]

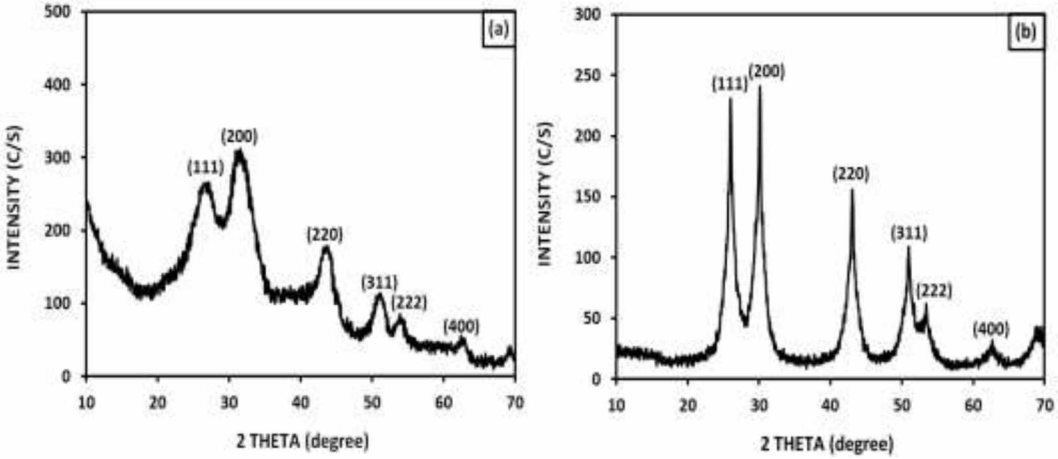

Figure 4.6 XRD of (a) PVP and (b) OA-capped PbS NPs.

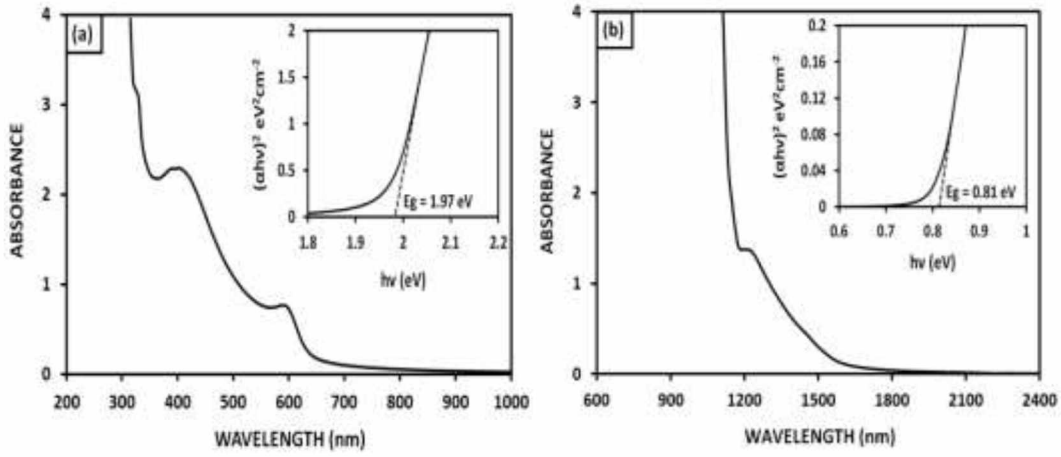

Figure 4.7 Absorption spectra of (a) PVP and (b) OA-capped PbS NPs. Insets show their respective band gap plots.

Figure 4.6(a) and **(b)** show the XRD of PVP and OA-capped PbS NPs. All diffraction peaks match well with the standard XRD lines of cubic PbS (JCPDS File No. 05-592) and are due to reflections from (111), (200), (220), (311), (222) and (400) planes for both PVP and OA-capped PbS NPs. The broadening peaks indicate that crystal size is in the nanometer range,

as confirmed by the TEM observation. As estimated from the broadening of XRD peaks using the Scherrer equation (**Eq. 4-1**), the average crystallite sizes for PVP and OA-capped PbS NPs were respectively 2.7 and 7.4 nm, which are close to those observed by TEM.

Figure 4.7(a) and **(b)** show the absorption spectra of PVP and OA capped PbS NPs, respectively. As shown in **Figure 4.7(a)**, PVP-capped PbS NPs present a broad absorption from about 650 nm to the UV region with two well-defined absorption peaks at 400 and 590 nm. The occurrence of these two peaks is an indication of the narrow size distribution of PbS NPs and the large shift in the visible region is due to their strong size confinement compared to bulk PbS. This result is in good agreement with that reported by Kuljanin et al.[40] and Nenadovic et al.[41] for polyvinyl alcohol (PVA) capped PbS NPs. In an earlier work, Patel et al.[21] reported that the absorption spectrum of PVP-capped PbS NPs didn't show any peak because their size was widely distributed with a mixture of cubic, needle and spherical shapes. However, in that work, PbS NPs were formed by spontaneous ion-ion reaction of H_2S and Pb $(NO_3)_2$ and this type of reaction is too fast for polymer matrix to restrict the growth of PbS NPs. Similar results were also observed for other polymers, such as, polyethylene (PE), poly (1-butene) (PB), poly (1-decene) (PD) and polystyrene (PS).[16] The absorption spectra of PbS NPs capped with these polymers didn't show any significant absorption peaks. Contrarily to those reported results, we showed that in our case, the Pb-TU complex was slowly decomposed into PbS NPs in the PVP matrix, which restricts their growth. As a result, we obtained PbS NPs of spherical shape with approximately a constant diameter. For OA-capped PbS NPs, a special purification (presented in section 2.3) was done before characterization in order to eliminate the surfactant excess. As shown by the absorption spectrum of **Figure 4.7(b)**, these NPs absorb strongly between 1000 to 1500 nm due to their strong size quantization effect compared to bulk PbS. For both PVP and OA-capped PbS NPs, their corresponding energy band gaps, respectively shown in the insets of **Figure 4.7(a)** and **(b)**, are around 1.97 and 0.81 eV. These values are in agreement with theoretical band gap values of PbS NPs of 3 and 8 nm in diameter, respectively.[42]

XPS curves of PVP and OA capped PbS NPs are presented in **Figure 4.8**. The Figure shows similar peaks as those observed for uncapped PbS NPs. HR XPS scans presented in **Figure 4.8**(graph(b)) shows no additional splitting in the Pb 4f region other than 4f7/2 peaks at

around 137.5 eV and 4f5/2 peaks at around 142.5 eV compared to XPS of pure PbS.[22,36] If we go back to **Figure 4.3**(graph (b)), the additional splitting in uncapped PbS NPs was due to PbO. Thus, it can be concluded that uncapped PbS NPs exhibit poor surface stability in air, due to their high surface energy, which leads to partial oxidation caused by atmospheric oxygen. The absence of oxidation in capped PbS NPs indicates that capping layers of PVP and OA effectively prevent surface oxidation of PbS NPs. Single and un-split peaks at around 160.7 eV shown in **Figure 4.8**(graph(c)) correspond to S 2p of capped PbS NPs.[22,36]

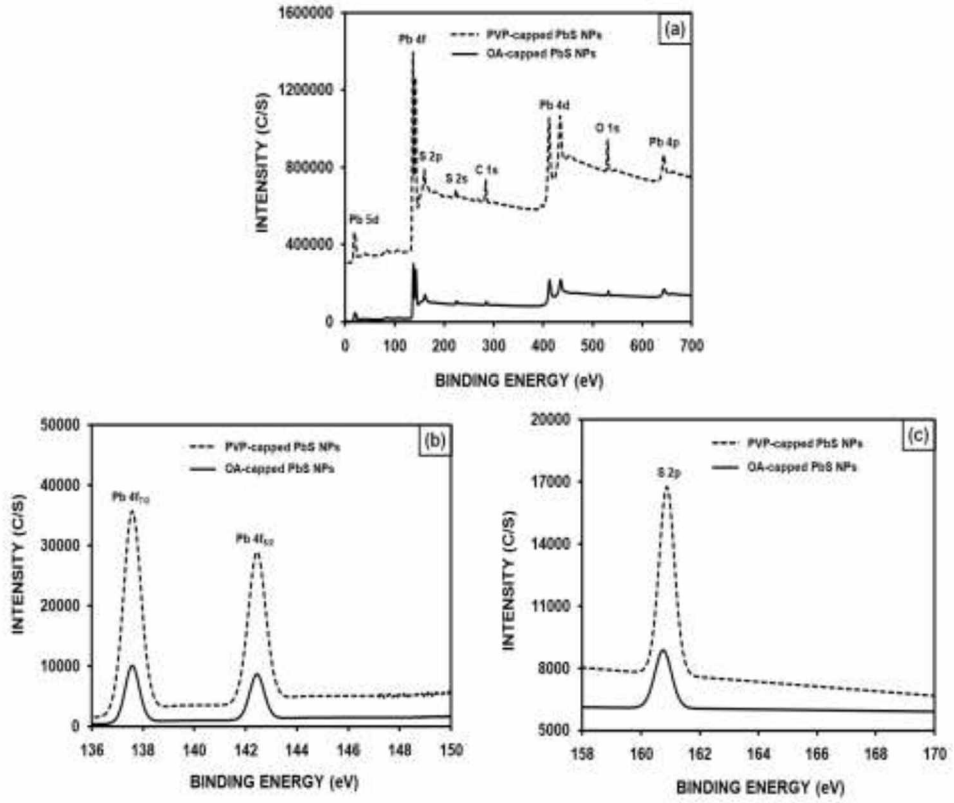

Figure 4.8 XPS spectra of PVP and OA- capped PbS NPs produced via CACBD: (a) a typical XPS survey scan; (b) HR XPS scans for Pb 4f core; (c) HR XPS scans for S 2p core.

Figure 4.9 shows the FTIR spectra for PVP (curve (a)) and PVP-capped PbS NPs (curve (b)). In curve a, the stretching band of C=O for PVP is observed at 1660 cm^{-1} and, as shown in curve (b), this band shows red shift of about 20 cm^{-1} after the formation of PbS NPs in PVP matrix. This red shift in C=O stretching is an indication of a chemical bonding between PbS NPs and PVP capping layer. FTIR of PVP also shows absorption bands in the region

1500-1100 cm^{-1}, which are due to the in-plane C-H bending of different CH moieties and C-N stretching modes. After the formation of PbS NPs inside the PVP matrix, these bands show a remarkable change in terms of size, shape and intensity due to interaction between N and PbS. The absorption bands due to asymmetric and symmetric C-H at 2989 and 2895 cm^{-1} also show some shift after PbS NPs formation. The overall FTIR absorption bands of PVP and PVP-capped PbS NPs are summarised in **Table 4.1**.

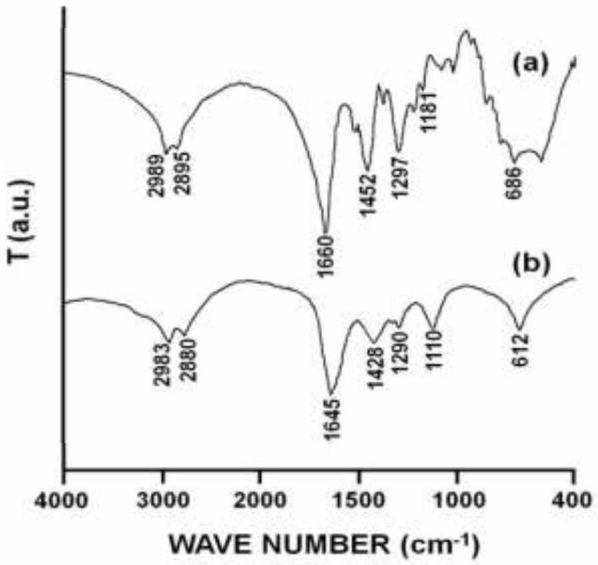

Figure 4.9 FTIR spectra of (a) PVP and (b) PVP- capped PbS NPs.

Such type of bonding was not observed in previously reported polymer-capped PbS NPs.[11,40] The decomposition of Pb-TU complex in a controlled manner in a polymer matrix led to a uniform particle shape and size due to particle/matrix interaction. As reported in literature,[11] spontaneous ion-ion reaction between Pb^{+2} and S^{-2} helps to break the interaction between Pb^{+2} and the polymer matrix. Such reaction is too fast for the polymer matrix to prevent diffusion and growth of particles. Also, polar functional group (like –OH and –C=O) in polymer chains could also affect the interaction between NPs and the polymer matrix.

Further FTIR characterization was performed on OA-capped PbS NPs. First, these NPs were washed several times with ethanol then dried at room temperature in order to investigate whether OM plays any part in surface capping or not. **Figure 4.10** (curve (b)) shows the corresponding FTIR spectrum, together with that of OA (curve (a)). The overall FTIR

absorption bands of OA and OA-capped PbS NPs are summarised in **Table 4.1**. The long alkyl chain, the double bond between carbon atoms and the carboxylic acid group of OA are clearly identified on curve (a). The bands at 2955 and 2852 cm^{-1} are the contributions from the asymmetric and symmetric CH_2 stretching, respectively. CH_2 deformation and rocking vibrations are identified by the sharp bands at 1470 and 710 cm^{-1}, respectively. The bands at 1435 and 960 cm^{-1} are appearing as O-H in-plane and out-of-plane bands, respectively. The band at 3010 cm^{-1} is assigned to the stretching vibration of C-H and the sharp band at 1716 cm^{-1} is the characteristic stretching vibration of C-O in carboxylic acid. IR spectrum of OA-capped PbS NPs (curve (b)) shows similar bands at around 3035, 2954, 2865, 1478, and 690 cm^{-1}. These bands indicate the presence of long alkyl chains on the surface of PbS NPs. However, the signature band (at 1716 cm^{-1}) of carbonyl in carboxylic acid doesn't appear in the FTIR spectrum of OA-capped PbS NPs. In place of carbonyl band, a new band is observed at 1525 cm^{-1}, which proves the existence of carboxylic acid salt in OA-capped PbS NPs. Such result is supported by previously reported FTIR studies for OA-capped PbS NPs.[22]

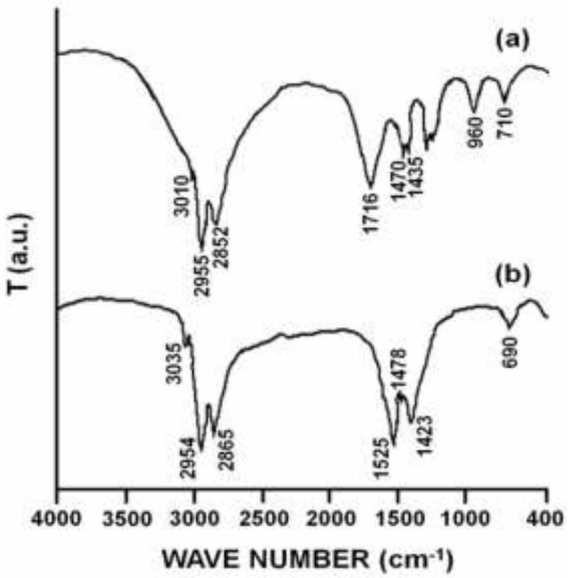

Figure 4.10 FTIR spectra of (a) OA and (b) OA- capped PbS NPs.

Table 4.1 FTIR absorption bands for PVP, PVP-capped PbS NPs, OA and OA-capped PbS NPs.

Absorption bands (cm^{-1})		Functional groups	Absorption bands (cm^{-1})		Functional groups
PVP	**PVP-capped PbS NPs**		**OA**	**OA-capped PbS NPs**	
2989 2895	2983 2880	Asymmetrical and symmetrical stretching of C-H moieties	3010	3035	Stretching vibration of C-H
1660	1645	-C=O stretching	2955 2852	2954 2865	Asymmetrical and symmetrical stretching of C-H moieties
1510 1452	1428	In plane C-H bending of different C-H moieties			
1360 1297 1233 1181	1290 1110	-C-N stretching mode	1716		Stretching vibration of C-O in carboxylic acid
1095 1015 935 870 815		Cyclic –C-C stretching mode		1525	Carboxylic acid salt
735 686	612	Amide rocking band	1470 710	1478 690	CH_2 deformation and rocking vibrations
465		Aliphatic –C-C- stretching of vinyl chain	1435 960	1423	O-H in plane and out-of-plane bands

4.4 Conclusions

In this work, a systematic study has been carried out on PbS particles produced using methanolic Pb-TU complex via different precipitation techniques. The decomposition of Pb-TU complex is a key factor controlling the size, the shape and the stability of PbS NPs. The different techniques used (CBD, SCBD and CACBD) to produce PbS NPs show how the type of precipitation technique affects the self-decomposition of PbS NPs. For CBD, the Pb-TU complex decomposes gradually and produces PbS nanostructured spherical NPs with intricate network of flakes. The size of these NPs is around 1.5-1.7 μm. In case of SCBD, Pb-TU complex decomposes itself under ultrasonic heating and produced PbS particles either cubic or spherical having sizes of 0.19 to 0.21 μm. The ultimate reason behind the formation of small and well-shaped PbS particles in SCBD is the ultrasonic effect. The initially formed particles break under ultrasonic frequency and produce smaller and well-shaped particles. In CACBD (at room temperature), first, Pb-TU complex is enveloped by PVP matrix and then, decomposition of the complex in PVP matrix produces PbS NPs of uniform size and shape. An interaction between particles and host polymer matrix allows the formation of monodispersed PbS NPs.

Another set of precipitation techniques is relying on thermal decomposition of Pb-TU complex. As discussed earlier, MACBD is the CBD at higher temperature and rapid microwave heating of solvent is not allowing the conversion of initially formed flakes into flaky nanostructured networks. In OA-capped PbS NPs, first Pb-TU complex is covered by OA at higher temperature and, after addition of oleylamine, it gets precipitated as PbS NPs with uniform size and shape.

Finally, for CACBD, in both cases, PbS NPs shows good dispersion with highly stable surface towards oxidation compared to uncapped PbS. A proper surface coating on PbS NPs helps them to retain their N-type nature and possibility of application for different devices because air oxygen works as a dopent for PbS.

Acknowledgements

The authors would like to thank the Natural Sciences and Engineering Research Council of Canada (NSERC) for financial support of this work.

4.5 References

1. N. Mukherjee, A. Sinha, G.G. Khan, D. Chandra, A. Bhaumik, A. Mondal, *Materials Research Bulletin* 46 **(2011)** 6-11.
2. T. Chaudhuri, N. Saha, P. Saha, *Materials Letters* 59 **(2005)** 2191-2193.
3. J.C. Colmenares, M.A. Aramendıa, A. Marinas, J.M. Marinas, F.J. Urbano, *Applied Catalysis A* 306 **(2006)** 120-127.
4. K.S. Suslick, *Ultrasound. Its Chemical, Physical, and Biological Effects*, VCH: Weinhein, Germany, **(1988)**.
5. M.M. Mdleleni, T. Hyeon, K.S. Suslick, *Journal of American Chemical Society* 120 **(1998)** 6189-6190.
6. Y. Zhao, X-H. Liao, J-M. Hong, J-J. Zhu, *Materials Chemistry Physics* 87 **(2004)** 149-153.
7. A.Kothari, T.K. Chaudhuri, *Materials Letters* 65 **(2011)** 847-849.
8. T. Ding, J-J. Zhu, *Materials Science and Engineering B* 100 **(2003)** 307-313.
9. T. Ding, J-R. Zhang, S. Long, J-J. Zhu, *Microelectronic Engineering* 66 **(2003)** 46-52.
10. R.E. Schwerzel, K.B. Spahr, J.P. Kurmer, V.E. Wood, J.A. Jenkins, *Journal of Physical Chemistry A* 102 **(1998)** 5622-5626.
11. P.A. Kurian, C. Vijayan, C.S. Suchand sandeep, R. Philip, K. Sathiyamoorthy, *Nanotechnology* 18 **(2007)** 075708 (1-7).
12. K. Parekh, R.V. Upadhyay, V.K. Aswal, *Journal of Nanoscience Nanotechnology* 8 **(2008)** 1-7.
13. M.A. Hines, G.D. Scholes, *Advanced Materials* 15 **(2003)** 1844-1849.
14. Y. Wang, A. Suna, W. Mahler, R. Kasowski, *Journal Chemical Physics* 87 **(1987)** 7315-7322.
15. R.J. Ellingson, M.C. Beard, J.C. Johnson, P. Yu, O.I. Micic, A.J. Nozik, A. Shabaev, A.L. Efros, *Nano Letters* 5 **(2005)** 865-871.
16. D.J. Asunskis, I.L. Bolotin, L. Hanley, *Journal of Physical Chemistry Letters C* 112 **(2008)** 9555-9558.
17. A.A.R. Watt, D. Blake, J.H. Warner, E.A. Thomsen, E.L. Tavenner, H. Rubinsztein-Dunlop, P. Meredith, *Journal of Physics D: Applied Physics* 38 **(2005)** 2006-2012.

18. S.A. McDonald, G. Konstantatos, S. Zhang, P.W. Cyr, E.J.D. Klem, L. Levina, E.H. Sargent, *Natural Materials* 4 **(2005)** 138-142.
19. L. Dong, Y. Chu, Y. Liu, M. Li, F. Yang, L. Li, *Journal of Colloid and Interface Science* 301 **(2006)** 503-510.
20. C. Zhang, Z. Kang, E. Shen, E. Wang, L. Gao, F. Luo, C. Tian, C. Wang, Y. Lan, *Journal of Physical Chemistry B* 110 **(2006)** 184-189.
21. A.A. Patel, F. Wu, J.Z. Zhang, C.L. Torres-Martines, R.K. Mehra Y. Yang, S.H. Risbud, *Journal of Physical Chemistry B* 104 **(2000)** 11598-11605.
22. S. Chen, W. Liu, *Materials Chemistry and Physics* 98 **(2006)** 183-189.
23. D. Berhanu, K. Govender, D. Smyth-Boyle, M. Archbold, D.P. Halliday, P.O. Brien, *Chemical Communications* **(2006)** 4709-4711.
24. Y. Ni, X. Wei, J. Hong, X. Ma, *Crystal Research and Technology* 41 **(2006)** 885-888.
25. P. Zhao, J. Wang, G. Chen, Z. Xiao, J. Zhou, D. Chen, K Huang, *Journal of Nanoscience and Nanotechnology* 8 **(2008)** 379-385.
26. Y.J. Yang, *Materials Science and Engineering B* 131 **(2006)** 200-202.
27. P. Balaz, E. Boldizarova, E. Godocikova, J. Briancin, *Materials Letters* 57 (2003) 1585-1589.
28. E. Leontidis, M. Orphanou, T. Kyprianidou-Leodidou, F. Krumeich, W. Caseri, *Nano Letters* 3 **(2003)** 569-572.
29. Y. Ni, F. Wang, H. Liu, G. Yin, J. Hong, X. Ma Z. Xu, *Journal of Crystal Growth* 262 **(2004)** 399-402.
30. T. Mandal, V. Stavila, I. Rusakova, S. Ghosh, K.H. Whitmire, *Chemistry of Materials* 21 **(2009)** 5617-5626.
31. F. Li, J. Wu, Q. Qin, Z. Li, X. Huang, *Powder Technology* 198 **(2010)** 267-274.
32. Z. Zhao, F. Geng, H. Cong, J. Bai, H-M Cheng, *Nanotechnology* 17 **(2006)** 4731-4735.
33. Y-H. Zhang, L. Guo, L. He, K. Liu, C. Chen, Q. Zhang, Z. Wu, *Nanotechnology* 18 **(2007)** 485609 (1-8).
34. J. Bloem, *Applied Scientific Research* 68 **(1956)** 92-100.
35. R.K. Joshi, A. Kanjilal, H.K. Sehgal, *Applied Surface Science* 221 **(2004)** 43-47.
36. P.K. Khanna, V.V.V.S. Subbarao, M. Wagh, P. Jadhav, K.R. Patil, *Materials Chemistry and Physics* 93 **(2005)** 91-94.

37. K.S. Suslick, S.B. Choe, A.A. Cichowlas, M.W. Grinsta, *Nature* 353 **(1991)** 414- 416.
38. S.A. Galema, *Chemical Society Reviews* 26 **(1997)** 233-238.
39. J.H. Warner, E. Thomsen, A.R. Watt, N.R. Heckenberg, H. Rubinsztein-Dunlop, *Nanotechnology* 16 **(2005)** 175-179.
40. J. Kuljanin, M.I. Comor, V. Djokovic, J.M. Nedeljkovic, *Materials Chemistry and Physics* 95 **(2006)** 67-71.
41. M.T. Nenadovic, M.I. Comor, V. Vasic, O.I. Micic, *Journal of Physical Chemistry* 94 **(1990)** 6390-6396.
42. I. Moreeles, K. Lambert, D. Smeets, D.D. Muynck, T. Nollet, J.C. Martins, F. Vanhaecke, A. Vantomme, C. Delerue, G. Allan, Z. Hens, *ACS Nano* 3 **(2009)** 3023-3030.

Chapter 5: Aminocaproic acid mixed methanolic lead-thiourea complex precursor and its thermal decomposition to star-shaped lead sulphide crystals

Jayesh D. Patel[a,b], Frej Mighri[a,b,*] and Abdellah Ajji[a,c]

[a]Center for Applied Research on Polymers and Composites, CREPEC

[b]Chemical Engineering Department, University of Laval, Quebec, QC, G1K 7P4 Canada

[c]Chemical Engineering Department, Ecole Polytechnique, C.P. 6079, Succ. Centre- Ville Montreal, QC, H3C 3A7 Canada

Published in ***Materials Letters*** 74 (2012) 183-186

Résumé

Dans ce travail, nous présentons pour la première fois une voie de synthèse simple pour fabriquer une structure de sulfure de plomb (PbS) contrôlée à l'aide du précurseur d'un mélange d'acides aminés. Un rendement élevé en cristaux de PbS en forme d'étoiles a été obtenu par la technique de la synthèse solvothermale (à 170°C durant 20 h) en utilisant un précurseur du complexe de Pb-TU méthanolique mélangé à un acide aminocaproique (ACA) respectueux de l'environnement. Le mécanisme conduisant à ces cristaux PbS en forme d'étoile a été discuté. Les cristaux de PbS telles que synthétisés ont été caractérisés par la diffractométrie de rayons X (XRD), la microscopie électronique à balayage (MEB), la spectroscopie à dispersion d'énergie (EDS), et la spectroscopie infrarouge à transformée de Fourier (FTIR). Les résultats obtenus montrent que les cristaux de PbS en forme d'étoile synthétisés sont exempts d'impuretés et sont cristallins à phase cubique. Enfin, l'analyse par FTIR indique que les molécules ont été délimitées sur la surface du cristal de PbS par l'intermédiaire du doublet libre de l'azote des groupes de tête aminés.

Abstract

In this work, we present for the first time a simple synthetic route to fabricate a controlled lead sulphide (PbS) structure using amino acid mixed precursor. High yield star-shaped PbS crystals were developed by solvothermal synthesis technique using an environment friendly aminocaproic acid (ACA) mixed methanolic Pb-TU complex precursor at 170°C for 20 h. The mechanism leading to these star-shaped PbS crystals was discussed. The as-synthesized PbS crystals were characterized by powder X-ray diffraction (XRD), scanning electron microscopy (SEM), energy dispersive spectroscopy (EDS), and Fourier transform infrared (FTIR). The obtained results show that the synthesized star-shaped PbS crystals were exempt of impurities and were crystalline with cubic phase. Finally, the FTIR study indicates that molecules were bounded on the surface of PbS crystal via nitrogen lone pair of the amino head groups.

5.1 Introduction

The development of inorganic crystals with controlled morphology is becoming a highly exciting research area because the special physiochemical properties of these inorganic materials are tunable through the control of their size and shape.[1] Properties of semiconducting materials are highly depend on their surface area. Greenham et al. showed that branched CdSe tetrapods in MDMO-PPV give an improved electron transport compared to linear CdSe nanorods due to high surface area, leading to solar cells with an efficiency of 2.4–2.8%.[2] PbS is considered as one of the most important semiconductors that can be synthesized with well-controlled morphologies leading to well quantization effect. The combination of such properties makes PbS suitable for efficient electroluminescent devices such as inorganic-organic bulk hybrid solar cells,[3] tunable near-infrared detectors,[4] and solid state lasers.[5] During the last few years, various PbS structures have been synthesized via solution phase methods. These structures include nanotubes, nanowires, cubes, octahedrons, flower structures, sheet-like shape, dendrite and macrostar-like hierarchical structures.[6-11] Their synthesis techniques generally include hydrothermal, solvothermal, chemical or thermal decomposition routes with suitable surfactants or capping molecules. Recently, biomolecule-assisted chemical route has become highly promising due to its novelty and its environmentally friendly character for a large variety of nanomaterials and also for its strong utility in morphology control.[12] Moreover, PbS nanostructures are also synthesized using amino acids as bio-capping molecules.[13,14] Among the various amino acids, aminocaproic acid (ACA) is very useful to produce size and shape controlled particles including their organized self-assembled nanostructure.[15]

To the best of our knowledge, the synthesis of PbS nanoparticles or nanostructures using ACA as a biomolecule is not reported in the literature. In this work, we propose a simple environment friendly solvothermal route for the synthesis of star-shaped PbS crystals with high yield using ACA biomolecule/methanolic lead-thiourea (Pb-TU) complex precursor.

5.2 Experimental

All chemicals were purchased from Sigma-Aldrich, Canada, and were used as received without further purification. ACA biomolecule mixed methanolic Pb-TU complex precursor

was prepared as follows: first, lead acetate trihydrate (0.05 mmol, 1.89 gm) and thiourea (0.05 mmol, 0.380 g) were dissolved in 100 mL of methanol to obtain a clear methanolic Pb-TU complex solution. Further, ACA (0.1 mmol, 1.31 g) was added to this solution under magnetic stirring at room temperature to obtain a final clear precursor solution. After 1h of stirring, this precursor solution was transferred to a Teflonlined stainless steel autoclave (capacity of 1L), which was filled with distilled water up to 80% of the total volume and treated at 170 °C for 20 h then cooled naturally to room temperature. The obtained product was filtered out, washed several times by ethanol and distilled water, and then dried at 50°C for 1 h.

Powder XRD data of the sample was recorded on a Siemens D5000 X-ray diffractometer, using Cu-Kα radiation (λ = 1.54059 Å). SEM and EDS were recorded using a Jeol JSM-6360/LV scanning electron microscope. The sample was dispersed sonochemically in methanol and a drop of methanolic dispersion placed on SEM stud (covered with carbon tape) and immediately evaporated at ambient temperature. FTIR of ACA and PbS crystals were obtained using a Nicolet (Thermo Fisher) Model 380 FTIR with an attenuated total reflectance sampling device, model Smart Performer with a ZnSe crystal. The infrared spectra were collected within the range of 650 to 4000 cm^{-1} with 10 scans per spectrum.

5.3 Results and discussion

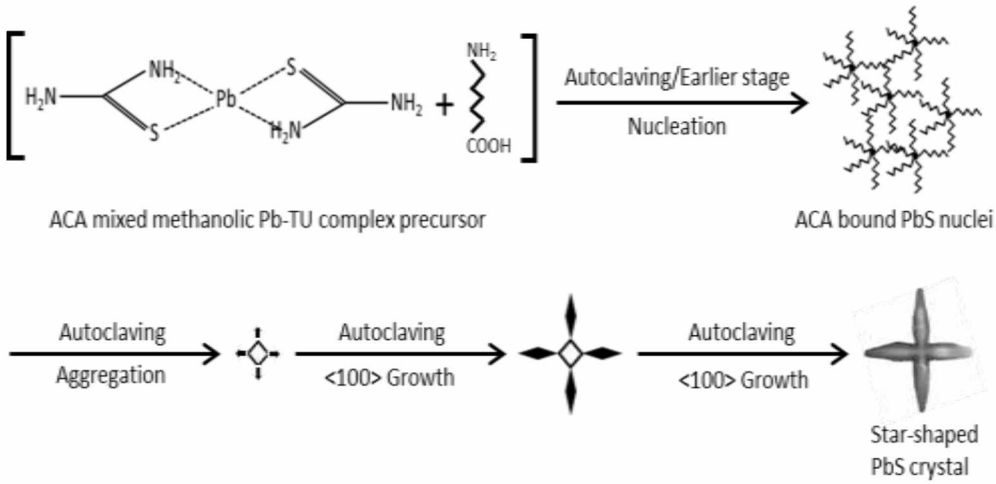

Scheme 5.1 The possible mechanism for the <100> directions growth process of star-shaped PbS crystals.

It's well known that methanolic Pb-TU complex is metastable and is slowly decomposed into nanostructured PbS particles at room temperature.[16] Controlled decomposition of Pb-TU complex is highly beneficial to regulate the size and morphology of the PbS particles. ACA biomolecule used in this study is composed of an alkyl chain and two head ends of $-NH_2$ and -COOH groups, which have strong abilities for coordination with the metal ions. At the initial stage of the synthesis, the thermal decomposition of Pb-TU complex may release Pb^{+2} cations and S^{-2} anions, which could form a highly active ACA bound PbS nuclei. In the primary formation stage of the nuclei, the decomposition rate of the Pb-TU complex is slow and crystals grow in the low Pb^{+2} concentration. Further, increasing Pb^{+2} concentrations promotes the two-dimensional nucleation and increases the growth rates along the four <100> directions. Finally, at the end of the synthesis, four <100> directions growth leads to star-shaped PbS crystals, as shown in **Scheme 5.1**.

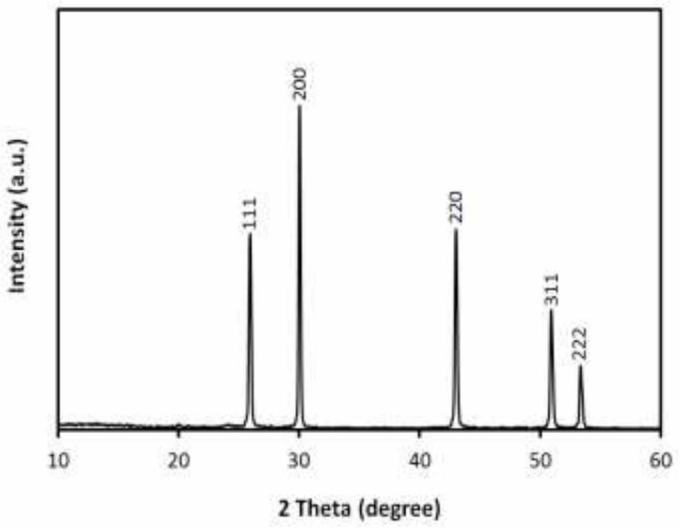

Figure 5.1 Powder XRD patterns of star-shaped PbS crystals.

It is well known that good crystallinity of semiconducting crystals have higher mobility of the charges and it shows good conductivity compared to their polycrystalline or nanocrystalline form. Powder XRD was performed to identify the composition and phase structure of the synthesized star-shaped PbS crystals. The corresponding results are shown in **Figure 5.1**. The sharp and intense diffraction patterns are a good indication of the high crystallinity of the developed PbS crystals. All the observed peaks, indexed on the basis of JCPDS standards,

correspond to face-centered cubic PbS (JCPDS Card No.05-0592) and are due to the reflections from (111), (200), (220), (311) and (222) planes. From **Figure 5.1**, the calculated ratio between the intensities of the (200) and (111) diffraction peaks is 1.65, which is higher than the standard ratio of 1.049 (according to JCPDS) indicating that PbS crystals abound in {100} facets, and grow along the <100> directions.

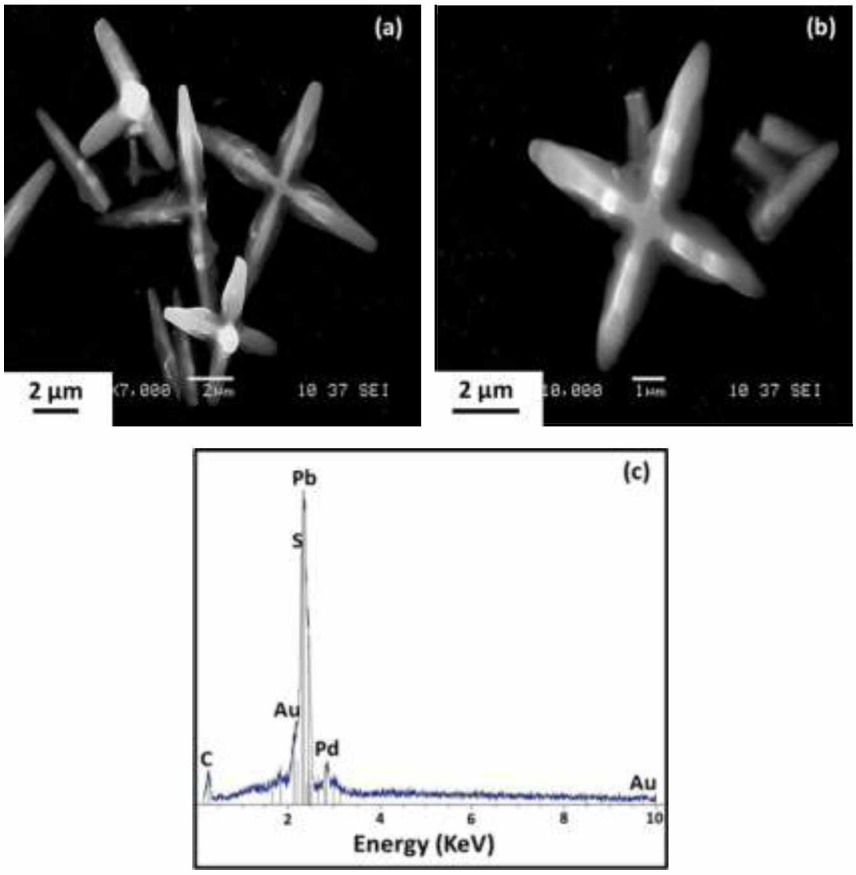

Figure 5.2 SEM images ((a) and (b)) with (c) EDS spectrum of star-shaped PbS crystals.

The morphology of the synthesized PbS crystals was examined by SEM. **Figure 5.2(a)** and **(b)** show typical SEM images of PbS crystals. From the low magnification SEM image (**Figure 5.2(a)**), it is clearly seen that PbS crystals exhibit star-shaped morphology with crystal size varying between 4 and 8 µm. Higher magnification of the individual PbS crystal (**Figure 5.2(b)**) not only shows a star-shaped morphology, but also reveals that the star-shaped PbS crystals are composed by single rod-like star morphology. This is completely different from previously reported results showing star-shaped PbS crystals with multi-rod or multi-armed

like morphologies.[17,18] As observed in SEM images of **Figure 5.2**, this could be due to the sonication treatment, which destroyed their morphology during the dispersion of the sample. In order to characterize the composition of the star- shaped PbS crystals, their EDS spectrum was obtained (**Figure 5.2(c)**). This spectrum reveals that the sample contains elements of Pb and S. The other peaks corresponding to C, Au and Pd are due to the stud and sample metallization before SEM examination.

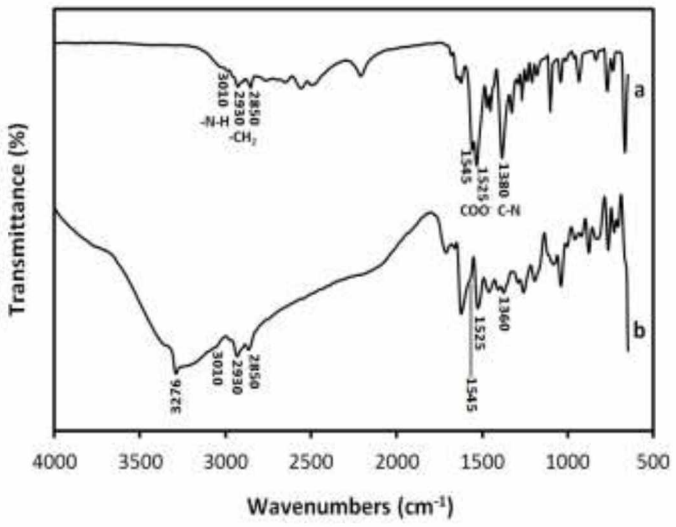

Figure 5.3 FTIR spectra of (a) ACA and (b) star-shaped PbS crystals.

FTIR spectra of pure ACA and star-shaped PbS crystals were characterized to investigate the interaction between them. The corresponding results are respectively shown by curves (a) and (b) of **Figure 5.3**. Curve (a) shows two bands at 2850 and 2930 cm^{-1} due to C-H stretching vibrations of methylene groups of the ACA carbon chain. The band at 3010 cm^{-1} is due to N-H stretching mode of ACA molecules and the two bands at 1525 and 1545 cm^{-1} are respectively attributed to the symmetric and asymmetric stretching vibrations of uncoordinated $-COO^-$ terminal groups of ACA. As shown on curve (b), these bands also exist in the FTIR spectrum of star-shaped PbS crystals at about same positions. The band at 1380 cm^{-1} on curve (a) is due to C-N stretching mode of ACA molecules. This band appears at 1360 cm^{-1} in the FTIR spectrum of star-shaped PbS crystals, showing a red shift of 20 cm^{-1}. Furthermore, curve (b) shows a new band at 3276 cm^{-1}, which is due to the asymmetric stretching of N-H. This indicates the binding of $-NH_2$ groups to the surface of PbS crystals

through nitrogen lone pair. The same bands at 1525 and 1545 cm^{-1} of $-COO^-$ shown on curves (a) also appear on curve (b), which proves that only $-NH_2$ groups of ACA molecules were bounded on the surface of PbS crystal and the free -COOH groups were oriented outward. From FTIR characterization, it can be concluded that only $-NH_2$ head groups of ACA molecules were bounded on the surface of the star-shaped PbS crystals via nitrogen lone pair, while carboxylic -COOH head groups were located at the other side of the ACA chain.

5.4 Conclusions

In summary, high yield star-shaped PbS crystals have been synthetized solvothermaly using an environmentally friendly biomolecule mixed with methanolic Pb-TU complex precursor at 170 °C for 20 h. A possible four <100> directions mechanism for the formation of the star-shaped PbS crystals was evocated. Powder XRD confirms the highly crystallinity of the cubic phase PbS crystals and SEM and EDS studies showed that these crystals are single-rod like star-shaped without any impurities. FTIR study of the star-shaped PbS crystals indicate that ACA molecules bound on PbS surface via nitrogen lone pair of the amino head groups.

5.5 References

1. X. Peng, L. Manna, W. Yang, J. Wickham, E. Scher, A. Kadavanich , A.P. Alivisatos, *Nature* 404 **(2000)** 59-61.
2. B.Q. Sun, H.J. Snaith, A.S. Dhoot, S. Westenhoff, N.C. Greenham, *Journal of Applied Physics* 97 **(2005)** 014914.
3. A.A.R Watt, D. Blake, J.H. Warner, E.H. Thomsen, E.L. Tavenner, H. Rubinsztein-Dunlop, H.P. Meredith, *Journal of Physics D: Applied Physics* 38 **(2005)** 2006-2012.
4. S.A McDonald, G. Konstantatos, S. Zhang, P.W. Cyr, E.J.D. Klem, L. Levina, E.H. Sargent, *Natural Materials* 4 **(2005)** 138-142.
5. P.T. Guerreiro, S. Ten, N.F. Borrelli, J. Butty, G.E. Jabbour, *Applied Physics Letters* 71 **(1997)** 1595-1597.
6. D. Berhanu, K. Govender, D. Smyth-Boyle, M. Archbold, D.P. Halliday, P. O'Brien P, *Chemical Communications* 45 **(2006)** 4709-4711.
7. E. Leontidis, M. Orphanou, T. Kyprianidou-Leodidou, F. Krumeich, C. Walter, *Nano Letters* 3 **(2003)** 569-572.

8. K. Singh, A.A. McLachlan, D. Gerrard Marangoni, *Colloids and Surfaces A: Physicochemical and Engineering Aspects* 345 **(2009)** 82-87.
9. Z. Zhao, K. Zhang, J. Zhang, K. Yang, C. He, F. Dong, B. Yang, *Colloids and Surfaces A: Physicochemical and Engineering Aspects* 355 **(2010)** 114-120.
10. N.B. Pendyala, K.S.R. Koteswara Rao, *Materials Chemistry and Physics* 113 **(2009)** 456-461.
11. G. Li, C. Li, H. Tang, K. Cao, J. Chen, *Materials Research Bulletin* 46 **(2011)** 1072-1079.
12. L. Shuzhen, X. Shenglin, B. Keyan, C. Jie, Q. Yitai, *Journal of Physical Chemistry C* 113 **(2009)** 13002-13007.
13. T. Thongtem, S. Kaowphong, S. Thongtem, *Ceramics International* 34 **(2008)** 1691-1695.
14. X. Shen, Z. Li, Y. Cui, Y. Pang, *International Journal of Electrochemical Science* 6 **(2011)** 3525-3535.
15. T.D. Nguyen, D. Mrabet, T.T.D. Vu, C.T. Dinh, T.O. Do, *CrystEngComm* 13 **(2011)** 1450-1460.
16. T. Chaudhuri, N. Saha, P. Saha, *Materials Letters* 59 **(2005)** 2191-2193.
17. Y. Ji, X. Ma, H. Zhang, J. Xu, D. Yang, *Journal of Physics: Condensed Matter* 15 **(2003)** 7611-7615.
18. G. Zhou, M. Lü, Z. Xiu, S. Wang, H. Zhang, Y. Zhou, S. Wang, *Journal Physical Chemistry B* 110 **(2006)** 6543-6548.

Chapte 6: Generalized chemical route to develop fatty acid capped highly dispersed semiconducting metal sulphide nanocrystals

Jayesh D. Patel[a,b], Frej Mighri[a,b,*] and Abdellah Ajji[a,c]

[a]Center for Applied Research on Polymers and Composites, CREPEC

[b]Chemical Engineering Department, University of Laval, Quebec, QC, G1K 7P4 Canada

[c]Chemical Engineering Department, Ecole Polytechnique, C.P. 6079, Succ. Centre- Ville

Montreal, QC, H3C 3A7 Canada

Published in ***Materials Research Bulletin*** 47 (2012) 2016-2021

Résumé

Ce travail traite de la synthèse de nanocristaux (NCs) semi-conducteurs à haute dispersion de sulfure de cadmium (CdS), de sulfure de zinc (ZnS) et de sulfure de plomb (PbS) par un procédé simple et généralisé en utilisant l'acide oléique (AO) comme surfactant. Pour synthétiser ces NCs, les complexes métal-oléate (M-O) ont été obtenus à partir de la réaction, à 140°C, entre les acétates de métal et l'AO dans une solution d'hexane. Par la suite, les complexes M-O ont été sulfurisés en utilisant le thioacétamide à la même température. La caractérisation par la microscopie électronique à transmission (TEM) et la diffractométrie de rayons X (XRD) montre que les produits synthétisés ont des tailles nanométriques avec une phase cubique à haute cristallinité. L'absorption optique des NCs du sulfure métallique recouvert d'acide oléique confirme que la quantification de leur taille induit un grand déplacement vers la région visible. Le spectre de photoluminescence (PL) des nanocristaux de CdS montre une large emission de bande de bord avec les émissions faibles et à forts piégeages, tandis que le spectre PL des NCs de ZnS révèle une large émission à cause des défauts sur la surface. Les analyses thermogravimétriques (TGA) et la spectroscopie infrarouge à transformée de Fourier (FTIR) indiquent que les acides gras monocouche étaient fortement liés à la surface du nanocristal an tant que carboxylate et les deux atomes d'oxygènes du carboxylate étaient coordonnées de façon symétrique à la surface des NCs. La forte liaison entre l'acide gras et la surface des NCs augmente la stabilité des colloïdes de NCs. En général, cette voie généralisée a un potentiel considérable dans le développement de sulfures métalliques à l'échelle nanométrique pour les dispositifs optoélectroniques.

Abstract

This work deals with the synthesis of highly dispersed semiconducting nanocrystals (NCs) of cadmium sulphide (CdS), zinc sulphide (ZnS) and lead sulphide (PbS) through a simple and generalized process using oleic acid (OA) as surfactant. To synthesize these NCs, metal-oleate (M-O) complexes were obtained from the reaction at 140 °C between metal acetates and OA in hexanes media. Subsequently, M-O complexes were sulphurized using thioacetamide at the same temperature. Transmission electron microscopy (TEM) and X-ray diffraction (XRD) characterizations show that the synthesized products are of nanoscale-size with highly crystalline cubic phase. The optical absorption of OA-capped metal sulphide NCs confirms that their size quantization induced a large shift towards visible region. Photoluminescence (PL) spectrum of CdS NCs shows a broad band-edge emission with shallow and deep-trap emissions, while PL spectrum of ZnS NCs reveals a broad emission due to defects states on the surface. The thermogravimetric analysis (TGA) and Fourier transform infrared (FTIR) spectroscopy indicate that fatty acid monolayers were bound strongly on the nanocrystal surface as a carboxylate and the two oxygen atoms of the carboxylate were coordinated symmetrically to the surface of the NCs. The strong binding between the fatty acid and the NCs surface enhances the stability of NCs colloids. In general, this generalized route has a great potential in developing nanoscale metal sulphides for optoelectronic devices.

6.1 Introduction

Colloidal sulphide NCs belonging to II-IV and IV-VI groups have attracted a surge of interest for their novel application in many possible technological fields, including biological labelling and bio-diagnostics, electroluminescent devices, photovoltaic devices, light-emitting diodes and lasers.[1-4] Since the properties of these NCs are dependent on their size and shape, it is necessary to tailor these two parameters with respect to their particular applications. As the size of the NCs decreases, the effect of their surface area becomes more significant because of the increase in the volume fraction of surface atoms with respect to the entire particle.[5]

The development of a stable colloidal suspension of semiconducting NCs is highly challenging due to their high surface energy. Therefore, it is essential to use surfactants or other capping materials during the chemical process to coat these NCs in order to prepare a well-dispersed and stable colloidal suspension in solvent media. Over the past few years, several groups have reported the synthesis of metal chalcogenides using various synthesis routes, including soft templates, such as liquid crystals and micelles,[6-8] solventless synthesis,[9] the thermolysis of metal-alkanethiolate precursors,[10.11] the thermolysis of metal-oleylamine complexes,[12] simple surfactant assisted solvothermal and hydrothermal routes,[13,14] green chemical approaches,[15] and thermolysis single-source precursors.[16] However, the above chemical routes are not applicable as a general route for the synthesis of metal sulphide NCs. Joo et al.[17] reported later a general route for the synthesis of metal sulphide NCs based on the thermolysis and sulfurization of metal-oleyamine complexes at around 220°C. Also, Choi et al.[18] investigated a simple generalized fabrication route for monodispersed metal sulphide NCs using the thermolysis and sulfurization of M-O complexes in alkanethiol at 300°C. More recently, Yu et al.[19] reported a general synthesis route based on the thermolysis of metal cysteinate at high temperature for the synthesis of metal sulphide NCs at large scale.

All of the synthesis routes mentioned above were based on the thermolysis of organometallic complexes at high temperature (200-300 °C). Bakshi et al.[20-22] have used low temperature synthetic routes to produce shape and size controlled PbS/Se and CuSe NCs using various capping materials, such as cationic twin-tail surfactants and bovine serum albumen. We report here the synthesis of semiconducting metal sulphide NCs through the sulfurization of

their M-O complexes. This generalized process is simple and cost effective because it produces metal sulphide NCs at low temperature (140 °C) using less expensive reagents, such as metal acetates, hexanes, thioacetamide and oleic acid. In this general route, OA was used as a fatty acid to obtain M-O complexes of cadmium, zinc and lead using their respective acetates, while thioacetamide was used to sulfurize the as obtained M-O complexes. The synthesized NCs via this generalized route were highly dispersed and stable at room temperature.

6.2 Experimental details

6.2.1 Materials

The following chemicals used in this study, cadmium acetate dihydrate ($Cd(CH_3COO)_2 \cdot 2H_2O$, ≥98.0%), zinc acetate dihydrate ($Zn(CH_3COO)_2 \cdot 2H_2O$, ≥98.0%), lead acetate trihydrate ($Pb(CH_3COO)_2 \cdot 3H_2O$, 99.0%), thioacetamide (CH_3CSNH_2, 99.0%), and oleic acid ($C_{18}H_{34}O_2$, 90%), were purchased from Sigma-Aldrich, Canada. Hexanes (C_6H_{14} (mixture of isomers), 99.9%) and ethanol (C_2H_6O, 98%) were purchased from Fisher chemicals, Canada. All chemicals were used as received without further purification.

6.2.2 Synthesis of CdS, PbS and ZnS NCs

In general, O-M complexes were prepared through thermal reaction between metal acetates and OA in hexanes medium (**Scheme 6.1**). A 0.05 M of metal acetate was mixed with 0.1 M of OA and 20 ml of hexanes. The mixture was then heated at 140°C with continuous stirring in an oil bath using water condenser. After 1 hour of heating and stirring, 75 mg (~0.05 M) of thioacetamide were added to the hot M-O complex solution. After 15 minutes of additional heating and stirring, the colour of the solution was changed due to the formation of metal sulphide NCs (for ZnS NCs, the solution remained transparent after sulfurization). The obtained solution was then cooled to room temperature and excess ethanol was added to precipitate the metal sulphide NCs. The NCs were centrifuged then washed many times with ethanol and hot water to remove the excess of OA and unreacted matters. The final NCs were dried in a vacuum oven at 50°C for 2h.

6.2.3 Materials characterization

TEM and selective area electron diffraction (SAED) characterizations were done using a

JEOL JEM 1230 electron microscope operated at 120 kV. Samples were prepared by placing a drop of diluted colloidal solution of NCs onto a 200 mesh carbon coated copper grid. The Solution was immediately evaporated at ambient temperature. The average size and size-distribution of the OA-capped CdS, ZnS and PbS NCs were also measured in solution at 25 °C and a detection angle of 90° using a Zetasizer Nano ZS90 dynamic light scattering (DLS) system equipped with a red laser (633 nm) and an Avalanche photodiode detector (quantum efficiency > 50% at 633 nm) (Malvern Instruments Ltd.). All DLS measurements were conducted with a fixed 10 runs (of 10 s each). XRD data were recorded on a Siemens D5000 X-ray diffractometer, using Cu-Kα radiation (λ = 1.54059 Å). Crystal size was estimated from the following Scherrer relation:

$$D = \frac{k\lambda}{B\cos\theta} \qquad \textbf{(6-1)}$$

where D is the particle size, k is the shape factor (taken as 0.9), λ is the wavelength of X-ray used, β is the broadening of line at half the intensity, and θ is the diffraction angle of the line under consideration. The absorption spectra of NCs were recorded on Varian Cary 500 Scan UV-Vis spectrophotometer. The energy band gaps (Eg) of the NCs were determined from the following Tauc relation:

$$(\alpha h\nu)^2 \sim h\nu - Eg \qquad \textbf{(6-2)}$$

where α (cm^{-1}) is the absorption coefficient, h (J.s) is the Plank constant, ν (Hz) is the frequency of radiation, and Eg (eV) is the energy band gap of the semiconductor. Photoluminescence (PL) spectra of CdS and ZnS NCs were measured at room temperature using Varian Cary Eclipse Fluorescence Spectrophotometer with spectral range of 190 – 1100 nm. TGA analysis of the samples was carried out from 50 to 650 °C using a TA, Q-5000 IR instrument with a heating rate of 10°C/min. Infrared spectra of OA and OA-capped NCs were obtained using a Nicolet (Thermo Fisher) Model 380 FTIR with an attenuated total reflectance (ATR) sampling device (model Smart Performer) with a ZnSe crystal. The infrared spectra were collected within the range of 650 to 4000 cm^{-1} with 10 scans per spectrum.

6.3 Results and discussion

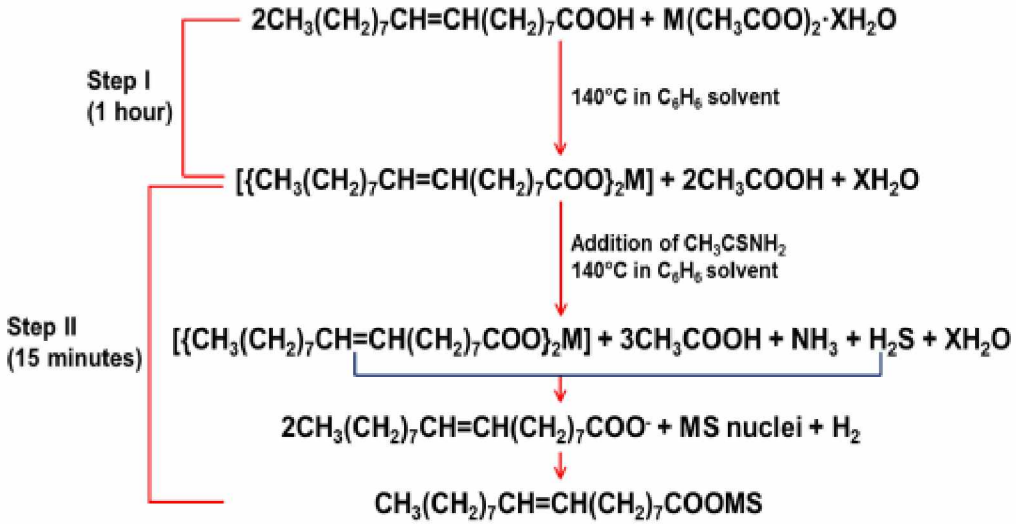

Scheme 6.1 The different steps of the possible reaction mechanism during the synthesis of OA-capped metal sulphide NCs. (i) For the two steps: M = Cd, Zn or Pb; (ii) 1st step: X = 2 for M = Cd or Zn and X = 3 for M = Pb; (iii) 2nd step: X = 0 for M = Cd or Zn and X = 1 for M = Pb.

As shown by the general reaction mechanism presented in **Scheme 6.1**, OA-capped metal sulphide NCs synthesis follows the following major two steps: during the first step, the hydrated metal acetate salt reacts with OA at 140 °C for 1 h in hexanes media to produce M-O complex with acetic acid and water molecules. During the second step, which takes around 15 min, thioacetamide is added directly into the reaction medium in which it is hydrolyzed in the presence of water molecules to produce acetic acid, ammonia and H_2S gas according to following reaction:[23]

$$CH_3CSNH_2 + 2H_2O \rightarrow CH_3COOH + NH_3 + H_2S \qquad \textbf{(6-3)}$$

The produced H_2S gas reacts at the same temperature of 140 °C with M-O complex to produce oleate ions, H_2 gas and highly active metal sulphide nuclei. The latter is immediately bounded with oleate ions to finally produce OA-capped metal sulphide NCs (see **Figure 6.1**).

Figure 6.1 Image of vials of OA-capped metal sulphide NCs.

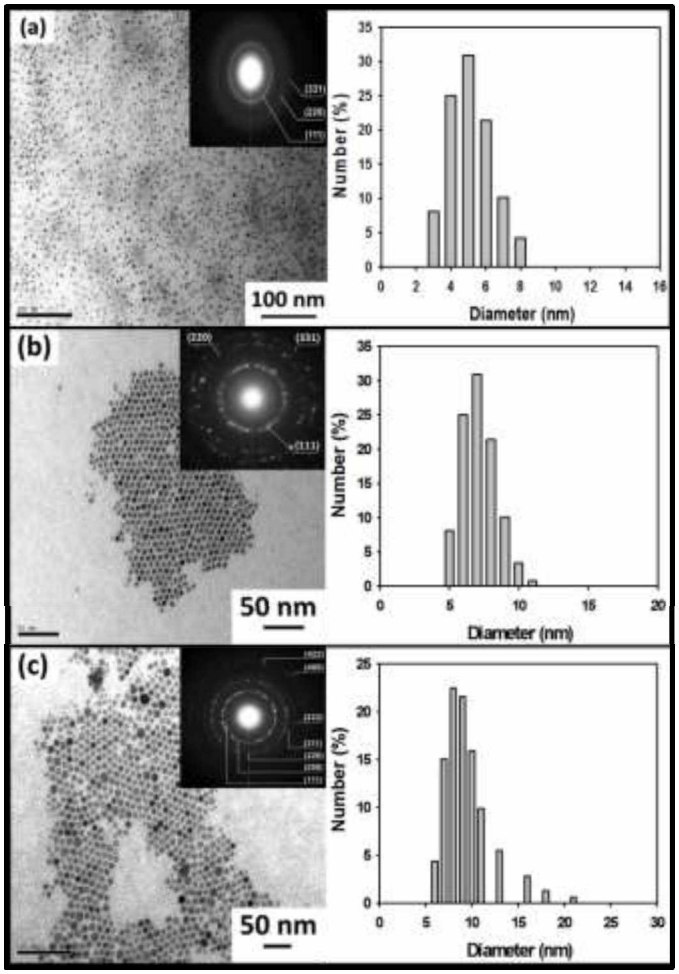

Figure 6.2 TEM images of OA-capped (a) CdS (b) ZnS and (c) PbS NCs along with SAED and size distribution histogram.

TEM micrographs and size distribution histograms of the synthesized CdS, ZnS and PbS NCs are respectively shown in **Figure 6.2(a)-(c)**, together with their respective SAED patterns (insets). These micrographs clearly show that spherical NCs were obtained via this generalized synthesis route with average diameters of about 4, 7 and 8 nm, respectively. The size distribution histograms of these NCs indicate that these CdS, ZnS and PbS NCs do not show a large size distribution and their respective average diameters are 5.5, 8.5 and 11.9, which are slightly higher than those estimated from TEM micrographs. The difference could be due to the fact that the histograms are obtained directly from solutions that contain higher number of NCs compared to diluted solutions (one drop) used for TEM characterization. These NCs are well defined in both size and shape compared to recently reported generalized synthesis process.[19] As shown, the SAED patterns of the three NCs consist of concentric rings, which indicate the cubic nature of CdS, ZnS and PbS NCs.

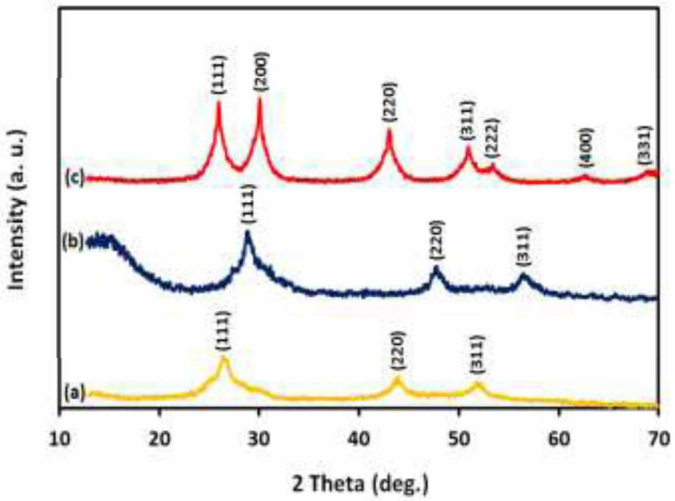

Figure 6.3 XRD patterns of OA-capped (a) CdS (b) ZnS and (c) PbS NCs.

The composition of the developed NCs was determined by XRD technique. XRD patterns of the three OA-capped CdS, ZnS and PbS NCs are shown in **Figure 6.3**. All of these patterns show well defined broad peaks, which confirm the high nanocrystalline nature of the three different NCs. Moreover, these patterns confirm that CdS NCs have a cubic structure (JCPDS Powder Diffraction File no. 5-0566), ZnS NCs have a zinc blende structure (JCPDS Powder Diffraction File no. 75-1546) and PbS NCs have a face-centered cubic structure (JCPDS

Powder Diffraction File no. 05-0592). The full width at half maximum (FWHM) of the (1 1 1) line of each metal sulphide was used to calculate the size of the developed NCs by using the Scherrer equation (**Eq. (6.1)**). As estimated by this equation, the sizes of OA-capped CdS, ZnS and PbS NCs were about 3.2, 6 and 7.3 nm, respectively. These sizes are in close agreement with those estimated from TEM micrographs.

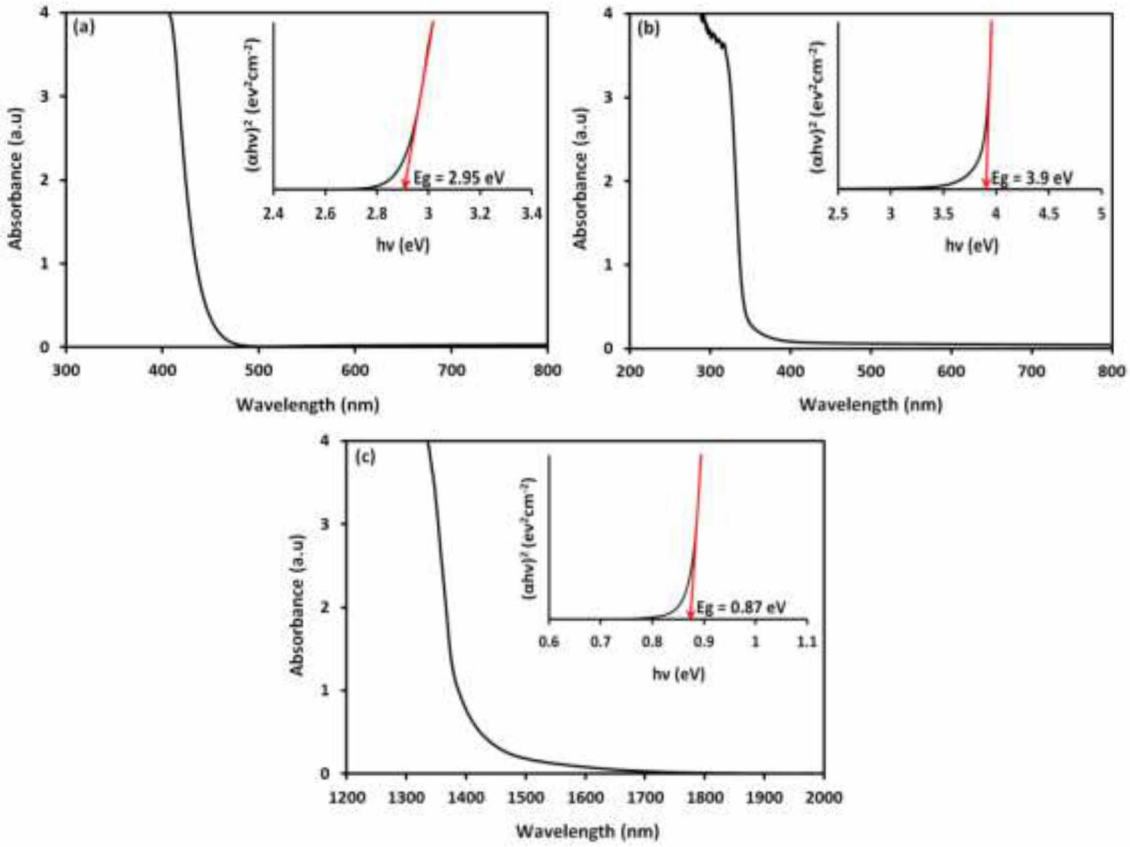

Figure 6.4 Absorption spectra of OA-capped (a) CdS (b) ZnS and (c) PbS NCs. Insets show their respective band gap plots.

In **Figure 6. 4**, we report the UV-vis absorption spectra of the three synthesized OA-capped CdS, ZnS and PbS NCs. All of these spectra clearly show a blue shift in the optical absorption edge compared to their respective bulk absorption edges. This indicates a strong quantum charges confinement in the three NCs. It should also be mentioned that the colloidal dispersion of these NCs remained highly stable with time since after few months, there was no noticeable precipitation. The fundamental absorption, which corresponds to the electron

excitation from valance to conduction bands, was used to determine the nature and the value of the optical band gap using the Tauc relation (**Eq. (6.2)**). As shown in the insets of **Figure 6.4**, the band gaps of OA-capped CdS, ZnS and PbS NCs were around 2.95, 3.9 and 0.87 eV, respectively.

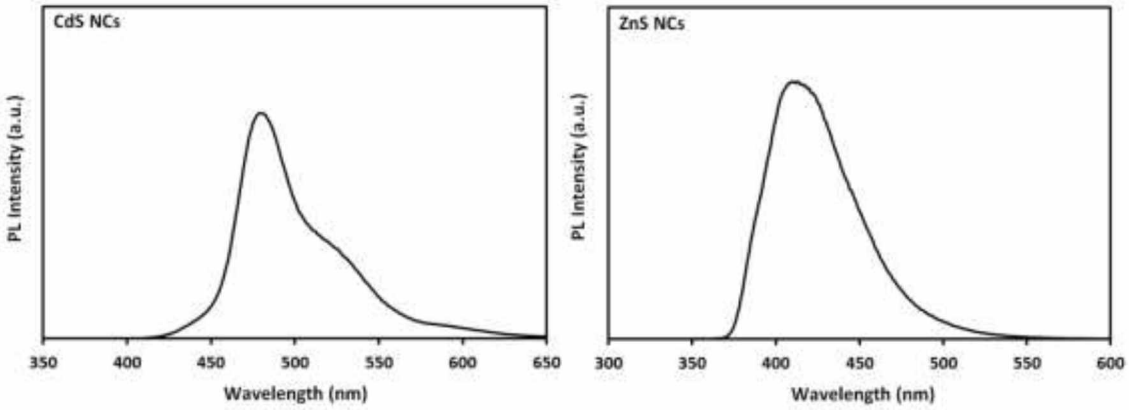

Figure 6.5 PL spectra of OA-capped CdS and ZnS NCs.

It is well known that, for the II-IV and IV-VI capped NCs, the optically excited charge carrier emits light by band-to-band and band-to-defect recombination processes.[24] The latter is mostly driven by the defects generated in the gap by surface states. In such case, the emission is almost 1.0 eV below the energy band gap of the most common NCs.[25] PL spectra of the synthesized CdS and ZnS NCs are presented in **Figure 6.5**. Unfortunately, it was not possible to measure the PL spectrum of PbS NCs since they absorb between 1300 and 1600 nm and the available spectrophotometer cannot go up to this wavelength range. The PL spectrum of CdS NCs shows a strong peak at around 482 nm, which is due to band-edge emission. It also shows a weak shoulder peak at around 534 nm assigned to a shallow-trap emission. The PL spectrum of ZnS NCs displays a broad emission between 370 and 525 nm with a peak at around 415 nm, which is red-shifted compared to the excitonic transition around 340 nm, as shown in **Figure 6.4(b)**. Sapra et al.[26] attributed this strong emission band to the carrier recombination of the defect states, which are mostly on the surface of the undoped ZnS NCs due to sulphur vacancies.

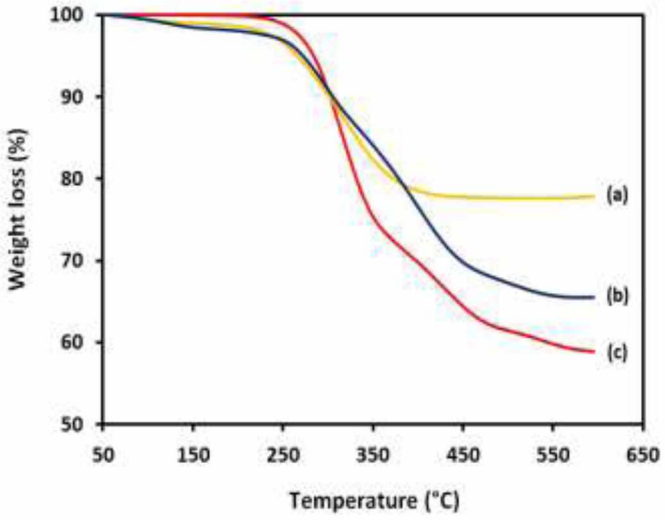

Figure 6.6 TGA plots of OA-capped (a) CdS (b) ZnS and (c) PbS NCs.

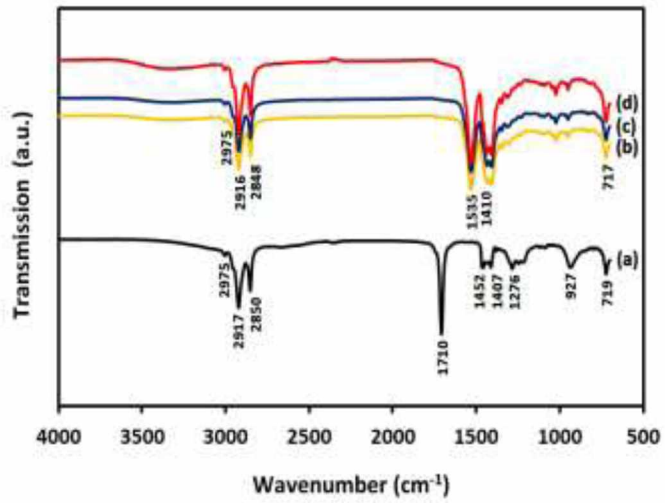

Figure 6.7 FTIR spectra of (a) OA with OA-capped (b) CdS (c) ZnS and (d) PbS NCs.

It is well known that the amount of the coating material at the surface of the NCs is a function of their size and the type of the cation present on their surface. TGA characterization in the presence of air of the three OA-capped CdS, ZnS and PbS NCs was done in order to determine the amount of OA capped skin on the surface of the NCs (**Figure 6.6**). For the three OA-capped NCs, the weight loss above 250 °C is due to the elimination of the OA skin from the surface of the NCs. The complete decomposition of the OA skin takes place between 425 and 450 °C. From TGA curves, the weight composition of OA capping shells of CdS,

ZnS and PbS NCs are respectively about 23 wt%, 32 wt% and 38 wt%. The sharp decrease in the weight loss is an indication of a strongly bounded OA monolayer coating on CdS, ZnS and PbS NCs surface.

FTIR characterization of pure OA and OA-capped CdS, ZnS and PbS NCs was done in order to investigate the interaction between the OA and the NCs. The corresponding FTIR spectra are shown in **Figure 6.7**. The FTIR spectrum of OA shows two vibration bands at 2917 and 2850 cm^{-1}, respectively attributed to the CH_2 asymmetric and symmetric stretching. The band at 2975 cm^{-1} is assigned to the stretching vibration of C-H. CH_2 rocking vibration is identified by the sharp band at 719 cm^{-1}. Similar peaks at around the same wavenumbers (2975, 2917, 2850, and 719 cm^{-1}) are also present in the FTIR spectra of OA-capped CdS, ZnS and PbS NCs. For the OA, the intense peak at 1710 cm^{-1} is due to the existence of the C=O stretching and the band at 1276 cm^{-1} is an indication of the presence of C-O stretching. Two bands at 1452 and 927 cm^{-1} are due to the in-plane and out-of-plane bandings of O-H. Compared to the FTIR spectrum of pure OA, FTIR spectra of OA-capped CdS, ZnS and PbS NCs do not show any peak at 1710 cm^{-1} (corresponding to C=O stretching). This indicates that no free OA is present in these three NCs. However, two new peaks appear at 1535 and 1410 cm^{-1} in all the three spectra, which are characteristic of $\nu_{asymmetric}$ (COO^-) and $\nu_{symmetric}$ (COO^-) stretching.[27] The existence of these two new peaks reveals that the OA is chemisorbed as carboxylate onto the surface of CdS, ZnS and PbS NCs.

It is clear from literature[28,29] that, when the carboxylic acid group is in contact with the metal surface, two different bonding types may exist: (i) two symmetric bidentate bonds through two equivalent oxygen atoms, or (ii) a monodentate bond with two inequivalent oxygen atoms. In monodentate bonding, the C=O bond is still present and the hydrogen of the acidic group is replaced by a metal atom. In our case, the FTIR characterization presented above shows that the peak at 1710 cm^{-1} of the OA spectrum disappeared in the spectra of the three OA-capped NCs. Therefore, it can be concluded that two oxygen atoms of the carboxylic moiety are attached symmetrically to the surface of the NCs. In addition, the interaction between the carboxylate head and the metal atoms is categorized in four different types: monodentate, bridging bidentate, chelating bidentate, and simple ionic interaction. [30,31] The wavenumber separation between nasym (COO^-) and nsym (COO^-) in the FTIR spectrum can

be used to detect the type of interaction between the carboxylate head and metal atoms. The largest wavenumber separation (320-200 cm^{-1}) corresponds to the monodentate interaction and the smallest one (less than 110 cm^{-1}) corresponds to the chelating bidentate. The wavenumber separation in medium range (120-200 cm^{-1}) is for the bridging bidentate. In our case, the wavenumber separation (1535-1410 = 125 cm^{-1}) is ascribed to the bridging bidentate, where the interaction between the COO moiety and NCs is covalent. The covalent bonding of COO moiety with metal atom surface leads to a high stability of the NCs at room temperature.

6.4 Conclusions

In summary, this study offers a simple and generalized synthesis route to develop various kinds of nanoscale metal sulphides with high dispersity. We have successfully synthesized OA-capped semiconducting metal sulphide NCs of CdS, ZnS and PbS through the thermolysis and sulphurization of their respective M–O complexes via the utilization of low cost reagents, such as metal acetates, OA and thioacetamide. The experimental results obtained in this study show that the OA was chemisorbed as a carboxylate onto the surface of CdS, ZnS and PbS NCs and two oxygen atoms in the carboxylate were coordinated symmetrically to the metal atoms. The strong interaction between the fatty acid and metal sulphide NCs enhances the stability and the dispersion of these metal sulphide NCs in non-polar solvents.

Acknowledgement

The authors would like to thank the Natural Sciences and Engineering Research Council of Canada (NSERC) for financial support of this work.

6.5 References

1. P.O. Anikeeva, J.E. Halpert, M.G. Bawendi, V. Bulović, *Nano Letters* 9 **(2009)** 2532 2536.
2. W.U. Huynh, J.J. Dittmer, A.P. Alivisatos, *Science* 295 **(2002)** 2425-2527.
3. M. Bruchez Jr, M. Moronne, P. Gin, S. Weiss, A.P. Alivisatos, *Science* 281 **(1998)** 2013-2016.

4. W.C.W. Chan, S.M. Nie, *Science* 281 **(1998)** 2016-2018.
5. N. Wu, L. Fu, M. Su, M. Aslam, K.C. Wong, V.P. Dravid, *Nano Latters* 4 **(2004)** 383-386.
6. C. Tura, N. Coombs, O. Dag, *Chemistry of Materials* 17 **(2005)** 573-579.
7. Y. Zhang, Y. Chen, H. Niu, M. Gao, *Small* 2 **(2006)** 1314-1319.
8. W. Xu, D.L. Akins, *Materials Letters* 58 **(2004)** 2623-2626.
9. L. Chen, Y.B. Chen, L.M. Wu, *Journal of American Chemical Society* 126 **(2004)** 16334-16335.
10. M.A. Hines, G.D. Scholes, *Advanced Materials* 15 **(2003)** 1844-1848.
11. T. Kuzuya, S. Yamamuro, T. Hihara, K. Sumiyama, *Chemistry Letters* 33 **(2004)** 352-353.
12. J.H. Yu, J. Joo, H.M. Park, S.-I. Baik, Y.W. Kim, S.C. Kim, T. Hyeon, *Journal of American Chemical Society* 127 **(2005)** 5662-5670.
13. G. Li, C. Li, H. Tang, K. Cao, J. Chen, *Materials Research Bullatin* 46 **(2011)** 1072-1079.
14. G.Q. Xu, B. Liu, S.J. Xu, C.H. Chew, S.J. Chua, L.M. Gana, *Journal of Physics and Chemistry of Solids* 61 **(2000)** 829-836.
15. Z.A. Peng, X.G. Peng, *Journal of American Chemical Society* 123 **(2001)** 183-184.
16. J. Aldana, N. Lavelle, Y. Wang, X. Peng, *Journal of American Chemical Society* 127 **(2005)** 2496-2504.
17. J. Joo, H.B. Na, T. Yu, J.H. Yu, Y.W. Kim, F. Wu, J.Z. Zhang, T. Hyeon, *Journal of American Chemical Society* 125 **(2003)** 11100-11105.
18. S.-H. Choi, K. An, E.-G. Kim, J.H. Yu, J.H. Kim, T. Hyeon, *Advanced Functional Materials* 19 **(2009)** 1645-1649.
19. L. Yu, Y. Lv, G. Chen, X. Zhang, Y. Zeng, H. Huang, Y. Feng, *Inorganica Chimica Acta* 376 **(2011)** 659-663.
20. M.V. Bakshi, P. Thakur, S. Sachar, G. Kaur, T.S. Banipal, F. Possmayer, N.O. Petersen, *Journal of Physical Chemistry C* 111 **(2007)**18087-18098.
21. M.V. Bakshi, P. Thakur, G. Kaur, H. Kaur, T.S. Banipal, F. Possmayer, N.O. Petersen, *Advanced Functional Materials* 19 **(2009)** 1451-1458.

22. M.V. Bakshi, P. Thakur, P. Khullar, G. Kaur, T.S. Banipal, *Crystal Growth & Design* 10 **(2010)** 1813-1822.
23. D. Rosenthal, T.I. Tyalor, *Journal of American Chemical Society* 79 **(1957)** 2684-2690.
24. M.N. Kalasand, M.K. Rabinal, B.G. Mulimani, *Journal of Physics D: Applied Physics* 43 **(2010)** 305301 (1-7).
25. H. Li, W.Y. Shih, W.-H. Shih, *Industrial and Engineering Chemistry Research* 46 **(2007)** 2013-2019.
26. S. Sapra, A. Prakash, A. Ghangrekar, N. Periasamy, D.D. Sarma, *Journal of Physical Chemistry B* 109 **(2005)** 1663-1668.
27. M.V. Limaye, S.B Singh, S.K. Date, D. Kothari, V.R. Reddy, A. Gupta, V. Sathe, R.J. Choudhary, S.K. Kulkarni, *Journal of Physical Chemistry B* 113 **(2009)** 9070-9076.
28. L.H. Dubois, B.R. Zegarski, R.G. Nuzzo, *Langmuir* 2 **(1986)** 412-417.
29. M. Wuhn, J. Weckesser, C. woll, *Langmuir* 17 **(2001)** 7605-1712.
30. K. Nakamoto, *Infrared and Raman spectra of inorganic and coordination compounds*, John Wiley & Sons: New York, **(1997)** page 59.
31. Y. Ren, K. Limura, T. Kato, *Langmuir* 17 **(2001)** 2688-2693.

Chapter 7: Facile synthesis of CdSe nanocrystals for bulk-heterojunction solar cells

Jayesh D. Patel[a], Frej Mighri[a,*], Abdellah Ajji[b], and Tapas K. Chaudhuri[c]

[a]CREPEC, Department of Chemical Engineering, Laval University, Quebec, QC, G1V 0A6 Canada

[b]CREPEC, Chemical Engineering Department, Ecole Polytechnique, Montreal, QC, H3C 3A7 Canada

[c]Dr. K.C. Patel Research and Development Centre, Charotar University of Science and Technology (CHARUSAT), Changa, Tal.-Petlad, Anand District, Gujarat 388421, India

Submitted to ***Synthetic Metals*** (2014)

Résumé

Les nanocristaux (NCs) de séléniure de cadmium (CdSe) recouvert d'acide oléique ont été synthétisés par une nouvelle voie à grande échelle. La diffraction des rayons X et la microscopie électronique à transmission ont confirmé que des nanocristaux de CdSe hexagonaux en forme de tiges (wurtzite) ayant une taille moyenne de 10 nm ont été obtenus avec cette nouvelle voie. Les nanocristaux CdSe obtenus ont été traités individuellement avec la pyridine et le tert-butylamine (t-BA) afin d'avoir un échange de ligands. L'analyse par spectroscopie infrarouge à transformée de Fourier de ces nanocristaux a confirmé l'élimination des ligands AO de la surface suite au traitement par la pyridine et le t-BA. Les dispositifs de cellules solaires à hétérojonction volumique (BHJ) ont été préparés en utilisant des nanocristaux de CdSe ayant subi un traitement de surface et d'autres non traités, mélangés avec le polymère poly(3-hexylthiophène-2,5-diyl) (P3HT). Les dispositifs de cellules solaires BHJ fabriqués à partir du mélange de P3HT avec des nanocristaux CdSe à surface traitée ont donné des performances photovoltaïques meilleures que celles du mélange de P3HT avecdes nanocristaux CdSe non traités. L'amélioration des performances photovoltaïques a été obtenue grâce à l'augmentation de la mobilité des électrons dans le mélange de P3HT avec des nanocristaux CdSe suite au traitement de surface des nanocristaux.

Abstract

Oleic acid (OA)-capped cadmium selenide (CdSe) nanocrystals (NCs) have been synthesized via a new high-scale route. X-ray diffraction and transmission electron microscopy confirmed that rod-like hexagonal (wurtzite) CdSe NCs with an average size of 10 nm were obtained via this new route. The obtained CdSe NCs were treated individually with pyridine and tert-butylamine (t-BA) for ligand exchange. Fourier transform infrared spectra of the as-synthesized and treated CdSe NCs confirmed the removal of OA ligands from the surface of CdSe NCs after treatments with pyridine and t-BA. Bulk-heterojunction (BHJ) solar cell devices were prepared using untreated and surface treated CdSe NCs blended with poly(3-hexylthiophene-2,5-diyl) (P3HT) polymer. BHJ solar cell devices made from P3HT:(surface treated CdSe NCs) blends showed greater improvement in photovoltaic performances compared to P3HT:(untreated CdSe NCs) blend. The improvement in photovoltaic performances was due to the increase of electron mobility in P3HT:(CdSe NCs) blends after surface treatment of CdSe NCs.

7.1 Introduction

Colloidal semiconductor nanocrystals (NCs) have attracted much attention in recent years for their wide use in many fields such as solar cells,[1] light-emitting diodes,[2] biological imaging,[3] lasers,[4] thin film transistors,[5] and other nanoscale devices.[6] In the past few years, a great part of research has been done on controlling the size and shape of II-IV group semiconductor NCs (such as TiO_2, ZnO and CdSe) for their potential applications as acceptors and electron transporters in low-cost/high-performance bulk heterojunction (BHJ) solar cells. Such cells use the high electron mobility of the inorganic NCs to overcome charge-transport limitations associated with polymer materials as donor phases with high absorption coefficients. Therefore, BHJ solar cell devices can combine the advantages of both types of materials: (i) the simplicity of solution processing of polymers, and (ii) the high charge carrier mobility of inorganic semiconductor NCs.[7]

CdSe NCs were the first candidates used in BHJ solar cells and still have the highest power conversion efficiency (PCE) compared to other types of NCs. Improvement in the performance of BHJ solar cells based on CdSe NCs were achieved through size/shape and surface alterations of the NCs,[8-12] post-deposition ligand exchange,[13] introducing low band gap conjugated polymers,[14-15] the functionalization of conjugated polymers,[16] and the improvement of device structures.[15] Among these solutions, surface modification is considered as the best way to enhance the performance of BHJ solar cells.[17,18]

The synthesis of NCs and nanorods can be carried out via the pyrolysis of organometallic reagents by their injection at high temperatures into a coordinating organic ligand solution with a high boiling point, such as OA and n-octadecyl phosphonic acid, trioctylphosphine (TOP), trioctylphosphine oxide (TOPO), and hexadecylamine (HDA).[19] The cost of large-scale synthesis of CdSe NCs or nanorods via these routes is very high due to the expensive chemicals, such as TOP or TOPO. Furthermore, TOP and TOPO are hazardous and not environmentally friendly solvents. Therefore, developing a less hazardous and simple method for synthesizing CdSe NCs for BHJ solar cell applications remains a challenge for materials scientists.

The presence of organic ligands on the surface of NCs improves their dispersion in various solvents and polymers. However, the presence of organic ligand coating on NCs surface results in poor charge transfer between them and the polymeric matrix. Therefore, it is necessary to remove parent organic ligands as much as possible from the NC surface in order to reduce the distance between NC-NC and NC-polymer, avoid recombination losses, and enhance the charge transport through the photoactive layer. A post-synthetic ligand exchange with pyridine is the most effective procedure to improve the efficiencies of BHJ solar cells based on CdSe NCs.[17] In this procedure, long alkyl chain capped CdSe NCs are washed by methanol several times and then overnight treated in boiling pyridine under inert atmosphere. After treatment, the insulating ligand are replaced by shorter and more conducting pyridine molecules. The treated CdSe NCs are then precipitated with hexene, recollected by centrifugation and then dispersed into a mixture of chloroform/pyridine (90:10, v/v) solvent. Similar types of treatments with other materials (such as amine, chloride, thiols and acetic acid) were also reported for CdSe NCs.[11, 20-22] Alternatively, other washing methods can also be applied to remove excess ligands from the NCs surface.[12, 23] Zhou et al.[12] reported a typical synthesis of spherical CdSe quantum dots using HDA as ligand, which was subsequently washed with hexanoic acid, resulting in salt formation and the reduction of the amount of HDA ligand on the surface of CdSe NCs. By applying this technique to (TOP/OA)-capped quantum dots (QDs) and HDA-capped QDs, they achieved high BHJ solar cell PCEs, respectively 2.7 and 3.1%.[23, 24]

Herein, we report on a new route to prepare high-scale rod-like CdSe NCs through the injection of selenium (Se) powder in cadmium-oleate (Cd-O) complex previously prepared in 1,2,4 trichlorobenzene. The obtained CdSe NCs were treated with pyridine and t-BA for ligand exchange. BHJ solar cell devices were then prepared using the as-synthesized CdSe NCs (both untreated and surface-treated) and poly(3-hexylthiophene-2,5-diyl) (P3HT) as the polymeric matrix. These devices were then characterized and compared in terms of their power conversion efficiency.

7.2 Experimental

7.2.1 Chemicals

Indium tin oxide (ITO) coated glass plates (sheet resistance of 10Ω/sq) were purchased from Delta Technologies, USA. Cadmium acetate dihydrate ($Cd(CH_3COO)_2 \cdot 2H_2O$, ≥98.0%), OA ($C_{18}H_{34}O_2$, 90%), selenium powder (Se, ≥99.9%), 1,2,4 trichlorobenzene ($C_6H_3Cl_3$, ≥99%), pyridine (C_5H_5N, anhydrous 99.8%), (tert-butylamine ($(CH_3)_3CNH_2$, 98%), poly(3,4-ethylenedioxythiophene):poly(styrenesulfonate)) (PEDOT:PSS), regioregular (P3HT), and chlorobenzene (C_6H_5Cl, ≥99%) were purchased from Sigma-Aldrich, Canada. Ethanol (C_2H_6O, 98%), methanol (CH_4O, 98%), hexanes (C_6H_{14} (mixture of isomers), 99.9%), acetone (C_3H_6O, 98%) and isopropanol (C_3H_8O, 98%) were purchased from Fisher chemicals, Canada. All reagents were used as received without any further purification.

7.2.2 Synthesis of CdSe NCs

First, Cd-O complex was prepared through thermal reaction between cadmium acetate dihydrate and OA in 1,2,4 trichlorobenzene. A 0.025 M (1.33 gm) of cadmium acetate dihydrate was mixed with 0.1 M of OA and 200 mL of 1,2,4 trichlorobenzene. The mixture was then treated at 180 °C with continuous stirring in an oil bath using a water condenser. After 3 h of heating and stirring, 0.025 M (390 mg) of Se powder was injected to the hot Cd-O complex solution and then the mixture was treated again at 210 °C. After 5 h of additional heating and stirring, the colour of the solution was changed in dark brown due to the formation of CdSe NCs. The obtained solution was then cooled to room temperature and excess ethanol was added to precipitate the CdSe NCs. The NCs were centrifuged then washed many times with methanol and hot water to remove the excess of oleic acid and unreacted matters. The final NCs with yield higher than 80% were dried in a vacuum oven at 50 °C for 2h.

7.2.3 Ligand exchange procedures

For ligand exchange, the as-synthesized CdSe NCs redissolved in excess pyridine were heated under permanent stirring in an oil bath for 24 h at 105°C. Afterward, excess hexanes were added to precipitate CdSe NCs and then isolated by centrifugation. Similarly, the as-synthesized CdSe NCs were redissolved in excess t-BA and stirred at room temperature for

24 h. Afterward, the CdSe QDs were precipitated with excess of acetone and then isolated by centrifugation.

7.2.4 Characterizations

X-ray diffraction (XRD) data of the as-synthesized CdSe NCs was recorded on a Siemens D5000 X-ray diffractometer, using Cu-Kα radiation (λ = 1.54059 Å). Transmission electron microscopy (TEM) and selective area electron diffraction (SAED) of the as-synthesized CdSe NCs were performed on a JEOL JEM-2100F electron microscope operated at 200 kV. Fourier transform infrared spectra (FTIR) of as-synthesized and treated CdSe NCs were obtained using a Nicolet (Thermo Fisher) Model 380 FTIR with an attenuated total reflectance (ATR) sampling device (model Smart Performer) with a ZnSe crystal. The FTIR were collected within the range of 650 to 4000 cm^{-1} with 10 scans per spectrum. The absorption spectra of CdSe NCs and P3HT:CdSe NCs blend films were recorded on Varian Cary 500 Scan UV-Vis spectrophotometer.

7.2.5 Fabrication of BHJ solar cell devices

The P3HT:as-synthesized CdSe NCs and P3HT:t-BA treated CdSe NCs blended solutions were prepared by dispersing CdSe NCs (60 mg) and dissolving P3HT (15 mg) in chlorobenzene (3 mL). P3HT:pyridine treated CdSe NCs blended solution was prepared by dispersing CdSe NCs (60 mg) and dissolving P3HT (15 mg) in a mixture solvent of chlorobenzene and pyridine (*v:v* = 9:1, 3mL). All three P3HT:CdSe NCs blended solutions were stirred overnight. P3HT:CdSe NCs BHJ solar cell devices were fabricated on ITO coated glass substrates (24 × 24 mm^2). Prior to this, etched ITO substrates were ultrasonically cleaned in (i) detergent, (ii) deionized water, (iii) acetone, and (iiii) isopropanol consecutively for every 15 min. The layer of PEDOT:PSS was spin-coated onto the cleaned ITO glass substrates at 3000 rpm for 60 s and subsequently annealed at 140°C for 5 min, resulting in a layer thickness of about 40 nm. Then the PEDOT:PSS coated ITO glass substrates were transferred to a glove box and P3HT:CdSe NCs blends were spin-coated onto the PEDOT:PSS layer at 2000 rpm for 2 min under nitrogen atmosphere. An Aluminum layer of 70 nm was deposited by thermal evaporation. The average thickness of P3HT:CdSe NCs layers, determined by a profilometer (Dektak IIa Solan), was between 90 and 100 nm. The

current density-voltage (*J-V*) characteristics of the BHJ solar cell devices were measured with a computerized Keithley 2400 source meter under AM1.5G illumination at 100 mW/cm^2 supplied by a solar simulator (Oriel, 1000 W). The active area of the each cell was 0.24 cm^2.

7.3 Result and discussion

A typical XRD pattern of the as-synthesized CdSe NCs is shown in **Figure 7.1**. All the reflection peaks can be indexed to hexagonal wurtzite CdSe (JCPDS: 08-0459). This is due to the fact that the thermodynamically-stable hexagonal (wurtzite) phase is achieved at higher temperature, at which thermodynamics govern the crystal growth (rather than the reaction kinetics).[25] No characteristic peaks of other phase or impurities are observed in this pattern. The XRD pattern of the as-synthesized CdSe NCs shows broad peaks corresponding to (100), (002), (101), (102), (110), (103), and (200) planes at 2θ values of 23.9°, 25.3°, 27.1°, 35.1°, 42°, 45.8°, and 49.6°, respectively. This broadening is mainly attributed to the small size of CdSe NCs. In addition, the strong broad peak at 2θ = 25.3° indicates that the growth direction is along the c-axis of the hexagonal lattice.[26]

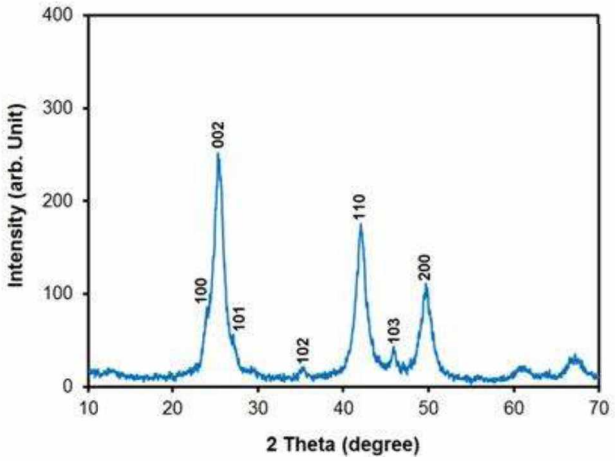

Figure 7.1 XRD pattern of the as-synthesized CdSe NCs.

Figure 7.2 shows high resolution TEM images (a, b) together with SAED pattern (c) of the as-synthesized CdSe NCs. The sample for TEM study was prepared by placing a drop of a diluted colloidal solution of CdSe NCs onto a carbon coated copper grid. **Figure 7.2b** clearly shows that road-like CdSe NCs were obtained with an average size of about 10 nm, and the SAED pattern (**Figure 7.2c**) shows well-defined rings of hexagonal wurtzite structure.

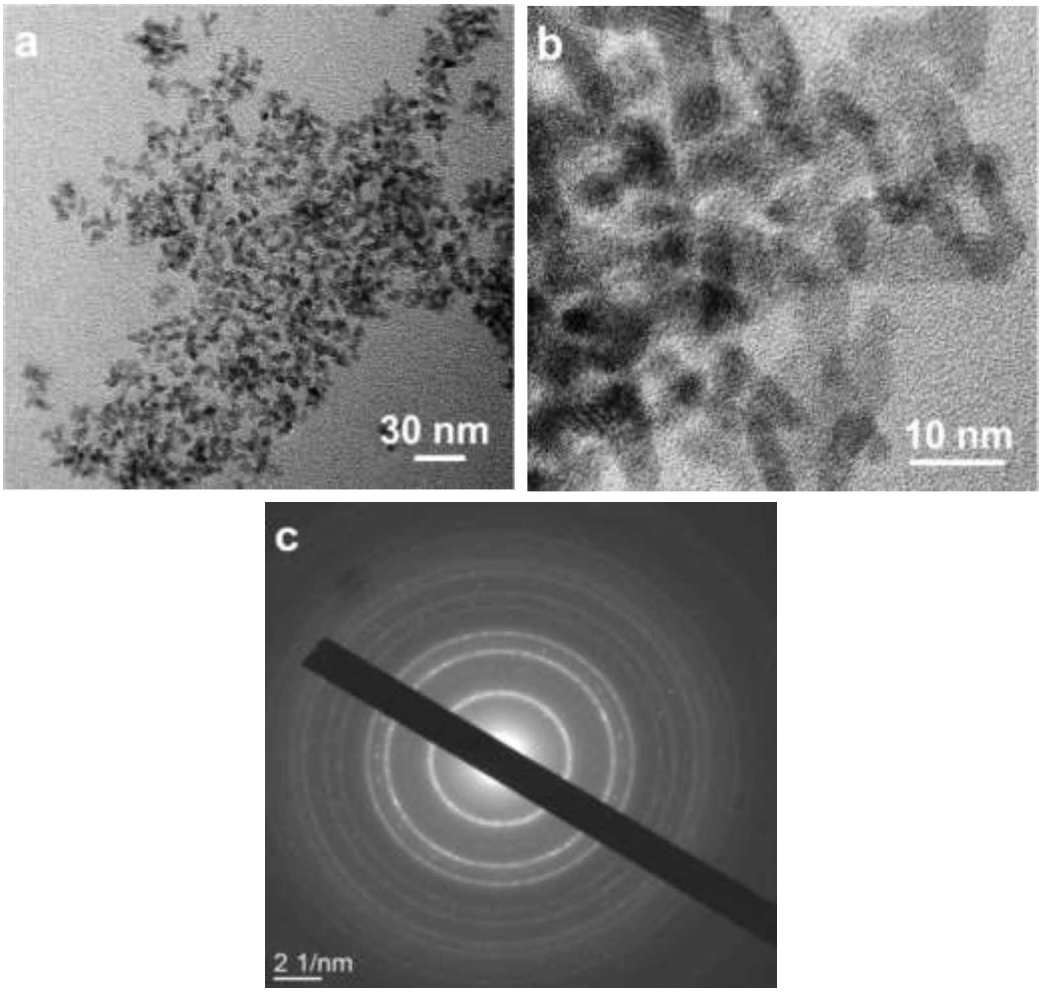

Figure 7.2 TEM images (a, b) and SAED pattern (c) of the as-synthesized CdSe NCs.

The improvement of the electron transfer is related to the surface properties of the CdSe NCs, which were studied by FTIR. **Figure 7.3** shows the FTIR spectra of pure OA, CdSe NCs, and pyridine and t-BA treated CdSe NCs. The FTIR spectrum of OA shows two vibration bands at 2917 and 2850 cm^{-1}, respectively attributed to the CH_2 asymmetric and symmetric stretching. The band at 2975 cm^{-1} is assigned to the stretching vibration of C-H. The intense peak at 1706 cm^{-1} is due to the existence of the C=O stretching and the band at 1240 cm^{-1} is an indication of the presence of C-O stretching. The two bands at 1462 and 936 cm^{-1} are due to the in-plane and out-of-plane bandings of O-H. Compared to pure OA, the FTIR spectrum of untreated CdSe NCs shows a small peak at 1706 cm^{-1}. This indicates that a small amount

of free OA is present in the sample. However, two new peaks appear at 1526 and 1410 cm^{-1}, which are characteristic of ν_{asym} COO^- and ν_{sym} COO^- stretching. The existence of these two new peaks reveals that the OA is chemisorbed as carboxylate onto the surface of CdSe NCs.[27] After pyridine and t-BA treatment, the intensities of the stretching vibrations of C-H (at 2917 and 2850 cm^{-1}) and those of $\nu_{asym\ \&\ sym}$ COO^- (at 1526 and 1410 cm^{-1}) is an indication of the removal of OA surfactant from the surface of the untreated CdSe NCs.[18]

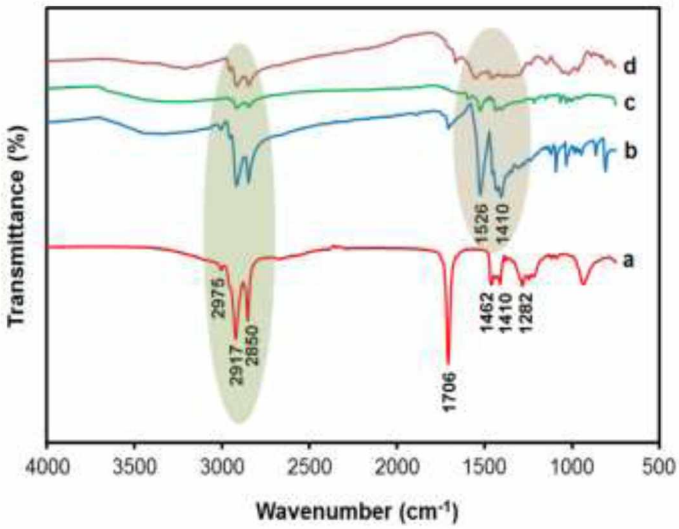

Figure 7.3 FTIR spectra of the OA (a), as-synthesized CdSe NCs (b), pyridine treated CdSe NCs (c) and t-BA treated CdSe NCs (d).

Figure 7.4 shows the UV-vis absorption spectra, as a function of wave length, for the untreated and surface treated CdSe NCs. The absorption spectrum clearly shows a blue shift compared to its bulk absorption edge due to quantum confinement.[28] The broad features centered in the absorption spectrum at around 450, 480 and 650 nm are probably due to the size distribution of the CdSe NCs. The figure also shows that the absorption of both pyridine and t-BA treated CdSe NCs are approximately identical over the whole wave length range but slightly lower compared to untreated CdSe NCs. This is an indication that that no oxidation, etching or aggregation of the CdSe NCs occurred after surface treatment, as already mentioned in literature.[29]

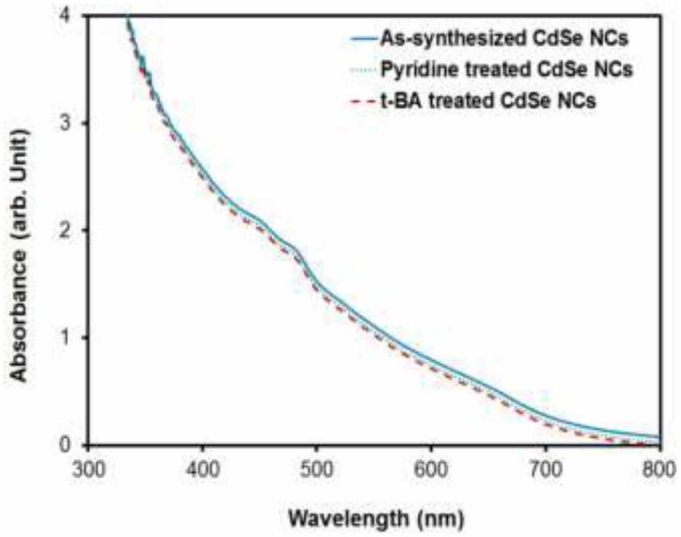

Figure 7.4 UV-vis spectra of the as-synthesized and treated CdSe NCs.

A sketch of the BHJ solar cell device and the corresponding prototype picture and energy diagram are shown in **Figure 7.5**. Based on the values of CdSe in bulk and the relative shift of the valence and conduction band edges in the NCs (due to the quantum confinement), the estimated values of electron affinity and ionization potential of the CdSe NCs are -4.4 and -6.3 eV, respectively.[9] Therefore, P3HT and CdSe NCs form a donor-acceptor heterojunction that enables the dissociation of photogenerated excitons in the blend films.[13]

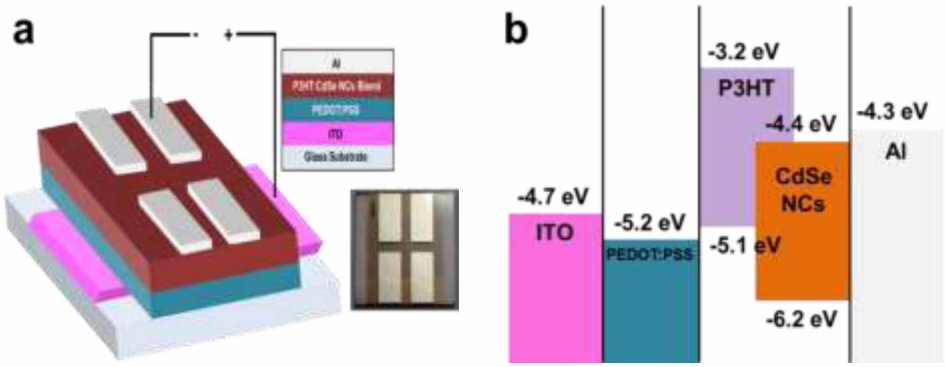

Figure 7.5 Schematic with prototype picture (a) and energy level diagram of the P3HT:CdSe BHJ solar cells (b).

Figure 7.6 shows J-V curves under dark (closed circles) and under illumination (open circles) for three BHJ solar cell devices prepared with untreated and treated CdSe NCs. The corresponding photovoltaic parameters (open-circuit voltage (V_{oc}), short-circuit current density (J_{sc}), fill factor (FF) and the PCE) are summarized in **Table 7.1**. For the two BHJ devices prepared with treated CdSe NCs, a highly improved photovoltaic performance was observed compared to the device prepared with untreated CdSe NCs, which presented very poor photovoltaic parameters, particularly a very low PCE (0.0013%). The best performance improvement was obtained with t-BA treated CdSe NCs, especially in terms of cell short-circuit current density and power current efficiency that jumped from 0.016 to 2.16 mA/cm^2 and from 0.0013 to 0.24% respectively. This could be explained by the fact that the long chain OA ligands are strongly bounded on the surface of CdSe NCs and t-BA is strong enough to replace a maximum number of these OA ligands (better than pyridine), which leads to the best photovoltaic performances.

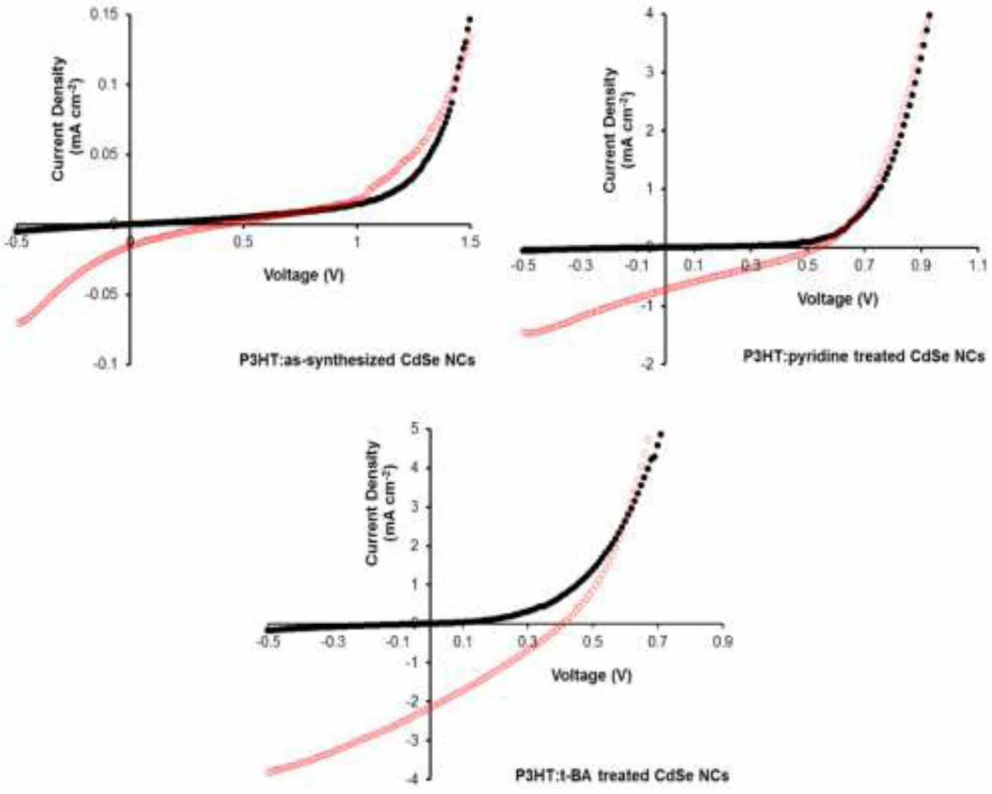

Figure 7.6 *J-V* characteristics of BHJ solar cells prepared from P3HT:CdSe NCs blends under dark (black circles) and illumination (red circles).

Table 7.1 Summary of the photovoltaic parameters of P3HT:CdSe NCs BHJ solar cells.

Device	V_{oc} (V)	J_{sc} (mA cm^{-2})	*FF*	*PCE* (%)
P3HT:OA-capped CdSe NCs	0.42	0.016	0.20	0.0013
P3HT:pyridine treated CdSe NCs	0.54	0.72	0.27	0.1
P3HT:t-BA treated CdSe NCs	0.41	2.16	0.28	0.24

Figure 7.7 compares the absorption for BHJ solar cell devices prepared with untreated and treated CdSe NCs. It is clearly shown that surface treatment of CdSe NCs didn't have any noticeable change in the absorption spectra of the P3HT:(CdSe NCs) blend films over the whole wavelength range. Therefore, the improved photovoltaic performances are not likely to be caused by the absorption of the blended films, as already observed by Fu et al.[18]

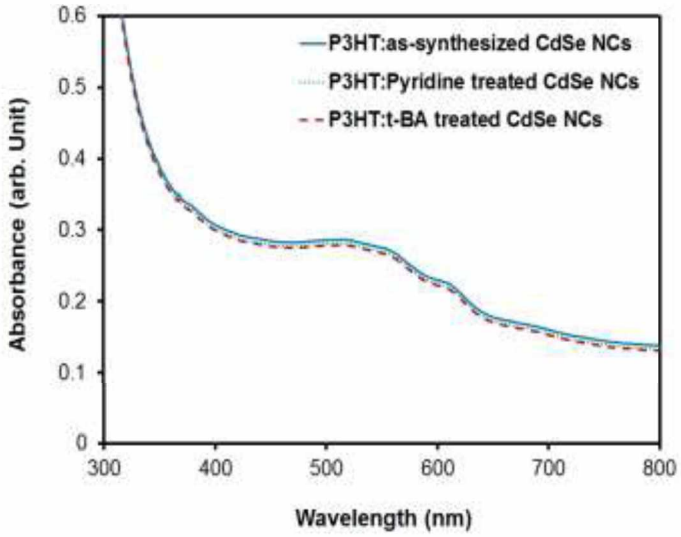

Figure 7.7 Abosrption sepctra of the P3HT:CdSe NCs blend films.

7.4 Conclusions

In conclusion, we reported in this work the detailed synthesis of OA-capped CdSe NCs via a new high scale route. It was shown that surface treatments of the as-synthesized nanocrystals with pyridine and t-BA are very effective to replace long chain OA ligands. BHJ solar cell

devices made from blends of P3HT polymer and surface treated CdSe nanocrystals showed greater improvement in photovoltaic performances compared to blends made from P3HT and untreated CdSe nanocrystals. The improvement in photovoltaic performances is due to the increase of electron mobility in the P3HT:CdSe NCs blends after the surface treatment of CdSe nanocrystals.

Acknowledgment

The authors would like to thank the Natural Sciences and Engineering Research Council of Canada (NSERC) for financial support of this work. They also appreciate the help of Dr. Hamed Najari (Department of Chemistry, Laval University) in the fabrication and characterization of solar cell devices.

7.5 References

1. W.U. Huynh, X.G. Peng, A.P. Alivisatos, *Advanced Materials* 11 **(1999)** 923-927.
2. V.L. Colvin, M.C. Schlamp, A.P. Alivisatos, *Nature* 360 **(1994)** 354-357.
3. W.C.W Chan, S.M. Nie, *Science* 281 **(1998)** 2016-2018.
4. V.I. Klimov, A.A. Mikhailovsky, S. Xu, A. Malko, J.A. Hollingsworth, C.A Leatherdale, H.J. Eisler, M.G. Bawendi, *Science* 290 **(2000)** 314-317.
5. X.F. Duan, C.M. Niu, V. Sahi, J. Chen, J.W. Parce, S. Empedocles, J.L Goldman, *Nature* 425 **(2003)** 274-278.
6. I. Gur, N.A. Fromer, M.L. Geier, A.P.livisatos, *Science* 310 **(2005)** 462-465
7. W.U. Huynh, J.J. Dittmer, W.C. Libby, G.L. Whiting, A.P. Alivisatos, *Advanced Functional Materials* 13 **(2003)** 73-79.
8. W.U. Huynh, J.J. Dittmer, A.P. Alivisatos, *Science* 295 **(2002)** 2425-2427.
9. J. Yang, A. Tang, R. Zhou, J. Xue, *Solar Energy Materials and Solar Cells* 95 **(2011)** 476-482.
10. S. Dayal, M.O. Reese, A.J. Ferguson, D.S. Ginley, G. Rumbles, N. Kopidakis, *Advanced Functional Materials* 20 **(2010)** 2629-2635.
11. J.D. Olson, G.P. Gray, S.A. Carter, *Solar Energy Materials and solar cells* 93 **(2009)** 519-523.

12. Y.F. Zhou, F.S. Riehle, Y. Yuan, H.F. Schleiermacher, M. Niggemann, G.A. Urban, M. Krueger, *Applied Physics Letters* 96 **(2010)** 013304.
13. W.-F. Fu, Y. Shi, L. Wang, M.-M. Shi, H.-Y. Li, H.-Z. Chen, *Solar Energy Materials and Solar Cells* 117 **(2013)** 329-335.
14. S. Dayal, N. Kopidakis, D.C. Olson, D.S. Ginley, G. Rumbles, *Nano Letters* 10 **(2010)** 239-242.
15. R. Zhou, Y. Zenng, L. Qian, Y. Yang, P. H. Holloway, J. Xue, *Nanoscale* 4 **(2012)** 3507-3514.
16. K. Palaniappan, J.W. Murphy, N. Khanam, J. Horvath, H. Alshareef, M. Quevedo-Lopez, M.C. Biewer, S.Y. Park, M.J. Kim, B.E. Gnade, M.C. Stefan, *Macromolecules* 42 **(2009)** 3845-3848.
17. N.C. Greenham, X.G. Peng, A.P. Alivisatos, *Physical Review B: Condensed Matter and Materials Physics* 54 **(1996)** 17628-17637.
18. W. F. Fu, Y. Shi, W. Qiu, L. Wang, Y. Nan, M. Shi, H. Li, H. Chen, *Physical Chemistry Chemical Physics* 14 **(2012)** 12094-12098.
19. D. Celik, M. Krueger, C. Veit, H.F. Schleiermacher, B. Zimmermann, S. Allard, I. Dumsch, U. Scherf, F. Rauscher, P. Niyamakom, *Solar Energy Materials and Solar Cells* 98 **(2012)** 433-440.
20. J.S. Owen, J. Park, P.E. Trudeau, A.P. Alivisatos, *Journal of American chemical society* 130 **(2008)** 12279-12281.
21. B.C. Sih, M. Wolf, *Journal of Physical Chemistry C* 111 **(2007)** 17184-17192.
22. D. Aldakov, F. Chandezon, R. De Bettignies, M. Firon, P. Reiss, A. Pron, *European Physical Journal Applied Physics* 36 **(2006)** 261-265.
23. Y. Zhou, M. Eck, C. Veit, B. Zimmermann, F. Rauscher, P. Niyamakom, S. Yilmaz, I. Dumsch, S. Allard, U. Scherf, M. Krüger, *Solar Energy materials and Solar Cells* 95 **(2011)** 1232-1237.
24. Y. Zhou, M. Eck, C. Men, F. Rauscher, P. Niyamakom, S. Yilmaz, I. Dumsch, S. Allard, U. Scherf, M. Krüger, *Solar Energy materials and Solar Cells* 95 **(2011)** 3227-3232.
25. S. Sapra, A.L. Rogach, J. Feldmann, *Journal of Materials Chemistry* 16 **(2006)** 3391-3395.
26. L. F. Xi, Y. M. Lam, *Journal of Colloid and Interface Science* 316 **(2007)** 771-778.

27. J. D. Patel, F. Mighri, A. Ajji, *Materials Research Bulletin* 47 **(2012)** 2016-2021.
28. K.A. Magarian, V.V. Fedyanin, K.R. Karimullin, I.A. Vasilieva, G.V. Klimusheva, Journal of Physics: Conference Series 478 **(2013)** 012007.
29. X. Ji, D. Copenhaver, C. Sichmeller, X. Peng, Journal of American Chemical Society, 130 **(2008)** 5726-5735.

Chapter 8: Spin-coating deposition of PbS and CdS thin films for solar cell application

Jayesh D. Patel[a], Frej Mighri[a,*], Abdellah Ajji[b], Devendra Tiwari[c] and Tapas K. Chaudhuri[c]

[a]CREPEC, Department of Chemical Engineering, Laval University, Quebec, QC, G1V 0A6 Canada

[b]CREPEC, Chemical Engineering Department, Ecole Polytechnique, Montreal, QC, H3C 3A7 Canada

[c]Dr. K.C. Patel Research and Development Centre, Charotar University of Science and Technology (CHARUSAT), Changa, Tal.-Petlad, Anand District, Gujarat 388421, India

Under Preparation (2014)

Résumé

Une technique simple de déposition selon la méthode de 'Spin coating' de films de sulfure de cadmium (CdS) et de sulfure de plomb (PbS) à partir du complexe méthanolique de métal-thiourée a été décrite dans ce travail. La caractérisation des films par les techniques de diffraction des rayons X et de spectroscopie photoélectronique des rayons X a révélé que des couches de CdS et Pbs à phase cubique pure ont été formées via cette méthode. Les deux films sont lisses et homogènes tel qu'indiqué par la microscopie à force atomique et la microscopie électronique à balayage. Les propriétés optiques montrent que les intervalles entre les bandes d'énergie correspondant aux films de PbS et de CdS sont de 1.65 et 2.5 eV, respectivement. Le film à base de PbS est de type-p avec une conductivité électrique (σ) de 0.8 S/cm. La concentration et la mobilité des trous, déterminées avec les mesures de l'effet Hall, sont de 2.35×10^{18} cm^{-3} et 2.16×10^{-3} $cm^2V^{-1}s^{-1}$, respectivement. Les films à base de CdS et PbS ont tout les deux été utilisés pour développer un dispositif de cellule solaire à films minces de graphite/PbS/CdS/ITO/verre. La caractérisation de ce dispositif montre une efficacité de conversion d'énergie de 0.24%. La tension en circuit ouvert, le courant de court-circuit et le facteur de remplissage correspondants, on été de 0.570 V, 1.32 mA/cm^2 et 0.32, respectivement.

Abstract

In this work, we describe a simple spin-coating deposition technique of lead sulfide (PbS) and cadmium sulfide (CdS) films from a methanolic metal-thiourea complex. The characterization of the films by X-ray diffraction and X-ray photoelectron spectroscopy techniques revealed that pure cubic phase PbS and CdS layers were formed via this method. As shown by atomic force microscopy (AFM) and scanning electron microscopy (SEM) techniques, both films were homogeneous and presented a smooth surface. Optical properties showed that the energy band gap of PbS and CdS films were around 1.65 and 2.5 eV, respectively. The PbS-based film was a p-type with an electrical conductivity (σ) of around 0.8 S/cm. The concentration and the mobility of holes were 2.35 x 10^{18} cm^{-3} and 2.16 x 10^{-3} $cm^2V^{-1}s^{-1}$, respectively, as determined from Hall measurement. Both PbS and CdS based films were used to develop a thin film solar cell device of graphite/PbS/CdS/ITO/glass. Device characterization showed a power conversion efficiency of around 0.24 %. The corresponding open circuit voltage, short circuit current and fill factor were 0.570 V, 1.32 mA/cm^2, and 0.32, respectively.

8.1 Introduction

Recently, nanoscale PbS has gained surge of interest because of its remarkable physical properties and potential applications in solar cells.[1] Bulk PbS has a narrow direct energy band gap of 0.41 eV at 300 K with a large exciton Bohr radius of 18 nm. Thus the absorption edge of PbS can be tuned to anywhere between near-infrared to violet (0.4 μm), covering the entire visible spectrum. A large exciton Bohr radius and a relatively small band gap make PbS one of the most important candidates for size quantization studies. Recently, about 300% of quantum efficiency due to multiple exciton generation was also observed in PbS nanoparticles.[2] Therefore, PbS thin films made of nanocrystallites having a band gap of around 1 eV can be used as an absorber for thin film solar cells. In recent years, vigorous investigations were conducted to develop 2 to 5% efficient solar cells based on PbS quantum dot thin films.[3-9] In an alternative way, chemically deposited PbS thin film layers were also used in thin film solar cells as a p-type absorber layer.[10,11]

On the other hand, CdS is considered as one of the most important II-IV semiconductors. It has a direct band gap of 2.42 eV at room temperature and is widely used as n-type window layer for p-type polycrystalline photovoltaic materials. Earlier, Romeo et al.[12] reported on a CdS/CdTe thin film solar cell with high efficiency (around 14.6%). Later, Ramanathan et al.[13] successfully achieved a ZnO/CdS/$CuInGaSe_2$ thin film solar cell structure of higher efficiency (around19.2%). Vorobive et al.[14] also developed a CdS/PbS thin film solar cell of 1.6% in efficiency through ammonia free chemical bath deposition (CBD) technique. Obaid et al.[15] used the microwave-assisted CBD route to develop the same CdS/PbS thin film solar cell device with an efficiency of around 1.3%.

Aqueous precursors containing metal salts and thiourea (TU) were frequently employed in CBD of the PbS and CdS thin films.[1, 16-18] Although these thin films have interesting properties, the majority of CBD routes are ammonia based, and it is known that ammonia is highly volatile, toxic and harmful to the environment at large scale deposition. Furthermore, the volatility of ammonia generally leads to irreproducible film properties.[14] To prepare metal chalcogenide thin films, the new ammonia-free simple precursors based on large scale deposition routes with less environmental issues is of great interest nowadays.

Metal-thiourea (M-TU) complex precursors are simple and low cost materials used to prepare various types of metal chalcogenide thin films. Chaudhuri et al. reported on the fabrication of PbS,[19] ZnS,[20] Cu_2ZnSnS_4[21] and $CuSnS_3$[22] thin films through the thermolysis of M-TU complex precursors. On the other hand, spin-coating deposition technique is simple, fast and known for uniform deposition. Moreover, it requires fewer amounts of material and processing time compared to CBD routes. According to our knowledge, no data have been reported in the open literature on the spin coating deposition of PbS and CdS thin films using non-aqueous M-TU complex precursors.

This study primarily aimed to develop PbS and CdS films from M-TU complex precursors through an easy and fast spin-coating route. After an extensive characterization of the developed films for their structural, morphological, optical and electrical properties, these films were used to develop thin film solar cell devices of graphite/PbS/CdS/ITO/glass.

8.2 Experimental details

8.2.1 Materials

Lead acetate trihydrate ($Pb(Ac)_2 \cdot 3H_2O$), cadmium acetate dihydrate ($Cd(Ac)_2 \cdot 2H_2O$) and TU were purchased from Sigma Aldrich. Methanol, acetone, isopropanol and microscopic glass substrates were purchased from Fisher chemicals. Indium tin oxide (ITO) coated glass plates (sheet resistance of 10Ω/sq) were purchased from Delta Technologies, USA. The glass substrates and etched ITO substrates were cleaned through ultrasonically in (i) detergent, (ii) deionized water, (iii) acetone, and (iiii) isopropanol sequentially before spin coating deposition.

8.2.2 Deposition of PbS and CdS films

Methanolic complex precursors were prepared by dissolving $Pb(Ac)_2 \cdot 3H_2O$ (0.1 mol/L) or $Cd(Ac)_2 \cdot 2H_2O$ (0.1 mol/L) and TU (0.1 mol/L) in methanol (50 mL) one by one. Few drops of acetic acid were added in Pb-TU complex solution to prevent decomposition at room temperature. The cleaned glass substrates were then spin-coated with methanolic Pb-TU and Cd-TU complex precursors at 2200 rpm for 2 min. Then both transparent precursor layer coated glass substrates were baked individually at different temperatures in air for 10 min.

After 10 min at 100°C, Pb-TU complex precursor layer was converted into brownish black PbS film, while Cd-TU complex precursor layer was converted into yellowish CdS film at 200°C. The thickness of PbS and CdS films was about 70 nm and 60 nm, respectively.

8.2.3 Characterization of films

The thickness of films was measured by profilometer Dektak IIa Solan. The composition of the layers was determined from X-ray diffraction analysis (XRD) with Siemens D5000 X-ray diffractometer. X-ray photoelectron spectroscopic (XPS) study of films was carried out on Axis Ultra Kratos, X-ray photoelectron spectrometer under a vacuum of 2-5 $x10^{-8}$ Torr. The binding energy values were charge-corrected to the C 1s signal (285.0 eV). The surface morphology of the films was examined by Atomic Force Microscope (AFM) (Nanoscope III Multimode system (Digital Instruments, Santa Barbara, CA)) and scanning electron microscope (SEM) (Jeol JSM-6360/LV scanning electron microscope). The optical transmittance spectra of films were recorded on Varian Cary 500 Scan UV-Vis spectrophotometer. Electrical conductivity of the films was measured by making gap cells with colloidal graphite ohmic contacts. The gap between the electrodes was 0.5 cm and the field applied was 20 V/cm. To determine the type of conduction, the thermoelectric power (TEP) was also measured. The photoconductivity of the films was measured by illuminating the samples with 80 mW/cm^2 light from a halogen lamp (50 W, 12 V, Phillips). The rise and decay of the photoconductivity was recorded with a Source/Meter (Keithley 2611).

8.2.4 Fabrication of CdS/PbS thin film solar cell device

Thin film solar cell device structure with graphite/PbS/CdS/ITO/glass was fabricated using the developed PbS and CdS thin films. Firstly, an ITO coated glass substrate (24×24 mm^2) was spin-coated once with CdS as window layer (~60 nm). Three layers of PbS (~210 nm) were then coated one by one on CdS and final electrical contacts were made by painting with colloidal graphite. To understand the contribution of both films (n-type and p-type) in the developed solar cell device, two clean glass substrates were also coated individually with three layers of PbS and one layer of CdS to investigate their optical and electrical properties. The current-voltage (*J-V*) characteristics of CdS/PbS thin film solar cells were characterized with a computerized Keithley 2400 source meter under AM1.5G illumination at 100

mW/cm^2 supplied by a solar simulator (Oriel, 1000 W). The active surface of the cell was 0.24 cm^2.

8.3 Results and discussions

8.3.1 Structure and composition

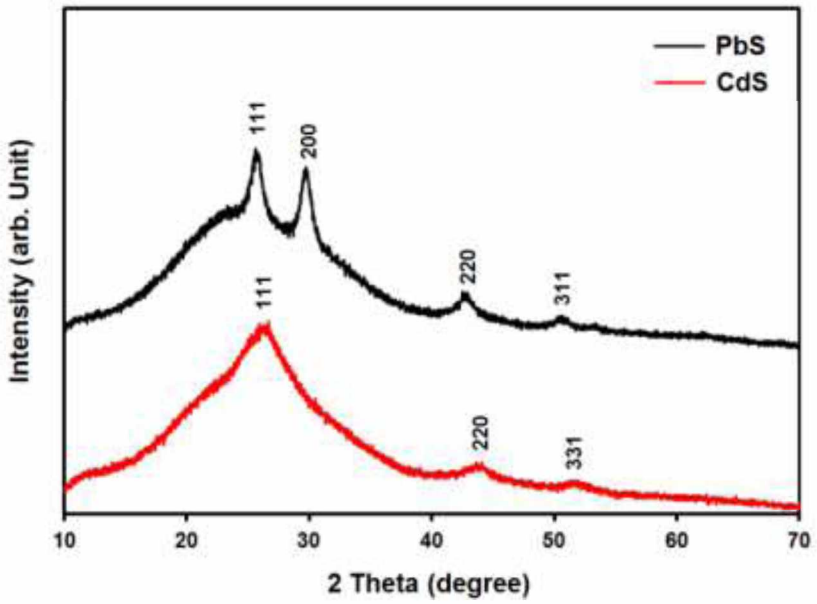

Figure 8.1 X-ray diffraction patterns of PbS and CdS films.

XRD patterns of PbS and CdS films are shown in **Figure 8.1**. Both patterns show well defined broad peaks. No characteristic peaks of other impurities are observed in these patterns, indicating the high purity of the as-synthesized PbS and CdS films. The average crystallite sizes were measured form the broadening of (111) lines using the following Scherrer equation.

$$D = k\lambda / B\cos\theta \qquad \textbf{(8-1)}$$

where D (nm) is the particle size, k is the shape factor (taken as 0.9), λ is the wavelength (nm) of X-ray used, β is the broadening of line at half the intensity, and θ (degree) is the diffraction angle of the line under consideration. The XRD pattern of PbS film is similar to that of recently reported nanocrystalline PbS film obtained by CBD route.[1] It shows four

broad peaks corresponding to (111), (200), (220) and (311) planes of cubic PbS (JCPDS: 05-592) at 2θ values of 25.9°, 30°, 43° and 50.9°, respectively. The corresponding average crystallite size is 9 nm. On the other hand, the XRD pattern of CdS film shows three broad peaks at 2θ values of 26.5°, 43.9° and 51.9° identified to be due to reflections from (111), (220) and (331) planes of cubic CdS (JCPDS: 5-0566). The corresponding average crystallite size is 5 mm.

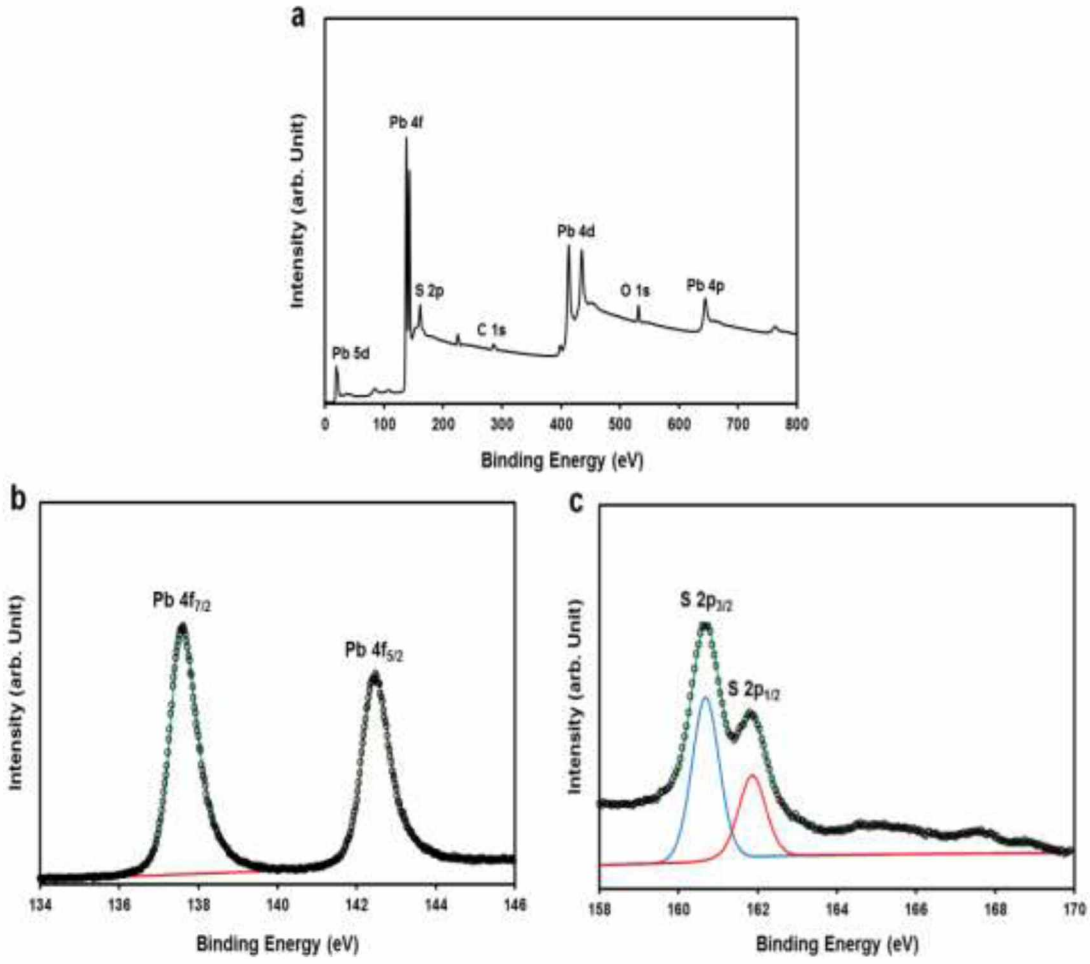

Figure 8.2 XPS of PbS film (a) survey scan and (b) Pb 2f core level (c) S 2p core level with fitting profiles (black circles for data, olive green color line for peak sum, red and blue lines for two different states).

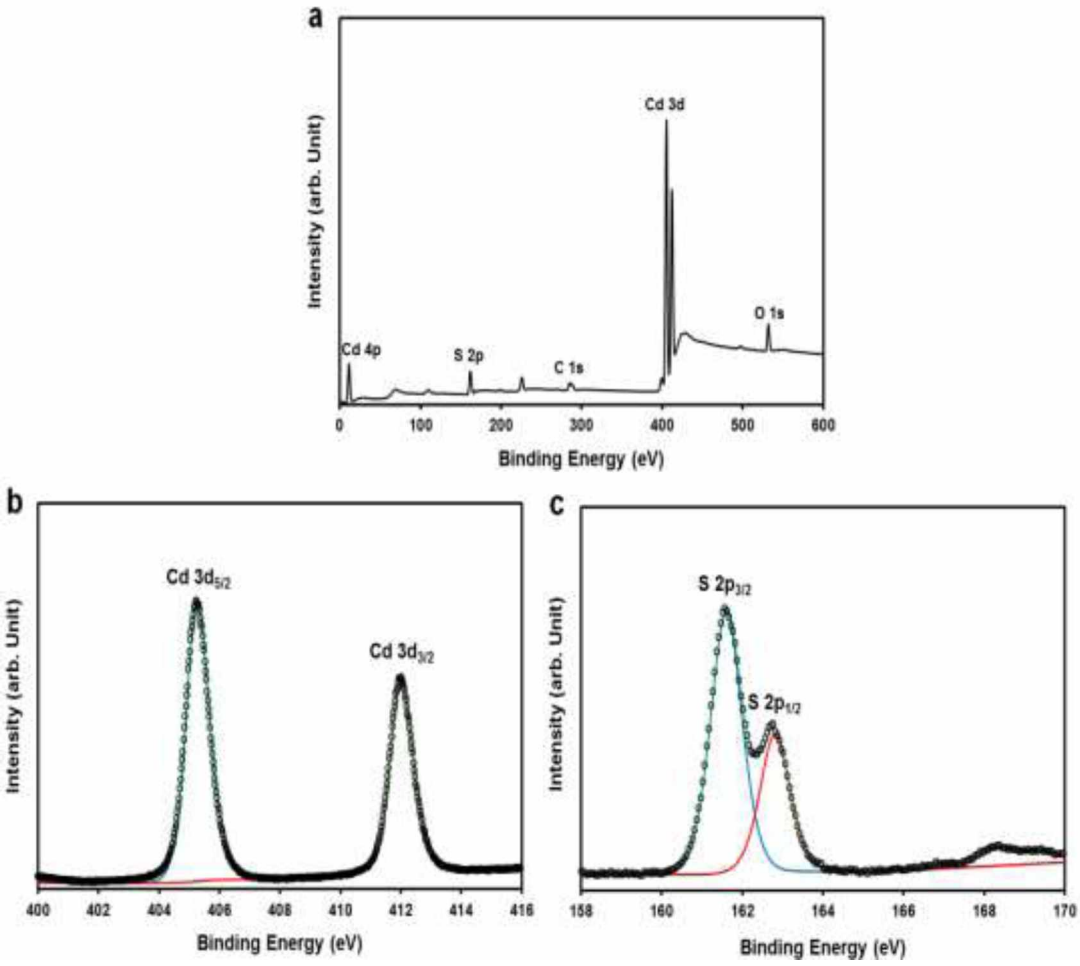

Figure 8.3 XPS of CdS film (a) survey scan and (b) Cd 3d core level (c) S 2p core level with fitting profiles (black circles for data, olive green color line for peak sum, red and blue lines for two different states).

The surface compositions of the PbS and CdS films were characterized by XPS analysis. The wide scanning XPS of the films are shown in **Figure 8.2a** & 8.**3a**. The existence of C and O in the films is probably due to the surface contamination under atmosphere condition.[23] Besides the presence of C and O, no other obvious impurity peaks were detected in both spectra. The chemical state of the films has been investigated by the narrow scanning XPS spectrum. The narrow scanning photoelectron spectra of the PbS film are shown in **Figure 8.2b** & **c**. The peaks at 137.6 and 142.4 eV are assigned to the binding energies of Pb $4f_{7/2}$ and Pb $4f_{5/2}$, which is in good accordance with data mentioned in literature.[24] The

corresponding binding energies of S $2p_{3/2}$ and S $2p_{1/2}$ are respectively 160.7 and 161.8 eV, analogous to those reported in literature for PbS.[24] The other small peaks observed between 167 to 170 eV are probably due to sulphite or sulphate. **Figure 8.3b & c** reveal the high resolution scanning XPS spectra of the Cd 3d core and S 2p core, respectively. The two strong peaks at 405.2 and 412 eV are attributed to Cd $3d_{5/2}$ and Cd $3d_{3/2}$, which show good agreement to the literature.[25] The binding energies of S $2p_{3/2}$ and S $2p_{1/2}$ are respectively 161.6 and 162.7 eV, respectively. These values are also consistent with those reported in literature for CdS.[25] Like PbS, the small peaks between 167 and 170 eV could also be due to sulphite or sulphate.

8.3.2 Morphology and microstructure

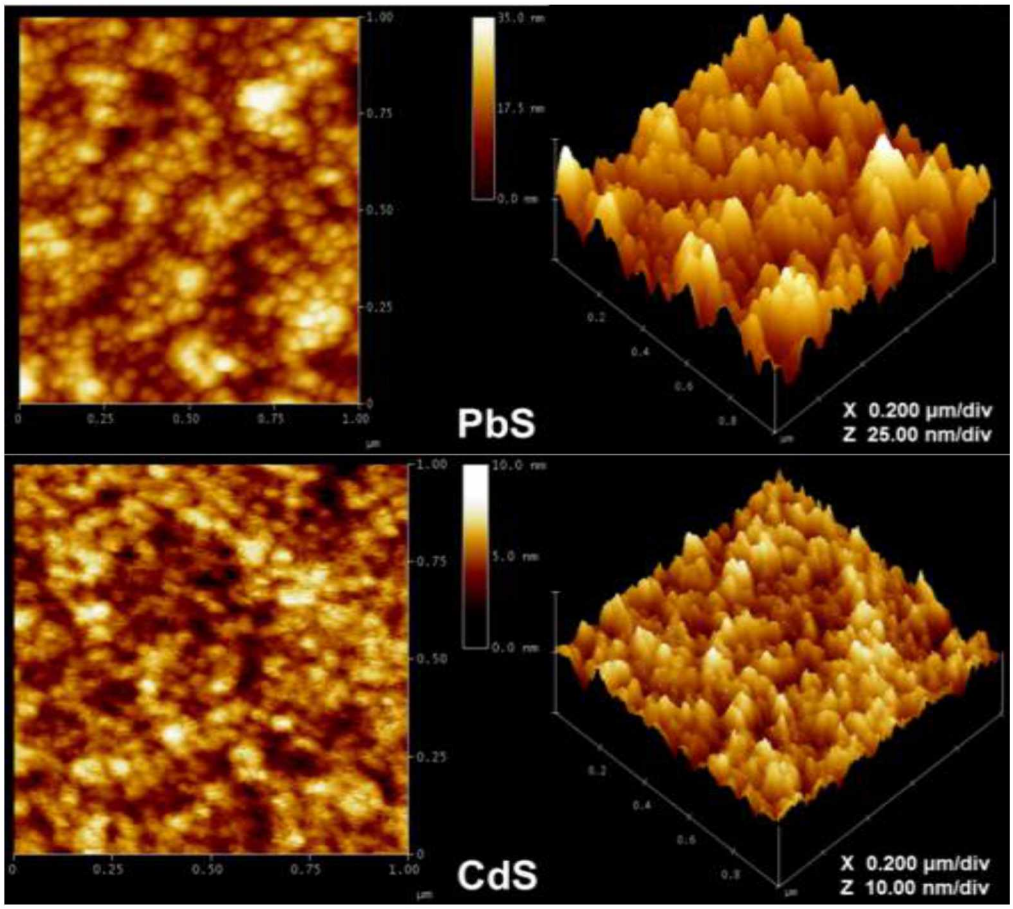

Figure 8.4 Atomic force micrographs of PbS and CdS films on glass with 2-dimentinal and 3-dimentinal view.

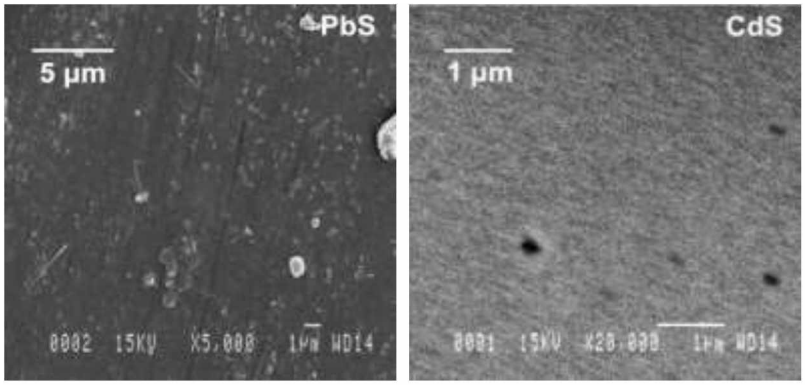

Figure 8.5 SEM images of PbS and CdS films.

The Atomic Force micrographs of the films on glass are shown in **Figure 8.4**. In general, the films are continuous with homogeneous well-connected grains. The average grain size and root-mean-square (RMS) roughness are respectively about 5 and 40 nm for PbS films and 15 and 1 nm for CdS films. Similar morphologies for both PbS and CdS films are also revealed by SEM, as shown in **Figure 8.5**. Both AFM and SEM results depict the formation of smooth, compact and dense films without any defects or cracks.

8.3.3 Optical, electrical and photovoltaic properties

Figure 8.6a shows the optical transmittance spectra of PbS and CdS films as a function of wavelength. As shown, the transmittance of the thrice coated PbS film decreases rapidly below 850 nm until about 450 nm, indicating absorption edge. On the other hand, the CdS film exhibits a high transmittance in the visible and near infrared regions, thus making the film suitable as window layers for thin film solar cell. It should be mentioned that high transmittance in visible region is one of the key features of ideal window layer of a heterojunction solar cell.[26] The energy band gaps (Eg) of the films were determined from the following Tauc relation:

$$(\alpha h\nu)^2 \sim h\nu - Eg \qquad \textbf{(8-2)}$$

where α (cm^{-1}) is the absorption coefficient, h (J.s) is the Plank constant, ν (Hz) is the frequency of radiation, and Eg (eV) is the energy band gap of the semiconductor.

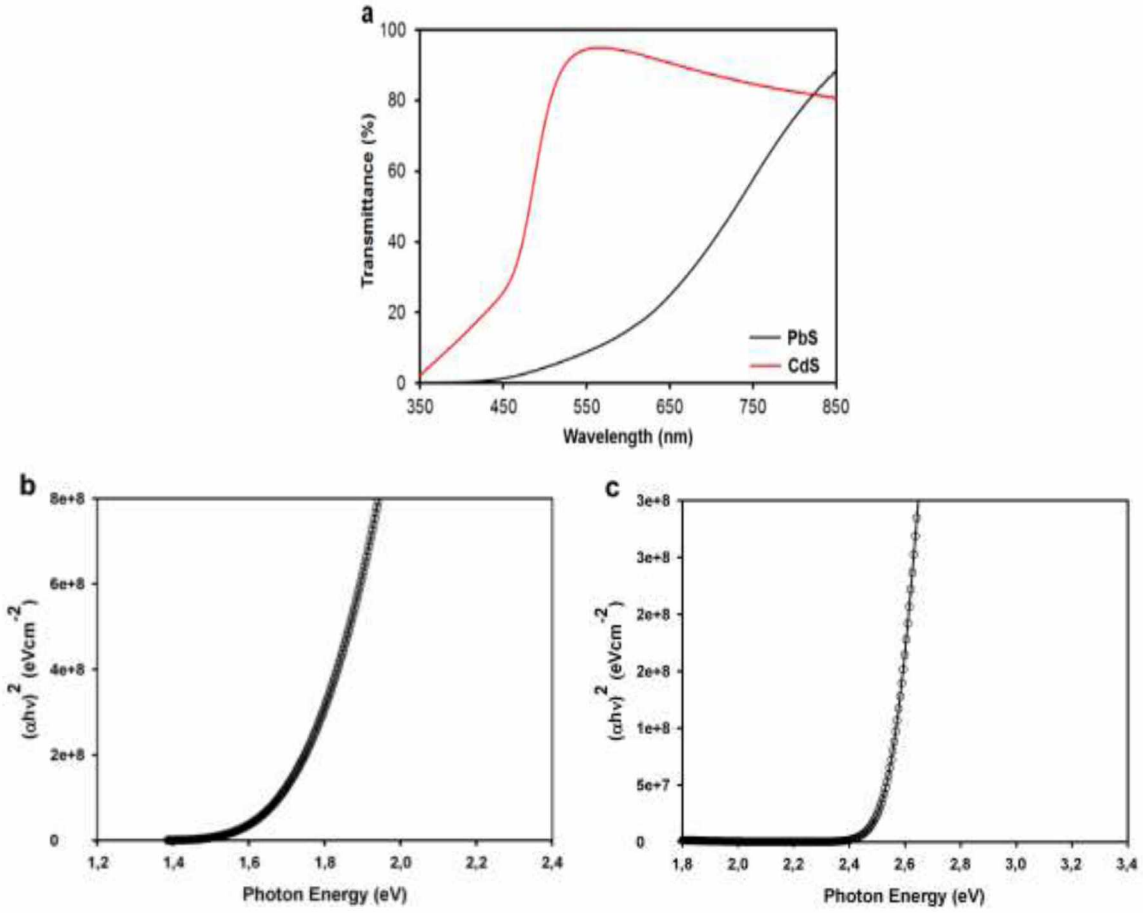

Figure 8.6 Optical transmittance spectra of the PbS and CdS films (a) and Tauc plots of $(\alpha h\nu)^2$ vs. $h\nu$ for determination of energy band gaps of PbS (b) and CdS (c) films.

Tauc plots of $h\nu$ vs, $(\alpha h\nu)^2$ for the PbS and CdS films are shown in **Figure 8.6b** and **c.** The band gap values of the films were deduced by extrapolating linear portion of the plots to zero. The determined band gaps for PbS and CdS film were found to be 1.7 and 2.5 eV, respectively. The band gap of PbS film shows significant blue shift from the bulk value of 0.41 eV due to quantum size effect induced by the nanocrystallites in the film. Thus, the optical studies also reveal that the spin-coated PbS film is nanocrystalline. Similarly, the value of band gap is found to increase from 2.42 to 2.5 eV for CdS film. A similar increase in band gap was observed recently by Hegde et al. in thermally evaporated indium doped CdS film.[26] An increase in the band gap of CdS film is advantageous to enhance the performance of the thin film solar cell.

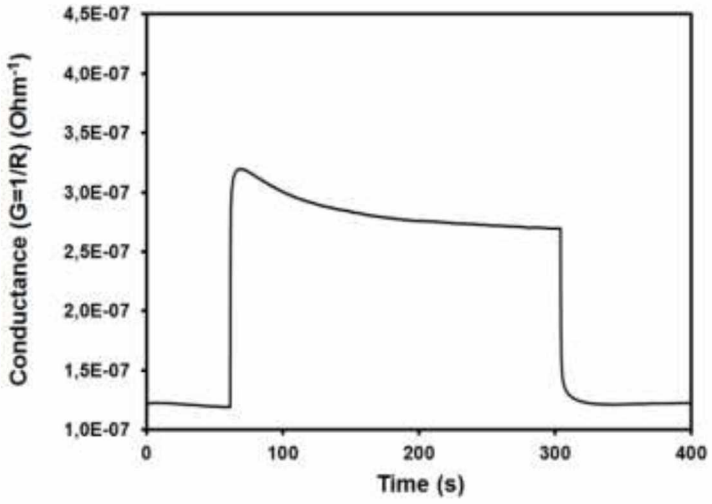

Figure 8.7 Rise and decay of photoconductivity of PbS film.

The room temperature dark conductivity of the PbS film is 0.8 S/cm. The thermoelectric power (TEP) is measured to be +235 μV/K. The positive sign of TEP suggests the p-type conduction i.e. holes as majority carriers. The electrical conductivity and TEP data are used to calculate hole concentration and hole mobility using the following relation:

$$p = N_v \exp(A - e\alpha_{th} / k) \qquad \textbf{(8-3)}$$

Where, N_v is the effective density of state in valence band (6.47 x 10^{17} cm^{-3} for PbS at 300 K), A is a constant that depends on scattering (4 for impurity scattering), α_{th} is the thermoelectric power, k is the Boltzmann constant (86.7 μV/K), and e is the electronic charge (coulombs).

The mobility of holes is determined from the equation:

$$\mu = \sigma / p.e \qquad \textbf{(8-4)}$$

where, μ (cm^{-3}) is the mobility and σ (S/cm) is the electrical conductivity. Thus calculated values for holes concentration and mobility are 2.35 x 10^{18} cm^{-3} and 2.16 x 10^{-3} $cm^2V^{-1}s^{-1}$, respectively.

The rise and decay curve demonstrating the photoconductivity of PbS film is shown in **Figure 8.7**. The atypical behavior of rise and decay curve, where the photocurrent first rises to a maximum upon illumination and decreases gradually with time, is an indication of quenching. It must be recalled here that the source of illumination is white light composed of UV, visible and IR spectra. The entire curve can be described as an overlapping of two phenomena:[27]

i) Upon illumination, the net generation rate of minority carrier increases, leading to a rise in photocurrent. Upon removing the light source, generation and recombination rates again equilibrate and the current comes back to the dark value.
ii) An excitation from a larger wavelength situated in the white light region causes the optical freeing of the electrons from the shallow traps, leading to an increase of the recombination rate of minority carriers, i.e., a photocurrent decrease.

Thus, illumination produces both photoconductivity due to excitation from the valence band to imperfection levels and quenching due to excitation from the sensitizing centers to the conduction level. Such anomalous rise and decay curves have been already observed in literature for other chalcogenides.[27-29]

The origin of traps is supposed to be due to oxygen atoms, which have been found commonly as sensitizing centers in PbS.[30] As shown XPS curve of **Figure 8.2**, the presence of oxygen at the surface of PbS is evident from the small peaks in O core level at 529. 4 eV and in S at around 167 eV. The sensitizing centers due to oxygen have been found to be located very near the bands, within few multiple of kT (k is the Boltzmann constant and T is the absolute temperature), and are in general shallow. The minority carrier lifetime, as deduced from the rise decay curve, is about 10 μs and is consistent with value determined from transient photoconductivity measurement.

Conductivity of the single CdS layer (<0.1 mS/cm) is too low to be measured with the available measurement facilities in our laboratory. However, it is known that the CdS films without special doping are usually of n-type conductivity.[14]

Figure 8.8 shows the J-V characteristic of a graphite/PbS/CdS/ITO/glass thin film solar cell. The schematic and prototype picture of the cell prototype are shown within the J-V curve.

The best cell prototype shows a power conversion efficiency (PCE) of 0.24%. The

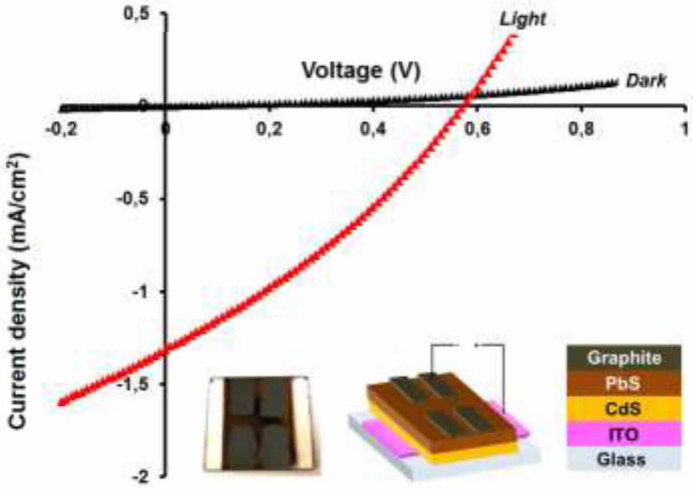

Figure 8.8 J-V characteristics of CdS/PbS solar cell under dark and illumination (AM 1.5, 100 mA/cm^2). Insets show schematic and prototype picture of solar cell.

corresponding open circuit voltage (V_{oc}), short circuit current density (J_{sc}), and fill factor (FF) are respectively 570 mV, 1.32 mA/cm^2 and 0.32. Compared to V_{oc} values currently reported in literature for CdS/PbS thin film solar cells,[14,15] our results show an evident enhancement of V_{oc}. On the other hand, the relatively low value of J_{sc} and FF could be due to ohmic and recombination losses, as already observed by Hegde et al.[26] The series (R_s) and shunt (R_{sh}) resistances are respectively 260 and 645 Ω, as determined from J to V characteristics. The low efficiency of the CdS/PbS of thin film solar cells is related to the large value of R_s and the low value of R_{sh}. The first is due to ITO and window (CdS) layer. This could be also the reason of low values of J_{sc} and FF of the cell. Nevertheless, it should be mentioned that, for better photovoltaic properties, R_{sh} must be higher than R_s. A high value of R_{sh} is also an indication that the spin-coating technique used helped us to develop a good heterojunction free from voids, homogeneous, and having a high V_{oc}.[22]

8.4 Conclusions

Spin-coating deposition of PbS and CdS films from methanolic solution of M-TU complex precursors was described in this work. XRD confirmed the formation of cubic phase PbS and CdS layers. The PbS and CdS films were smooth and compact and presented a band gap of respectively 1.7 and 2.5 eV. Electrical properties revealed that PbS film is p-type with an electrical conductivity of around 0.8 S/cm. By using the developed PbS and CdS thin films, a thin film solar cell prototype of graphite/PbS/CdS/ITO/glass was developed. This prototype had a power conversion efficiency of around 0.24 %. Although a relatively low efficiency due to the the large value of R_s and the low value of R_{sh} of the CdS/PbS thin film , this route may useful as an alternative of CBD to deposit other metal sulphide thin films.

Acknowledgments

The authors would like to thank the Natural Sciences and Engineering Research Council of Canada (NSERC) for financial support of this work. The authors appreciate the help of Dr. Hamed Najari, (Department of Chemistry, Laval University) in fabrication and measurements of solar cell devices.

8.5 References

1. N.B. Kotadiya, A.J. Kothari, D. Tiwari, T.K. Chaudhuri, *Applied Physics A: Materials Sciecne and Processing* 108 **(2012)** 819-824.
2. R.J. Ellingson, M.C. Beard, J.C. Johnson, P. Yu, O.I. Micic, A.J. Nozik, A. Shabaev, A.L. Efros, *Nano Letters* 5 **(2005)** 865-871.
3. J. Tang, X. Wang, L. Brzozowski, D.A.R. Barkhouse, R. Debnath, L. Levina, E.H. Sargent, *Advanced Materials* 22 **(2010)** 1398-402.
4. J.M. Luther, J. Gao, M.T. Lloyd, O.E. Semonin, M.C Beard, A.J. Nozik, *Advanced Materials* 22 **(2010)** 3704-3707.
5. K.P. Bhandari, P.J. Roland, H. Mahabaduge, N.O. Haugen, C.R. Grice, S. Jeong, T. Dykstra, J. Gao, R.J. Ellingson, *Solar Energy Materials and Solar Cells* 117 **(2013)** 476-482.

6. P.R. Brown, R.R Lunt, N. Zhao, T.P. Osedach, D.D. Wanger, L.-Y. Chang, M.G. Bawendi, V. Bulović, *Nano letters* 11 **(2011)** 2955-2961.
7. K. Szendrei, W. Gomulya, M. Yarema, W. Heiss, M.A. Loi, *Applied Physics Letters* 97 **(2010)** 203501.
8. J. Gao, C.L. Perkins, J.M. Luther, M.C. Hanna, H.-Y. Chen, O.E. Semonin, A.J. Nozik, R.J. Ellingson, M.C. Beard, *Nano Letters* 11 **(2010)** 3263-3266.
9. A.G. Pattantyus-Abraham, I.J. Kramer, A.R. Barkhouse, X. Wang, G. Konstantatos, R. Debnath, L. Levina, I. Raabe , M.K. Nazeeruddin, M. Grätzel, E.H. Sargent, *ACS Nano* 4 **(2010)** 3374-3380.
10. H. Moreno-García, M.T.S. Nair, P. K. Nair, *Thin Solid Films* 519 **(2011)** 2287-2295.
11. H. Moreno-García, M.T.S. Nair, P.K. Nair, *Thin Solid Films* 519 **(2011)** 7364-7368.
12. N. Romeo, A. Bosio, R. Tedeschi, A. Romeo, V. Canevari, V. *Solar Enrgy Materials and Solar Cells* 58 **(1999)** 209-218.
13. K.Ramanathan, M.A. Contreras, C.L. Perkins, S. Asher, F.S. Hasoon, J. Keane, Y. David, R. Manuel, M. Wyatt, N. Rommel, W. James, A. Duda, *Progress in Photovoltaics: Research and Applications* 11 **(2003)** 225-230.
14. J. Hernández-Borja, Y.V. Vorobiev, R. Ramírez-Bon, *Solar Enrgy Materials and Solar Cells* 95 **(2011)** 1882-1888.
15. A.S. Obid, M.A. Mahdi, Z. Hassan, M. Bououdina, *International journal of Hydorgen Energy* 38 **(2013)** 807-815.
16. M.M. Abbas, A. Ab-M. Shehab, N-A. Hassan, A-K. Al-Samuraee, *Thin Solid Films 519* **(2011)** 4917-4922.
17. J. Hiie, T. Dedova, V. Valdna, K. Muska, *Thin Solid Films* 511-512 **(2006)** 443-447.
18. G. Pérez-Hernández, J. Pantoja-Enríquez, B. Escobar-Morales, D. Martinez-Hernández, L.L. Díaz-Flores, C. Ricardez-Jiménez, N.R. Mathews, X. Mathew, *Thin Solid Films* 535 **(2013)** 154-157.
19. T.K. Chaudhuri, H.N. Acharya, B.B. Nayak, *Thin Solid Films* 83 **(1981)** L169-L172.
20. T.K. Chaudhuri, B. Pathak, *Materials Letters* 61 **(2007)** 5243-5246.
21. T.K. Chaudhuri, D. Tiwari, *Solar Enrgy Materials and Solar Cells* 101 **(2012)** 46-50.
22. D. Tiwari, T.K. Chaudhuri, T. Shripathi, U. Deshpande, R. Rawat, *Solar Energy Materials and Solar Cells* 113 **(2013)** 165-170.

23. J.W. Cheon, D.S. Talaga, J.I. Zink, *Chemistry of Materials* 9 **(1997)** 1208-1212.
24. J.D. Patel, F. Mighri, A. Ajji, S. Elkoun, *Materials Sciences and Applications* 3 **(2012)** 125-130.
25. S. Rengaraj, S. Venkataraj, S.H. Jee, Y. Kim, C-w Tai, E. Repo, A. Koistinen, A. Ferancova, M. Sillanpaa, *Langmuir* 27 **(2011)** 352-358.
26. S.S. Hegde, A.G. Kunjomana, M. Prashantha, C. Kumar, K. Ramesh, *Thin Solid Films* 545 **(2013)** 543–547.
27. R.H. Bube, *Physical Review* 99 **(1955)** 1105-1116.
28. D. Ruiz-León, V. Manríquez, J. Kasaneva, R.E. Avila, *Materials Research Bulletin* 37 **(2002)** 981-989.
29. S.K. Tripathi, A. Kumar, *Journal of Electronic Materials* 17 **(1988)** 45-51
30. S. Espevik, C. Wu, R.H. Bube, *Journal of Applied Physics* 42 **(1971)** 3513-3529

Chapter 9: Fatty acid-assisted synthesis of CdS microspheres: physicochemical properties and photocatalytic activity

Jayesh D. Patel[a,*], Frej Mighri[a,*], Abdellah Ajji[b] and Tapas K. Chaudhuri[c]

[a]CREPEC, Chemical Engineering Department, Laval University, Quebec, QC, G1K 7P4 Canada

[b]CREPEC,Chemical Engineering Department, Ecole Polytechnique, C.P. 6079, Succ. Centre- Ville Montreal, QC, H3C 3A7 Canada

[c]Dr. K.C. Patel Research and Development Centre, Charotar University of Science and Technology, Changa, Tal.-Petlad, Anand District, Gujarat 388421, India

Published in ***Materials Letters*** 110 (2013) 94-97

Résumé

Ce travail porte sur la synthèse de microsphères mésoporeuses (MSs) de sulfure de cadmium (CdS) à haut rendement. La synthèse a été réalisée par traitement solvothermal à 180°C du précurseur du complexe d'oléate de cadmium (Cd-O) mélangé au thiourée (TU). Le complexe Cd-O a subi une sulfurisation lors de la décomposition thermique du TU et a produit des microsphères de CdS mésoporeux ayant la forme de chou-fleur et composées de nanocristaux (NC) de CdS couverts d'acide oléique (AO) avec une taille moyenne de 1.5 μm. Les MSs de CdS telles que synthétisées présentent de bonnes propriétés physico-chimiques. En outre, ils ont une activité photocatalytique prononcée pour dégrader la rhodamine B (RhB) en milieu aqueux. Cela suggère que les MSs CdS synthétisées peuvent être utilisées comme photocatalyseurs pour traiter les polluants organiques par l'irradiation de la lumière visible.

Abstract

This work deals with fatty acid-assisted high yield synthesis of cadmium sulphide (CdS) mesoporous microspheres (MSs). The synthesis was conducted by solvothermal treatment of thiourea (TU) mixed cadmium-oleate (Cd-O) complex precursor at 180 °C. The Cd-O complex sulphurized upon thermal decomposition of TU and produced OA-capped CdS nanocrystals (NCs) composed cauliflower-like mesoporous CdS MSs with an average size of 1.5 μm. The as-synthesized CdS MSs exhibit good physicochemical properties. Moreover, the as-synthesized CdS MSs showed pronounced photocatalytic activity to degrade rhodamine B (RhB) in aqueous medium. This suggested that the as-synthesized CdS MSs might be used as a photocatalyst to treat the organic pollutants under visible light irradiation.

9.1 Introduction

As an important II-VI semiconductor, CdS has gained much attention due to its unique properties and its potential applications in biological labelling, light emitting diodes, lasers, logic gates, transistors and solar cells.[1-5] It is well known that properties and applications of the semiconducting materials significantly depend on their size and morphology. Various studies have been devoted to synthesize a variety of CdS nanomaterials for photocatalytic application, such as flower-like shape,[6] microspheres,[7] flower-like 3D assemblies,[8] mesoporous nanospheres,[9] dendritic hierarchical structures,[10] and quantum dots.[11]

Anatase TiO_2 is the most studied photocatalyst due to its low cost, high stability and biocompatibility.[12] However, TiO_2 responds to UV light only and its wide band gap limits its practical application as photocatalyst. Therefore, an interesting task is to find an efficient photocatalyst that can effectively degrade organic pollutants under visible light irradiation. The photocatalyst generates reactive hydroxyl radicals, which oxidize the toxic organic pollutants and break them into smaller fragments.[13] However, high oxidative capacity and stability are the important criteria for the semiconductor to get selected as a photocatalyst.[14] Photocatalysis using nanoscale CdS material is also potentially promising strategy to solve such environmental issues. In this strategy, nanoscale CdS photocatalyst is used to decompose organic pollutants from the aqueous medium.[6-10]

Herein, a facile high yield approach is introduced to synthesize NCs composed cauliflower-like CdS MSs via solvothermal sulphurization of Cd-O complex using TU. It is reported that oleic acid plays an important role in the synthesis of microsphere nanostructure.[15] In the solvothermal synthesis of CdS MSs reported here, oleic acid ligands cover the surfaces of the initially formed CdS NCs; this stabilizes the CdS NCs and effectively confines their random Brownian motions and various rotations. This results in oriented assembly of the CdS NCs into cauliflower-like CdS MSs after 20 h. Furthermore, the as-synthesized CdS MSs exhibit good physicochemical properties and found an efficient photocatalyst for the degradation of RhB in aqueous medium under visible light irradiation.

9.2 Experimental

First, Cd-O complex was prepared through thermal reaction between cadmium acetate dihydrate (Cd $(AC)_2 \cdot 2H_2O$) and oleic acid (OA) in methanol. A 0.1 M of Cd $(AC)_2 \cdot 2H_2O$ was mixed with 0.15 M of OA and 100 mL of methanol. The mixture was then refluxed at 135°C with stirring in an oil bath using water condenser. After 1 h, 0.1 M TU was added to the Cd-O complex solution and transferred to the Teflon lined stainless steel autoclave (capacity of 125 mL). The Teflon lined stainless steel autoclave was treated at 180 °C for 20 h and then naturally cooled to room temperature. The obtained product with yield higher than 90% was collected, washed several times by methanol and hot distilled water, and dried at 50 °C for 1 h.

Powder X-ray diffraction (XRD) data of the CdS MSs was recorded on a Siemens D5000 X-ray diffractometer, using Cu-Kα radiation (λ = 1.54059 Å). Scanning electron microscopy (SEM) images were recorded with a JEOL JSM-840a scanning electron microscope. The UV-visible absorption spectrum was recorded on Varian Cary 500 Scan UV-Vis spectrophotometer. Photoluminescence (PL) spectrum was measured at room temperature using Varian Cary Eclipse Fluorescence Spectrophotometer. Infrared spectra (IR) of OA and CdS MSs were obtained using a Nicolet (Thermo Fisher) Model 380. The specific surface area of the CdS MSs was calculated from the linear part of the Brunauer–Emmett–Teller equation ($P/P0 \approx 0.05$-0.2). The pore diameter distribution was obtained from analysis of the desorption branch of the isotherms using the Barrett–Joyner–Halenda model.

For photocatalytic activity evaluation, 30 mg of CdS MSs and 6 mL of freshly prepared RhB aqueous solution (100ppm) were mixed in 24 mL distilled water. Further, the mixture was stirred under high speed stirring in the dark for 90 minutes to establish adsorption/equilibrium between the catalyst and the solution. The final mixture requires high speed stirring due to hydrophobic surface of the CdS MSs photocatalyst. After 90 minutes, CdS MSs were suspended properly under stirring in aqueous medium. Afterwards, the mixture was exposed to the irradiation of 300 W xenon lamp for photocatalytic degradation of dye under high speed stirring. The samples were collected at different time intervals and preserved. The hydrophobic nature of CdS MSs helps to separate them easily from the solutions. The

degradation of RhB was evaluated from the absorption spectrum of retrieved samples upon separation of the CdS MSs.

9.3 Results and discussion

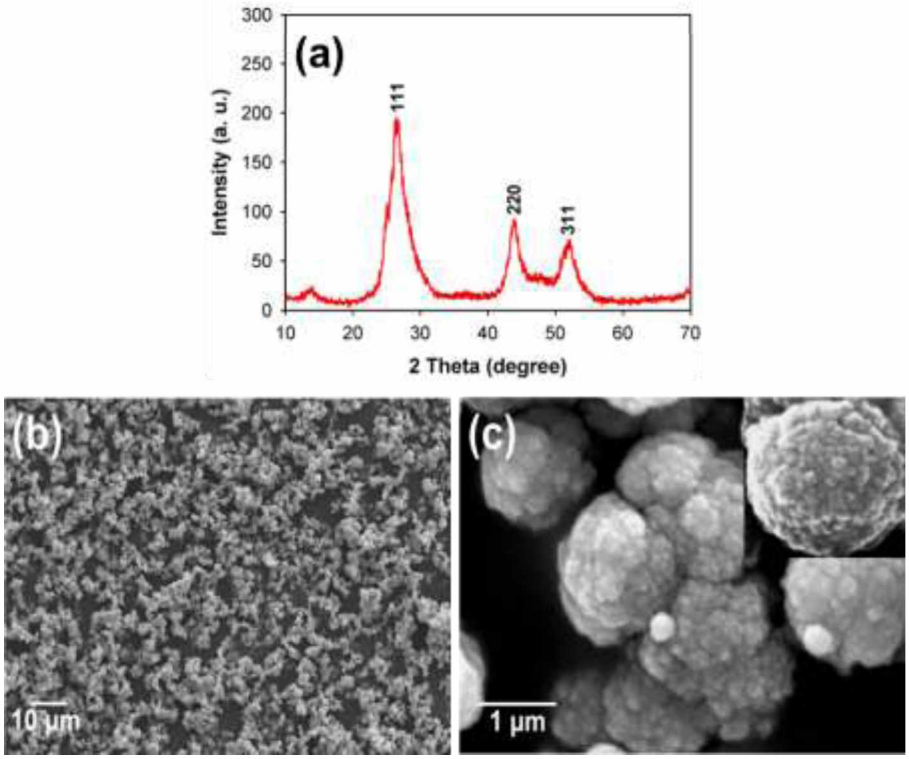

Figure 9.1 Powder XRD pattern (a) and SEM micrographs (b & c) of the CdS MSs.

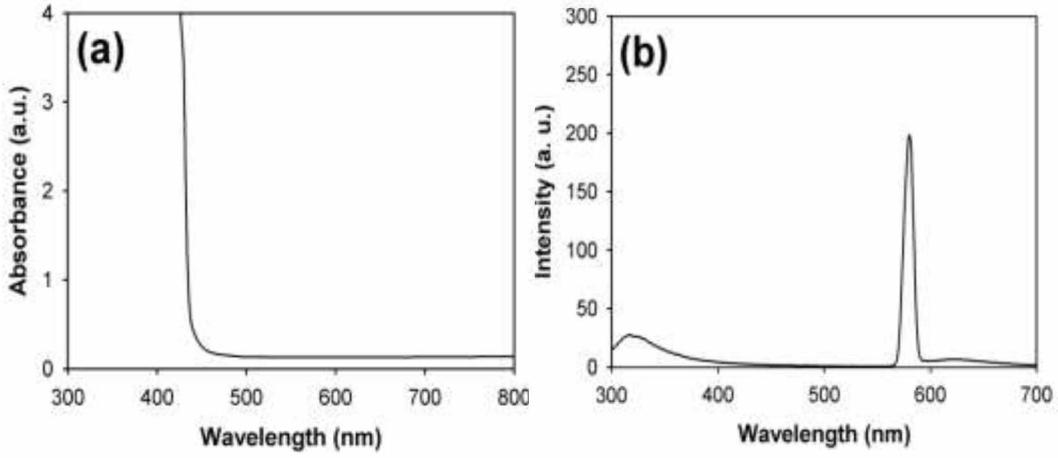

Figure 9.2 UV-vis (a) and PL (b) spectra of the CdS MSs.

The XRD pattern of CdS MSs is shown in **Figure 9.1(a)**. All of the diffraction peaks can be readily indexed to a cubic CdS. No characteristic peaks of other impurities are observed in this pattern, indicating the high purity of the as-synthesized product. On the other hand, the broad peaks in XRD pattern indicate that the building blocks of CdS MSs are nanocrystalline with small crystallite size. **Figure 9.1(b & c)** shows typical SEM micrographs of as-synthesized CdS MSs. It is clearly seen that CdS MSs exhibit cauliflower-like shape composed of small NCs with an average size of 1.5 μm.

Figure 9.2 shows the UV-vis absorption and PL spectra of CdS MSs. The UV-vis absorption spectrum **(Figure 9.2(a))** shows that CdS MSs absorb in visible region and showing sharp absorption age at 450 nm. The as-prepared CdS MSs exhibit strong green emissions at 580 nm upon excitation at 290 nm **(Figure 9.2(b))**. It also shows a weak shoulder peak at around 625 nm assigned to a shallow-trap emission. The difference in absorption and emission value is probably due to the difference in the stoichiometric ratio of Cd/S.[16]

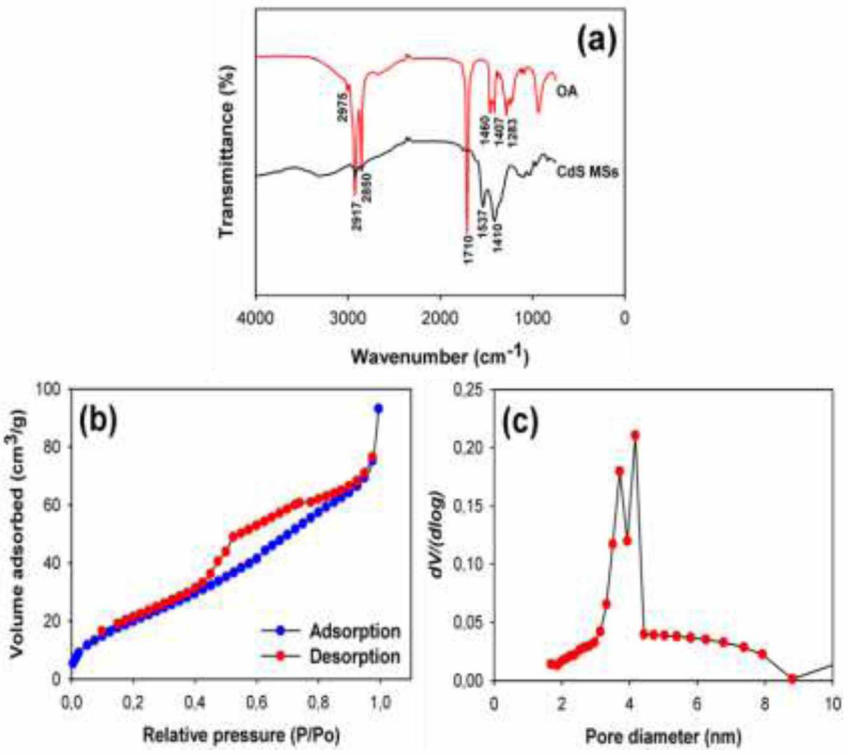

Figure 9.3 FTIR spectra (a) of the OA and CdS MSs. N_2 adsorption/desorption isotherm (b) and corresponding BJH pore size distribution curve (c) of the CdS MSs.

Figure 9.3(a) shows FTIR spectra of OA and as-synthesized CdS MSs. The FTIR spectrum of OA shows two vibration bands at 2917 and 2850 cm^{-1}, respectively attributed to the CH_2 asymmetric and symmetric stretching. The band at 2975 cm^{-1} is assigned to the stretching vibration of C-H. For the OA, the intense peak at 1710 cm^{-1} is due to the existence of the C=O stretching and the band at 1240 cm^{-1} is an indication of the presence of C-O stretching. Two bands at 1460 and 936 cm^{-1} are due to the in-plane and out-of-plane bandings of O-H. Compared to the FTIR spectrum of pure OA, FTIR spectrum of CdS MSs don't show any peak at 1710 cm^{-1}. This indicates that no free OA is present in the sample. However, two new peaks appear at 1537 and 1410 cm^{-1} in the FTIR spectrum of CdS MSs, which are characteristic of $\nu_{asymmetric}$ (COO^-) and $\nu_{symmetric}$ (COO^-) stretching.[17] The existence of these two new peaks reveals that the OA is chemisorbed as carboxylate onto the surface of CdS MSs. To examine the specific surface area and pore size distribution of CdS MSs, N_2 adsorption-desorption isotherm measurements were performed. According to **Figure 9.3(b)**, CdS MSs exhibit type IV adsorption isotherm with hysteresis loop ranges P/P_o = 0.4-0.9, which is the typical characteristic of mesoporous materials.[18] The corresponding specific surface area is 30m^2/g. As shown in **Figure 9.3(c)**, the pore size distribution is 3.8 to 4.2 nm, which agrees well with SEM characterization.

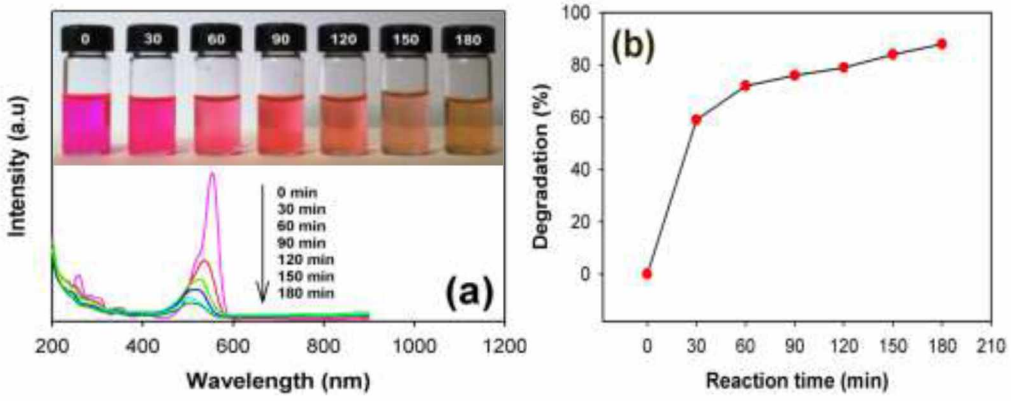

Figure 9.4 Original degradation spectra (a) and % photodegradation (b) of RhB in the presence of as-synthesized CdS MSs.

In order to investigate the photocatalytic activity of CdS MSs, the photodegradation of RhB as a function of irradiation time was studied **(Figure 9.4(a))**. It is clear that CdS MSs exhibit a pronounced photocatalytic activity towards photodegradation and degrade around 90% of

RhB in aqueous medium after 180 min **(Figure 9.4(b))**. The concentration of dye decreased as the irradiation time was increased (see inset of **Figure 9.4(a)**). The photocatalytic activity of the CdS MSs is slower compared to previously reported CdS photocatalysts.[8,9,11] It is well known that photocatalysis is a surface reaction and photodegradation rate is depends on the amount of dye absorb on the surface of photocatalyst. The surface of oleic acid-stabilized CdS MSs is hydrophobic in nature, which reduces the absorption of RhB on the surface of CdS MSs in aqueous medium and results in slow photodegradation rate.

The decolorization of dye (RhB) in aqueous suspension is initiated by the photoexcitation of the CdS nanostructure, followed by the generation of electron-electron hole pair on the surface of the CdS nanostructure (**Eq. (9-1)**).

$$\text{CdS nanostructure} + h\nu \rightarrow \text{CdS}(e_{cb}^{-} + h_{vb}^{+}) \qquad \textbf{(9-1)}$$

The high oxidative potential of the hole on the CdS nanostructure surface allows the direct oxidation of the dye to reactive intermediates (**Eq. (9-2)**).

$$h_{vb}^{+} + \text{Dye} \rightarrow \text{Dye}^{*+} \rightarrow \text{oxidation of dye molecule} \qquad \textbf{(9-2)}$$

Another possibility is hydroxyl radical, which may have contributed in the photodegradation reaction (**Eq. (9-3)**). The hydroxyl radical may generated by the decomposition of water molecule (**Eq. (9-4)**) or by the reaction of the hole with hydroxyl ion (**Eq. (9-5)**). The hydroxyl radical is non-selective and strong oxidant which leads to the oxidation of several organic chemicals.

$$\text{OH}^{*} + \text{Dye} \rightarrow \text{Dye}^{*+} \rightarrow \text{oxidation of dye molecule} \qquad \textbf{(9-3)}$$

$$h_{vb}^{+} + \text{H}_2\text{O} \rightarrow \text{H}^{+} + \text{OH}^{*} \qquad \textbf{(9-4)}$$

$$h_{vb}^{+} + \text{OH}^{-} \rightarrow \text{OH}^{*} \qquad \textbf{(9-5)}$$

9.4 Conclusions

In summary, NCs composed cauliflower-like mesoporous CdS MSs were synthesized

successfully through sulphurization of Cd-O complex. The as-synthesized CdS MSs has good physicochemical properties with pronounced photocatalytic ability to degrade organic pollutants in the waste water under visible light irradiation. Finally, this synthetic strategy can also be useful to synthesize other metal sulphide nanostructures for different applications.

Acknowledgement

The authors would like to thank the Natural Sciences and Engineering Research Council of Canada (NSERC) for financial support of this work.

9.5 References

1. K. Sato, Y. Tachibana, S. Hattori, T. Chiba, S. Kuwabata, *Journal of Colloid Interface Science* 324 **(2008)** 257-260.
2. H. Pan, C.K. Poh, Y.W. Zhu, G.C. Xing, K.C. Chin, Y.P. Feng, J.Y. Lin, C.H. Sow, W. Ji, A.T.S. Wee, *Journal of Physical Chemistry C* 112 **(2008)** 11227-11230.
3. Y.F. Lin, J.H. Song, Y. Ding, S.Y. Lu, Z.L. Wang, *Advanced Materials* 20 **(2008)** 3127-3130.
4. G.Z. Shen, J.H. Cho, J.K. Yoo, G.C. Yi, C.J. Lee, *Journal of Physical Chemistry B* 109 **(2005)** 9294-9298.
5. H.C Leventis, S.P. King, A. Sudlow, M.S. Hill, K.C. Molloy, S.A. Haque, *Nano Letters* 10 **(2010)** 1253-1258.
6. X. Di, S.K. Kansal, W. Deng, *Separation and Purification Technology* 68 **(2009)** 61-64.
7. S. Rengaraj, S.H. Jee, S. Venkataraj, Y. Kim, S. Vijayalakshmi, E. Repo, A. Koistinen, M.J. Sillanpaa, *Journal of Nanoscience and Nanotechnology* 11 **(2011)** 2090-2099.
8. Y. Guo, J. Wang, L. Yang, J. Zhang, K. Jiang, W. Li, L. Wang, L. Jiang, *CrystEngComm* 13 **(2011)** 5045-5048.
9. Y. Guo, J. Wang, Z. Tao, F. Dong, K. Wang, X. Ma, P. Yang, P. Hu, Y. Xu, L. Yang, *CrystEngComm* 14 **(2012)** 1185-1188.
10. Z. Yu, X. Wu, J. Wang, W. Jia , G. Zhub, F. Qu, *Dalton Transactions*, 42 **(2013)** 4633-4638.
11. Y. Guo, L. Wang, L. Yang, J. Zhang, L. Jiang, X. Ma, *Materials Letters* 65 **(2011)** 486-489.

12. M. Mrowetz, E. Selli, *Journal of Photochemistry and Photobiology A: Chemistry* 180 **(2006)** 15-22.
13. R. Comparelli, E. Fanizza, M.L. Curri, P.D. Cozzoli, G. Mascolo, A. Agostiano, *Applied Catalysis B* 60 **(2005)** 1-11.
14. R. Wahab, I.H. Hwang, Y.S. Kim, H-S.Shin, *Chemical Engineering Journal* 168 **(2011)** 359-366.
15. G. Xi, C. Wang, X. Wang, *European Journal of Inorganic Chemistry* **(2008)** 425-431.
16. S. Mahanty, D. Basak, F. Rueda, M. Leon, *Journal of Electronic Materials* 28 **(1999)** 559-562.
17. J.D. Patel, F. Mighri, A. Ajji, *Materials Research Bullatin* 47 **(2012)** 2016-2021.
18. S. Lowell, J.E. Shields, M.A. Thomas, *Characterization of Porous Solids and Powders: Surface Area, Pore Size and Density*, Kluwer Academic Publisher: Dordrecht, The Netherlands **(2004)**.

Chapter 10: Development of CdS nanostructures by thermal decomposition of aminocaproic acid-mixed Cd-thiourea complex precursor: Structural, optical and photocatalytic characterization.

Jayesh D. Patel[1], Frej Mighri[1,*], Abdellah Ajji[2] and Tapas K. Chaudhuri[3]

[1]CREPEC, Chemical Engineering Department, Laval University, Quebec, QC, G1K 7P4 Canada.

[2]CREPEC, Chemical Engineering Department, Ecole Polytechnique de Montréal, C.P. 6079, Succ. Centre- Ville, Montreal, QC, H3C 3A7 Canada.

[3]Dr. K.C. Patel Research and Development Centre, Charotar University of Science and Technology (CHARUSAT), Changa, Tal.-Petlad, Anand District, Gujarat 388421, India.

In press, ***Journal of Nanoscience and Nanotechnology*** (2014)

Résumé

Le présent travail porte sur deux nanostructures de CdS différentes produites via les décompositions solvothermale et hydrothermale du précurseur du complexe Cd-thiourée mélangé à l'acide aminocaproïque (ACA) à 175 °C. Les deux nanostructures ont été largement caractérisées pour leurs propriétés structurale, morphologique et optique. La caractérisation par diffraction des rayons X a révélé que les deux nanostructures de CdS présentent une morphologie 'wurtzite'. La caractérisation par microscopie à balayage électronique et par spectroscopie aux rayons X a révélé que la décomposition hydrothermale produit des CdS sous forme de fleurs bien formées, composées de pétales à six dendrites et que la décomposition solvothermale produit des microsphères de CdS avec une composition à stœchiométrie chimique très semblable. L'absorption dans l'UV-vis et le spectre de photoluminescence des fleurs dendritiques de CdS et des nanostructures microsphèriques ont montré que les deux nanostructures présentent une grande absorption entre 200 et 700 nm et exhibent de fortes émissions du vert à 576 et à 520 nm sous des excitations à 290 et 260 nm, respectivement. Les caractérisations par microscopie électronique à transmission (TEM) et par Brunauer-Emmett-Teller (BET) ont confirmé que les microsphères de CdS étaient mésoporeuses et étaient composées de petits nanocristaux. Un mécanisme de croissance possible dans la formation des nanostructures de CdS a été proposé en se basant sur l'évolution de la morphologie en fonction du temps de la réaction. De plus, il s'est avéré que les nanostructures de CdS ainsi synthétisées ont des activités photocatalytiques très efficaces pour la dégradation des teintures à base d'orange méthylique (MeO) et de rhodamine B (RhB).

Abstract

The present work deals with two different CdS nanostructures produced via hydrothermal and solvothermal decompositions of aminocaproic acid (ACA)-mixed Cd-thiourea complex precursor at 175°C. Both nanostructures were extensively characterized for their structural, morphological and optical properties. The powder X-ray diffraction characterization showed that the two CdS nanostructures present a wurtzite morphology. Scanning electron microscopy and energy-dispersive X-ray characterizations revealed that the hydrothermal decomposition produced well-shaped CdS flowers composed of six dendritic petals, and the solvothermal decomposition produced CdS microspheres with close stoichiometric chemical composition. The UV-vis absorption and photoluminescence spectra of CdS dendritic flowers and microsphere nanostructures showed that both nanostructures present a broad absorption between 200 and 700 nm and exhibit strong green emissions at 576 and 520 nm upon excitations at 290 nm and 260 nm, respectively. The transmission electron microscopy (TEM) and Brunauer-Emmett-Teller (BET) characterizations confirmed that CdS microspheres were mesoporous and were composed of small nanocrystals. A possible growth mechanism in the formation of the CdS nanostructures was proposed based on morphology evolution as a function of the reaction time. Furthermore, the as-synthesized CdS nanostructures were found to exhibit highly efficient photocatalytic activities for the degradation of methyl orange (MeO) and rhodamine B (RhB) dyes.

10.1 Introduction

Recently, amino acid-assisted chemical route has become highly promising due to its novelty and its environmentally friendly character for a large variety of nanomaterials. Amino acids have unique structures with strong coordinating groups, such as amine, carboxyl, hydroxide and thiol groups. They also have the ability to control the morphology of nanomaterials.[1] On the other way, semiconductor photocatalysis is a potentially promising approach to solve environmental issues.[2] In this approach, photocatalysts use solar energy to decompose pollutants from the air and aqueous medium.[3-5] These photocatalyst generate reactive hydroxyl radicals, which oxidize the toxic organic pollutants and break them into smaller fragments.[6,7] However, the high oxidative capacity and stability are the important criteria for the semiconductor to get selected as an efficient photocatalyst.[7,8] Anatase titanium dioxide (TiO_2) is the most studied photocatalyst due to its low cost, high stability and biocompatibility.[9] However, TiO_2 responds to UV light only and its wide band gap limits its practical application as photocatalyst. Therefore, an interesting task is to find an efficient photocatalyst that can effectively degrade organic pollutants under visible light irradiation. Metal oxides, like CdS sensitized TiO_2, doped ZnO, MgO, Fe_2O_3, or $SrTiO_3$ and metal sulphides, like ZnS, In_2S_3 or SnS_2 are also used as a photocatalysts to degrade organic pollutants from the waste water.[10-17]

As an important II-VI semiconductor, CdS with its large direct band gap energy of 2.4 eV at room temperature has gained much attention due to its unique properties and its potential applications from electronics to targeted drug delivery.[18] Recently, a verity of studies have been devoted to synthesize CdS nanomaterials with controlled size and various architectures for photocatalytic applications, such as flower-like shape,[19] microspheres,[20,21] flower-like 3D assemblies,[22] lotus flower-like microflowers,[23] nanowhiskers,[24] nanospheres,[25] quantum dots and nanoparticles.[26-31] Various amino acids were used to synthesize nanoscale CdS materials used as photocatalysts to degrade organic pollutants from the waste water.[26-28] Among these amino acids, aminocaproic acid (ACA) was used to produce size and shape controlled oxides with organized self-assembled nanostructures.[32] Our group has recently reported a simple solvothermal route for the synthesis of star-shaped PbS crystals with high yield using ACA-mixed methanolic lead-thiourea (Pb-TU) complex precursor.[33] This has motivated us to

extend our work by studying the decomposition of ACA-mixed cadmium-thiourea (Cd-TU) complex precursor via two different thermal routes. To the best of our knowledge, there is no literature report on the two CdS nanostructures presented in this work, which were synthesized from the single complex precursor via two different thermal decomposition routes. As will be presented later, we were able to develop via the hydrothermal decomposition of ACA-mixed Cd-TU complex precursor six petal CdS dendritic flowers, which were entirely different from the previously reported flower-like CdS shapes.[19, 22, 23, 34] Furthermore, the solvothermal decomposition of ACA-mixed Cd-TU complex precursor produced nanocrystals (NCs) composed CdS microspheres, which were quite similar in shape to our recently reported microspheres.[21] A series of time dependent experiments were performed to identify the growth mechanisms of both CdS nanostructures, which were extensively characterized for their structural, morphological and optical properties. Furthermore, the as-synthesized CdS nanostructures were found to exhibit highly efficient and fast photocatalytic activities for the degradation of MeO and RhB in aqueous medium.

10.2 Experimental Section

10.2.1 Materials and synthesis

All chemicals were used as received without further purification. Cadmium acetate dihydrate ($Cd(CH_3COO)_2 \cdot 2H_2O$ or $Cd(AC)_2 \cdot 2H_2O$, ≥98.0%), thiourea ($CS(NH_2)_2$ or TU, 99.0%), aminocaproic acid ($HOOCC_5H_{10}NH_2$, ACA, 70%), methyl orange and rhodamine B were purchased from Sigma-Aldrich. Methanol and ethanol were purchased from Fisher chemicals, Canada.

Aqueous and methanolic Cd-TU complex solutions were prepared as follows: first, $Cd(CH_3COO)_2 \cdot 2H_2O$ (0.05 mmol, 1,33 g) and TU (0.05 mmol, 0.380 g) were dissolved one by one in 100 mL of distilled water and 100 mL of methanol to obtain clear aqueous and methanolic Cd-TU complex solutions. Further, ACA (0.1 mmol, 1.31 g) was added to these solutions under magnetic stirring at room temperature to obtain final clear precursor solutions. After 1 h of stirring, these precursor solutions were transferred to Teflon lined stainless steel autoclaves (capacity of 125 mL). The aqueous and methanolic precursors were respectively treated at 175 °C for 40 h and 10 h then naturally cooled to room temperature.

The obtained products were filtered out, washed several times by hot distilled water and ethanol, and dried at 50 °C for 1 h.

10.2.2 Characterization

Powder X-ray diffraction (XRD) data of the CdS nanostructures were recorded on a Siemens D5000 X-ray diffractometer, using Cu-Kα radiation (λ = 1.54059 Å). Scanning electron microscopy (SEM) images and energy-dispersive X-ray (EDX) analysis were recorded with a JEOL, JSM-840a and JEOL JSM-6360/LV scanning electron microscopes. Transmission electron microscopy (TEM) images of the solvothermally synthesized CdS nanostructure were recorded at 120 kV with JEOL JEM 1230 electron microscope. The UV-visible absorption spectra were recorded on Varian Cary 500 Scan UV-Vis spectrophotometer. The energy band gaps (Eg) of the nanostructures were determined from the following Tauc relation:

$$(\alpha h\nu)^2 \sim h\nu - Eg$$

Photoluminescence (PL) spectra were measured at room temperature using Varian Cary Eclipse Fluorescence Spectrophotometer. Infrared spectra (IR) of ACA and CdS nanostructures were obtained using a Nicolet (Thermo Fisher) Model 380 FTIR with an attenuated total reflectance (ATR) sampling device (model Smart Performer) with a ZnSe crystal. The IR spectra were collected within the range of 650 to 4000 cm^{-1} with 10 scans per spectrum. The specific surface area of the solvothermally synthesized CdS nanostructure was calculated from the linear part of the Brunauer–Emmett–Teller equation (P/P0 ≈ 0.05–0.2). The pore diameter distribution was obtained from analysis of the desorption branch of the isotherms using the Barrett–Joyner–Halenda model.

10.2.3 Photocatalytic activity measurement

For photocatalytic activity evaluation, 50 mg of CdS nanostructures were suspended in 24 mL distill water individually. Further, 6 mL of freshly prepared MeO or RhB aqueous solution (100ppm) added in the suspension and stirred in the dark for 1 h to establish an adsorption/desorption equilibrium. Afterwards, the suspension was exposed to the irradiation of 300 W xenon lamp for photocatalytic degradation of dyes under stirring. The samples were

collected at different time intervals and preserved. The degradation of MeO and RhB were evaluated by centrifuging the retrieved samples and recording the intensities of absorption peaks of MeO (463 nm) and RhB (554 nm) relative to their initial intensities.

10.3 Results and Discussion

10.3.1 Structure and morphology characterization

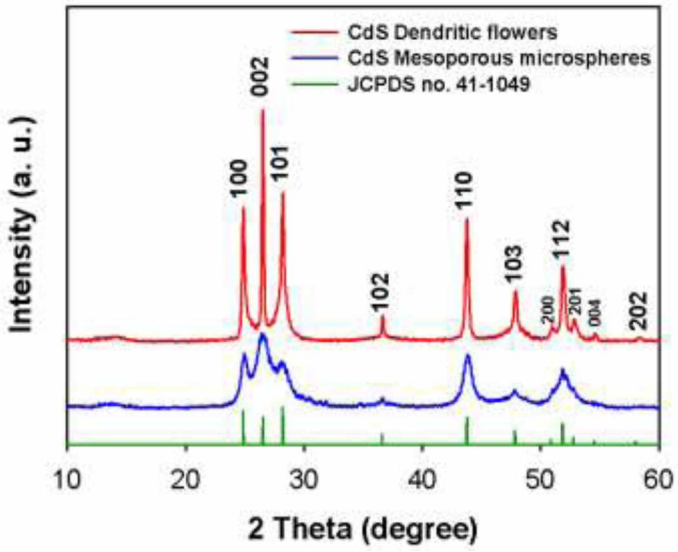

Figure 10.1 Powder XRD patterns of the hydrothermally and solvothermally developed CdS dendritic flower and mesoporous microsphere nanostructures.

The XRD patterns of both CdS nanostructures are shown in **Figure 10.1**. All of the diffraction peaks can be readily indexed to a hexagonal wurtzite-structured CdS. No characteristic peaks of other impurities are observed in these patterns, indicating the high purity of the synthesized products. The sharp and intense diffraction peaks of the hydrothermally synthesized CdS nanostructure is a good indication of its high crystallinity, the strong (002) diffraction peak is supposed to be due to the growth of wurtzite-structured CdS along the [001] direction.[35] On the other hand, the weak and broad peaks of the solvothermally synthesized CdS nanostructure is an indication of its low crystallinity and small crystallite size.

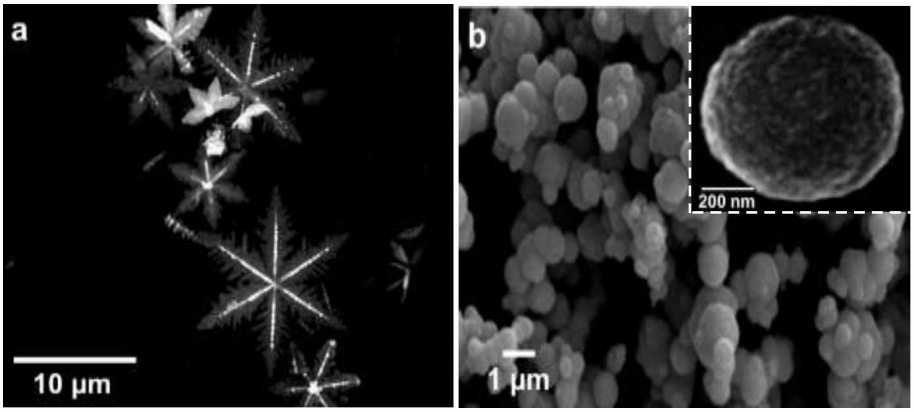

Figure 10.2 SEM images of synthesized CdS dendritic flower (a) and mesoporous microsphere (b) nanostructures.

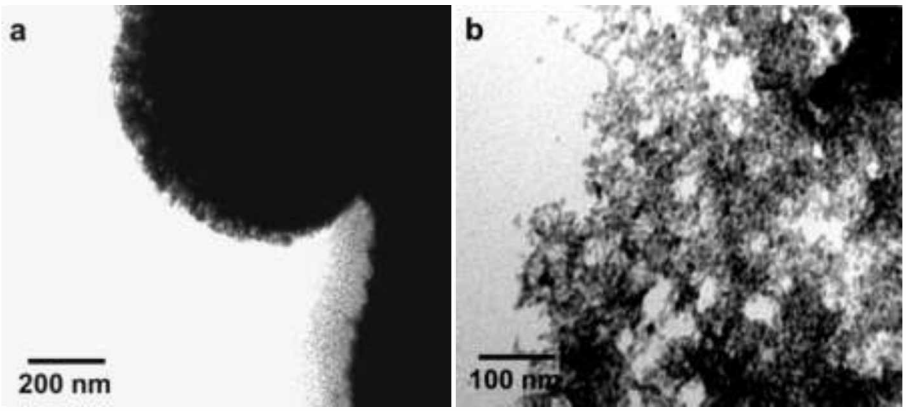

Figure 10.3 TEM images taken on the surface (a) and after ultrasonic treatment of CdS mesoporous microspheres (b).

Figure 10.2 shows typical SEM micrographs of both CdS nanostructures prepared by hydrothermal and solvothermal decomposition routes. It is clearly seen that the hydrothermally synthesized CdS nanostructure exhibits flower-like architecture composed by six dendritic petals with sizes varying between 7 to 12 μm (image a). As shown in image b, the solvothermal decomposition of ACA-mixed Cd-TU complex precursor produced microspheres with diameters varying between 0.5 and 1.5 μm. The high magnification SEM image (inset of image b) reveals that CdS microspheres are composed of small NCs. The TEM image shown **Figure 10.3** (a) was taken on the surface of microsphere. It also shows a

self-assembly of NCs in the form of a porous network, which is in good agreement with the SEM observation. To have an idea about the structure inside microspheres, the latter were cracked by ultrasonic treatment in a water bath for 1 h. As seen in **Figure 10.3** (b), their inner structure is composed of small blocks of NCs.

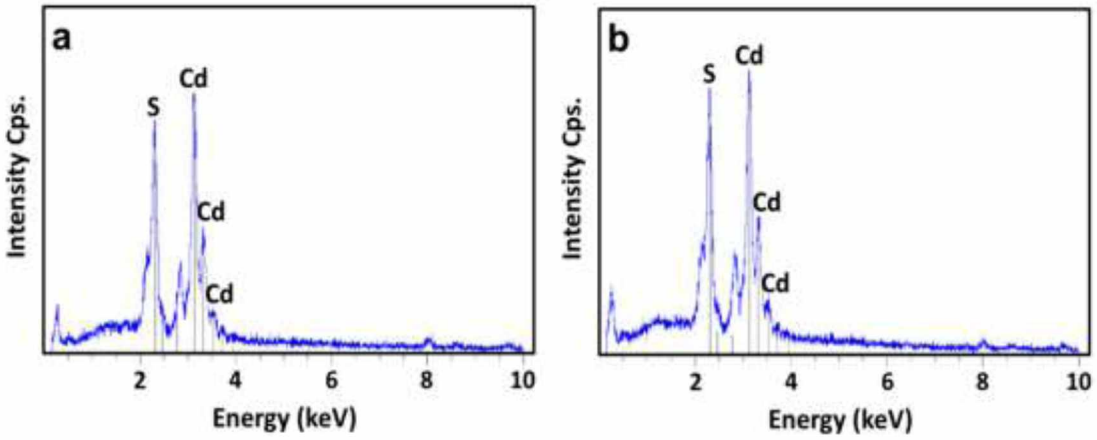

Figure 10.4 EDX spectra of CdS dendritic flower (a) and mesoporous microsphere (b) nanostructures.

Elemental analysis of both CdS dendritic flower and microsphere nanostructures was performed by EDX (**Figure 10.4**). The EDX analysis confirmed that there are no elements, other than Cd and S, were present in both samples. EDX spectra of both samples display cadmium Lα1 (3.16 keV), Lβ1 (3.37 keV) and Lβ2 (3.56 keV) peaks and sulphur Kα1 (2.30 keV) peak. The other peaks corresponding to C, Au and Pd are due to the stud and sample metallization before SEM examination. EDX analysis of CdS dendritic flower and microsphere nanostructures suggest that the stoichiometry of Cd/S is approximately 1.27 and 1.08, respectively. The stoichiometry values for both synthesized nanostructures are near the standard stoichiometry of bulk CdS, suggesting that they both have a closely stoichiometric composition.

10.3.2 Growth mechanism

To investigate the growth mechanism of both CdS nanostructures, time dependent hydrothermal and solvothermal treatments were performed and the corresponding CdS nanostructures were collected and characterized by SEM at different stages.

Hydrothermal reaction

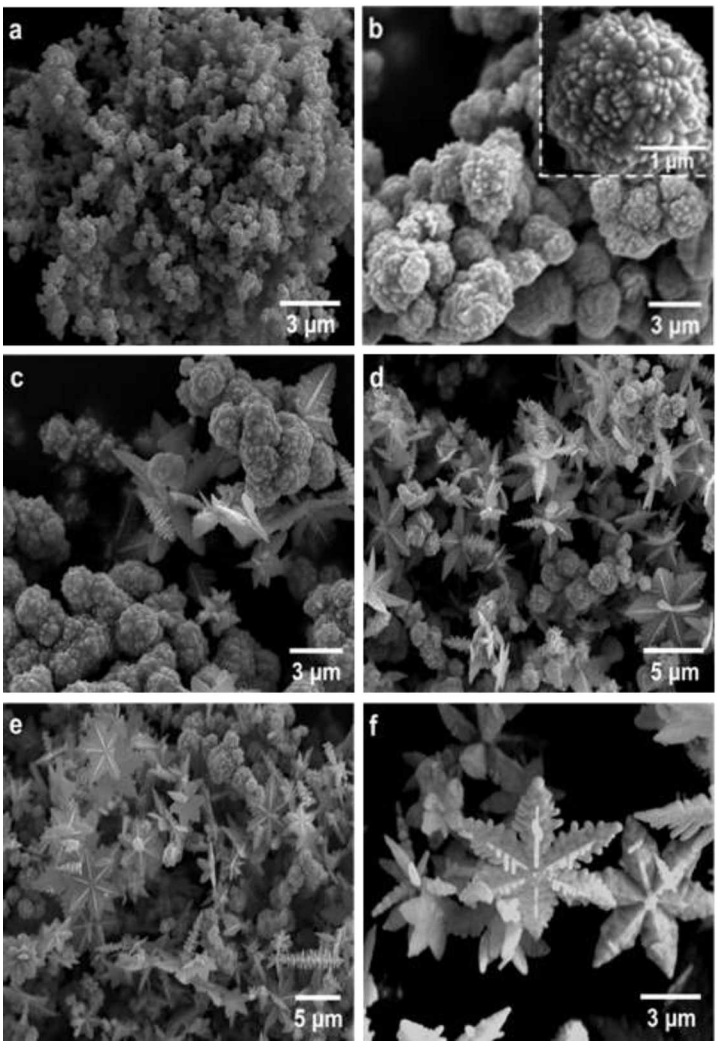

Figure 10.5 The evolution of CdS dendritic flower morphology at different hydrothermal reaction times. (a) 0.5 h (b) 3 h, (c) 10 h, (d) 20 h, (e) 30 h and (f) 40 h.

After 0.5 h of hydrothermal treatment, irregular CdS nanospheres were obtained, as shown in **Figure 10.5** (image a). Further growth of these nanospheres produced lotus-like

microflowers after 3 h (image b). A similar type of lotus flower-like CdS microflowers was synthesized by Sahoo et al.[23] via solvothermal decomposition of morpholine-4-carbdithioate complex of Cd at 180°C. After 10 h of hydrothermal treatment, lotus flower-like superstructure slowly started then rapidly converted to dendritic flower-like nanostructure (image c). As shown in images d and e, the conversion rate of the flower-like superstructure to six petal dendritic flowers increased with increasing the reaction time from 20 to 30 h. Finally, after 40 h, the flower-like CdS superstructures were fully converted to well-shaped dendritic flowers, as shown in image f.

Solvothermal reaction

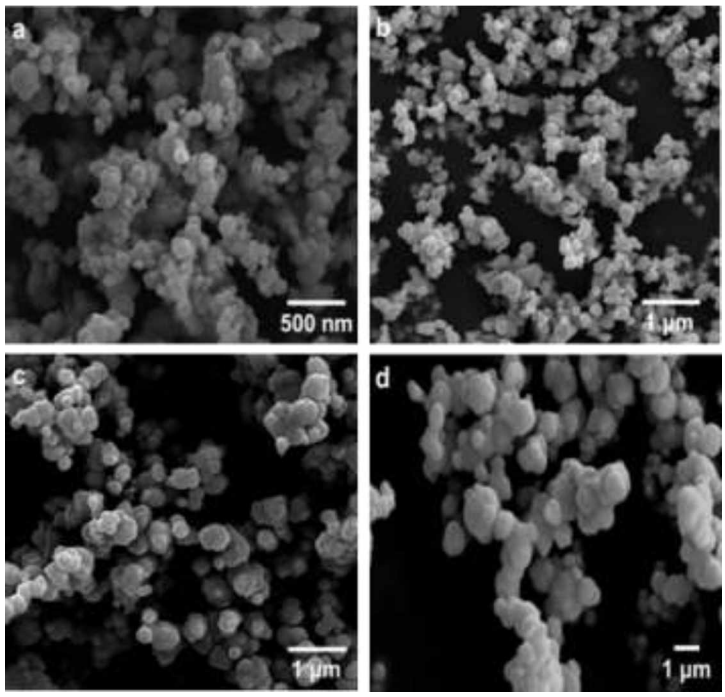

Figure 10.6 The evolution of CdS mesoporous microsphere morphology at different solvothermal reaction times. (a) 0.5 h, (b) 3 h, (c) 6 h, and (d) 10 h.

After 0.5 h of solvothermal treatment, NCs composed irregular CdS nanospheres of 50 to 100 nm in diameter were obtained, as shown in **Figure 10.6** (image a). With increasing the reaction time, the size of CdS nanospheres increased from nanometer to micrometer range, as shown in images b and c of **Figure 10.6**. After 10 h, the average size of CdS microspheres

was around 1.5 μm (image d) and no further significant change was observed with increasing the reaction time over 10 h.

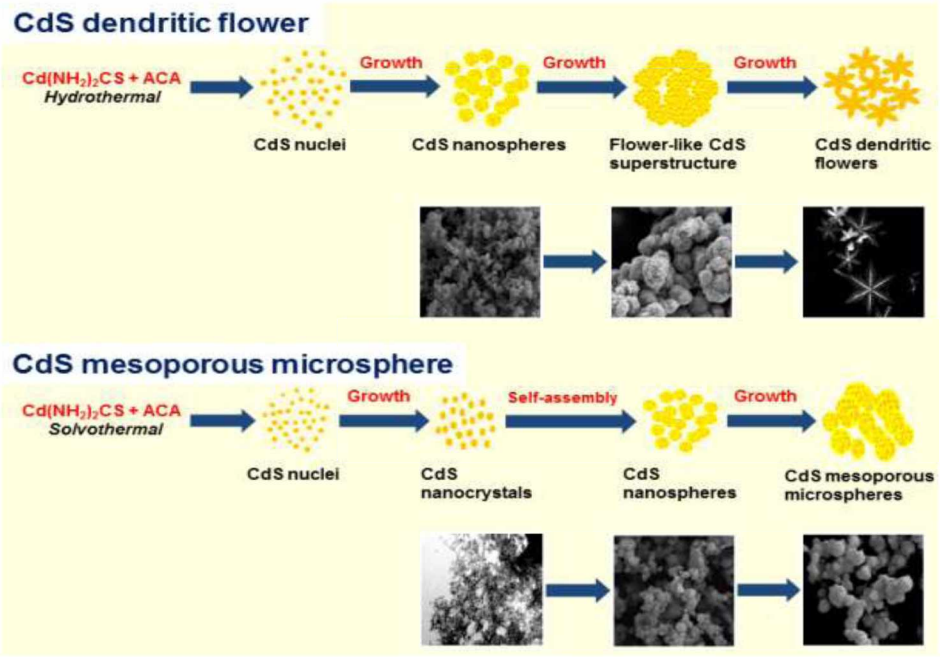

Scheme 10.1 Possible growth mechanisms for the production of CdS nanostructures.

Based on both time dependent hydrothermal and solvothermal reactions, the possible reaction mechanisms are schematically illustrated in **Scheme 10.1**. By mixing aqueous or methanolic solutions of $Cd(AC)_2 \cdot 2H_2O$ and TU at room temperature, a stable Cd-TU complex is produced. TU may act not only as the coordinate agent or sulphur source, but also as a soft template for arranging CdS nucleus to form a dendritic nanostructure.[36] In Cd-TU complex, TU coordinated to Cd through the S atom, and forming tetrahedral or destroyed tetrahedral coordination in the structure of $Cd(SC(NH_2)_2)_2(CH_3COO)_2$ complex.[37] Thermal decomposition of Cd-TU complex leads to the formation of CdS nanoparticles or nanostructures through the following reaction[38];

$$Cd(SC(NH_2)_2)_2(CH_3COO)_2 \xrightarrow{\Delta} CdS + NH_3 + HCNS + CH_3COCH_3 + CH_2CO \quad \textbf{(10-1)}$$

In hydrothermal reaction, at certain temperature and reaction time, the tetrahedral Cd-TU complex becomes weaker and slowly releases Cd^{+2}. On the other hand, C=S bonds of

thiourea are attracted by the nucleophilic oxygen atoms of water molecules, leading to the weakening of the C=S double bonds. The latter will then be broken and S^{-2} anion will be developed slowly then reacts with Cd-TU complex to form CdS nuclei. This stage is followed by crystal growth process. The final nanostructures are then capped by the amino head groups of ACA biomolecule. The fresh CdS nuclei are thermodynamically unstable because of their high surface energy, so they prefer to aggregate together to minimize the interfacial energy leading to many agglomerates. It is known that no dendrites could form if most of the S^{-2} are consumed at the nucleation stage due to rapid releasing of S^{-2}.[36] The slow release of reaction ions, especially S^{-2}, leads to a favored growth along the [001] direction of the rod-like structure.[36] Moreover, during the growth process, the amino acid biomolecule may be selectively absorbed on certain facets of CdS seeds, therefore, the growth rate is generally faster along the *c*-axis [001] direction for the highly anisotropic wurtzite CdS structure.[34] In the present work, CdS dendrite grows along the [001] direction, and each array branch grows along the [110] direction, keeping the angle of the trunk and branches at 60°. However, the CdS nanostructure prefers to grow along the [001] direction rather than [110] direction due to its high surface energy. This makes the branch growth direction of the CdS dendrites adjusted from the onset growth direction [110] to the normal growth direction [001].[39] During the adjustment, the organic molecules that selectively adhere to a particular crystal face determine the conversion step of the branches. The adherence of ACA and its degree of interaction with Cd^{+2} decide the angle of branches to the central trunk during the adjustment procedure. Staking faults at the connection sports are formed from the short tubers rotating from the onset growth direction to the preferential *c*-axis direction gradually.[36, 39]

In the solvothermal process, the decomposition of thiourea was very fast and most of the S^{-2} ions were consumed at the nucleation stage. The initially formed Cd^{+2} and S^{-2} react and form CdS nuclei. The fresh CdS nuclei gradually crystallized and ACA molecule was simultaneously bounded to the surface atoms of CdS and formed ACA -stabilized CdS NCs. Finally, during the building of microspheres, the ACA-stabilized CdS NCs were self-assembled homogeneously to form microspheres.

10.3.3 Optical, FTIR and BET measurement

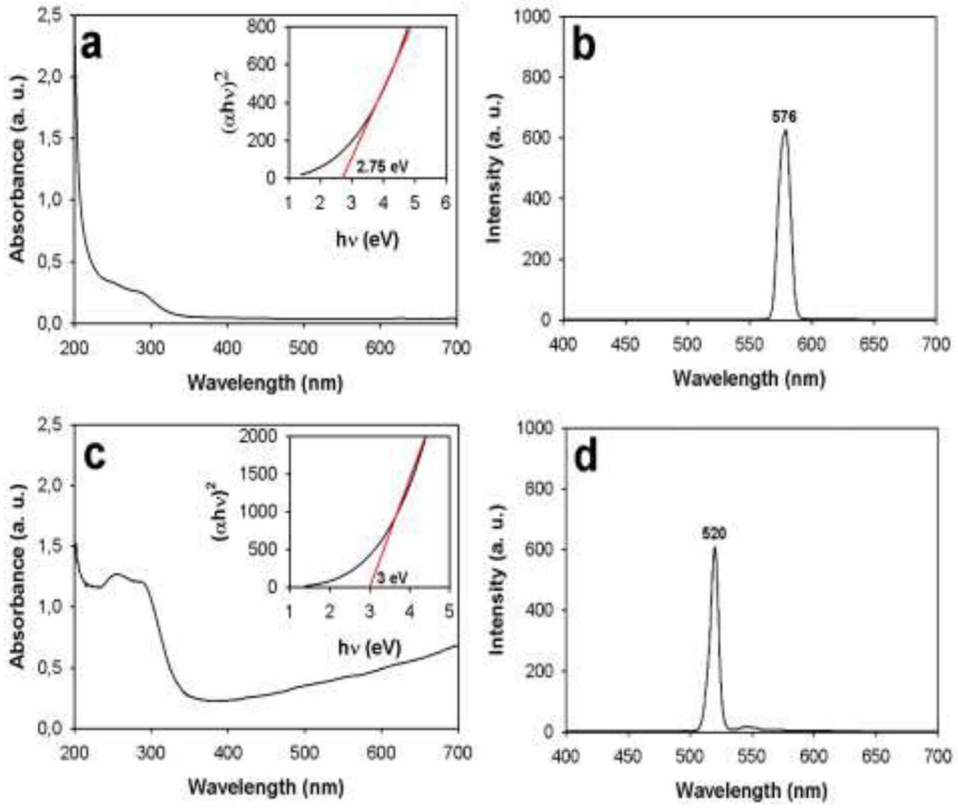

Figure 10.7 Absorption and PL spectra of CdS dendritic flower (a & b) and mesoporous microsphere (c & d) nanostructures. Insets of absorption spectra (a & c) show their respective band gap plots.

Figure 10.7 shows the UV-vis absorption and PL spectra of CdS dendritic flower and microsphere nanostructures. The UV-vis absorption spectra (**Figure 10.7a & 10.7c**) show that both nanostructures present a broad absorption between 200 to 700 nm. The fundamental absorption, which corresponds to the electron excitation from valance to conduction bands, was used to determine the nature and the value of the optical band gap using the Tauc relation. As shown in the insets of **Figure 10.7a and 10.7c**, the band gaps of CdS dendritic flower and microsphere nanostructures were around 2.75, and 3 eV, respectively. The slow increase in Tauc plots indicates that the building blocks of both nanostructures are polydispersed in size. The as-prepared CdS dendritic flower and microsphere nanostructures exhibit strong green emissions at 576 and 520 nm upon excitations at 290 nm and 260 nm, respectively (**Figure**

10.7b and 10.7d). The difference in band gap and PL emission values for both nanostructures are probably due to the difference in the stoichiometric ratio of Cd/S for both nanostructures.[40]

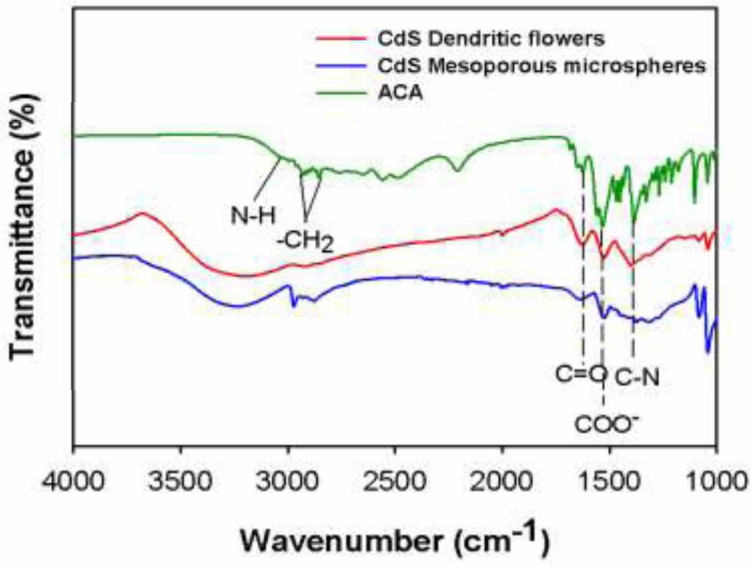

Figure 10.8 FTIR spectra of ACA and CdS nanostructures.

To investigate the interaction between ACA and CdS nanostructures, FTIR spectra of pure ACA and CdS nanostructures were measured. The corresponding results, presented in **Figure 10.8**, show bands at 2877 cm^{-1} and 2975 cm^{-1} due to C-H stretching vibrations of methylene groups of the ACA carbon chain for pure ACA and both CdS nanostructures. The two bands at 1380 cm^{-1} and 3050 cm^{-1} are respectively due to C-N and N-H stretching modes of ACA molecules. These bands also exist in the FTIR spectrum of both CdS nanostructures at around the same positions, which indicates the binding of amino ($-NH_2$) groups to the CdS surface through nitrogen lone pair. The two bands at 1530 cm^{-1} and 1545 cm^{-1} in the FTIR spectrum of ACA are attributed to the symmetric and asymmetric stretching vibrations of uncoordinated $-COO^-$ terminal groups of ACA. The spectra of both CdS nanostructures also show two bands at the same wavenumbers, which proves that only amino ($-NH_2$) groups of ACA molecules were bounded on the CdS surface and the free carboxylic (-COOH) groups were oriented outward. Finally, the broad band between 3300 cm^{-1} and 3600 cm^{-1} for both CdS nanostructures is due to the presence of adsorbed water.

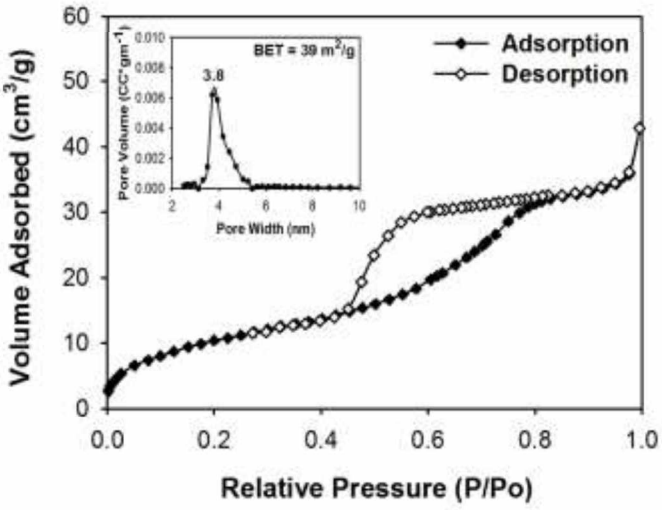

Figure 10.9 Nitrogen adsorption/desorption isotherm of CdS mesoporous microspheres. The inset presents the corresponding BJH pore size distribution curve.

To examine the specific surface area (SSA) and pore size distribution of CdS microspheres, N_2 adsorption-desorption isotherm measurements were performed and the corresponding results are shown in **Figure 10.9**. According to the IUPAC classification, the measured isotherm is considered as a type IV isotherm, which is the typical characteristic of mesoporous materials.[41] As shown by the inset of the figure, the average pore size is around 3.8 nm, which agrees well with SEM characterization. The corresponding specific surface area is 39 m^2/g indicates the high active reaction sites available for the organic dyes.

10.3.4 Photocatalytic performances

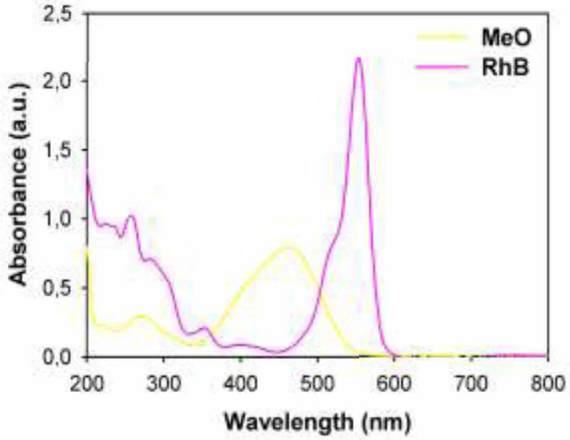

Figure 10.10 Typical blank data of MeO and RhB dyes (without photocatalysts).

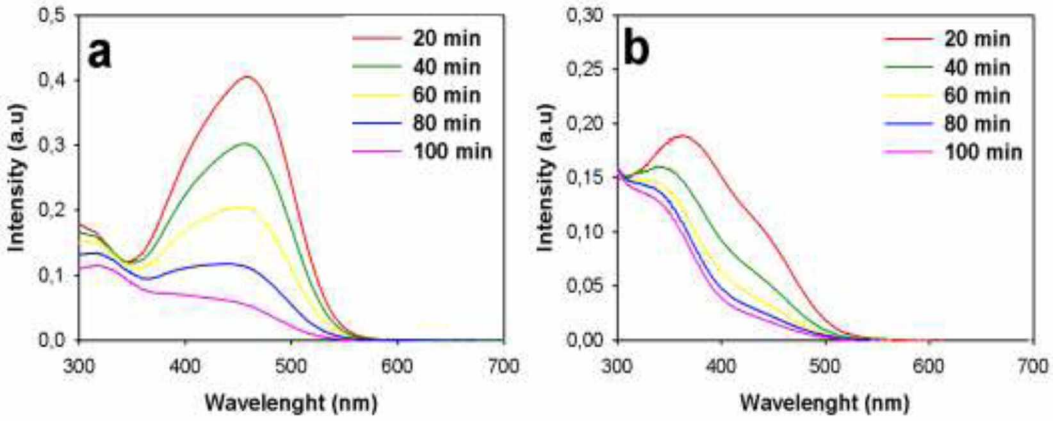

Figure 10.11 UV-visible spectra after photodegradation reactions of MeO with CdS dendritic flower (a), and mesoporous microsphere (b) nanostructures inside.

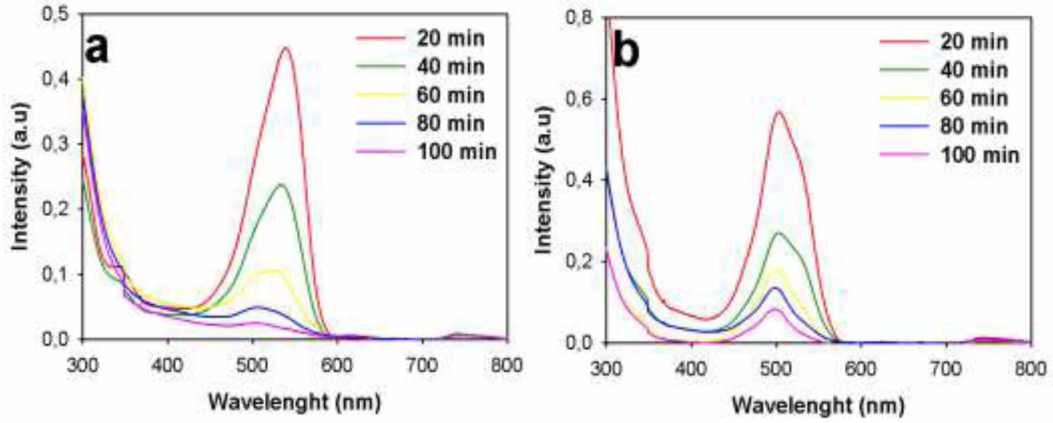

Figure 10.12 UV-visible spectra after photodegradation reactions of RhB with CdS dendritic flower (a), and mesoporous microsphere (b) nanostructures inside.

In order to investigate the photocatalytic activities of both synthesized CdS nanostructures in present of MeO and RhB dyes, the photodegradation of MeO and RhB as a function of irradiation time was studied. We have first checked the UV-visible spectroscopy on our blank dyes (**Figure 10.10**) and then the degradation spectra of photo degradation reactions (**Figure 10.11 and 10.12**). It is clear that both CdS nanostructures exhibit a pronounced and fast photocatalytic activity towards the MeO and RhB degradation. The concentration of dyes decreased as the irradiation time was increased. The efficiencies of photocatalysts at different time intervals are calculated from following formula (**Eq. (10-2)**) and plots are shown in **Figure 10.13**.

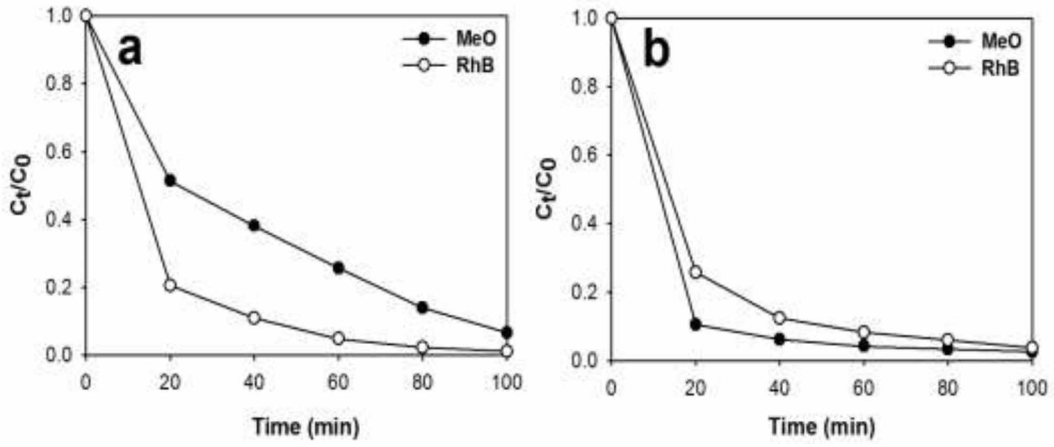

Figure 10.13 Photodegradation of MeO and RhB in presence of CdS dendritic flower (a) and mesoporous microsphere (b) nanostructures under visible light irradiation.

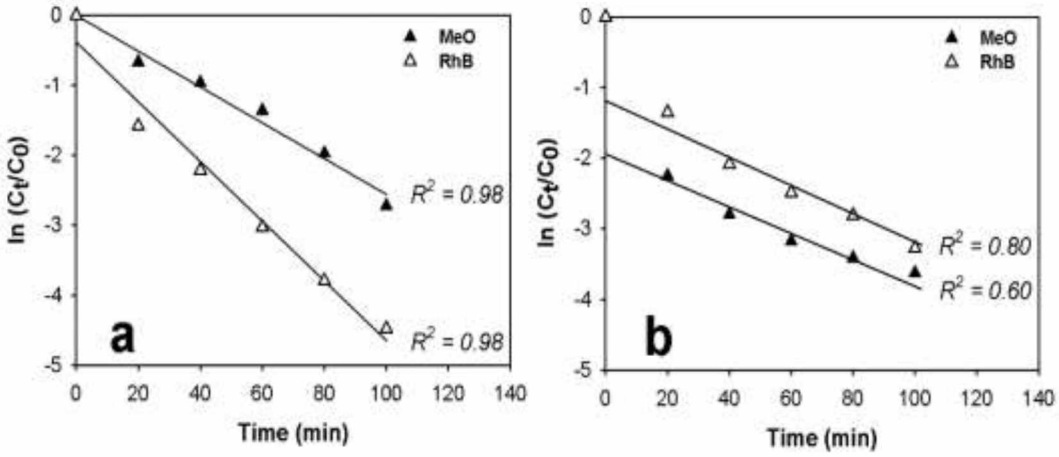

Figure 10.14 First order plots of photocatalytic degradation under visible light irradiation of MeO and RhB by CdS dendritic flower (a), and mesoporous microsphere (b) nanostructures.

Table 10.1 Photodegradation after 100 min of visible light irradiation of MeO and RhB dyes using the as-synthesized CdS dendritic flower and mesoporous microsphere nanostructures as photocatalysts.

Photocatalyst	MeO		RhB	
	Degradation	k_{app} (min^{-1})	Degradation	k_{app} (min^{-1})
CdS Dendritic flowers	93%	0.026	99%	0.043
CdS Mesoporous microspheres	97%	0.018	96%	0.012

$$\text{Degradation}(\%) = \left(C_0 - C_{final}\right)/C_0 \quad \textbf{(10-2)}$$

The photodegradation kinetic of both dyes follows the following pseudo-first-order reaction equation:

$$k_{app} = \ln\ (C_t / C_0) / t \quad \textbf{(10-3)}$$

where k_{app} (min^{-1}) is the apparent degradation rate constant, and C_0 and C_t represent respectively the initial dye concentration and the concentration measured at any time t (min) of photo irradiation. The values of k_{app} of photocatalytic reactions were calculated from the slope of the first order reaction plots presented in **Figure 10.14** and the corresponding results are summarized in **Table 10.1**, which also presents the % of MeO and RhB degradation after 100 min. As shown in the **Table 10.1**, after 100 min of photodegradation, both CdS nanostructures show better and fast photodegradation ability compared to previously reported CdS photocatalysts for MeO and RhB.[19,21,22,24-26] CdS dendritic flower and microsphere nanostructures degrade 93% and 97% of MeO, respectively. Like MeO, the degradation of RhB also takes place effectively in the presence of both CdS nanostructures, which degrade RhB up to 99% (by dendritic flowers) and 96% (by microspheres). The decolorization of both dyes (MeO and RhB) in aqueous suspensions are initiated by the photoexcitation of the CdS nanostructre, followed by the generation of electron-electron hole pair on the surface of the CdS nanostructure (**Eq. (10-4)**).

$$\text{CdS nanostructure} + h\nu \rightarrow \text{CdS}(e^-_{cb} + h^+_{vb}) \quad \textbf{(10-4)}$$

The high oxidative potential of the hole on the CdS nanostructure surface allows the direct oxidation of the dye to reactive intermediates (**Eq. (10-5)**).

$$h^+_{vb} + \text{Dye} \rightarrow \text{Dye}^{*+} \rightarrow \text{oxidation of dye molecule} \quad \textbf{(10-5)}$$

Another possibility is hydroxyl radical, which may have contributed in the photodegradation reaction (**Eq. (10-6)**). The hydroxyl radical may generated by the decomposition of water molecule (**Eq. (10-7)**) or by the reaction of the hole with hydroxyl ion (**Eq. (10-8)**). The

hydroxyl radical is non-selective and strong oxidant, which leads to the oxidation of several organic chemicals.[42]

$$OH^{*} + \text{Dye} \rightarrow \text{Dye}^{*+} \rightarrow \text{oxidation of dye molecule} \quad \textbf{(10-6)}$$

$$h_{vb}^{+} + H_2O \rightarrow H^{+} + OH^{*} \quad \textbf{(10-7)}$$

$$h_{vb}^{+} + OH^{-} \rightarrow OH^{*} \quad \textbf{(10-8)}$$

It is well known that photocatalysis is a surface reaction and depends on the active surface area available for the reaction. The as-synthesized CdS dendritic flower and microsphere nanostructures have large surface area, which may help to enhanced photodegradation rate of dyes and therefore, we can conclude that both CdS nanostructures have a good potential use as photocatalysts to treat the organic dyes in the waste water.

10.4 Conclusions

Two different CdS nanostructures were synthesized from the single complex precursor via two different thermal decomposition routes. The hydrothermal decomposition of ACA-mixed Cd-TU complex precursor produced six petal CdS dendritic flowers, while the solvothermal decomposition of the same precursor produced CdS nanocrystals composed of CdS microspheres. For both nanosctructures, useful information on crystal growth and intermediate morphology was obtained by performing a series of time dependent experiments. Both CdS nanostructures exhibited good structural, morphological and optical properties, and fast photocatalytic activities for the degradation of MeO and RhB in aqueous medium.

Acknowledgments

The authors would like to thank the Natural Sciences and Engineering Research Council of Canada (NSERC) for financial support of this work.

10.5 References

1. L, Shuzhen, X. Shenglin, B. Keyan, C. Jie, Q. Yitai, *Journal of Physical Chemistry C* 113 **(2009)** 13002-13007.
2. X.B. Chen, L. Liu, P.Y. Yu, S.S. Mao, *Science* 331 **(2011)** 746-750.
3. Z.G. Yi, J.H. Ye, N. Kikugawa, T. Kako, S.X. Ouyang, H. Stuart-Williams, H. Yang, J.Y. Cao, W.J. Luo, Z.S. Li, Y. Liu, R.L. Withers, *Nature Materials* 9 **(2010)** 559-564
4. H. Tong, S.X. Ouyang, Y.P. Bi, N. Umezawa, M. Oshikiri, J.H. Ye, *Advanced Materials* 24 **(2012)** 229-251.
5. P. Wang, B.B. Huang, X.Y. Qin, X.Y. Zhang, Y. Dai, J.Y. Wei, M.H. Whangbo, *Angewandte Chemie International Edition* 47 **(2008)** 7931-7933.
6. R. Comparelli, E. Fanizza, M.L. Curri, P.D. Cozzoli, G. Mascolo, A. Agostiano, *Applied Cataysis B* 60 **(2005)** 1-11.
7. S. Baruah, M.A. Mahmood, M.T.Z. Myint, T. Bora, J. Dutta, *Beilstein Journal Nanotechnology* 1 **(2010)** 14-20.
8. R. Wahab, I.H.Hwang, Y.S. Kim, H.-S. Shin, *Chemical Engineering Journal* 168 **(2011)** 359-366.
9. M. Mrowetz, E. Selli, *Journal of Photochemistry and Photobiology A: Chemistry* 180 **(2006)** 15-22.
10. H. Xie, T. Zeng, S. Jin, Y. Li, X. Wang, X. Sui, X. Zhao, *Journal Nanoscience and Nanotechnol*ogy 13 **(2013)** 1461-1466**.**
11. R. Ullah, J. Dutta, *Journal of Hazardous Materials* 156 **(2008)** 194-200.
12. T. Sriskandakumar, N. Opembe, C-H. Chen, A. Morey, C. King'ondu, S.L. Suib, *Journal of Physical Chemistry A* 113 **(2009)** 1523-1530.
13. X. Zhou, J. Lan, G. Liu, K. Deng, Y. Yang, G. Nie, J. Yu, L. Zhi, *Angewandte Chemie International Edition* 51 **(2012)** 178-182**.**
14. Q.I. Rahman, M. Ahmad, S.K. Misra, M. Lohani, *Journal Nanoscience and Nanotechnol*ogy 12 **(2012)** 7181-7186.
15. X. Wu, K. W. Li, H. Wang, *Journal of Alloys and Comppounds* 487 **(2009)** 537-544.
16. Y. He, D. Li, G. Xiao, W. Chen, Y. Chen, M. Sun, H. Huang, X. Fu, *Journal of Physical Chemistry C* 113 **(2009)** 5254-5262.

17. R. Lucena, F. Fresno, J.C. Conesa, *Applied Catalysis A: General* 415-416 **(2012)** 111-117.
18. N.V. Hullavarad, S.S. Hullavarad, P.C. Karulkar, *Journal of Nanoscience and Nanotechnology* 8 **(2008)** 3272-3299.
19. X. Di, S.K. Kansal, W. Deng, *Separation and Purification Technol*ogy 68 **(2009)** 61-64.
20. S. Rengaraj, S.H. Jee, S. Venkataraj, Y. Kim, S. Vijayalakshmi, E. Repo, A. Koistinen, M. Sillanpaa, *Journal of Nanoscience and Nanotechnol*ogy 11 **(2011)** 2090-2099.
21. J.D. Patel, F. Mighri, A. Ajji, T.K. Chaudhuri, *Materials Letters* 100 **(2013)** 94-97.
22. Y. Guo, J. Wang, L. Yang, J. Zhang, K. Jiang, W. Li, L. Wang, L. Jiang, *CrystEngComm* 13 **(2011)** 5045-5048.
23. A.K. Sahoo, S.K. Srivastava, *Journal of Nanoparticle Res*earch 15 **(2013)** 1591-1606.
24. H.A.M. Ardon, F.U.Paredes, I.H.J. Arellano, S.D.Arco, *Materials Letters* 91 **(2013)** 96-99.
25. Y. Guo, J. Wang, Z. Tao, F. Dong, K. Wang, X. Ma, P. Yang, P. Hu, Y Xu, L. Yang, *CrystEngComm* 14 **(2012)** 1185-1188.
26. Y. Guo, L. Wang, L. Yang, J. Zhang, L. Jiang, X. Ma, *Materials Lett*ers 65 **(2011)** 486-489.
27. Y. Guo, L. Jiang, L. Wang, X. Shi, Q. Fang, L. Yang, F. Dong, and C. Shan, *Materials Lett*ers 74 **(2012)** 26-29.
28. Y. Guo, X. Shi, J. Zhang, Q. Fang, L. Yang, F. Dong, K. Wang, *Materials Lett*ers 86 **(2012)** 146-149.
29. R.K. Upadhyay, M. Sharma, D.K. Shinh, S.S. Amritphale, N. Chandra, *Separation and Purification Technol*ogy 88 **(2012)** 39-45.
30. F. Chen,Y. Cao,D. Jian, X. Niu, *Ceramics International* 39 **(2013)** 1511-1517.
31. L. Duan, W. Zhao, L. Xu, X. Chen, A. Lita, Z. Liu, *Journal of Nanoscience and Nanotechnol*ogy 13 **(2013)** 2242-2246.
32. T.D. Nguyen, D. Mrabet, T.T.D. Vu, C.T. Dinh, T.O. Do, *Cryst. Eng. Comm* 13 **(2011)** 1450-1460.
33. J.D. Patel, F. Mighri, A. Ajji, *Materials Lett*ers 74 **(2012)** 183-186.
34. F. Gao, Q. Lu, X. Meng, S. Komarneni, *Journal of Physical Chemistry C* 112 **(2008)** 13359-13365.

35. G. Lin, J. Zheng, R. Xu, *Journal of Physical Chemistry C* 112 **(2008)** 7363-7370.
36. W. Qingqing, X. Gang, H. Gaorong, *Crystal Growth & Design* 6 **(2006)** 1776-1780.
37. A.V. Naumov, V.N. Semenov, E.G. Goncharov, *Inorganic Materials* 37 **(2001)** 539-543.
38. N. Bao, L. Shen, T. Takata, K. Domen, A. Gupta, K.Yanagisawa, C.A. Grimes, *J. Phys. Chem. C* 111 **(2007)** 17527-15534.
39. P. Zhao, K. Huang, *Crystal Growth & Design* 8 (2008) 717-722.
40. S. Mahanty, D. Basak, F. Rueda, M. Leon, *Journal Electronic Materials* 28 **(1999)** 559-562.
41. K.S.W. Sing, D.H. Everett, R.A.W. Haul, L. Moscow, R.A. Pieroffl, J. Rouquerol, T. Siemieni-Ewska, *Pure & Applied Chemistry* 57 **(1985)** 603-619.
42. S.K. Kansal, M. Singh, D. Sud, *Journal of Hazardous Materials* 141 **(2007)** 581-590.

Chapter 11: Conclusion and Prospects

11.1 General conclusions

In this thesis, we developed simple synthetic routes for preparing metal chalcogenide nanomaterials and thin films using metal-organic complex precursors. The use of the developed nanocrystals, nanostructures and thin films in solar cells and in photocatalytic degradation of organic dyes in aqueous medium has been evaluated.

The obtained results presented in chapter 4 illustrated the effect of different precipitation techniques on the decomposition of methanolic Pb-TU complex precursor into PbS nanomaterials. The decomposition of Pb-TU complex under different conditions played an important role in the preparation of PbS nanomaterials of various sizes and shapes. The solvothermal decomposition of amino acid-mixed methanolic Pb-TU complex precursor resulted in PbS nanostructures. In chapter 5, we presented results on high yield solvothermal synthesis of star-shaped PbS crystals using and environmentally friendly ACA-mixed methanolic Pb-TU complex precursor. In chapter 11, we presented the solvothermal and hydrothermal routes for the preparation of CdS nanostructures using amino acid-mixed Cd-TU complex precursor. The hydrothermal decomposition of amino acid-mixed Cd-TU complex precursor produced six petal CdS dendritic flowers, while the solvothermal decomposition of the same precursor produced CdS NCs composed of CdS MSs. Both CdS nanostructures exhibited good physicochemical properties, and fast photocatalytic degradation of MeO and RhB in aqueous medium.

Like M-TU, M-O complex precursors are also advantageous in controlled synthesis of metal sulphide and selenide nanomaterials. In chapter 6, a generalized chemical route for the preparation of OA-capped metal sulphide NCs of CdS, ZnS and PbS using M-O complex precursors was presented in details. Sulphurization of M-O complex precursors at a relatively low temperature helped to produce highly stable metal sulphide NCs due to the presence OA chemisorbed as a carboxylate on the surface of metal sulphide NCs. It was shown that M-O complex precursors were useful to prepare metal selenide NCs but they required high boiling point non-polar solvent and prolonged the reaction time. In chapter 7, we presented results on high yield synthesis of OA-capped CdSe NCs using Cd-O complex and selenium powder

in 1,2,4 trichlorobenzene. It was shown that surface treatments of the as-synthesized CdSe NCs with pyridine and t-BA were very effective to replace long chain OA ligands. For the BHJ devices prepared with treated CdSe NCs, highly improved photovoltaic performance was observed compared to the device prepared with untreated CdSe NCs, which presented very poor photovoltaic parameters, particularly a very low PCE (0.0013%). The best performance improvement was obtained with t-BA treated CdSe NCs, especially in terms of cell short-circuit current density and power current efficiency that jumped from 0.016 to 2.16 mA/cm^2 and from 0.0013 to 0.24%, respectively. The improvement in photovoltaic performances was due to the increase of electron mobility in the P3HT:CdSe NCs blends after surface treatment of CdSe NCs. As revealed in chapter 9, surfactant-mixed M-O complex precursor was also useful to synthesize metal sulphide nanostructures. Solvothermal decomposition of thiourea-mixed Cd-O complex precursor produced NCs composed of cauliflower-like CdS MSs. The as-synthesized CdS MSs had good physicochemical properties with pronounced ability to degrade RhB in aqueous medium.

Results of chapter 8 described the spin-coating deposition of PbS and CdS films from methanolic solution of M-TU complex precursors. The resulted PbS and CdS films presented good structural, optical and photovoltaic properties. This route could be useful as an alternative of CBD to deposit other metal sulphide thin films.

11.2 Prospects

There are several directions that can be further pursued in the future:

1. Study of other M-TU complex precursors to see if a single precursor can be useful to synthesize metal sulphide nanomaterials of different sizes and morphologies via different routes.

2. Test of mild solvothermal and hydrothermal routes by using different surfactant-mixed M-TU complex precursors to obtaine metal sulphide nanomaterials of different sizes and morphologies.

3. Synthesize different metal selenide NCs using M-O complex precursors.

4. Study the effect of different surface treatments on photovoltaic performance of the polymers: CdSe NCs blends in BHJ solar cells.

5. Studies on spin-coating deposition and properties of different metal sulphide (like ZnS, $CuInS_2$, CZTS etc) thin films from their metal-thiourea complex precursors.

6. It is also very interesting to study the effect of chemical doping on PbS and CdS films to improve their performance in thin film solar cell

List of Publications

- **International Journals**

1. **Jayesh D. Patel**, Frej Mighri, Abdellah Ajji, and Tapas K. Chaudhuri. "Morphology and size control of lead sulphide nanoparticles produced using methanolic lead acetate trihydrate-thiourea complex via different precipitation techniques" ***Materials Chemistry and Physics*** 132 **(2012)** 747-755.

2. **Jayesh D. Patel**, Frej Mighri, and Abdellah Ajji. "Aminocaproic acid mixed methanolic lead-thiourea complex precursor and its thermal decomposition to star-shaped lead sulphide crystals" ***Materials Letters*** 74 **(2012)** 183-186.

3. **Jayesh D. Patel**, Frej Mighri, and Abdellah Ajji. "Generalized chemical route to develop fatty acid capped highly dispersed semiconducting metal sulphide nanocrystals" ***Materials Research Bulletin*** 47 **(2012)** 2016-2021.

4. **Jayesh D. Patel**, Frej Mighri, Abdellah Ajji, and Tapas K. Chaudhuri. "Fatty acid-assisted synthesis of CdS microspheres: physicochemical properties and photocatalytic activity" ***Materials Letters*** 110 **(2013)** 94-97.

5. **Jayesh D. Patel**, Frej Mighri, Abdellah Ajji, and Tapas K. Chaudhuri. "Development of CdS nanostructures by thermal decomposition of aminocaproic acid-mixed Cd-thiourea complex precursor: Structural, optical and photocatalytic characterization" ***In press, Journal of Nanoscience and Nanotechnology*** **(2014)**.

6. **Jayesh D. Patel**, Frej Mighri, Abdellah Ajji, and Tapas K. Chaudhuri. "Solution processed approaches for bulk-heterojunction solar cells based on Pb and Cd chalcogenide nanocrystals (Review Article)" ***Nano Energy*** 5 **(2014)** 36-51.

7. **Jayesh Patel**, Frej Mighri, Abdellah Ajji, and Tapas K. Chaudhuri. "Facile synthesis of CdSe nanocrystals for bulk-heterojunction solar cells" (***Submitted to Journal of Materials Science: Materials in Electronics***).

8. **Jayesh D. Patel**, Frej Mighri, Abdellah Ajji, Devendra Tiwari, and Tapas K. Chaudhuri. "Spin-coating deposition of PbS and CdS thin films for solar cell application" (***Submitted soon***).

- **Presentations in Symposiums/Conferences**

1. Frej Mighri, **Jayesh D. Patel**, Abdellah Ajji, A., 'Photovoltaic Cell Based on Lead Sulfide\Conjugated Polymer Bilayer Heterojunction' ***European Polymer Congress***, Granada, Spain, **2011**.

2. Frej Mighri, **Jayesh D. Patel**, Abdellah Ajji, 'Lead Sulphide (PbS) Nanostructured Thin Films and PbS Nanoparticles for Photovoltaic Application' ***International Workshop on Advanced Materials and Technologies for Global Energy and Environmental Challenges***, Pretoria, South Africa, **2010**.